

Structural and Functional Dissection of Allosteric Pathways in Myosin Motor Domains

der Naturwissenschaftlichen Fakultät
der Gottfried Wilhelm Leibniz Universität Hannover

zur Erlangung des Grades
Doktor der Naturwissenschaften
Dr. rer. nat.

genehmigte Dissertation

von

M. Sc. Krishna Chinthalapudi
geboren am 23.07.1982 in Srikakulam (India)

2011

Referent: Prof. Dr. Dietmar J. Manstein

Korreferent: Prof. Dr. Markus Kalesse

Tag der Promotion: 15.09.2011

Erklärung

Hiermit erkläre ich, Krishna Chinthalapudi, dass ich meine Dissertation selbständig verfasst und die benutzten Hilfsmittel und Quellen sowie gegebenenfalls die zu Hilfeleistungen herangezogenen Institutionen vollständig angegeben habe.

Dedicated to
My Beloved Parents

Acknowledgments

I owe my thanks to a number of people, each of whom contributed in their own way in achieving my goal in order to successfully finish my thesis work.

First of all, I would like to thank my supervisor Prof. Dr. Dietmar J. Manstein for giving me an opportunity to carry out my PhD thesis in his lab. I have benefited significantly from his deep insights and his passion for subtle details, which have made a significant impact on this research. It has been great to work in a very well equipped lab including the possibility to test crystals in the in-house X-ray facility.

I thank Prof. Dr. Markus Kalesse for his kind acceptance of being my thesis co-supervisor and examiner.

I thank PD Dr. Heiner Wolfes for his kind acceptance of being my examiner.

I thank Dr. Roman Fedorov for his constructive suggestions during the period of my research.

I would like to thank Prof. Dr. William Fenical for his generosity in providing ammosamide compounds.

I thank Ms. Lina Sell for her kind help in administration stuff. Also thanks to Dr. Joachim Griepel and Andreas Blaskowitz for the IT support.

I would like to thank my colleagues Dr. Amrita Rai, Dr. Manuel H. Taft, Jayashankar Selvadurai, Gunnar Wenninger, and Anne Hennig for creating pleasant atmosphere in the lab.

I would like to thank Dr. Sarah M. Heissler for sharing and helping me in preparing human myosin motor domain proteins. I deeply appreciate the efforts of her in making me understand the stopped-flow stuff.

I thank Dr. Gourinath Samudrala for his great contribution in engendering my interest in crystallography.

I thank my friends Shiva, Saleem, Jagan, Vijay, Kalyan and Bala Sai for their support outside the scientific world.

I thank my friends Dr. Sarah M. Heissler and Matthias Preller for their wonderful camaraderie, who made my stay in Germany very beautiful and special. Without their constant help, motivation and warmth, this thesis wouldn't have been reached this stage.

Finally, I owe absolutely everything to my parents, who are constant source of encouragement and great inspiration in pursuing my research. Without their love and affection, I wouldn't have reached this stage in my life.

**Asatoma Sadgamaya
Thamaso Maa Jyothir Gamaya
Mrithyor Maa Amrutham Gamaya
Aum Shanti Shanti Shantihi**

Meaning: Lead me from the unreal to the real. Lead me from darkness to light.

Lead me from death to immortality. May there be peace everywhere.

Summary

Myosins are molecular nanomachines that produce mechanical force from ATP hydrolysis by cyclically interacting with actin filaments. They are implicated in wide variety of diseases such as cancer, loss of neurosensory functions, nephritis, and familial hypertrophic cardiomyopathy. In this thesis, small molecule effectors were used to elucidate the molecular mechanisms underlying the function of disease-related myosin motors such as human nonmuscle myosin-2C and class-1 myosins and myosin-14 from apicomplexan parasites. X-ray crystallographic approaches were used to determine the first structure of human nonmuscle myosin-2.

The natural compound pentachloropseudilin (PCIP) was identified as a reversible and allosteric inhibitor of myosin ATPase and motor activities. In mammalian cells, PCIP selectively inhibits myosin-1c function. To elucidate the structural basis for PCIP-induced allosteric coupling and isoform-specific differences in the inhibitory potency of the compound, a multifaceted approach combining assays probing myosin kinetics and motor function, X-ray crystallography, and *in silico* modeling studies was used. The results indicate that allosteric inhibition by PCIP is mediated by the combined effects of global changes in protein dynamics and direct communication between the catalytic and allosteric sites via a cascade of conformational changes along a conserved communication pathway.

Ammosamides, another class of natural compounds produced by marine microorganisms, were used for the structural dissection of allosteric inhibition of myosin. Crystal structures of myosin motor domains in complex with ammosamides revealed two allosteric binding sites. The first site is identical to the 'pseudilin-binding' pocket. The second one is a novel-binding site near the helix-loop-helix region. Both binding sites undergo no major conformational changes upon ammosamide binding.

Work targeted at the structural and functional characterization of human nonmuscle myosin-2 isoforms led to determination of the crystal structure of the nonmuscle myosin-2c motor domain in the pre-power stroke state. The structure was solved to a resolution of 2.25 Å. Dissection of the structure provides novel insights about the molecular mechanisms underlying allosteric coupling in the myosin motor domain, which were further extended by the detailed analysis of nonmuscle myosin-2A mutant A454S.

Homology modeling of *Toxoplasma* MHC-MLC complexes showed that *TgMLC1:MyoA* and *TgMLC2:MyoD* form tight clamp like structures. Special features in both the light and heavy chains contribute to the compactness and uniqueness of the MLC-MHC interface. These structural features of the MLC-MHC interface make it an attractive drug target for the development of anti-apicomplexan drugs.

Key words:

Myosin, allostery, and energetic coupling

Zusammenfassung

Myosine sind molekulare Nanomaschinen, welche die Energie der ATP-Hydrolyse in mechanische Kraft umsetzen, indem sie zyklisch mit Aktinfilamenten interagieren. Myosine sind an der Entstehung einer Vielzahl von Krankheiten, beispielsweise Krebs, Nephritis und hypertropher Kardiomyopathie beteiligt. In der vorliegenden Arbeit wurden niedermolekulare Effektoren eingesetzt, um die molekularen Mechanismen von krankheitsrelevanten Myosin Motoren, wie beispielsweise nichtmuskulärem Myosin-2 sowie Myosinen der Klasse-1 des Menschen und des Myosins-14 von Apicomplexa Parasiten zu analysieren. In diesem Zusammenhang wurde mittels Röntgenstrukturanalyse die erste Struktur eines humanen Myosins, des nichtmuskulären Myosins-2C, bestimmt.

Der Naturstoff Pentachloropseudilin (PCIP) wurde als reversibler, allosterischer Inhibitor der Myosin ATPase und Motoraktivität identifiziert. In Säugerzellen konnte gezeigt werden, dass PCIP selektiv die Funktion des Myosins-1c inhibiert. Um die strukturelle Grundlage der PCIP-induzierten allosterischen Mechanismen und isoform spezifischen Unterschiede in der inhibitorischen Aktivität zu erforschen, wurde eine Kombination aus direkt funktionalen, kristallographischen und *in silico* Modeling Techniken eingesetzt. Die Ergebnisse dieser Studien deuten darauf hin, dass die allosterische Inhibition durch PCIP aus einer Kombination von globalen Veränderungen in der Proteindynamik sowie der direkten Kommunikation zwischen katalytischem und allosterischem Zentrum, vermittelt durch eine Kaskade aus Konformationsänderungen entlang eines konservierten Kommunikationswegs, entsteht.

Ammosamide, eine Naturstoffklasse produziert durch marine Mikroorganismen, wurden für die strukturelle Analyse der allosterischen Inhibition von Myosin eingesetzt. Die Kristallstrukturen von Myosin-Motordomänen im Komplex mit Ammosamiden zeigen zwei allosterische Bindungsstellen. Eine dieser Bindungsstellen ist die "Pseudilin-Bindungsstelle" während die zweite eine bisher unbekannte Bindungsstelle in räumlicher Nähe der Helix-Schleife-Helix Region darstellt. Beide Bindungsstellen zeigen keine prominenten Ammosamid-induzierten Konformationsänderungen im Proteinerückgrat.

Studien zur strukturellen und funktionalen Charakterisierung von Isoformen des humanen nichtmuskulären Myosins-2 resultierten in der Bestimmung der ersten Kristallstruktur der Motordomäne des humanen nichtmuskulären Myosins-2C im pre-power stroke Zustand mit einer Auflösung von 2.25 Å. Die Strukturanalyse gibt neue Einsichten in die Allosterie der Myosin-Motordomäne, welche durch die funktionale Analyse des nichtmuskulären Myosins-2A und dessen Mutante A454S erweitert wurde.

Homologiemodellierung von *Toxoplasma* MHC-MLC zeigte, dass die Komplexe *Tg*MLC1:MyoA und *Tg*MLC2:MyoD klammerartige Strukturen ausbilden. Ausgeprägte Merkmale sowohl in den leichten Ketten als auch der schweren Kette tragen zur Kompaktheit sowie der Spezifität der MLC-MHC Kontaktregion bei. Niedermolekulare Verbindungen können in diesem Kontext neue Einblicke in die Struktur- und Funktionsdynamik von molekularen Motoren und damit in die Funktionsweise und molekulare Kopplung ermöglichen. Die einzigartige Zusammensetzung der engen MLC-MHC Kontaktfläche macht diese zu einer attraktiven Zielstruktur für die Entwicklung von Anti-Apicomplexa Wirkstoffen.

Schlüsselwörter:

Myosine, Allosterie, und energetische Kopplung

Acronyms and Symbols

Å	Angstrom
A	Ampere
A	2'-desoxyadenosine-5'-monophosphate
Aa	Amino acid(s)
ADP	Adenosine-5'-diphosphate
AMP	Adenosine-5'-monophosphate
Amp	Ampicillin
AP	Alkaline Phosphatase
ATP	Adenosinetriphosphate
Bp	Base pair(s)
BEVS	Baculo Expression Vector System
BLAST	Basic Local Alignment Search Tool
BSA	Bovine Serum Albumin
C	2'-desoxycytosine-5'-monophosphate
C-	Carboxy-
°C	Degree Celsius
CCD	Charge Coupled Device
CIAP	Calf Intestine Alkaline Phosphatase
CM-	Cardiomyopathy-
Cryo-EM	Cryo-electron microscopy
CV	Column Volume
D	desoxy
<i>Dd</i>	<i>Dictyostelium discoideum</i>
Da	Dalton
DNA	Desoxyribonucleic acid

DTT	Dithiothreitol
<i>E.coli</i>	<i>Escherichia coli</i>
EDTA	Ethylenediaminetetraacetic acid
EGTA	Ethylenglycoltetraacetic acid
ELC	Essential Light Chain
F-actin	Filamentous Actin
FPLC	Fast Performance Liquid Chromatography
FRET	Förster Resonance Energy Transfer
<i>g</i>	Gravitational constant
g	Gram
G-actin	Globular Actin
<i>Gg</i>	<i>Gallus gallus</i>
h	hours
HEPES	(4-(2-HydroxyEthyl)-1-PiperazineEthaneSulfonic acid
His	Histidine
(His) ₈ -tag	Octahistidine-tag
HMM	Heavy Mero Myosin
IPTG	IsoPropyl β-D-1-ThioGalactopyranoside
IR	Infra Red
k	kilo
kDa	Kilodalton
l	litre
LDH	Lactate Dehydrogenase
LB	Luria Bertani
μ	Micro
μM	Micro Molar
μm	Micro Meter

mM	Milli Molar
mm	Milli Meter
M	Mole
Mant	N-Methylantraniloyl-
MCS	Multiple Cloning Site
Mg	Magnesium
min	Minutes
MLC	Myosin Light Chain
MME	Mono Methyl Ether
MPD	2-Methyl-2,4-PentanDiol
MR	Molecular Replacement
MW	Molecular Weight
N-	Amino-
NAD	Nicotinamide adenine dinucleotide
NADH	Nicotinamide adenine dinucleotide, reduced form
Ni-NTA	Nickelnitriloacetic
nm	Nano Meter
OD	Optical Density
PAGE	Polyacrylamide Gel Electrophoresis
PBS	Phosphate buffered saline
PCIP	PentaChloroPseudilin
PCR	Polymerase Chain Reaction
PDB	Protein Data Bank
PEG	Poly Ethylene Glycol
PEP	Phosphoenolpyuvate
P _i	Inorganic Phosphate
PK	Pyruvate Kinase

PSO	Particle Swarm Optimization
2R	Artificial Lever Arm
RLC	Regulatory Light Chain
RT	Room temperature
rpm	Revolutions per minute
RMSD	Root Mean Square Deviation
s	Seconds
S1	Myosin Subfragment S1
SDS	Sodiumdodecylsulfate
<i>Sf9</i>	<i>Spodoptera frugiperda</i>
T	2'-desoxythymidine-5'-monophosphate
TIRF	<i>Total Internal Reflection Fluorescence</i>
TRITC	Tetramethyl Rhodamine Iso-Thiocyanate
U	Units
UV	Ultra-violet
V	Volt
VdW	Vander Waal
v/v	Volume/volume
w/v	Weight/volume

Table of Contents

1. INTRODUCTION	1
1.1 Molecular Motors.....	1
1.2 Myosin Super Family.....	3
1.2.1 Nonmuscle Myosin-2	5
1.2.2 Toxoplasma Myosins	7
1.3 Myosin-2 Structure	9
1.3.1 Myosin Motor Domain and its Key Structural Features	10
1.3.2 Nucleotide Binding Pocket.....	11
1.3.3 Relay Helix and Converter Domain.....	13
1.3.4 Surface Loops and their Functional Importance.....	14
1.3.5 The ATPase Cycle.....	16
1.4 Allosteric Regulation.....	18
1.4.1 Allosteric Communication in Myosin Motor Domains.....	19
1.4.2 Small Molecule Effectors	20
2. Material and Methods	27
2.1 Materials.....	27
2.1.1 Consumables.....	28
2.1.2 Chemicals.....	29
2.1.3 Enzymes.....	33
2.1.4 Reagent Kits	33
2.1.5 Vectors	34
2.1.6 Protein Standards	34
2.1.7 Antibodies.....	34
2.1.8 Microorganisms	34
2.2 METHODS	35
2.2.1 Protein Preparation from <i>Sf9</i> Cells.....	35
2.2.2 Actin Preparation	37
2.2.3 The Baculovirus/ <i>Sf9</i> -System.....	40
2.2.3.3 Insect Cell Culture	42
2.2.3.4 Transfection.....	44
2.2.3.5 Amplification and Isolation of Recombinant Baculovirus	44
2.2.3.6 Protein Production and Isolation of Expressing Cells	45
2.2.4 Dictyostelium discoideum Cell Culture	45
2.2.5 Biophysical Methods.....	52
2.2.5.1 Steady-State ATPase Assay.....	52
2.2.5.2 Transient kinetics.....	54
2.2.5.3 Stopped-flow techniques.....	54
2.2.5.4 <i>In vitro</i> Motility assay	57
2.2.6 Crystallographic Methods	59
2.2.7 Homology Modeling	66
2.2.8 Docking	68
3. RESULTS	71
3.1 Small Molecule Effectors	71
3.1.1 Pentachloropseudilin	71
3.1.1.1 Mechanism of PCIP-Mediated Inhibition of Myosin Motor Activity	72
3.1.1.2 PCIP is a Reversible Inhibitor of Myosin Motor Activity	75

3.1.1.3 <i>In vitro</i> Motility Assay of <i>Dd</i> myosin-1B in the Presence of PCIP.....	76
3.1.1.4 PCIP Inhibits Cellular Functions of Human Myosin-1c.....	77
3.1.1.5 The Structural Basis of PCIP-Mediated Inhibition.....	79
3.1.1.6 Myosin Isoform-Dependent Interactions with PCIP	83
3.1.2 Ammosamides.....	89
3.1.2.1 Ammosamides Target Myosin-2	89
3.1.2.2 Ammosamides Inhibit Myosin-2 ATPase Activity.....	90
3.1.2.3 Single-Turnover Experiments with Ammosamides	92
3.1.2.4 Structural Basis of Ammosamides Inhibition	93
3.2 Human Nonmuscle Myosin-2C (NMH-2C).....	97
3.2.1 Crystal Structure of Human Nonmuscle Myosin-2C (NMH-2C) Motor Domain in the Pre-Power Stroke State	98
3.2.2 Comparison of Pre-power Stroke State Structures of Class-2 Myosins.....	101
3.2.3 Unique Features of Lever Arm	106
3.3 Structural Models of <i>Toxoplasma gondii</i> Myosin Heavy Chain (MHC) and Myosin Light Chain (MLC) Complexes.....	109
3.3.1 Structural model of <i>Tg</i> MLC1 in Complex with <i>Tg</i> MyoA-tail	109
3.3.2 The Compact Structure of <i>Tg</i> MLC2 in Complex with <i>Tg</i> MyoD-tail	112
3.4 Structural and Kinetic Characterization of Human Nonmuscle Myosin-2A and its Switch-2 Mutant.....	116
3.4.1 Switch-2 Motif in Different Myosin Isoforms	116
3.4.2 <i>In silico</i> modeling of <i>Hs</i> NM2A and its switch mutant A454S.....	118
3.4.3 Expression and Purification	120
3.4.4 Kinetic Measurements	121
4. Discussion.....	137
4.1 Pentachloropseudilin as a Potent Class-1 Myosin Inhibitor.....	137
4.1.1 Conformational Changes in the Allosteric Binding Pocket.....	138
4.1.2 PCIP Induced Novel Allosteric Relay Mechanism	139
4.2 Ammosamides as Allosteric Myosin Effectors.....	141
4.3 Pre-power Stroke State of Nonmuscle Myosin-2C	143
4.4 <i>Toxoplasma</i> MHCs: MLCs Interaction.....	144
4.5 Kinetic and Structural Characterization of Nonmuscle Myosin-2A Switch-2 Mutant A454S.....	145
5. References.....	149
6. Publications and Presentations.....	162
6.1 Publications:.....	162
6.2 Poster Presentations.....	163

1. INTRODUCTION

1.1 Molecular Motors

Various forms of motion in the cell are driven by molecular motors, which convert the chemical energy of nucleoside triphosphate (NTP) hydrolysis into mechanical force (Bourne et al, 1991; Lymn & Taylor, 1971). Most forms of directed movement are powered by cytoskeletal molecular motors from the dynein, kinesin and myosin superfamilies (Vale, 2003) (Figure 1.1). Members of the myosin superfamily can traffic towards the plus-end or the minus-end of actin filaments. Kinesins move in the plus or minus-end direction of microtubule tracks, and all dyneins move to the minus-end of microtubule tracks (Kolomeisky & Fisher, 2007).

The multitude of cellular functions driven by molecular motors is possible because the structure and regulation of the particular motors in each family can vary considerably, despite strong similarities in their catalytic cores (Veigel & Schmidt, 2011). It is therefore not surprising that defects in motor-dependent transport are associated with a wide range of diseases, including neurodegeneration, tumorigenesis and developmental defects (Afflitto & Inchiosa, 1979; Hirokawa et al, 2009). Basic principles of motor design and mechanism have been derived, and an understanding of their complex cellular roles is emerging rapidly (Schliwa & Woehlke, 2003).

Studies on the eukaryote-specific molecular motors and their diversification within the cytoskeleton have proved to be particularly useful for understanding phylogenetic patterns, domain evolution and functional traits. Gene families with numerous paralogues, such as myosins, are often considered unfavorable for rebuilding ancient evolutionary relationships because of their very complexity. However, *Richards et al.* has shown that domain architecture of myosins is one of the criteria for sufficient taxon sampling and reliable mapping of ancient molecular motors evolution (Richards & Cavalier-Smith, 2005).

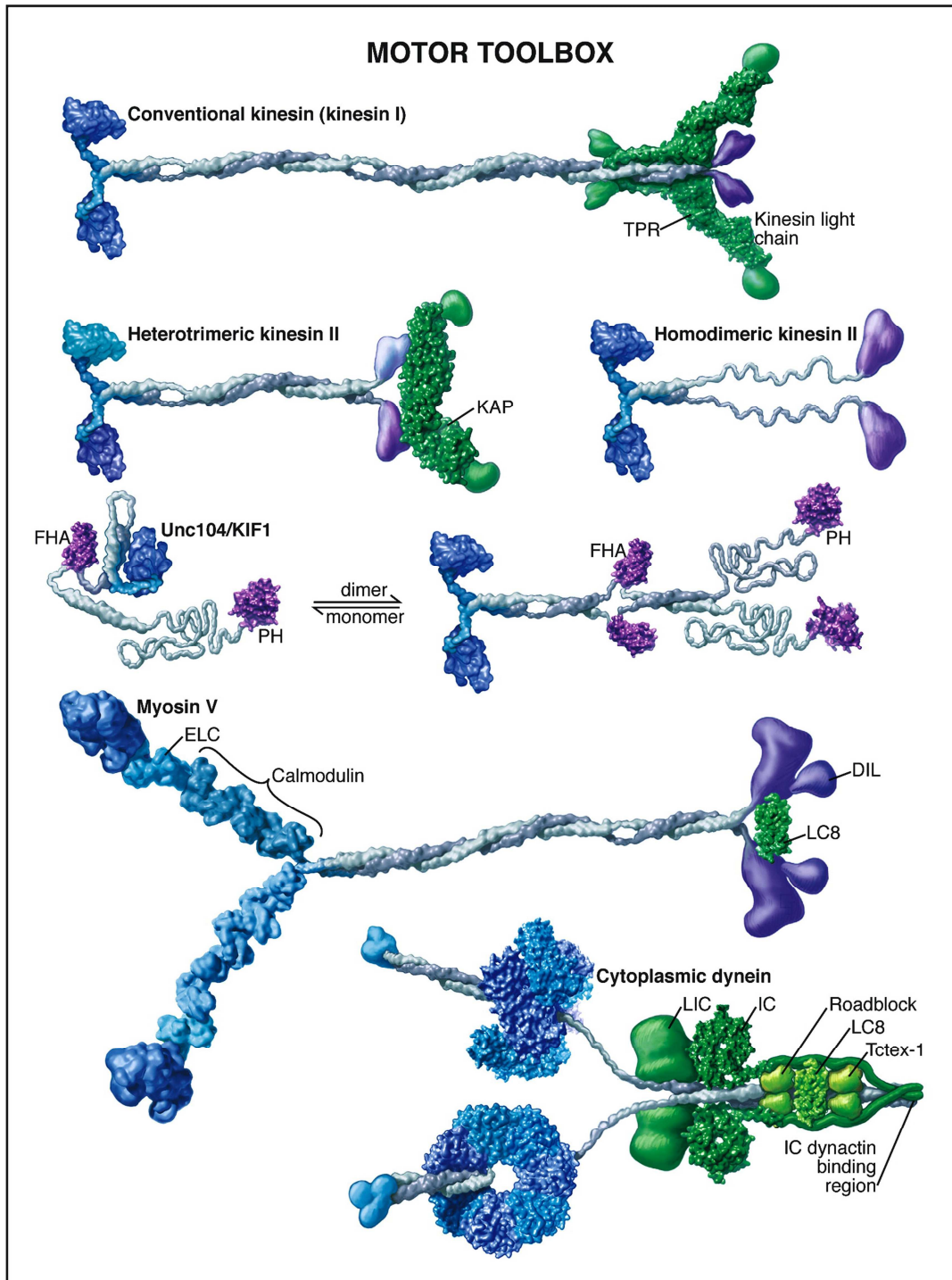


Figure 1.1: Overview of selected cytoskeletal motor proteins. The motor catalytic domains are displayed in blue, mechanical amplifiers in light blue, and tail domains implicated in cargo attachment are shown in purple. Tightly associated motor subunits (light chains) are shown in green. This figure is adapted from Vale R. D, *Cell* (Vale, 2003).

1.2 Myosin Super Family

Myosins are molecular nanomachines that produce mechanical force from ATP hydrolysis by cyclically interacting with actin filaments (Geeves et al, 2005). As ATPases, they convert the free energy obtained from ATP hydrolysis into mechanical work and force production, thereby carrying out essential functions ranging from the movement of entire cells to intracellular structural dynamics and transport, muscle contraction, and mechanical signal transduction (Mermall et al, 1998; Veigel & Schmidt, 2011; von Delius et al, 2010).

The first myosin found was the double-headed skeletal muscle myosin, which was discovered in the 19th century (Kühne, 1864). A hundred years after the discovery of muscle myosin, Pollard and Korn discovered myosins consisting of a single myosin heavy chain in *Acanthamoeba* (Pollard & Korn, 1973). Following their discovery, Korn and colleagues termed these myosins class-1 myosins in contrast to the conventional myosins comprising two myosin heavy chains, each associated with two light chains (Hammer et al, 1986). However, it soon became clear that this is not a valid basis for the classification of the members of the myosin superfamily. Therefore, class numbers were assigned later in the order in which the novel myosin sequences were first described in the scientific literature (Mooseker & Foth, 2008).

All myosin classes observed today are likely to be derived from a single progenitor molecule by a process involving gene duplications and diversification (Hodge & Cope, 2000). Members of the myosin superfamily consist of a 'generic' motor domain attached to a variety of unique and functionally specialized tail domains anchored by a neck domain. Myosin heavy chains have been categorized into 24 classes, based on comparisons and phylogenetic analysis of the 'generic' motor domain (Foth et al, 2006). Figure 2 embraces the phylogenetic tree of all different myosin classes identified so far. As schematically depicted in figure 2, the myosin class-2 family comprises the largest number of known members (Figure 1.2) including the classical two headed, filament forming dimeric myosins found in skeletal muscle, cardiac

muscle, smooth muscle and virtually all non-muscle cells (Korn et al, 1988). Conventional myosins are solely represented by members of myosin class-2 family, whereas all other myosins are classified as unconventional (Redowicz, 2007).

In this thesis, different myosins from classes-1, -2, -5 and -14 over a vast range of organisms from *D.discoideum*, mammals and Apicomplexans have been used. Therefore, selected myosins of classes-2 and -14 are presented in more detail in the following sections.

A Myosin Family Tree

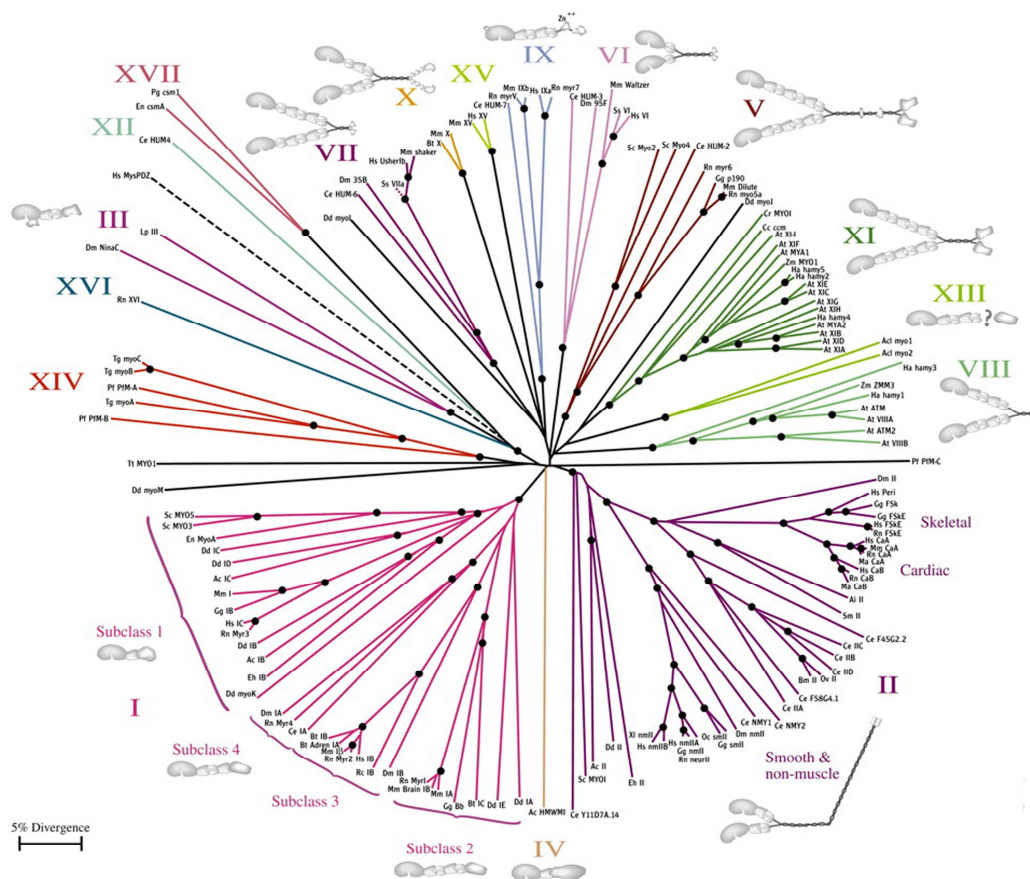


Figure 1.2: Unrooted phylogenetic tree of myosin superfamily (Hodge & Cope, 2000).

1.2.1 Nonmuscle Myosin-2

Nonmuscle myosin-2s are members of the class-2 myosin family. The term nonmuscle myosin is a misnomer because nonmuscle myosins can be expressed in both muscle and nonmuscle cells. They represent a branch of the myosin superfamily that is closely related to skeletal and smooth muscle myosins (Buxton et al, 2003) (Figure 1.3).

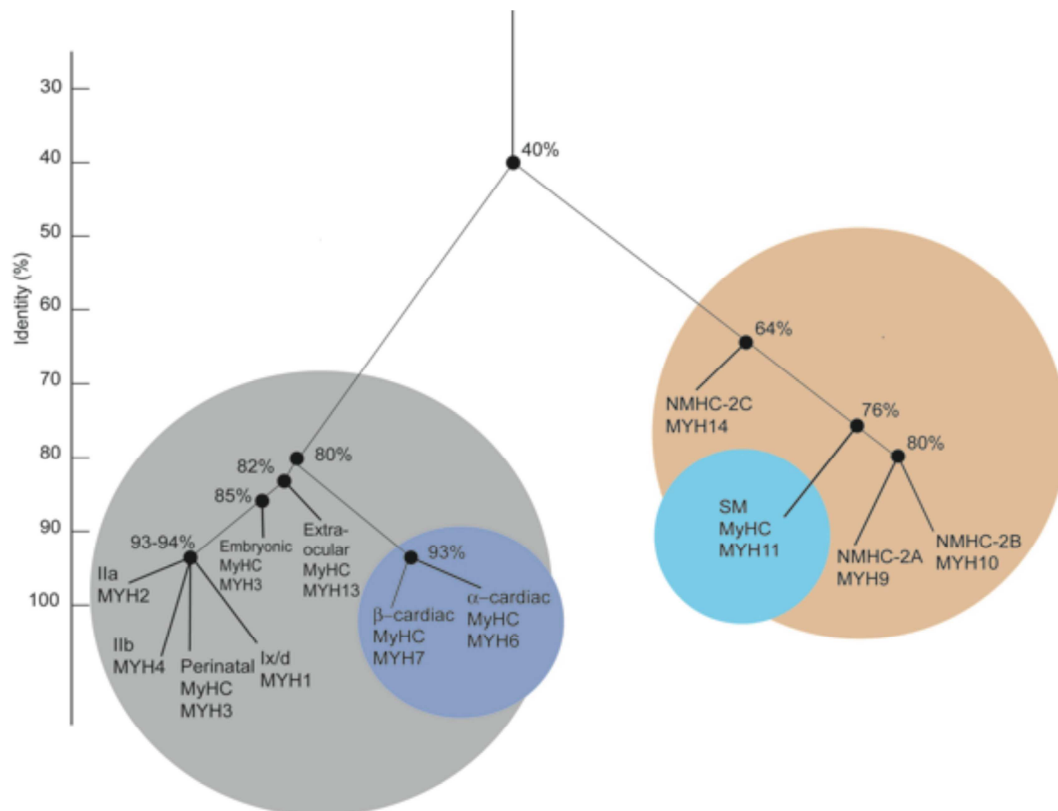


Figure 1.3: Phylogenetic tree of the human class-2 myosin heavy chains based on the sequence analysis of the motor domain. The y-axis displays the scale of amino acid sequence identity. Members of the nonmuscle myosin subclass are highlighted in brown and smooth muscle myosin in teal. Cardiac and skeletal muscle myosins are highlighted in blue and grey, respectively. Figure adapted and modified after Golomb *et al*, *JBC* (Golomb et al, 2004).

Three types of nonmuscle myosin-2 isoforms are identified so far: nonmuscle myosin heavy chain-2A (NMHC-2A), nonmuscle myosin heavy chain-2B (NMHC-2B) and nonmuscle myosin heavy chain-2C (NMHC-2C). The genes encoding the nonmuscle myosin-2 isoforms are designated *MYH9*, *MYH10* and *MYH14*. At protein level, nonmuscle myosins follow classical domain architecture of myosin-2 molecules consisting of an N-terminal motor domain, a neck domain and an

adjacent α -helical coiled coil terminating in a short non-helical tail. The coiled coil region forms the rod-like domain and enables the dimerization of two myosin heavy chains (Sellers, 2000b). The assembly allows the interaction between the myosin filament and adjacent actin filaments. Remarkably, these filaments are substantially (20-30 fold) shorter than those of skeletal or cardiac muscle myosin and comprise around 28 myosin molecules (Rosenfeld et al, 2003); (Verkhovskiy & Borisov, 1993). To date, there is no evidence about the formation of co-filaments between different nonmuscle myosin-2 isoforms (Golomb et al, 2004; Vicente-Manzanares et al, 2009b).

Nonmuscle myosin-2 isoforms show > 85% sequence similarity in their catalytically active motor domain. Alternative splicing is the major source of functional diversity among the nonmuscle myosin-2 isoforms (Kondrashov & Koonin, 2003). Alternate splicing of the *MYH14* gene leads to the production of different splice variants in humans (Golomb et al, 2004; Jana et al, 2009; Leal et al, 2003). The putative amino acid sequences between the NMHC-2C motor domains of the transcript variants are well conserved with an identity of 96-99% (Heissler & Manstein, 2011). Isoform 2C1 differs only by an 8 amino acid extension of loop-1. Isoform 2C2 has the same extension of loop-1 and an additional 33 amino acid extension in loop-2 and isoform 2C0 represents the shortest isoform without loop extensions (Heissler & Manstein, 2011).

The function of nonmuscle myosins is diverse, ranging from cell adhesion, cell division to cell migration (Vicente-Manzanares et al, 2009b). In smooth muscles, nonmuscle myosins are required for maintaining tension whereas in skeletal muscles they are important for muscle development and differentiation (Vicente-Manzanares *et al*, 2009). Due to the universal expression pattern and their participation in fundamental cellular processes, it is not surprising that mutations in nonmuscle myosins are associated with a large range of diseases, such as macrothrombocytopenia, deafness, nephritis and many more (Donaudy et al, 2004). *MYH9*-related diseases include giant-platelet disorders like May-Hegglin anomaly and Fetchner syndrome (Althaus & Greinacher, 2009; Hu et al, 2002).

MYH14 is implicated in autosomal dominant nonsyndromic neural hearing loss (Donaudy et al, 2004).

1.2.2 *Toxoplasma* Myosins

The phylum Apicomplexa comprises protozoan parasites of several medically and veterinary relevant obligate intracellular parasites such as *Plasmodium* (malaria), *Toxoplasma* (toxoplasmosis), *Cryptosporidium* (cryptosporidiosis), *Babesia* (babesiosis) and *Eimeria* (coccidiosis). Parasitic infections with Apicomplexans lead to considerable economic losses by infecting livestock (Homer et al, 2000; Morris, 1843; Wolf et al, 1939). Members of the Apicomplexa are morphologically unified by a common set of apical structures, including the conoid, the polar ring complex, sub-pellicular microtubules and secretory organelles including micronemes, rhoptries and dense granules (Morrissette & Sibley, 2002). The pellicle of the invasive forms of these parasites consists of the plasma membrane and the two membranes of the inner membrane complex (IMC), a continuous layer of flattened vesicles underlying the plasma membrane. In the absence of locomotive organelles such as cilia or flagella, the invasive forms of these parasites have an unusual form of substrate-dependent motility that is essential for host cell invasion (Sibley et al, 1998). Like most Apicomplexans, the invasive stages of *T.gondii* enter host cells by an active process dependent on gliding motility. *T.gondii* tachyzoites exhibit three distinct modes of locomotion: circular gliding, upright twirling and helical rotation (Hakansson et al, 1999), and all three are powered by the parasite actomyosin system (Opitz & Soldati, 2002). Among the Apicomplexans, the *T.gondii* genome comprises the largest known myosin repertoire of 11 myosin heavy chains (*TgMyoA* to *TgMyoK*) allocated to different classes, including class XIV (Foth et al, 2006).

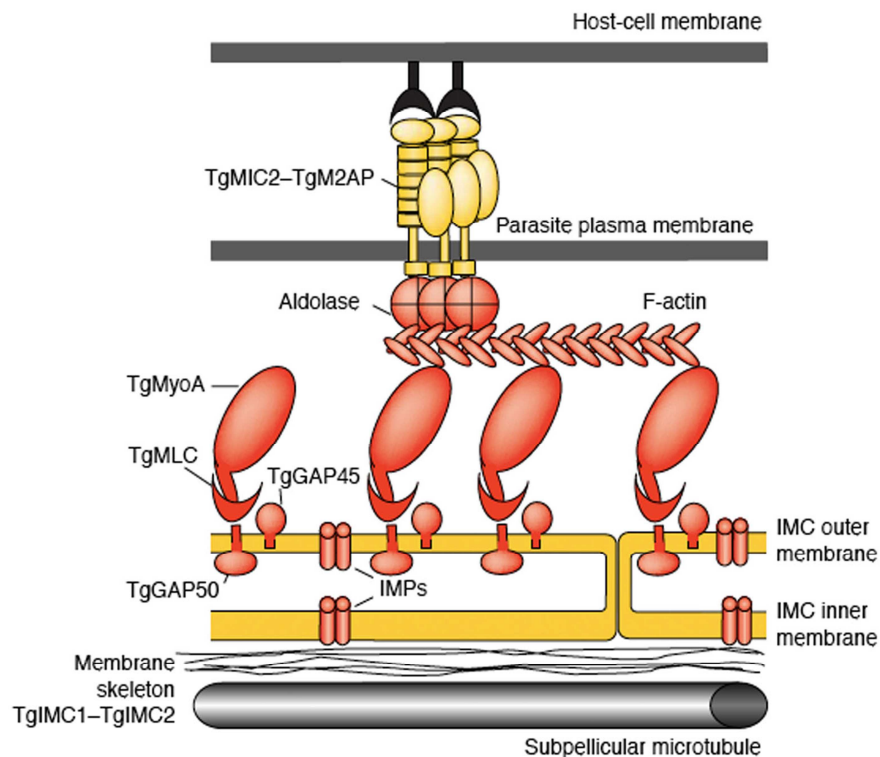


Figure 1.4: Schematic architecture of the glideosome in *T. gondii*. *T. gondii* comprises the motor complex [myosin A (*TgMyoA*), the myosin light chain (*TgMLC*), *TgGAP45* and *TgGAP50*], which is anchored to the outer membrane of the IMC and connected via F-actin and the aldolase to the hexameric micronemes protein complex (*TgMIC2-TgM2AP*), which, in turn, interacts with host-cell receptors. Adopted from Keeley A and Soldati D. 2004, *Trends in Cell Biol.* (Keeley & Soldati, 2004)].

TgMyoA and *TgMyoD* belong to class XIVa myosins (Foth et al, 2006; Hettmann et al, 2000). *T. gondii* MyoA orthologues have been found in other Apicomplexan genomes, including *Neospora caninum*, *Cryptosporidium parvum* and *Eimeria tenella*. *TgMyoA* is associated to the myosin light chain MLC1 (also called myosin A tail interacting protein (MTIP)) in *Plasmodium* species (Bergman et al, 2003; Herm-Gotz et al, 2002) and plays an essential role in parasite motility and invasion (Meissner et al, 2002). This motor was previously shown to be part of a large complex composed of the gliding-associated proteins GAP45 and GAP50 (Gaskins et al, 2004). This complex initially described as the “glideosome” (Opitz & Soldati, 2002) is located to the pellicle, in the space between the plasma membrane (PM) and the IMC (Keeley & Soldati, 2004) (Figure 1.4).

Depletion of *TgMyoA* impairs both host cell invasion and parasite egress (Meissner et al, 2002). As the inhibitors of actin filament polymerization (cytochalasin D) and the myosin ATPase (butanedione monoxime (BDM)) disrupt the three forms of *T.gondii* gliding motility (Hakansson et al, 1999), parasite movement suggests the involvement of more than one myosin. *TgMyoD* is the shortest *T.gondii* myosin identified so far, with a size of 91-kDa (Herm-Gotz et al, 2006). *TgMyoD* is a motor found only in coccidians and shown to be dispensable for tachyzoites (Herm-Gotz et al, 2006). Since *TgMyoD* is more prominently expressed in bradyzoites, it may fulfill an important function in the invasive stage. Recently, *Toxoplasma* myosin light chain 2 (*TgMLC2*) was identified as the interaction partner of *TgMyoD*. *TgMLC2*, only found in coccidians, is associated with *TgMyoD* via its calmodulin-like domain and anchored to the plasma membrane of *T.gondii* via its N-terminal extension (Polonais et al, 2011).

1.3 Myosin-2 Structure

Skeletal muscle myosin-2 is the conventional myosin prototype responsible for producing muscle contraction. It is a hexamer with a total molecular weight of 520 kDa. It is composed of two heavy chains and four light chains. Each of the two heavy chains has a molecular weight of 220 kDa and is characterized by a globular head domain at the N-terminus and a α -helix at the C-terminus. The C-terminal tail region is periodically interspersed with hydrophobic residues to give a “coiled coil” type rod. The tails are connected to the heads at the neck, which is the location of the hinge region or the pliant region (Geeves & Holmes, 1999; Gourinath et al, 2003). The four light chains weigh about 20 kDa each and are paired into two regulatory chains and two essential light chains. Each head of the protein has one chain of each type.

The proteolytic fragment S1 comprises the first 843 residues of the heavy chain together with the two light chains. Myosin S1 is a fully competent actin-activated ATPase that transports actin in *in vitro* motility assays. Further limited proteolysis breaks the S1 into three fragments named after apparent molecular masses; the N-terminal 25 kDa domain, the 50 kDa middle domain [divided into 50 kDa upper

and lower sub-domains] and the C-terminal 20 kDa domain (Geeves & Holmes, 1999) (Figure 1.5). The first X-ray crystal structure of a myosin motor was obtained using S1 from chicken pectoralis muscle without nucleotide but with a sulfate ion in place of the γ -phosphate in the active site (Rayment et al, 1993). The structure shows the S1 to be tadpole-like in form. All three proteolytic fragments (25 kDa, 50 kDa, and 20 kDa) contribute to the central 7-stranded β -sheet. The α -helices that surround this central β -sheet form a deep cleft extending from the nucleotide-binding site to the actin-binding region.

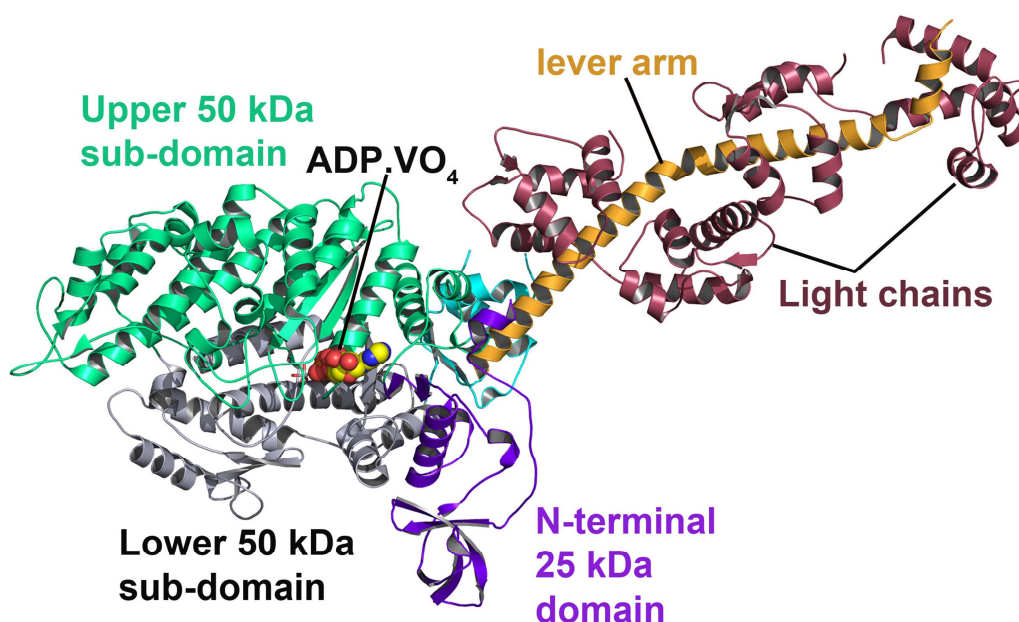


Figure 1.5: Crystal structure of myosin S1 from scallop striated adductor muscle (pdb-code: 1QVI). The proteolytic fragments are labeled as follows: 25 kDa (N-terminal), 50 kDa (middle) and 20 kDa (C-terminal). The 50 kDa fragment actually spans two domains, called as the 50 kDa upper subdomain and the 50 kDa lower subdomain. The ATP-binding site is in this large domain near the 25 kDa – 50kDa fragment boundary and contains a characteristic P-loop similar to that found in many ATPases and G-proteins. S1 has an elongated head consisting of a seven-stranded β -sheet and a C-terminal α -helical tail or ‘neck’, which carries two calmodulin-like light chains - the regulatory chain and the essential light chain. The C-terminal tail with its associated light chains has been called the “neck” or the “lever arm”.

1.3.1 Myosin Motor Domain and its Key Structural Features

In several structural studies, myosin head fragments (761 residues) from *Dictyostelium discoideum* were generated genetically by terminating the myosin heavy chain in the long α -helix that forms the backbone of the light chain-binding

motif (Fedorov et al, 2009; Fisher et al, 1995; Gulick et al, 2000). This truncated myosin head retains a limited ability to move and crystallizes readily without the need for chemical modification. High-resolution crystal structures of the myosin head with and without nucleotides bound have provided detailed structural analysis of the motor domain (Gulick et al, 1997; Reubold et al, 2003).

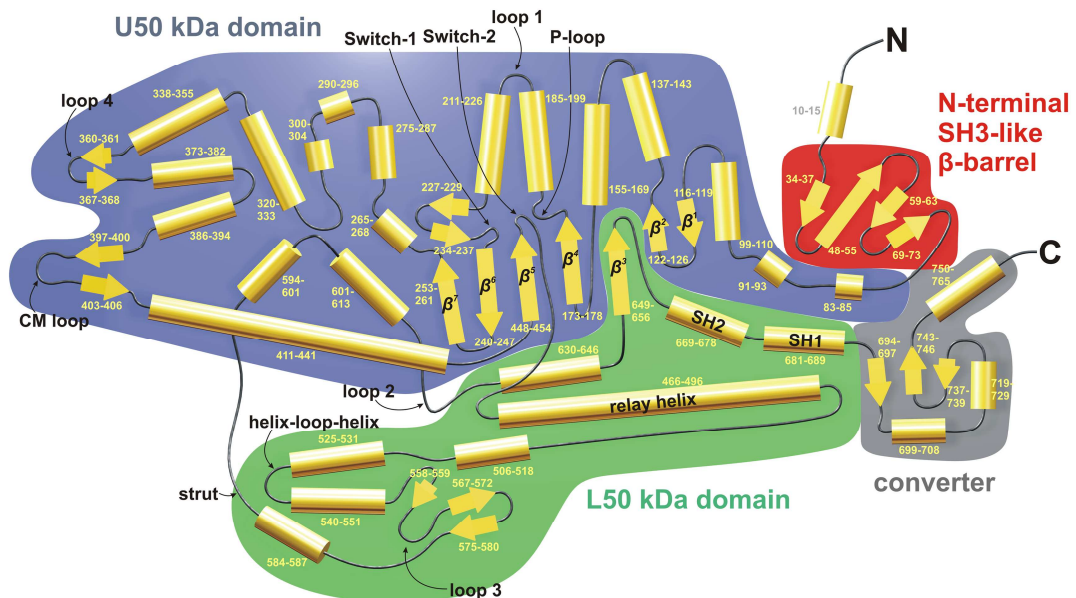


Figure 1.6: Topological representation of myosin motor domain. Helices are shown as cylinders and β -strands as arrows. The core of the myosin motor domain is formed by central, seven-stranded β -sheet and surrounding α -helices. Figure adapted from Preller *et al* (Preller & Manstein, 2011).

Comparison of these structures has shown that the motor domain (MD) is most simply described as comprising four major subdomains that are linked by three major structural elements, so-called joints that are highly conserved in sequence (Figure 1.6). A first joint, switch-2, links the upper and lower 50 kDa subdomains near the γ -phosphate pocket. The other two joints, the relay and the SH1 helix, link the converter to the lower 50 kDa and the N-terminal subdomains, respectively.

1.3.2 Nucleotide Binding Pocket

The nucleotide binding pocket is located at the interface between the 50 kDa and N-terminal subdomains. It is composed of four major loops that are highly

conserved not only among myosins but also among the G-proteins (Vale, 1996). The nucleotide binding pocket comprises the purine-binding loop or adenine binding loop [A-loop] (NPxxxxxY) on one side and the switch-1 (NxxSSR), P-loop (GESGAGKT) and switch-2 (DlxGFE) elements that sandwich the polyphosphate moiety of the nucleotide on the other side (Figure 1.7A).

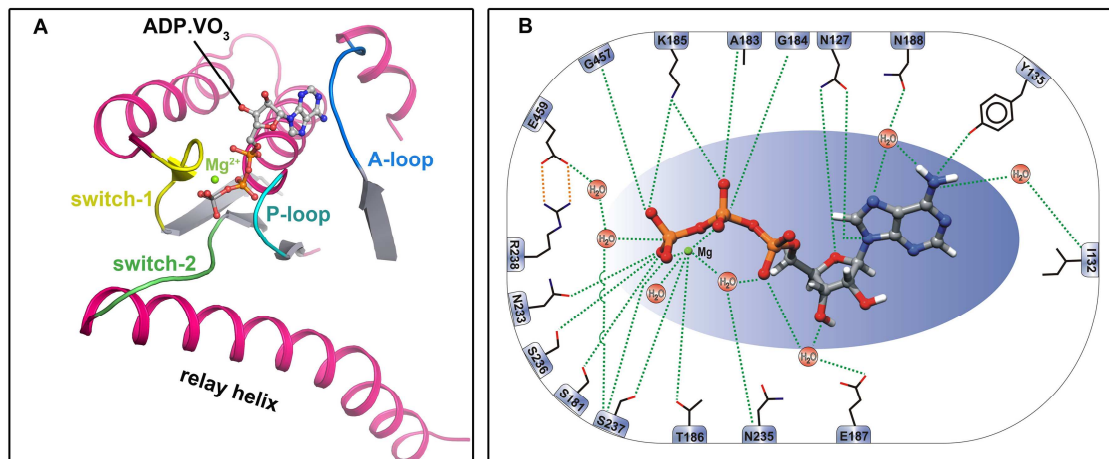


Figure 1.7: (A) Cartoon representation of the active site of myosin-2 motor domain. Key elements in the active site are color coded and labeled accordingly. (B) Schematic representation of the coordination of the Mg•ATP in the nucleotide-binding pocket of myosin-2 motor domain. This figure adapted from Preller & Manstein, 2011.

The purine ring of the nucleotide is in anti-conformation relative to the ribose, which exhibits a C3'-endo ring pucker. The binding site for the purine ring is formed almost exclusively from residues in the N-terminal subdomain (Rayment et al, 1996). The P-loop, the switch-1 and -2 loops together form the so-called “phosphate tube” around the phosphate moieties of ATP. The P-loop is a glycine rich element that binds to the γ -phosphate end of the nucleotide. The two switch loops obtained their names from the observation that they can adopt different conformations and thereby serve as a switch for information transduction by changing their conformation (Koppole et al, 2006); (Reubold et al, 2003).

Several high-resolution motor domain structures have shown that the Mg^{2+} ion shows hexacoordination with surrounding structural elements in the nucleotide-binding pocket (Figure 1.7B). These elements include two oxygens of the γ - and the β -phosphates of ATP, the side chains of S237 and T186, and two water

molecules. Mutational studies have shown crucial roles of residues K185 of the P-loop, R238 of switch-1 and G457 as well as E459 of switch-2 in the ATP hydrolysis reaction. Mutation of these residues resulted in a loss or substantial decrease of the myosin ATPase activity (Sasaki et al, 1998; Shimada et al, 1997). Residues R238 and E459 form a salt-bridge between switch-1 and switch-2. Myosin motor domains with mutations E459R or R238E, blocking salt-bridge formation, show defects in nucleotide-binding, reduced rates of ATP hydrolysis, and a 10-fold reduction in actin affinity (Furch et al, 1999). Further, these results have shown that the salt-bridge between switch-1 and switch-2 is required to support efficient ATP hydrolysis, normal communication between different functional regions of the myosin head, and motor function (Furch et al, 1999).

1.3.3 Relay Helix and Converter Domain

The relay helix is one of the longest helices in the motor domain of myosin, which joins the lower and upper 50kDa subdomains through switch-2 loop (Figure 1.7). Adjacent to relay helix, β -sheet-3 (β 3) from the seven-stranded β -sheet is followed by a turn and a broken helix containing two reactive thiols (SH1 707 and SH2 697). Comparison with other structures shows that the distal part of the SH1-SH2 helix forms the hinge for the ensuing lever. Further, these two helices are followed by a small compact domain generally referred to as the “converter”. The converter domain functions as a communication hub and socket for the C-terminal α -helical tail (Rayment et al, 1993).

The converter domain is tightly coupled to the relay helix. A kink that can form in the relay helix induces a rotation of the converter domain through 60° , which is one of the key structural events during the power stroke (Figure 1.8). In the *rigor-like state*, in the absence of nucleotide, the relay helix is straight. In the *pre-power stroke state*, which mimics the ADP•Pi state, the relay helix is kinked (Coureux et al, 2003; Fedorov et al, 2009) (Figure 1.8A).

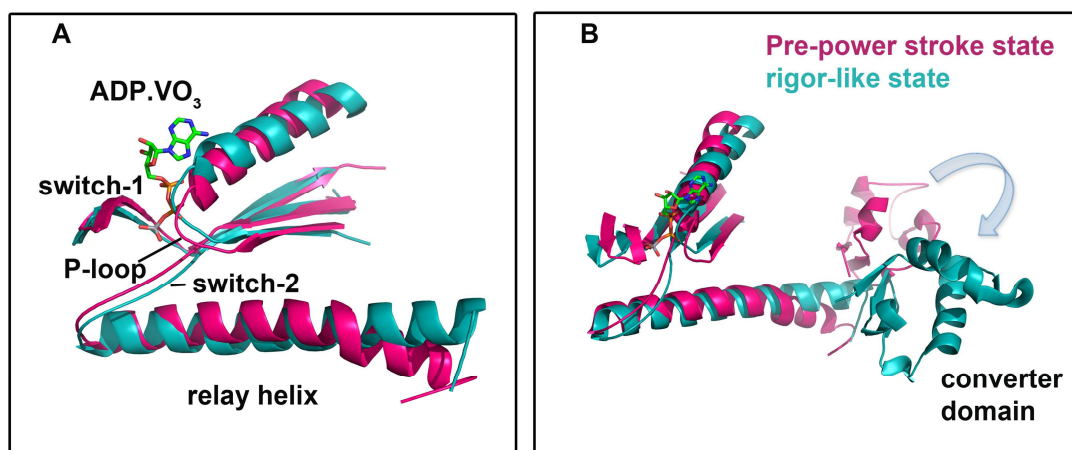


Figure 1.8: (A) Rearrangements of key structural elements in the nucleotide binding pocket of myosin-5 motor domain in the *rigor-like state* [nucleotide-free] (1OE9) and myosin-2 motor domain (2JJ9) in the *pre-power stroke state* [ADP•VO₃]. (B) Large movements of converter domain are shown for the *rigor-like* myosin-5 motor domain (1OE9) and the *pre-power stroke state* of myosin-2 motor domain (2JJ9) structures.

It was observed in different myosin-2 isoform motor domain structures that the ATP analogue, ADP•VO₃ or ADP•VO₄, forms strong interactions with the switch-1 residues in the active site, inducing switch-1 to close (moving towards the β - and γ -phosphates of the bound nucleotide (Figure 1.8A). Concomitant changes occur as switch-2 closes by moving back the lower part of β -strand 5 into the plane of the seven-stranded β -sheet (Gourinath et al, 2003; Kliche et al, 2001). Furthermore, switch-2 closing induces formation of the kink in the relay helix, causing a 60° rotation of the converter domain and the neck helix into the up position (Figure 1.8B) (Fedorov et al, 2009).

1.3.4 Surface Loops and their Functional Importance

The myosin motor domain comprises several surface loops, which were proven to be of functional importance (Figure 1.6). The solvent-exposed, proteolytically sensitive surface loops of myosin that join the proteolytically defined myosin subdomains are highly variable in their sequences, both in length and composition. Furthermore, many myosin isoforms differ in these surface loops as a result of alternative splicing. The splice variants are differentially expressed in various tissues. Among these are vertebrate cardiac, smooth muscle, skeletal

myosin, catch muscle myosins and nonmuscle myosins (Kondrashov & Koonin, 2003; Murphy & Spudich, 2000; Perreault-Micale et al, 1996).

One of these surface loops, loop-1 or the so-called 25-50 kDa loop, is situated near the nucleotide binding site. The length and composition of loop-1 has a considerable influence on the binding of nucleotides. Biochemical studies have shown that loop-1 affects the affinity of actomyosin for ADP, the ADP release from actomyosin, the *in vitro* motility and V_{\max} of the actin-activated Mg^{2+} -ATPase activity, possibly through P_i release (Uyeda et al, 1994).

Structural and biochemical studies have shown that loop-2, a highly positive surface segment of the myosin motor domain, interacts with the negatively charged amino-terminal part of F-actin, and this electrostatic interaction is mainly responsible for the weak binding of the myosin head to F-actin (Ponomarev et al, 2000; Schröder et al, 1993). Molecular genetic manipulations of loop-2 have been shown to alter myosin's affinity for F-actin and its actin-activated ATPase activity (Furch et al, 1998). Three-dimensional reconstructions of electron-microscopy images and solution experiments performed on the actomyosin complex suggest that loop 3, in addition to loop-2, is involved in electrostatic contacts with F-actin (Holmes et al, 2003; Lorenz & Holmes, 2010). Cross-linking experiments have shown that loop-3 mediated interaction with F-actin occurs in striated muscle myosin isoforms but is apparently not essential for the formation of a high-affinity actin-myosin interface or modulation of actomyosin ATPase activity (Van Dijk et al, 1999).

Furthermore, loop-4 of the upper 50 kDa subdomain, the cardiomyopathy loop [CM-loop] and the helix-loop-helix motif of lower 50 kDa subdomain contribute to F-actin binding. The CM-loop lies at the apex of the motor domain, in close proximity of the entrance of the large cleft that separates the lower and upper 50 kDa subdomains (Geeves et al, 2005). A point mutation at position R403Q in human β -cardiac myosin was the first one to be identified as the cause of familial hypertrophic cardiomyopathy (Geisterfer-Lowrance et al, 1990). The strut loop is one of the three loops that connect the upper and lower 50 kDa subdomains

(Figure 1.6). This loop is strongly conserved among the myosin superfamily, and mutagenesis studies have shown that the residue D590 plays an important role in maintaining the disposition of the upper and lower 50 kDa subdomains (Fujita-Becker et al, 2006; Sasaki et al, 2000).

1.3.5 The ATPase Cycle

Myosin is a product-inhibited ATPase that is strongly stimulated by F-actin, which is a nucleotide exchange factor for myosin. This mechanism was first established by Lymn&Taylor (Lymn & Taylor, 1971). At present, a more detailed modified version of this method known as 'swinging lever hypothesis' is in practice (Anson et al, 1996a; Holmes, 1997; Rayment et al, 1993) (Figure 1.9). This hypothesis suggests that rather than the bulky head region of the molecule swing about that only the smaller tail portion moves relative to the filament axis.

On account of the number of experimentally solved high-resolution X-ray structures, electron microscopy experiments with the isolated proteins, and solution kinetics, this chemomechanical cycle was further refined by assigning chemical states, which are defined by the nucleotide bound at the active site, to experimentally observed structural states (Figure 1.9). Starting with a nucleotide-free myosin or *apo-state* and the lever arm in the *post-rigor* position, the motor protein is tightly bound to the F-actin filament [A·M]. Binding of ATP to myosin initiates the dissociation of the actomyosin complex, due to the negative cooperativity between F-actin and ATP, converting the motor to a state that is referred to as *near-rigor* or *pre-hydrolysis state*.

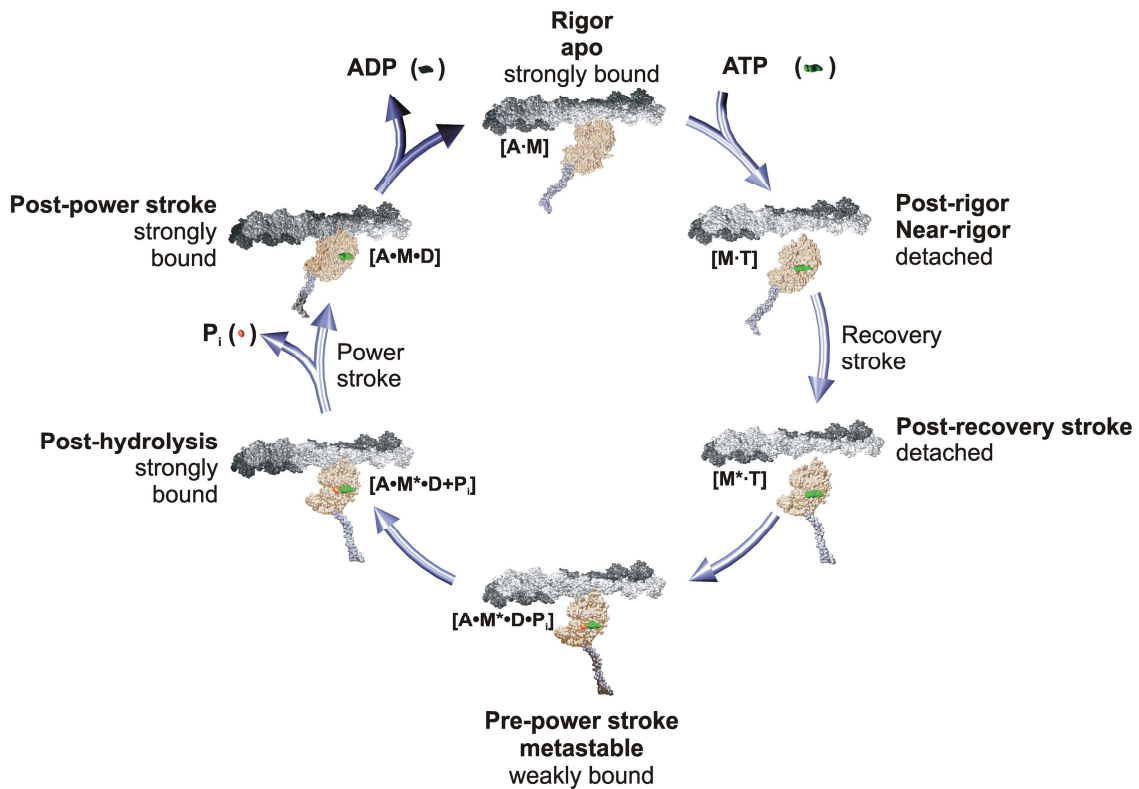


Figure 1.9: The acto-myosin ATPase cycle. Figure adapted from Preller *et al*, (Preller & Manstein, 2011). The abbreviations are indicated as M=Myosin, A=F-Actin, D=ADP and P_i= inorganic phosphate. The asterisk symbol represents different conformational states of the myosin motor domain.

Conformational changes in the motor domain lead to the repositioning of the lever arm and the formation of the hydrolysis competent *post-recovery stroke state* [M*·T]. In this detached state, the hydrolytic cleavage of the ATP to ADP·P_i takes place. The equilibrium constant for the hydrolysis step is close to 1 for most myosins examined. Subsequently, myosin rebinds to the actin filament takes place, initially resulting in the formation of the weak affinity, metastable *pre-powerstroke state* [A·M*·D·P_i] and progressing to the *post-hydrolysis state* with moderate actin-affinity [A·M*·D+P_i]. Isomerization steps concurrent with strong binding to actin, swinging of the lever arm, and force generation are coupled to the release of inorganic phosphate (P_i) [A·M·D] and subsequently ADP [A·M]. Except for the *rigor state* most of the states described in this scheme are difficult to approach experimentally. Electron density maps of the actomyosin complex obtained by cryoEM are still of comparatively low resolution and crystal

structures of the myosin head were only obtained in the absence of F-actin. Nevertheless, it is possible to ascribe individual X-ray structures to certain states of the ATPase cycle. As its name implies, F-actin was early on recognized to serve not only as the passive track on which myosins move but to play an active role in catalysis. Myosin displays poor ATPase activity in the absence of F-actin and requires the interaction with F-actin for fast release of the products of the hydrolysis reaction, P_i and ADP (Preller & Manstein, 2011).

1.4 Allosteric Regulation

Over the years, static pictures of allosterically-regulated proteins indicated a change in the shape of the substrate binding site between the On/Off states depending on whether the effector molecule is bound or absent at the allosteric site. This has led to the paradigm that allostery involves conformational change. The two classical models, the Monod-Wyman-Changeux (MWC model) (Monod et al, 1965) and the Koshland-Nemethy-Filmer (KNF) (Koshland et al, 1966) described allostery as a binding event at one site altering protein activity via a conformational change at the second site. The MWC model emphasized that the conformational transition is a concerted action between two co-existing, distinct states (relaxed and tense, or R and T); on the other hand, the KNF model formulated it as a sequential, induced conformational change by the binding at the first site. In contrast to the “old” view, Gunasekaran *et al*/ stated that the native states are ensembles of pre-existing populations; thus, an allosteric effector leads to an equilibrium shift of pre-existing conformational and dynamic states (Gunasekaran et al, 2004). Proteins such as G protein-coupled receptors, hemoglobins, serine proteases, and cyclin-dependent kinases use allostery to mediate function. Recent studies indicate that even if there is no visual change in the shape of the protein backbone at the allosteric binding site upon binding of the effector, there may still be an associated change in the substrate binding site and hence in protein activity (Daily & Gray, 2007; Popovych et al, 2006; Tsai et al, 2008).

1.4.1 Allosteric Communication in Myosin Motor Domains

In the crowded environment of a typical eukaryotic cell, any object larger than 50 nm is effectively immobile and cannot rely on diffusion to arrive at its destination. As a result, myosin motors evolved to generate force for the transport of cargoes, cell motility, and cell division, processes that are critical for life itself. These motors convert chemical free energy by changing shape in a controlled manner while bound to actin filaments. A fundamental feature of all motor proteins is that their movements are carefully coordinated, so that the motor travels through a specific sequence of coupled biochemical and mechanical states. The nature of this coordination remains obscure, but it is clearly essential for proper motor function. The recent recognition that each myosin class has evolved specific structural and kinetic features allows for the comparison of different coordination mechanisms across the myosin super family.

Recently, it was reported that myosin motors use intrinsic allostery to mediate their functions (Cecchini et al, 2008; Tang et al, 2007). Remote sites in the motor domain communicate through pathways that connect distant sites, trigger large conformational changes, and induce 10,000-fold and greater affinity changes in F-actin and nucleotide binding during the normal ATPase cycle (Conibear et al, 2003; Reubold et al, 2003). X-ray crystallography and biochemical experiments have identified the following major myosin motor conformations that correspond to discrete stages of the actomyosin cycle.

- a) The structure of the *pre power-stroke* state is characterized by hydrolyzed ATP in the catalytic site, an open 50 kDa cleft between the catalytic site and the actin binding site, and the lever arm in its cocked, or “up” position.
- b) During the power stroke the lever arm swings to its “down” position.
- c) Release of phosphate and ADP results in the *rigor state*, characterized by a closed 50kDa cleft, strong binding to F-actin, and the lever arm in the “down” position.

- d) When the catalytic site is reoccupied by ATP, myosin releases from F-actin and the molecule reaches its *post-rigor* conformation characterized by its lever arm still in the “down” position and the cleft is open.

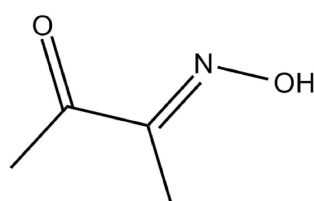
In addition to the above changes, opening and closing of the active site elements, bending and straightening of relay helix and the communication between the active site and the converter domain, play a crucial role in different stages of the ATPase cycle. The mechanochemical properties indicate that these nanomachines inherently possess different intrinsic allosteric mechanisms. Understanding all or some of these mechanisms in detail will need the application of different methodologies. In this thesis, small molecule effectors were used for dissecting the allosteric mechanisms in the myosin motor domain.

1.4.2 Small Molecule Effectors

Cytoskeletal proteins, including microfilaments, microtubules, and intermediate filaments, play a pivotal role in the treatment of cancer, as their regulation by small molecules arrests progression through the cell cycle (Reayi & Arya, 2005). Natural compounds are valuable tool for searching more potent and highly specific compounds against a wide variety of diseases ranging from cancer to malaria (Bai et al, 2010; Martin et al, 2009b; Shang et al, 2010; Shen et al, 2010). The role of myosins for a wide range of diseases has been established in numerous instances (Anan et al, 1994; Anderson et al, 2000; Liang et al, 1998; Melchionda et al, 2001; Probst et al, 1998). Due to their rapid, conditional, and reversible mode of action, small molecule modulators of protein function are useful tools in cell biological research and can serve as lead compounds in the development of therapeutic agents (Lehar et al, 2008; Walsh & Chang, 2006).

Several small molecule allosteric effectors of myosin motor have been reported in the last two decades. In 1989, the first myosin inhibitor, 2,3-butanedione 2-monoxime (BDM) was reported (Higuchi & Takemori, 1989) (Figure 1.10). Initially, it was identified as well-characterized, low-affinity, no-competitive inhibitor of skeletal muscle myosin-2. It has been widely used at millimolar concentrations in

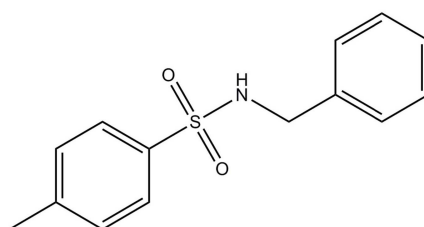
cell biological experiments with the assumption that it is an ATPase inhibitor of the class-2 myosins. Kinetic studies showed that BDM decreases the ATPase rate and force production by inhibiting P_i release and stabilizing the weakly actin-bound Myosin•ADP• P_i state (Herrmann et al, 1992).



2,3-butanedione 2-monoxime (BDM)

Figure 1.10: Schematic representation of the 2,3-butanedione 2-monoxime (BDM).

BDM not only inhibits some myosins but also has shown highly non-specific inhibitory action against non-myosin proteins like acetylcholinesterase, serine/threonine phosphorylation in kinases and lot of other proteins (Sellin & McArdle, 1994). Cheung *et al.* reported *N*-benzyl-*p*-toluene sulphonamide (BTS) as a specific inhibitor of the actin-stimulated ATPase activity of rabbit muscle myosin-2 S1 (Cheung et al, 2002) (Figure 1.11).



N-benzyl-*p*-toluenesulfonamide (BTS)

Figure 1.11: Schematic representation of the *N*-benzyl-*p*-toluenesulfonamide (BTS)

Although BTS does not compete for the nucleotide-binding site of myosin, it weakens myosin's interaction with F-actin, leading to dissociation of myosin in the presence of ADP. BTS reversibly suppressed force production in skinned skeletal muscle fibers from rabbit and frog skin at micro molar concentrations (Cheung et al, 2002). The mode of action and the binding-site of the inhibitor in the myosin motor domain are unknown at present.

The phenothiazine, trifluoperazine (TFP) has long been known to be a potent antagonist of calmodulin action (Levin & Weiss, 1976) (Figure 1.12). At millimolar concentrations, TFP has also been reported to remove the regulatory light chain subunits from both vertebrate smooth muscle (Trybus et al, 1994) and scallop muscle myosin-2 (Patel et al, 2000). Patel *et al.* demonstrated that TFP inhibits the actin-activated MgATPase activity of scallop adductor muscle myosin-2 without bound regulatory light chains at concentrations of 100-200 μM (Patel et al, 2000). Sellers *et al.* has shown that TFP inhibits the actin-activated MgATPase of a proteolytic fragment of myosin-5 that contains not only the motor domain and no calmodulin, suggesting that the site of action of TFP is on the myosin heavy chain (Sellers et al, 2003).

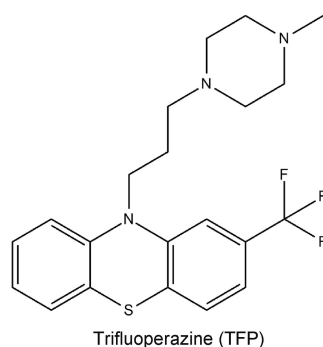


Figure 1.12: Schematic representation of the Trifluoperazine (TFP).

Blebbistatin, a 1-phenyl-2-pyrrolidinone derivative, represents an effective inhibitor of some class-2 myosins with IC_{50} values ranging from submicromolar ($\text{IC}_{50} \sim 0.5 \mu\text{M}$) to nearly 100 μM (Limouze *et al.*, 2004). Blebbistatin has been shown to potently inhibit nonmuscle myosin-2B, rabbit skeletal muscle myosin-2, and *Dd* myosin-2, but does not inhibit smooth muscle myosin-2, or myosins from classes-1, -5, or -10. The structural basis for the mode of action of blebbistatin was reported for the *Dd* myosin-2 motor domain (Allingham et al, 2005).

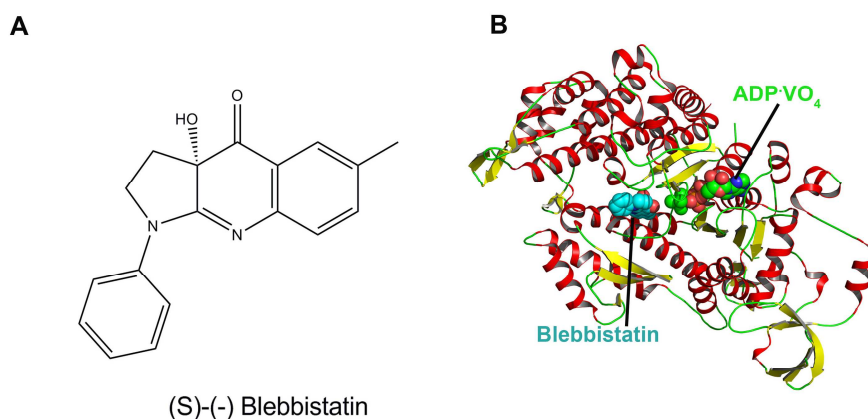


Figure 1.13: (A) Schematic representation of the (S)-(-) blebbistatin (B) Blebbistatin binding site in *Dd* myosin-2 motor domain (1YV3). Color-coding has been done according to the secondary structure of the myosin motor domain.

Blebbistatin binds in a hydrophobic pocket at the apex of the 50 kDa cleft, close to the γ -phosphate-binding pocket (Figure 1.13). Allingham *et al.* proposed that the inhibitor is complementary to the metastable state; consistent with proposition that blebbistatin inhibits P_i release in MgADP- P_i complex by stabilizing this conformation (Kovács *et al.*, 2004). Blebbistatin binding doesn't induce any major conformational changes in the myosin motor domain (rmsd of C_α is 0.407 Å only). This fact supports the newly proposed allostery mechanism by Tsai *et al.*: Even if there is no visual change in shape of backbone at the substrate binding site upon binding of the allosteric effector, there could be still an allosteric change in the substrate binding site, and in protein activity (Tsai *et al.*, 2008).

The use of small molecule effectors of myosin function such as *N*-benzyl-*p*-toluenesulfonamide (BTS) and blebbistatin help to provide important new insights in a range of cellular functions that require the active participation of at least one member of the myosin family. Compounds like blebbistatin and BTS display preferred interactions with selected members of myosin class-2 (Cheung *et al.*, 2002; Limouze *et al.*, 2004). However, there is a requirement for developing specific small molecule inhibitors of other classes of myosins.

Recently, the total synthesis of halogenated pseudilins; natural products containing a 2-arylpyrrole moiety and their synthetic analogues have been described (Martin et al, 2009a). Pentabromopseudilin (PBP) was shown to inhibit myosin-2 dependent processes such as isometric tension development and unloaded shortening velocity in muscle cells. PBP was subsequently identified as a potent inhibitor of vertebrate myosin-5 motor activity (Figure 1.14). An IC_{50} of 400 nM was determined for the inhibition of vertebrate myosin-5 ATPase activity by PBP (Fedorov et al, 2009).

The novel allosteric binding pocket of PBP is about 16 Å away from the nucleotide-binding pocket and is close to the actin-binding cleft, at the apex of 50 kDa cleft (Fedorov et al, 2009). Based on this finding, related compounds to identify myosin effectors with altered selectivity for the members of different myosin classes were screened.

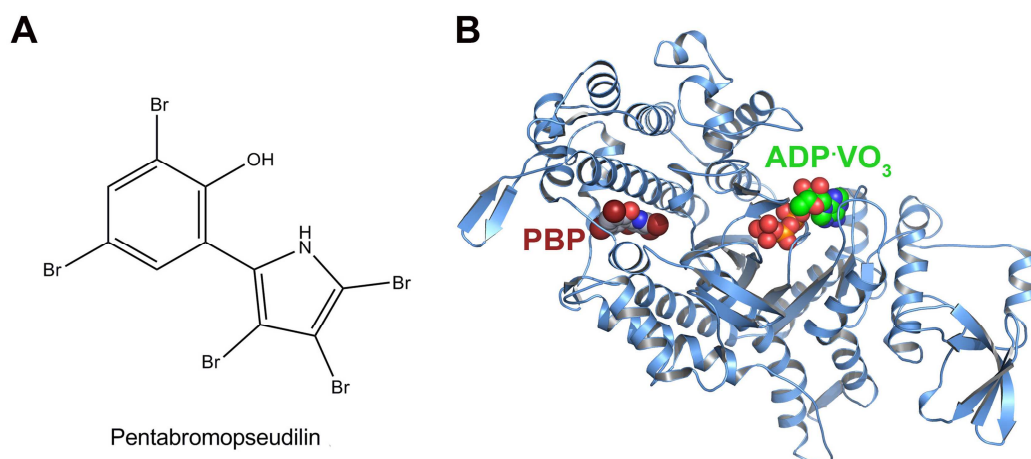


Figure 1.14: (A) Schematic representation of pentabromopseudilin (PBP) (B) Crystal structure of *Dd* myosin-2 complexed with PBP in the presence of MgADP•VO₃.

Pentachloropseudilin (PCIP), a chemical and structural analogue of PBP, was identified in this screening as a potent inhibitor of class-1 myosins. The main aim of this thesis is to dissect the molecular and structural basis of inhibition of PCIP on myosin motor domains.

Ammosamides structural scaffold is similar to the microbial product 'lymphostin' (Aotani et al, 1997) and several sponge-derived pyrroloiminoquinone natural

products, including 'batzelline A', isobatzelline D, and makaluvamine A (Antunes et al, 2005) [Figure 1.15]. Ammosamide A and B exhibited significant *in vitro* cytotoxicity against HCT-116 colon carcinoma, each with $IC_{50}=320$ nM. These compounds also demonstrated pronounced selectivity in a diversity of cancer cell lines with values ranging from 20 nM to 1 μ M, indicating a specific target mechanism of action. To explore the intracellular target of the ammosamides, ammosamide B was converted to a highly fluorescent molecule by conjugation (Hughes et al, 2009a). Treatment of HCT-116 colon carcinoma or HeLa cells with this fluorescent molecule produced immediate and irreversible labeling of a specific protein in the cellular cytosol. By using cell biology studies, the target of the ammosamides was identified as a member of the myosin family, important cellular proteins that are involved in numerous cell processes, including cell cycle regulation, cytokinesis, and cell migration (Hughes et al, 2009a).

The main ammosamide derivatives, Ammosamide A and Ammosamide B, differ only in one functional group. The fact that the ammosamides are highly colored (ammosamide A: $\lambda_{max}=580$ nm; ammosamide B: $\lambda_{max}=530$ nm), yet lack quinone or iminoquinone functionalities, leads to speculation about the electronic character and reactivity of these metabolites (Hughes et al, 2009b). The functionality within the ammosamide structure was very important for targeting myosin and has been proved (Hughes et al, 2009a).

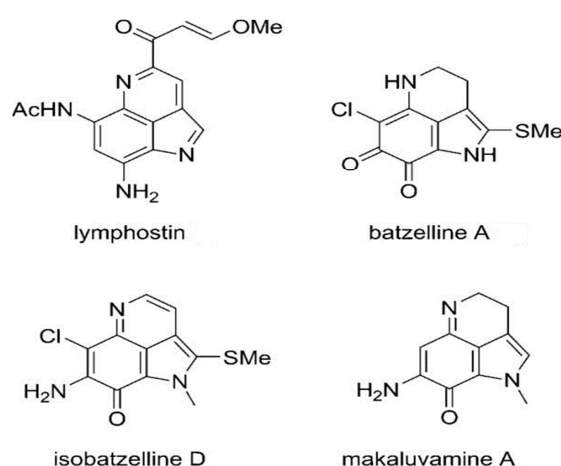


Figure 1.15: Related metabolites from bacteria and sponges. These compounds have similar structural scaffold as ammosamides. This figure is taken from Hughes *et al* (Hughes et al, 2009b).

This thesis focuses on myosin motor domains, whose function and structure was dissected using an approach that involves the use of small molecules and different combinations of biochemical and biophysical techniques. Furthermore, this thesis will address critical questions about the underlying inhibitory mechanisms of myosin motor domains using small molecule inhibitors.

2. Material and Methods

2.1 Materials

Table 1: List of equipment

Equipment	Company
Centrifuge 5415 D	Eppendorf
Centrifuge Avanti Centrifuge J-20 XP with rotors JLA 16.250, JA 25.50	Beckman Coulter
Centrifuge J-HC with rotor JS4.2	Beckman Coulter
Centrifuge Megafuge 1.0R	Heraeus
Econo Column chromatography	Bio-Rad
Fluorescence microscope CK 40	Olympus
Fluorescence microscope IX70	Olympus
FPLC Äkta-Purifier 10	Amersham Biosciences
Gel filtration column Highload 26/60 Superdex 200 PG	Amersham Biosciences
Incubator, <i>E.coli</i>	Heraeus
Incubator, <i>Sf9</i>	Sanyo
Laboratory refrigerator and freezer	Liebherr
Laboratory water bath	GFL
Laminar flow cabinet	COJAIR
Linbro plates	Hampton Research
Magnetic stirrer MR Hei-Standard	Heidolph
Micro scale	Sartorius
Microwave	Daewoo
Mini-PROTEAN 3 cell	Bio-Rad
Molecular Imager ChemiDoc	Bio-Rad

Orbital shaker, <i>E.coli</i> and <i>D.discoideum</i>	Thermo
Orbital shaker, Innova 44, Sf9	New Brunswick
pH-meter 3520	Jenway
Photometer DU800	Beckman Coulter
Pipettes 2-1000 µl	Gilson
Plate reader, Multiscan FC	Thermo
Power pack EV265	Consort
Sample Loop 7.8 ml	Amersham Biosciences
Semi-dry blotting chamber	PHASE
Sonifier Sonoplus HD2200	Bandelin
Stopped-flow SF-61SX2	Hi-Tech Scientific
Thermostat plus	Eppendorf
Ultracentrifuge Optima LE-80K with rotors 45Ti, 70Ti	Beckman Coulter
Ultracentrifuge Optima Max with rotor TLA 120.1	Beckman Coulter
Vortex-Genie 2	Scientific Industries

2.1.1 Consumables

Table 2: List of consumables used and the corresponding companies

Consumable	Company
Bottle top filter, 22 µM and 45 µm PES	Nalgene
Cell culture flasks, T25-T175	Sarstedt
Cell culture plate, 6 well	Nunc
Cell scraper	Greiner
Cryotubes	Sarstedt
Cover slip (22 mmx22mmx22mm, thickness 0.01 mm)	Roth

Dialysis tubing	Serva
Falcon tubes, 15 and 50 ml	Sarstedt
Flasks with vent cap, sterile, 125-1000 ml	Corning
Microscope slide	Roth
Microtiter plate, 96 well, UV transparent, half-size area	Corning
Petri dish	Sarstedt
Pipette tips, 10-1000 μ M	Sarstedt
Pipette tips, sterile 2-1000 μ M	Star Lab
Reaction tubes, 1.5 and 2 ml	Sarstedt
Serological pipettes, 2-50 ml	Sarstedt
Sterile filter, 22 μ M and 45 μ M PES	Millipore
Storage bottles, 200-500 ml	Corning
Syringe Omnifix, 2-50 ml	Braun
Ultrafiltration unit, Vivaspin, PES 4 ml and 20 ml, MWCO 50000 Da	Vivascience
PVDF membrane	Millipore
Whatman paper	Whatman

2.1.2 Chemicals

Table 3: List of chemicals and corresponding companies

Chemicals	Company
Acetone	J.T.Baker
Acrylamide: Bisacrylamide	Merck
ADP	Sigma-Aldrich
Agar	Serva
Agarose, LE GQ	Fermentas

Material and Methods

Ampicillin	Sigma-Aldrich
Amylacetate	Sigma-Aldrich
Ammonium Peroxide Sulfate	Merck
ATP, sodium salt	Sigma-Aldrich
Beta-Mercaptoethanol	Sigma-Aldrich
Bovine Serum Albumin, BSA	Sigma-Aldrich
Bromophenol blue	Sigma-Aldrich
2,3 Butanediol	Sigma-Aldrich
Calcium chloride	Calbiochem
Casein	Serva
Chloramphenicol	Fluka
Calcium acetate	Sigma-Aldrich
Cacodylic acid	Sigma-Aldrich
2'-desoxy-mantADP	BIOLOG
2'-desoxy-mantATP	Jena Biosciences
Dipotassiumhydrogenphosphate (K_2HPO_4)	Merck
Dithiothreitol (DTT)	Sigma-Aldrich
Dimethylsulfoxide (DMSO) > 99 %	Sigma-Aldrich
EDTA, Triplex II	Merck
EGTA, Triplex VI	Merck
Ethanol, absolute >99%	J.T.Baker
Ethanol	J.T.Baker
Ethidium Bromide	Fluka
Gentamicin	PAA
Glucose	Sigma-Aldrich
Glycerine	Merck
Glycerol	Sigma-Aldrich

Material and Methods

Glycine	Sigma-Aldrich
HiFi Extract	Serva
HEPES, 4-(2-Hydroxyethyl)-piperazine-1-ethanesulfonic acid	Sigma-Aldrich
Imidazole	Sigma-Aldrich
Inhibitor tablets, Complete Mini, EDTA free	Roche
IPTG, Isopropyl- β -D-1-thiogalactopyranoside	Fermentas
Isopropanol, 2-Propanol	J.T.Baker
Kanamycin	Merck
Lithium Citrate	Sigma-Aldrich
Lithium hydroxide	Jena Bioscience
Magnesium Chloride ($MgCl_2 \cdot 6H_2O$)	Calbiochem
Manganese Chloride	Sigma-Aldrich
mantADP	Jena Biosciences
mantATP	Jena Biosciences
Methanol	J.T.Baker
Microloops	MiTeGen
MOPS, 3-(N-Morpholino)-propansulfonic acid	J.T.Baker
N-(1-prenyl) iodoacetamide (Pyrene)	Fluka
NADH, Disodium salt	Roche
Nickel-Nitrilotriacetate-column material, Ni^{2+} -NTA-superflow	QIAGEN
Nitrocellulose	Sigma-Aldrich
PageBlue stain	Fermentas
PEP, Phosphoenolpyruvate	Roche
Peptone	Serva

Material and Methods

Phosphoric acid	J.T.Baker
Potassium Chloride	Merck
Potassium Dihydrogen Phosphate (KH ₂ PO ₄)	Merck
Potassium Hydroxide (KOH)	Merck
Sodium Azide (NaN ₃)	Merck
Sodium Carbonate (Na ₂ CO ₃)	J.T.Baker
Sodium Chloride	Merck
Sodium-Dodecyl Sulfate, SDS	Merck
Sodium hydrogen Carbonate (NaH ₂ CO ₃)	Merck
Sodium Hydroxide (NaOH)	Merck
TEMED, N,N,N',N'- Tetramethylethylenediamine	Merck
Tetracycline	Sigma-Aldrich
Tetramethyl-Rhodamine-iso-Thiocyanate (TRITC)-phalloidin	Sigma-Aldrich
Trehalose	Fluka
Tri Chloro Acetic Acid (TCA)	Fluka
Triton-X-100	Sigma-Aldrich
Tryptone	Serva
Vanadate, Sodium salt	Sigma-Aldrich
X-Gal	Fermentas
Xylene Cyanol FF	Merck

2.1.3 Enzymes

Table 4: List of enzymes used.

Enzymes	Company
CIAP, calf intestine alkaline phosphatase (1U/ml)	Fermentas
Glucose Oxidase	Sigma-Aldrich
Catalase	Sigma-Aldrich
Lactate dehydrogenase (LDH)	Roche
Phusion High Fidelity (Hot Start) DNA-Polymerase	Finnzymes
Pyruvate Kinase (200 U/mg)	Roche
Quick T4 DNA Ligase	NEB
T4 DNA Ligase	Fermentas
Taq Polymerase	QIAGEN

2.1.4 Reagent Kits

Table 5: Kits used in this thesis.

Kit	Company
Cellfectin [®] Reagent	Invitrogen
JCSG++ Suite	Jena Biosciences
NeXtal DWBlock AmSO4 Suite	QIAGEN
NeXtal DWBlock Anions Suite	QIAGEN
NeXtal DWBlock Cations Suite	QIAGEN
NeXtal DWBlock Classics Suite	QIAGEN
NeXtal DWBlock MPD Suite	QIAGEN
NeXtal DWBlock PEGs Suite	QIAGEN
NeXtal DWBlock pHClear Suite	QIAGEN

2.1.5 Vectors

Table 6: Vectors used for cloning.

Vector	Company
pDEST8	Invitrogen
pDONR201	Invitrogen
pDXA-3H	Lab made
pGEM [®] -T Easy	Promega
pFastBac1 [™]	Invitrogen
pFASTBac [™] Dual	Invitrogen

2.1.6 Protein Standards

PageRuler[™] Protein Ladder, Fermentas, (Bands : 170, 130, 100, **70**, 55, 40, 35, 25, 15, 10 kDa)

2.1.7 Antibodies

Penta-His Antibody, BSA-free, QIAGEN

2.1.8 Microorganisms

Following microorganisms have been used for cloning, plasmid amplification and the generation of recombinant bacmid.

Table 7: Chemically competent *E.coli* cells used for the amplification and production of plasmid DNA and bacmid DNA, respectively.

<i>E.coli</i> Strain	Genotype	Company
DH5 α	Φ 80d, <i>lacZ</i> Δ M15, <i>recA1</i> , <i>endA1</i> , <i>gyrA96</i> , <i>thi-1</i> , <i>hsdR17</i> , (<i>rk</i> ⁻ <i>mK</i> ⁺), <i>supE44</i> , <i>relA1</i> , <i>deoR</i> , Δ (<i>lacZYA-argF</i>), U169, F ⁻	Invitrogen
DB3.1	F ⁻ , <i>gyrA462</i> , <i>endA1</i> , Δ (<i>sr1-recA</i>), <i>mcrB</i> , <i>mrr</i> , <i>hsdS20</i> (<i>rB</i> -, <i>mB</i> -), <i>supE44</i> , <i>ara14</i> , <i>galK2</i> , <i>lacY1</i> , <i>proA2</i> , <i>rpsL20</i> (<i>Smr</i>), <i>xyl5</i> , Δ <i>leu</i> , <i>mtl1</i>	Invitrogen
DH10Bac	F ⁻ <i>mcrA</i> D(<i>mrr-hsdRMS-mcrBC</i>) f80 <i>lacZ</i> M15 D <i>lacX74</i> <i>recA1</i> <i>endA1</i> <i>araD139</i> D(<i>ara,leu</i>) 7697 <i>galU</i> <i>galK</i> I- <i>rpsL</i> <i>nupG</i> / bMON14272 / pMON7214	Invitrogen
NEB 10-beta	<i>araD139</i> Δ (<i>ara-leu</i>)7697, <i>fhuA</i> , <i>lacX74</i> , <i>galK</i> , (Φ 80 Δ (<i>lacZ</i>)M15), <i>mcrA</i> , <i>galU</i> , <i>recA1</i> , <i>endA1</i> , <i>nupG</i> ,	NEB

	<i>rpsL</i> , $\Delta(mrr-hsdRMS-mcrBC)$	
XL1-Blue	<i>recA1</i> , <i>endA1</i> , <i>gyrA96</i> , <i>thi-1</i> , <i>hsdR17</i> , <i>supE44</i> , <i>relA1</i> , <i>lac[F proABlac^IZΔM15 Tn10 (Tet^r)]</i>	Stratagene

2.1.9 Cell culture

Table 8: List of cellculture media and other accessories.

Material	Company
Dulbecco's PBS (no Ca ²⁺ & Mg ²⁺)	PAA
HL-5c Medium	FORMEDIUM
Luria Broth	USB
Sf9 cells (SFM adapted)	Invitrogen
Trypan Blue	Invitrogen

2.2 METHODS

2.2.1 Protein Preparation from Sf9 Cells

The purification of His₈-tagged recombinant myosin constructs from Sf9 insect cells was either carried out from frozen or fresh cell material. All purification steps were carried out at a temperature of 4°C and all buffers and solutions were prechilled to 4°C prior to use. Cell pellets from 5-10 litres Sf9 suspension culture were resuspended in 600 ml Lysis-Buffer and sonicated (power setting: 40%, duty cycle: 50%) on ice for 3 x 30 seconds with 30 second cooling periods between the burst periods. The lysate was ultracentrifuged (13000 × g, 30 min, 4°C, rotor 45Ti). In order to prepare the Ni-NTA matrix for the affinity purification of His₈-tagged myosin construct under native conditions, 10 ml of a 50% Ni-NTA (Ni-NTA-super flow, QIAGEN) slurry was added to 120 ml Column Buffer and centrifuged (700 × g, 5 min, 4°C). The cleared lysate was added to the resin and mixed gently by shaking at 4°C for 150 minutes. After a centrifugation step (700 × g, 5 min, 4°C), the resin was resuspended in 300 ml ATP Buffer and incubated for 15 minutes. The slurry was centrifuged (700 × g, 5 min, 4°C), resuspended in

Low Salt Buffer and again centrifuged ($700 \times g$, 5 min, 4°C). The pellet was resuspended in 300 ml High Salt Buffer and the mixture was transferred into an empty column. The flowthrough was collected and the His₈ fusion protein was eluted with Elution Buffer. The eluent was collected and analyzed by SDS-PAGE. Fractions containing myosin were pooled and dialyzed over night against 3 l Dialysis Buffer. The protein solution was concentrated through ultracentrifugation (MWCO 50 kDa, $3000 \times g$, 4°C) to a final volume of 2.5 ml. The concentrated protein solution was sterile filtered ($0.22 \mu\text{m}$) and loaded on a preequilibrated Superdex 26/60-200 prep grade gel filtration column with a flow rate of 0.5 ml/min. The sample was eluted with Dialysis Buffer (flow-rate: 0.5 ml/min, maximal pressure: 0.5 MPa) and the eluent was collected in 1 ml fractions. The fractions were analyzed by SDS-PAGE and myosin-containing fractions were pooled and concentrated up to 4-18 mg/ml via ultrafiltration (MWCO 50 kDa, $3000 \times g$, 4°C). Aliquots of the protein samples were flash frozen in liquid nitrogen and stored at -80°C for future usage.

Table 9: Buffers for the preparation of His₈-tagged myosin motor domain constructs from *Sf9* insect cells

Lysis Buffer	Column Buffer	ATP Buffer	Low Salt Buffer
50 mM HEPES pH 7.3	25 mM HEPES pH 7.3	25 mM HEPES pH 7.3	25 mM HEPES pH 7.3
300 mM NaCl	300 mM NaCl	600 mM NaCl	300 mM NaCl
3 mM MgCl ₂		0.5 mM ATP	0.1 mM EGTA
2 mM ATP		0.1 mM EGTA	3 mM MgCl ₂
10 mM β- Mercaptoethanol		3 mM MgCl ₂	40 mM Imidazole
4 mM Imidazole		20 mM Imidazole	
6 Complete-Tablets		7 mM β- Mercaptoethanol	
		1 % Triton X-100	
High Salt Buffer	Elution Buffer	Dialysis Buffer	Storage Buffer
25 mM HEPES pH 7.3	25 mM HEPES pH 7.3	25 mM HEPES pH 7.3	25 mM HEPES pH 7.3
500 mM NaCl	400 mM NaCl	400 mM NaCl	400 mM NaCl
0.1 mM EGTA	0,2 mM EGTA	1 mM EGTA	1 mM EGTA
3 mM MgCl ₂	3 mM MgCl ₂	1 mM EDTA	1 mM EDTA
65 mM Imidazole	100-850 mM Imidazole	1 mM DTT	1 mM DTT
		3 % Trehalose	10 % Trehalose

2.2.2 Actin Preparation

F-actin is required for the functional, biochemical and kinetic characterization of myosin. The preparation of G-and F-actin was carried out according to a two-step protocol. In the first step, actin acetone powder was extracted from rabbit muscle. The powder was the starting material for the second step, in which monomeric and filamentous actin was prepared. All steps were carried out at a temperature of 4°C and all buffers and solvents were prechilled to 4°C prior to use.

2.2.2.1 Preparation of Actin Acetone Powder

For the preparation of actin acetone powder four New Zealand white rabbits (*Oryctolagus cuniculus*) were sacrificed and the dorsal lateral skeletal muscles and the hind leg muscles are excised and chilled on ice. The muscles were freed from tendons and fat, sliced and minced in a prechilled meat grinder. The mince is extracted by stirring for 10-20 minutes in 3 volumes Guba Straub Buffer. Further, the solution was supplemented with 12 volumes of cold water and stirred. The extract was filtered through two layers of cheesecloth. Later, the filtered muscle mince was resuspended in 5 volumes Carbonate Buffer A (w/v) and stirred for 30 minutes. The extract was filtered through 2 layers of cheesecloth and the filtered residue was resuspended in the same volume (w/v) Carbonate Buffer B. The extract was stirred for 10 minutes and diluted with 5 volumes of warm water and this was filtered through 2 layers of fine meshed cheesecloth. The filtered residue was resuspended in 2.5 l (per kg of rabbit meat) cold acetone and stirred for 30 minutes and filtered through the fine meshed cheesecloth. This procedure was repeated once and the final pellet was spread on filter paper and allowed to dry overnight in the chemical hood. The acetone powder was stored at -20°C.

Table 10: Buffers for the preparation of actin acetone powder

Guba Straub Puffer	Carbonate Buffer A	Carbonate Buffer B
0.3 M KCl	47.6 mM NaHCO ₃	10 mM NaHCO ₃
0.1 M KH ₂ PO ₄	0.1 mM CaCl ₂	10 mM Na ₂ CO ₃
0.05 M K ₂ HPO ₄		0.1 mM CaCl ₂
pH 6.5		

Around 225 g dry acetone powder could be obtained from 2.5 kg rabbit meat. The actin acetone powder was the starting material for the preparation of G- and F-actin.

2.2.2.2 Preparation of G- and F-actin from Acetone Powder

Actin acetone powder was prepared from the rabbit muscle as described above. 5 g of actin acetone powder was mixed with 80-100 ml Actin Buffer and stirred at 4°C for 30 minutes. The extract was filtered through 2 layers of filter paper through a vacuum tank filter. The filter paper was washed 4 times with Actin Buffer to increase the protein yield. After filtration, the volume of the extract was typically 120 ml. The solution was then ultracentrifuged (70,000 × g, 60 min, 4°C, rotor 70Ti). The volume of the actin containing supernatant was measured and supplementing the solution with 100 mM KCl and 2 mM MgCl₂ induced the polymerization of monomeric G-actin to filamentous F-actin. The solution was kept at room temperature for 2 hours and subsequently ultracentrifuged (70,000 × g, 180 min, 4°C, rotor 70Ti). The sediment was homogenized in 50 ml Depolymerization Buffer by using a hand held glass homogenizer and dialyzed over night against 5 l Depolymerization Buffer.

The G-actin solution was clarified by centrifugation (70,000 × g, 60 min, 4°C, rotor 70Ti). The volume of the supernatant was measured and the actin concentration determined by measuring the absorption at 280 nm ($\epsilon_{280} = 46\,000\text{ cm}^{-1}\text{M}^{-1}$, MW = 41.7 kDa). The actin concentration was adjusted to 1-2 mg/ml by adding Depolymerization Buffer and G-actin polymerization was induced by supplementing the solution with KCl and MgCl₂ to 100 mM and 2 mM, respectively. The solution was kept at room temperature for 1 h. The F-actin containing solution was ultracentrifuged (70,000 × g, 60 min, 4°C, rotor 70Ti) and the sediment was either stored at 4°C or directly resuspended. For resuspension, the pellet was removed with a stainless steel spatula by scraping it into 1-2 ml Homogenisation Buffer and transferred it into a hand held glass homogenizer, gently homogenized and the concentration of the F-actin solution was measured. The typical yield was approximately 50 mg F-actin from 5 g actin acetone powder.

Table 11: Buffers for the preparation of G- and F-actin

Actin Buffer	Depolymerization Buffer	Homogenization Buffer
10 mM HEPES pH 8.0	5 mM HEPES pH 7.5	5 mM HEPES pH 7.5
0.5 mM ATP	0.2 mM CaCl ₂	2 mM MgCl ₂
0.2 mM CaCl ₂	1 mM NaN ₃	100 mM KCl
1mM DTT	0.5 mM ATP	0.02 % NaN ₃

2.2.2.3 Preparation of Pyrene-Labeled Actin

Pyrene (N-(1-pyrene)iodoacetamide) labeled F-actin was required for the transient kinetic studies of the interaction between myosin and F-actin. Site-specific labeling of Cys374 with pyrene was carried out as described by Kouyama *et al* (Kouyama & Mihashi, 1981). The strong fluorescence of the reporter moiety in combination with the quench in fluorescence makes this label an ideal tool for transient kinetic study (Criddle *et al*, 1985). Further, the labeling reaction was carried out by slowly mixing F-actin with pyrene in a ratio of 1:5 (w/w) and the solution was stirred for 16 hours protected from light. The solution was centrifuged (4700xg, 15 min, 4°C, rotor 70Ti) to pellet the precipitated dye and denatured protein. In addition, the F-actin containing supernatant was centrifuged (7000xg, 180 min, 4°C, rotor 70Ti) and the sediment was resuspended in Homogenization Buffer (Table 11). Later, concentration of pyrene actin was determined under consideration of the absorbance of pyrene at a wavelength of 280 nm. The pyrene concentration was determined photometrically at 344 nm ($\epsilon=23000 \text{ cm}^{-1}\text{M}^{-1}$) and the contribution of pyrene ($\epsilon=22000 \text{ cm}^{-1}\text{M}^{-1}$) to the total absorption of the sample at 280 nm was determined and subtracted from the total absorption at 280 nm. The extent of labeling degree was typically 60-90%.

2.2.2.4 Preparation of TRITC-Phalloidin Actin

TRITC (Tetramethylrhodamine-B-isothiocyanate)-labeled actin was required for the visualization of actin filaments in the *in vitro* motility assay (Bereiter-Hahn & Kajstura, 1988). TRITC-phalloidin is a fluorescent rhodaminy-coupled phalloidin derivative that selectively interacts and stabilizes filamentous actin and prevents F-actin depolymerization to G-actin. F-actin was labeled with TRITC-phalloidin by

incubating 2 μ M F-actin and 3 μ M TRITC-phalloidin in the appropriate assay buffer for at least 12 hours protected from light.

2.2.3 The Baculovirus/Sf9-System

Recombinant baculoviruses are widely used to produce heterologous genes in cultured insect cells. Baculoviruses are double-stranded, circular, supercoiled DNA molecules in a rod-shaped capsid. For the recombinant production, isolates of the *Autographa californica* multiple nuclear polyhedrosis virus (AcMNPV) are used. In the baculovirus expression system, the naturally occurring polyhedrin gene is replaced with a recombinant gene or cDNA and produced under the control of the naturally occurring polyhedrin promoter. Usually, the recombinant proteins are processed, modified and targeted to the appropriate cellular locations (Smith et al, 1983).

2.2.3.1 Transformation

In order to generate recombinant bacmid for the heterologous production of recombinant human myosin motor domains, the transfer vectors containing the cDNA encoding the expression construct (from Sarah Heissler, Institute of Biophysical Chemistry, Hannover Medical School) were transformed in chemically competent DH10Bac cells. The composite bacmid can be isolated and transfected into Sf9 insect cells as described under section 2.2.3.2.

For the transformation procedure, competent DH10Bac cells (100 μ l) were thawed on ice and 100 ng of transfer vector was added. The cell suspension was gently mixed and incubated on ice for 30 minutes. To heat-shock the cells, the suspension was heated 45 seconds in a 42°C thermostat and incubated on ice for two minutes. 900 μ l S.O.C. medium was added and the cell suspension was incubated at 37°C for 4 hours with a shaking speed of 225rpm. After the incubation, the reaction mix was diluted 1:10 and 1:100 with S.O.C. medium and 150 μ l of the suspension were spread on LB agar plates (supplemented with 50 μ g/ml kanamycin sulfate, 7 μ g/ml tetracycline, 10 μ g/ml gentamicin, 300 μ g/ml X-gal and 40 μ g/ml IPTG) and incubated for 18 hours at 37°C.

Colonies containing the composite bacmid appeared as white colonies on the selective medium. These transformants were selected and grown at 37°C overnight in 3 ml LB broth (225 rpm) containing 50 µg/ml kanamycin sulfate, 7 µg/ml gentamicin and 10 µg/ml tetracycline for the bacmid preparation (see section 2.2.3.2).

Table 12: Medium for the cultivation of *E.coli*

LB broth ^a	LB agar ^a	S.O.C. medium
10 g/l Tryptone	10 g/l Tryptone	20 g/l Peptone
10 g/l Casein	10 g/l Casein	5 g/l Yeast extract
10 g/l Yeast extract	10 g/l Yeast extract	10 mM NaCl
5 g/l NaCl	5 g/l NaCl	2,5 mM KCl
	15 g/l Agar	10 mM MgCl ₂
		10 mM MgSO ₄
		20 mM Glucose

^a The media was supplemented with additives after autoclaving at temperatures below 37°C.

2.2.3.2 Bacmid Preparation

Composite bacmid was prepared from 3 ml selective LB medium after incubating for approximately 16 hours at 37°C with the buffers supplied with the QIAGEN Plasmid Midi Kit. The cells were harvested by centrifugation (2000xg, 5 min, RT) and resuspended in 300 µl buffer P1. After the addition of 300 µl buffer P2, the cell suspension was incubated for 5 minutes at RT. 300 µl buffer P3 were added and the sample was mixed immediately by inverting 5 times prior to 10 minutes incubation on ice. The solution was centrifuged (14000 × g, 10 min, RT) and the cleared lysate was isolated and centrifuged (14000 × g, 10 min, RT) again. The supernatant containing the bacmid DNA was precipitated by adding 800 µl of room-temperature isopropanol and incubated for 10 minutes on ice. The DNA was pelleted (14000 × g, 15 min, RT), washed with 500 µl of 70% ethanol and centrifuged (14000 × g, 5 min, RT). The pellet was air-dried for 10 minutes and the bacmid DNA was dissolved in 40 µl buffer EB or water and either stored at -20°C or directly transformed in *Sf9* insect cells.

2.2.3.3 Insect Cell Culture

2.2.3.3.1 Cell Line and Cell Growth

In this thesis, *Sf9* insect cells were used for the recombinant production of human myosin motor domain constructs using the baculovirus expression system. *Sf9* cells are a clonal isolate originated from the IPLB-Sf21-AE cell line, derived from the pupal ovarian tissue of the armyworm *Spodoptera frugiperda* (Smith et al, 1983). The morphology of typical *Sf9* cell is round and short spindle-shaped. *Sf9* insect cells have a doubling time of 72 hours. *Sf9* cells were maintained under sterile conditions in monolayer and suspension culture. The insect cells grow optimally at 27°C in serum-free suspension as well as in adhesion culture and do not require CO₂ supplement. Insect cell medium was equilibrated to room temperature prior to use. Handling of *Sf9* cells was carried out in a laminar flow hood.

2.2.3.3.1.2 Initiation

A vial of frozen cells was removed from liquid nitrogen and thawed on ice. The cells were directly added to 10 ml medium and centrifuged (1000 × *g*, 5 min, 4°C). The cell pellet was resuspended in fresh medium and transferred to an Erlenmeyer flask. The cells were maintained between 0.8·10⁶ cells/ml and 2·10⁶ cells/ml for a time period of 10 days.

2.2.3.3.1.3 Cultivation of *Sf9* Cells in Adhesion- and Suspension Culture

Sf9 insect cells need to be sub-cultured by diluting the cells back to a density that is required to maintain logarithmic growth and provides maximum viability.

Subculture procedure for adherent cultures: Adherent cultures were passaged at confluence and diluted 1:5 in fresh media. The conditioned media was removed from the cells and replaced with fresh media. The cells were dislodged from the culture with a cell scraper. One fifth of the cell suspension was transferred into a new culture flask and diluted to the original volume with fresh media. The cells were incubated at 27°C until they reach confluency. The following table summarizes parameters for the cultivation of *Sf9* cells in monolayer culture.

Table 13: Flask sizes and medium volumes

Flask Size [cm ²]	Cell density at confluency	Volume [ml]
9.6 (6-well plate)	$1.2 \cdot 10^6$	2
T-25	$4.0 \cdot 10^6$	4
T-75	$1.2 \cdot 10^7$	13
T-175	$2.7 \cdot 10^7$	35

Alternatively, *Sf9* insect cells were maintained in suspension culture. Cells were grown in sterile Erlenmeyer flasks in a 27°C constant-temperature incubator with an orbital shaker platform. For shaker cultures, the working volume was maximum 50% of the indicated volume for adequate aeration. Suspension cultures were diluted before they reached a maximum density of $4 \cdot 10^6$ cells/ml and diluted back with fresh medium to a minimum of $0.8 \cdot 10^6$ cells/ml. This procedure maintains the cells in the logarithmic growth phase.

2.2.3.3.1.3 Cryoconservation

Sf9 insect cells were frozen when they doubled regularly and were >95% viable at as low passage number as possible. This was typically after 10-14 days after the initiation of a new culture. The cells density was determined and the cells were centrifuged ($1000 \times g$, 5 min, 4°C). The conditioned medium was removed and saved in order to prepare the freezing medium (Table 14). The cells were resuspended to a density of $1.5-2 \cdot 10^7$ cells/ml in Freezing-Medium. One milliliter of the cell suspension was transferred to sterile cryovials and incubated on ice for 30 minutes. The vials were placed at -20°C for 1 hour in a Styrofoam box, transferred to -80°C for 24 hours and finally stored in liquid nitrogen.

Table 14: Medium for cryoconservation

Freezing-Medium	
50%	Conditioned medium
42.5%	Fresh medium
7.5%	DMSO

2.2.3.3.1.4 Cell Density and Viability

The number of viable cells per milliliter cells and the relative amount of viability can be determined with a hemocytometer. For determining cell viability and cell number, 10 μ l of *Sf9* suspension culture are mixed with 10 μ l trypan blue dye. 10 μ l of the solution are infused in a hemocytometer. Dead cells appear blue in the since their membranes are no intact and they take up the dye. Live cells have intact membranes that exclude the dye. The total amount of cells as well as the amount of dead cells is determined over 25 squares of the hemocytometer. The number of living cells was calculated from the counted number of cells multiplied with the dilution factor of the solution as well as the factor 10^4 . The viability of the *Sf9* cells should be at least 98%.

2.2.3.4 Transfection

The transfection of *Sf9* insect cells was carried out with the cationic lipid reagent Cellfectin II according to the manufacturer. 0.8×10^5 cells in 2 ml medium were seeded in each well of a 6-well plate and the cells were allowed to attach for 30 minutes. Meanwhile, 8 μ l Cellfectin II were diluted in 100 μ l medium and combined with a solution containing 1-2 μ g bacmid in 100 μ l medium. The combined transfection mixture was incubated for 15-30 minutes at room temperature. After the incubation, the transfection mixture was added drop-wise onto the cells. The cells were incubated for 3-5 hours before the transfection mixture was removed and replaced with 2 ml medium. The cells were incubated for 4 days or until they showed signs of viral infection. Baculovirus containing medium was harvested as described under section 2.2.3.3.1.3.

2.2.3.5 Amplification and Isolation of Recombinant Baculovirus

Recombinant baculovirus stocks were amplified from low passage seed stocks in order to produce larger volumes of virus and high titer stocks. This step is necessary to generate a viral stock for the large-scale production is recombinant myosin motor domain constructs in *Sf9* insect cells.

To amplify recombinant baculovirus in monolayer culture, cells were infected at 70% confluency with 1/50 - 1/100 (volume of virus/final volume of medium) with

recombinant baculovirus (Table 13). The cells were incubated for 4 days prior to harvesting the supernatant from the plate. Cellular debris was removed by centrifugation (1000 × *g*, 5 min, 4°C). The virus containing supernatant was sterile filtered (0.22 μM) and stored in a sterile container at 4°C protected from light.

To amplify recombinant baculovirus from suspension culture, cells were infected at a maximal density of 1.6·10⁶ cells/ml with 1/50 or 1/100 volume of virus/final volume of medium with recombinant baculovirus. The cell suspension was cultivated for 4 days and cells and cell debris were isolated by centrifugation (1000 × *g*, 5 min, 4°C). The supernatant was isolated, sterile filtered and stored at 4°C, protected from light.

2.2.3.6 Protein Production and Isolation of Expressing Cells

For the recombinant production of human myosin motor domain constructs in *Sf9* insect cells, cells in suspension cultures were inoculated at a cell density of 1.6·10⁶ cells/ml with 1/10 volume of recombinant virus/final volume of medium. The cells were grown for 72 hours in suspension culture and harvested by centrifugation (1000 × *g*, 5 min, 4°C). The cell pellet was resuspended in 1/10 of the initial volume PBS, centrifuged (1000 × *g*, 5°C, 4°C) and stored at -80°C upon usage.

2.2.4 Dictyostelium discoideum Cell Culture

Dictyostelium discoideum's (*D.discoideum*) ability to be easily cultivated in the lab adds to its appeal as a model organism. They can be grown in liquid culture and also in petri dishes best at 20 to 22 °C. AX-2 and AX-4 cells of *D.discoideum* were used in this study for cell culture and also for recombinant protein production.

2.2.4.1 Recombinant Protein production In *D.discoideum*

The eukaryotic organism *Dictyostelium discoideum* (*D.discoideum*) is one of the preferred organisms of choice for the overproduction of recombinant myosins and myosin fragments (Manstein & Hunt, 1995).

The expression vectors used in this work are derivatives of the *D.discoideum* pDXA vector (Manstein & Hunt, 1995). The vectors comprise the origin of replication (*ori*) of the *D.discoideum* high-copy-number plasmid Ddp2. The expression cassette of all vectors contain the strong, constitutive actin promoter *act15*, a start codon upstream of the multiple cloning site (MCS) as well as C- or N-terminal sequences for affinity tags. They also have the *act6* neo^R Tn5 cassette for resistance to G418 for selection of positive transformants. Downstream of the MCS, polyadenylation and termination signals are present. In this work, the vector pDXA-3H was used, which comprises the DNA sequence coding for a C-terminal histidine octamer downstream of the MCS (Manstein et al, 1991). The incorporation of cDNA sequence encoding for *D.discoideum* myosin-2 motor domain into the MCS of the vector results in the recombinant production of His₈ tagged protein, which can be purified by Ni²⁺-NTA-affinity chromatography.

2.2.4.2 Analytical Preparation of Recombinant Myosin Motor Domains Expressed in *D.discoideum*

The recombinant production of myosin motor domain constructs was carried out according to the protocol for transformation and selection of positive transformants as described (Manstein et al, 1989). The selected transformants were picked and used for the production of His₈-tagged motor domain construct of *Dd* myosin-2, which was fused to single strand binding protein tail (SSB tail). Initially, the expression of myosin-2 motor domain proteins was carried out in the petri plate (9 cm plate) until the cells reach confluency ($2-5 \times 10^7$ cells). For the analytical test of protein expression, the attached cells were scraped from the plate, resuspended in Lysis Buffer 1 and transferred to a reaction tube. After centrifugation (5,000 rpm, 2min, 4°C), the pellet was washed in 1 ml Extraction Buffer. The pellet was resuspended in 500 μ l Lysis Buffer 2 and cells were lysed by adding the same volume of Lysis Buffer 3. The cells were incubated (1 hour on ice) and centrifuged (13000 rpm, 30 min, Eppendorf 5415C). The pellet was washed with 500 μ l Lysis Buffer 1 and centrifuged (13000 rpm, 25 min, Eppendorf 5415C). The pellet contains the insoluble actomyosin complex, which is extracted in the presence of Mg²⁺-ATP by homogenizing the pellet in 50-70 μ l

Lysis Buffer 4. The extract was centrifuged (13000 rpm, 20 min). The supernatant was removed and mixed with 50-70 μ l SDS Loading Buffer for the qualitative and quantitative analysis of the extracted protein via SDS-PAGE. Routinely, more than 90% of the protein in the soluble fraction correspond to actin, myosin, and the recombinant myosin fragments. Therefore, it is easy to detect any differences in expression levels between individual myosin constructs via SDS-PAGE analysis. Furthermore, the presence of a band corresponding to the recombinant protein indicates that the overexpressed protein has at least some of the functional properties that are characteristic for a myosin motor (Manstein & Hunt, 1995).

Table 15: Buffers and inhibitor mixes for the analytic preparation of myosin motor domain constructs from *D.discoideum*.

Lysis Buffer 1	Lysis Buffer 2	Lysis Buffer 3
50 mM Tris/HCl pH 8.0 2.5 mM EDTA 0.2 mM EGTA Protease-Inhibitor Mix 1 (freshly prepared) 1x Protease-Inhibitor Mix 2 (freshly prepared)	Lysis Buffer 1 1 U CIAP/sample (freshly prepared)	Lysis Buffer 1 1% (v/v) Triton-X 100
Lysis Buffer 4	100x Protease-Inhibitor Mix 1	1000x Protease-Inhibitor Mix 2
Extraction Buffer 12 mM MgCl ₂ 10 mM ATP (freshly prepared)	10 mg/ml TAME 8 mg/ml TPCK 0.2 mg/ml Pepstatin A 0.5 mg/ml Leupeptin, absolute Ethanol	100 mM PMSF, in absolute ethanol

2.2.4.3 Overexpression and Purification of *Dd* Myosin-2 Motor Domain

Once the expression of the motor domain is confirmed by analytical preparation (see section 2.2.4.2), the volume of the cells can be scaled up for the preparative protein purification. In principle, the protocol for the preparative protein purification is similar to the analytical minipreparation. The two procedures differ only in the amount of cells processed, and by an affinity chromatography step following the extraction of the myosin motor domain construct (Manstein and Hunt, 1995).

If not stated otherwise, all steps were carried out at a temperature of 4°C and all buffers and solvents were prechilled to 4°C prior to use. In this work, 18 l of cells were harvested at a cell density of 6×10^6 - 1×10^7 cells/ml. The cells were pelleted (4200 rpm, 5 min, 4°C, rotor JS-4.2), washed with 0.5 l of cold PBS Buffer and pelleted (4200 rpm, 5 min, 4°C, rotor JS-4.2) again. The wet weight of the pellet was determined. The washed cells (10-25 g) were resuspended in 5-vol/g cell of Lysis Buffer 1 and transferred to a glass flask. After adding the same volume of Lysis Buffer 2, the suspension was sonicated for 1-2 minutes with a 30 s pause ($\frac{3}{4}$ " tip, 50% power setting, 40% duty cycle). The suspension was incubated for further cell lysis for 45 minutes with gentle stirring at 4 °C. The lysate was ultracentrifuged (40000 rpm, 1h, 4°C, rotor 45Ti). After centrifugation, the supernatant was discarded and the pellet was washed with 60-100 ml of Wash Buffer and centrifuged (45000 rpm, 45 min, 4°C, rotor 45Ti). The supernatant was discarded and the solid pellet, containing the myosin motor domain construct, was extracted by resuspension in 1.6 vols./g cells of Extraction Buffer supplemented with 10 mM ATP. The cell extract was centrifuged (60000 \times g, 1h, 4°C, rotor 70Ti) and the supernatant was applied in the following Ni²⁺-NTA affinity chromatography step.

Table 16: Buffers for the preparative production of myosin motor domain constructs from *D.discoideum*.

Lysis Buffer 1	Lysis Buffer 2	Wash Buffer	Extraction Buffer
50 mM Tris:HCl, pH 8.0	Lysis Buffer 1	50 mM Tris:HCl, pH 7.3	50 mM HEPES, pH 7.3
2.5 mM EDTA	1% (v/v) Triton-X 100	30 mM Potassium acetate	30 mM Potassium acetate
0.2 mM EGTA	15 µg/ml Ribonuclease A	15 mM Magnesium acetate	15 mM Magnesium acetate
1 mM DTT (freshly prepared)	100 U absolute CIAP (freshly prepared)	7 mM β-mercapto ethanol (freshly prepared)	0-300 mM KCl
5 mM benzamidine (freshly prepared)		5 mM benzamidine (freshly prepared)	7 mM β-mercapto ethanol (freshly prepared)
40 µg/ml TLCK			5 mM benzamidine (freshly prepared)
Protease-Inhibitor Mix 1 (Table 15)			15 µg ATP (freshly prepared)
Protease-Inhibitor Mix 2 (Table 16)			

2.2.4.4 Ni²⁺-NTA affinity chromatography

The myosin-containing supernatant was filtered through a sterile filter with the pore size of 45 µm. By using the Äkta FPLC system, the filtrate was applied on to a Ni-NTA affinity chromatography column (2 x 20 cm) via a super-loop (capacity 150 ml). Before loading the sample, the column was pre-equilibrated with 10 column volumes (CV) of Low Salt Buffer. Once, the sample was loaded completely, the column was washed with 10 CV Low Salt Buffer, 5 CV of High Salt Buffer followed by a wash with Low Salt Buffer containing 25mM imidazole was used for removal of non-specific proteins. The elution of the protein was realized by a gradient of 3 to 100% Ni-NTA imidazole buffer containing the

NiNTA Low Salt Buffer (6 CV at 2 ml/min flow rate). The elution profile of the myosin-2 motor domain was followed on the OD_{280nm} trace. Appropriate fractions were collected and analyzed by SDS-PAGE. The fractions containing the myosin motor domain were pooled and dialyzed against 2L Storage Buffer. The pure protein was concentrated by ultracentrifugation using Vivaspin devices.

Table 17: Buffers for the Ni²⁺-NTA affinity chromatography of myosin motor domain constructs from *D.discoideum*.

Low Salt Buffer	High Salt Buffer	Imidazole Buffer	Storage Buffer
50 mM HEPES, pH 7.3	50 mM HEPES, pH 7.3	1 M Imidazole, pH 7.3	50 mM HEPES-KOH, pH 7.4
30 mM Potassium acetate	300 mM Potassium acetate	3 mM benzamidine (freshly prepared)	0.5 mM EDTA
3 mM benzamidine (freshly prepared)	3 mM benzamidine (freshly prepared)		1 mM DTT
			1 mM MgCl ₂
			1 mM benzamidine (freshly prepared)
			3% (w/v) sucrose and 150 mM KCl

2.2.4.5 Gel Filtration

In order to attain high purities of the recombinant myosin motor domain constructs, impurities were removed by gel filtration. Hence, the concentrated protein solution was sterile filtered (0.22 µM) and loaded on a pre-equilibrated Superdex 26/60-200 prep grade gel filtration column with a flow rate of 0.5 ml/min. The sample was eluted with Storage Buffer (Table 17) (flow-rate: 0.5 ml/min, maximal pressure: 0.5 MPa) and the eluate was collected in 1 ml fractions. The fractions were analyzed by SDS-PAGE and myosin containing

fractions were pooled and concentrated up to 10-20 mg/ml. Aliquots of the protein samples were flash-frozen in liquid nitrogen and stored at -80°C for future usage.

2.2.4.6 Protein Quantitation

Since proteins contain tryptophan, tyrosine or cysteine-cysteine disulfide bonds that absorb in the UV range (280 nm), purified proteins can be directly quantified by determining the UV absorbance at 280 nm in a UV-visible spectrophotometer. The Lambert-Beer equation was used to correlate the absorbance at 280 nm with the protein concentration.

$$A = \varepsilon \cdot c \cdot d$$

Where A, is the absorbance, ε is the molar extinction coefficient ($M^{-1} \cdot cm^{-1}$), c is the protein concentration (M=moles/liter) and d is the path length in centimeters. The molar extinction coefficient was determined, based on the protein sequence, by using the online tool 'Protparam' (Gasteiger et al, 2005).

2.2.4.7 Sodium Dodecyl Sulfate Polyacrylamide Gel Electrophoresis (SDS-PAGE)

SDS-PAGE is a method to separate proteins according to their size using a denaturing and discontinuous method developed by Laemmli (Laemmli, 1970). For the determination of the purity and size of prepared proteins from *Sf9* and *D.discoideum* cells, precast 4-20% gradient gels (Pierce) were used. The protein samples were supplemented with 3x SDS Loading Buffer and boiled (10 min, 95°C). The samples were loaded on the gel together with an appropriate protein marker.

Table 18: Buffers for the SDS-PAGE

HEPES-Running Buffer	3x Loading Buffer
0.1 M Tris pH 8.0	0.2 M Tris/HCl pH 6.8
0.1 M HEPES	33 % Glycerol
3 mM SDS	3% SDS
	3.2 % β -Mercaptoethanol
	0.0016 % Bromphenol Blue

The gel was run at a constant current of 30 mA for a time period of one hour in HEPES-Running Buffer. After the separation of the protein samples, the gel was subsequently stained with PageBlue solution.

2.2.4.8 PageBlue-Staining

Subsequent to the SDS-PAGE, the gel was transferred into a plastic container, covered with deionized water and microwaved for 2 minutes on high power. The water was discarded and the gel was covered with PageBlue solution, heated in the microwave for 30 seconds on high power and subsequently shaken for 15 minutes at room temperature. The staining solution was discarded. The gel was destained by washing with water and microwaving for 5-10 minutes.

2.2.5 Biophysical Methods

2.2.5.1 Steady-State ATPase Assay

The myosin steady-state ATPase activity in the presence or absence of F-actin was assayed in a spectrophotometric assay, which is based on the regeneration of hydrolyzed ATP, coupled to the oxidation of NADH. This coupled enzymatic assay, as schematically depicted in figure 2.1 is based on the ADP dependent conversion of phosphoenolpyruvate (PEP) to pyruvate, catalyzed by the enzyme pyruvate kinase (PK). Subsequently, pyruvate is converted to L-lactate by the enzyme lactate dehydrogenase (LDH). This step requires NADH, which is oxidized to NAD⁺. NADH oxidation is accompanied with a decrease in NADH absorbance at 340 nm, which is directly proportional to the rate of the myosin steady-state ATP hydrolysis.

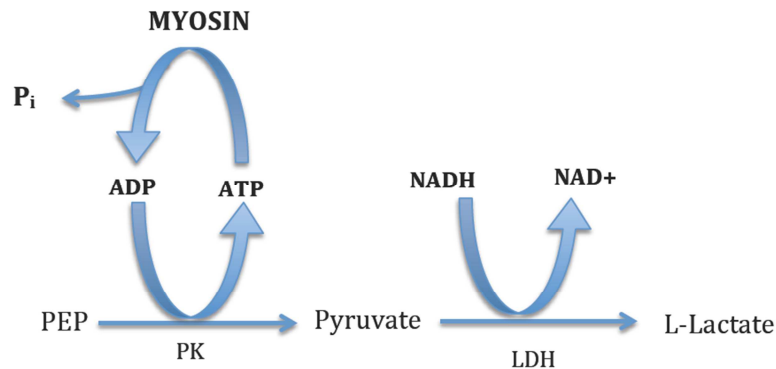


Figure 2.1: Schematic representation of the myosin steady-state ATPase assay.

The steady-state ATPase activity in the presence or absence of F-actin was performed at 25 °C. Typically 0.2-0.5 μM myosin was mixed with either 30, 40 or 140 μM F-actin (depends upon the type of myosin) in a total volume of 100 μl ATPase Buffer.

Measurements of the steady-state ATPase activity were either performed in UV-transparent microtiter plates (96 well, half area, flat bottom) or quartz cuvetts in a spectrophotometer. In 96 well plates (Corning half area UV transparent), a standard reaction volume of 100 μl corresponds to a path length of 0.56 cm. Data acquisition was performed with the software SkanIt 2.5.1 (Thermo Scientific). The change in absorbance was detected at a wavelength of 340 nm, a temperature of 25°C and a time period of max. 10 minutes. The data acquisition interval was 4-5 second. Analysis of the time series was performed with ORIGIN 8 (OriginLab).

The rate of ATP hydrolysis (k_{ATPase}) is calculated from the following equation:

$$k_{\text{ATPase}} = \frac{-\Delta\text{Abs}/\text{min}}{60\text{s} \cdot \text{min}^{-1} \cdot \epsilon_{\text{NADH}(340\text{nm})} \cdot d \cdot [\text{myosin}]}$$

Where, $\epsilon_{\text{NADH}(340\text{nm})}$ is the molar absorption coefficient of NADH at a wavelength of 340 nm and equals $6620 \text{ cm}^{-1}\text{M}^{-1}$. $\Delta\text{Abs}/\text{min}$ is the time-dependent change of the absorption signal; d is the path length of the well/cuvette and $[\text{myosin}]$ is the myosin concentration.

Table 19: Buffers for the steady-state ATPase assay.

ATPase Buffer		
25 mM HEPES pH 7.4	0.2 mM NADH	2 mM ATP
0-25 mM KCl	0.05 mg/ml PK	0-140 μ M F-Actin
5 mM MgCl ₂	0.5 mM PEP	0.2-0.5 μ M Myosin
0.5 mM DTT (fresh)	0.02 mg/ml LDH	

2.2.5.2 Transient kinetics

Transient kinetic analysis defines the elementary steps along the pathway of an enzyme catalyzed reaction. The methods rely on rapidly mixing a substrate with a sufficient concentration of enzyme to allow a direct observation of intermediates and products formed at the active site during a single enzyme cycle. Stopped-flow methods afford observation of reactions by monitoring changes in optical signals (i.e., absorbance, fluorescence, and light scattering) as a function of time after mixing. Analysis of the substrate concentration dependence of the rates and the amplitudes of observable species can define the sequence of events that occur after substrate binding (Johnson, 1998; Johnson & Porter, 1982).

2.2.5.3 Stopped-flow techniques

Stopped-flow techniques were used to study the kinetics of myosin in the presence of nucleotides and F-actin in solution. Figure 2.2 shows the scheme of a typical stopped-flow apparatus. A Stopped-flow spectrophotometer contains two syringes with reactant solutions that are rapidly mixed and pushed in a mixing chamber and then in an observation cell. The flow fills the stop syringe, which hits the trigger. The trigger switch stops the flow and starts data acquisition by monitoring an optical signal.

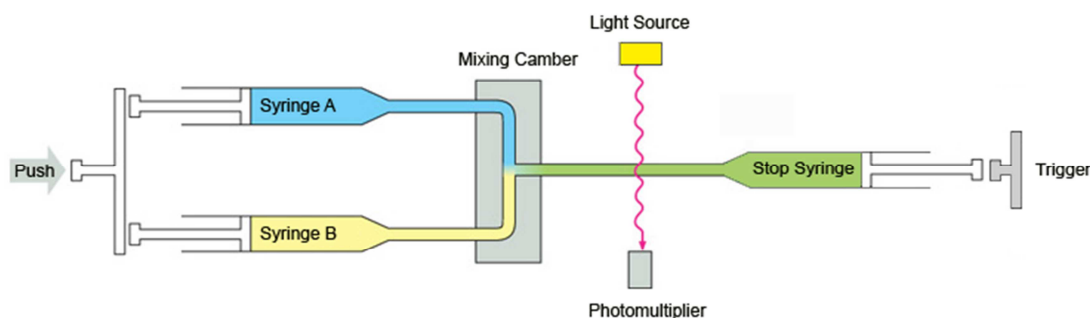


Figure 2.2: Schematic representation of a stopped-flow spectrophotometer. (Scheme was adapted and modified from this reference link: <http://porpax.bio.miami.edu/~cmallery/255/255enz/ecb3x28.jpg>).

In the present work, transient kinetic assays were performed with a SF-61SX2 stopped-flow system (Hi-Tech Scientific) equipped with a 75W Hg/Xe lamp. The performance of the instrument is limited by the dead time, which is ~ 1 ms.

To study the interaction between myosin, F-actin and nucleotides either the intrinsic tryptophan fluorescence signal or the light scattering signal was detected. Mant-fluorophores (N-methylanthraniloyl) (Figure 2.3B) or the fluorescent label pyrene (Figure 2.3A) enabled the detection of extrinsic fluorescence signals.

Usage of fluorescent probes like mant-nucleotides is a valuable tool to determine the kinetic properties of the myosin motor domain (Batra et al, 1999; Ritchie et al, 1993; Stewart et al, 2010). Since the mant moiety is very compact and its attachment position on the ribose ring of nucleotides result in minimal perturbations of the nucleotide-protein interaction. Furthermore, the fluorescence is polarity-sensitive and enables the direct detection of the nucleotide-myosin interaction (Batra & Manstein, 1999; Friedman et al, 1998).

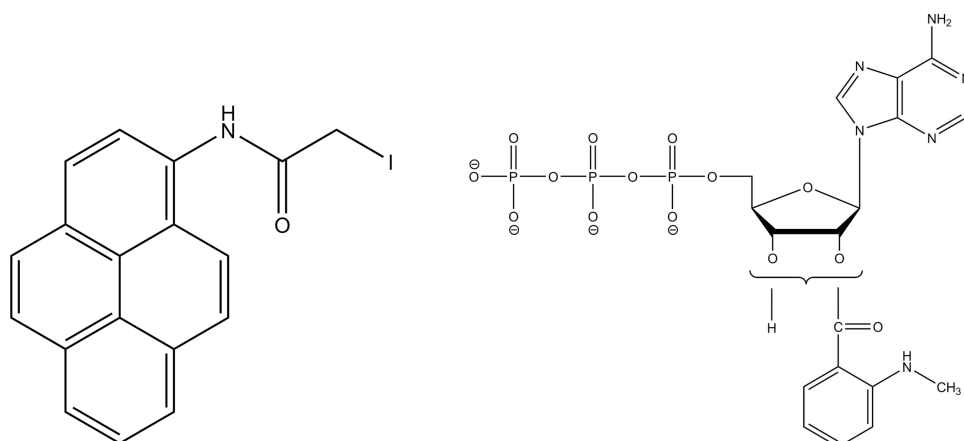


Figure 2.3: A (right panel): Pyrene is a UV excitable thiol-reactive fluorophore that can be used to monitor the reaction between myosin and F-actin. B (left panel): MantATP has an excitation/emission maximum at 355/448 nm. The quantum yield of the fluorophore is highly environmental sensitive and increases significantly upon binding to myosin motor domains. B (left panel): Pyrene is a UV excitable thiol-reactive fluorophore that can be used to monitor the reaction between myosin and F-actin.

The interaction between myosin and F-actin can be assayed directly by using the fluorescently labelled pyrene-actin. The strong fluorescence of the pyrene moiety in combination with the strong quench in fluorescence (up to 70%) upon myosin binding makes pyrene an ideal marker for the transient kinetic studies of the actin-myosin interaction (Criddle et al, 1985).

When assaying the interaction between myosin and nucleotides, the intrinsic protein fluorescence was excited at 297 nm and the emitted light was detected after the passage of a WG320 cut-off filter. The WG320 filter eliminates the emission light (wavelength of 348 nm) from the excitation light. When using mant-nucleotides, the fluorescence was excited at a wavelength of 365 nm and the fluorescence emission was monitored through a KV389 filter. Alternatively, the FRET signal, arising from the radiationless transition from myosin to the mant-moiety, was excited at a wavelength of 297 nm and the fluorescence emission was monitored after passage through a KV389 filter. Pyrene-fluorescence was excited at a wavelength of 365 nm and the emitted light was detected after the passage of a KV389 cut-off filter.

If not stated otherwise, given concentrations are final concentrations after mixing the reactants in a 1:1 ratio in the stopped-flow apparatus. The reaction volume was 50 μl per shot. Each experimental condition was at least assayed 3 times to optimize the signal-to-noise ratio. Data acquisition and evaluation was performed with the software Kinetic Studio 1.12 (TgK Scientific). The time-dependent change of the spectroscopic signal was approximated with single or double exponential regressions. If not stated otherwise, all assays were carried out at a constant temperature of 20°C in MOPS-Buffer with a fixed MgCl_2 concentration of 5 mM. Before usage, the buffer was sterile filtered (0.22 μm) and degassed.

Table 20: Buffer for the stopped-flow assays.

MOPS-Buffer
20 mM MOPS pH 7.0
100 mM KCl
0-20 mM MgCl_2

2.2.5.4 *In vitro* Motility assay

The *in vitro* motility assay is a simplified model of force and motion generation by myosin motors (Warshaw et al, 1990a; Warshaw et al, 1990b). In the present work, the assay was performed with recombinant myosin motor domain constructs fused to an artificial lever arm in order to study the interaction of the myosins with small molecule effectors.

Preparation of flow cells: For the preparation of the flow cells, 1% (w/v) nitrocellulose was incubated in amyl acetate overnight at a temperature of 4°C. A 1.5 μl drop of this solution was placed on a coverslip and spread over the surface with a 10 μl tip. The coverslip was dried for 10 minutes at room temperature. Two parallel strips of double-sided tape were placed 4 mm apart from each other on a microscope slide. The coated coverslip was placed up side down on a microscope slide. This generates flow cells with a volume of approximately 10 μl . The flow cells were constructed and stored up to 3 days at 4°C.

To ensure a good quality of movement, inactive motors were separated from active motors via an actin-purification step. Therefore, 0.4-0.5 mg/ml myosin was

mixed 1:1 (mass ratio) with unlabelled F-actin in the presence of 3.5 mM ATP in AB Buffer and sedimented (70000 rpm, 20 min, 4°C, rotor 120.1) in an ultracentrifuge. TRITC-phalloidin actin was prepared as described under section 2.2.2.4.

For the preparation of the flow cell, 10µl penta-histidine-antibody (0.025 mg/ml antibody dissolved in water) was filled in the flow cell and allowed to remain in the cell for 5 minutes. The flow cell was washed with 10 µl Buffer 1 in order to prevent unspecific binding. 10 µl myosin solution was filled in the flow cell. After incubation for 2 minutes, the flow cell was washed with 10 µl Buffer 1, followed by the infusion of 10 µl fragmented F-actin solution (approx. 20 nM). The chamber was incubated for 2 minutes in order to block non-specific binding. The flow cell was subsequently washed with 10 µl Buffer-4 and 10 µl Buffer 1. 10 µl TRITC-phalloidin labelled F-actin (approx. 20 nM) were perfused and incubated for 2 minutes. The flow cell was washed with 10 µl Buffer 1 and 10 µl Buffer-2. After the addition of Buffer 2, the decoration of the myosin with TRITC-labelled F-actin was checked under the microscope. The assay was started with the addition of 10 µl Buffer 3.

The movement of actin filaments over the myosin-decorated nitrocellulose surface was determined with an Olympus IX70 microscope equipped with an 60x oil-immersion objective (PLAPO/TIRF) in an enclosed box at a temperature of 30°C. The pixel size was defined by the reaction setup: When a camera-binning of 2x2, a microscopic magnification of 1 or 1.5 together with a 60-fold objective magnification was used, calibration with an object micrometre resulted in a pixel size of 0.215 µM and 0.144 µM, respectively. TRITC-fluorescence was excited at a wavelength of 545 nm and the fluorescence emission was detected at a wavelength of 570 nm. The corresponding filters were implemented in the microscope.

In a standard assay, 100 images were acquired with a 1394 Orca-ERA CCD-camera (Hamamatsu Photonics). The exposure time of the fluorophore was 230 ms. The interval between two images was 300 or 600 ms. The resulting movie is

a split screen image of actin filaments over a myosin- decorated nitrocellulose surface. The images were converted to 'TIFF' images with the program Cell^R (Olympus). Actin sliding velocities were determined by an automatic tracking system (DiaTrack 3.01, Semasopht). The software determines the mean sliding velocity of the centre of single actin filaments along trajectories. For the evaluation of the mean sliding velocities, the data was exported in ORIGIN 8 (OriginLab) and up to 10 individual data were merged. The sliding velocities were graphed as histogram and the mean velocity was calculated with a Gaussian function according to the following equation:

$$y = \frac{1}{\sigma\sqrt{2\pi}} e^{\left(-\frac{1}{2}\left(\frac{x-\mu}{\sigma}\right)^2\right)}$$

In this equation, the parameter μ equals the statistical average and σ equals the standard deviation.

Table 21: Buffers for the *in vitro* motility assay.

AB Buffer	Buffer 1	Buffer 2	Buffer 3	Buffer 4
25 mM Imidazole	10 mM DTT	5 mg/ml Glucose	5 mg/ml Glucose	4 mM ATP
25 mM KCl	0.5 mg/ml BSA	0.1 mg/ml Glucose oxidase	0.1 mg/ml Glucose oxidase	in AB Buffer
0.5-10 mM MgCl ₂	in AB Buffer	0.02 mg/ml Catalase	0.02 mg/ml Catalase	
1 mM EGTA pH 7.4		in AB Buffer	4 mM ATP in AB Buffer	

2.2.6 Crystallographic Methods

2.2.6.1 Crystallization

To determine the structure of proteins and protein-effector complexes, highly purified protein was used in all the instances. To form crystals, proteins had to attain an ordered arrangement. Since this formation of crystals is influenced by different factors such as homogeneity, concentration, temperature, pH, salt and many other factors, one has to initially consider these factors before starting any crystallization setups.

For crystallization purpose, the most common and effective vapour diffusion method “hanging drop” and “sitting drop” were used. Both entail a droplet containing protein, buffer, and precipitant being allowed to equilibrate with a larger reservoir containing similar buffer and precipitant. In the hanging drop method; the protein solution is placed on a siliconised glass cover slide. An aqueous buffered solution with precipitant, known as mother liquor, is mixed with the protein drop at a concentration just below that necessary to precipitate the protein (Figure 2.4). Usually, the protein solution and the mother liquor are mixed in a 1:1 ratio such that the reagents of the resulting drop have half of their original concentration. The cover slide is then inverted over a reservoir containing the crystallization solution (500 μ l) and sealed with grease. Since the reagents in the reservoir solution have double the concentration to those in the drop, water gradually evaporates from the drop. When the precipitating condition or supersaturated state is reached; protein crystals may form. In the sitting drop method; the protein solution is placed in a post inside the well of a 24 well Linbro plate. Equal volume (1:1) mixing of mother solution with protein solution has been done in all cases. The same procedure of vapour diffusion principles applies in this method also.

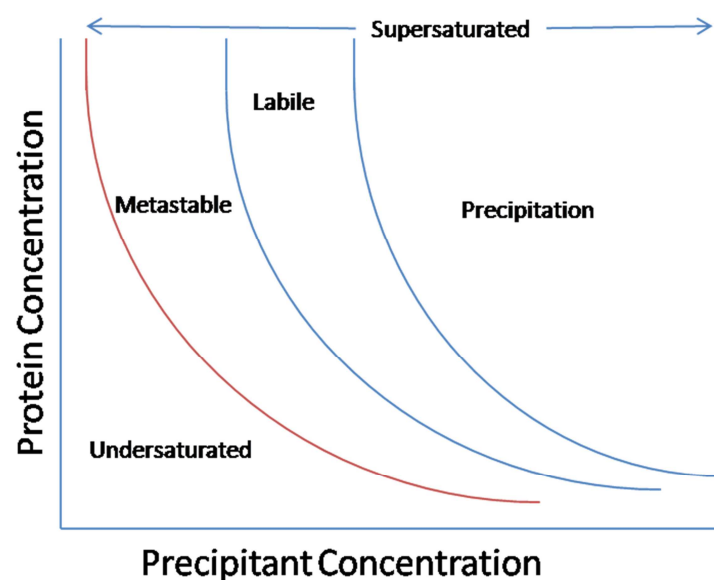


Figure 2.4: Phase diagram of macromolecule crystallization. This figure adapted from, Neer Asherie (Asherie, 2004).

2.2.6.2 Screening of Crystallization Conditions

In order to find a proper crystallization condition, different commercial sparse-matrix and grid screens were tested. For initial crystallization conditions, the crystallization screens MFS (myosin fusion screen, in house prepared), JCSG++ suite, PEGs suite, Ammonium Sulfate suite, MPD suite, pH suite, Anion & Cation suite and Classics suite were employed. Conditions containing hints of crystal formation were optimized by individually devised screens around the initial condition by altering buffer, precipitant, and additive concentrations and identities, as well as altering the temperature of crystallization (12 °C, 8 °C and 4°C) and protein concentration. Therefore, 500 µl of precipitant solution were filled into a Linbro crystallization plate containing 24 wells. 2 µl of mother liquor was mixed with 2 µl of protein solution on a siliconised cover slide. The cover slide containing the drop hanging upside down was sealed with grease (hanging drop vapour diffusion method). In most cases, crystals grew in 2 weeks but the biggest and best diffracting crystals took 3-4 weeks to grow.

2.2.6.3 Crystallization of Pentachloropseudilin with *Dd* Myosin-2

The *Dd* myosin-2 motor domain construct M761 was used for crystallization in the presence of pre-incubated (1 hour, 4 °C) mixture of sodium meta-vanadate (2 mM), ADP (2 mM), and PCIP (0.5 mM). A mother liquor of 50 mM HEPES pH 7.4, 140 mM NaCl, 11% w/v PEG8000, 2% (v/v) MPD, 5 mM MgCl₂, 5 mM DTT, and 1 mM EGTA was mixed in 1:1 ratio with the pre-incubated protein solution. Hanging-drop method was used.

2.2.6.4 Crystallization of Ammosamides with *Dd* Myosin-2

The *Dd* myosin-2 motor domain construct M761 was used for crystallization. Initial trials of sparse and grid matrix as well as attempts of co-crystallization Ammosamides with the *Dd* myosin-2 motor domain failed. However, *Dd* myosin-2 motor domain crystals grew at 4°C in a mother liquor containing 50 mM HEPES pH 7.6, 140 mM NaCl, 11% (w/v) PEG5K-MME, and 2% (v/v) MPD. Prior to crystallization, the protein was preincubated (1 hour, 4 °C) with a mixture of sodium ortho-vanadate (2 mM) and ADP (2 mM). *Dd* myosin-2 crystals were

grown in 3 weeks in the absence of any effector to a size of 500-600 μm . The crystals were used for soaking with the effectors Ammosamide A, Ammosamide B, Ammosamide 272 and Deschloroammosamide B. The crystals were soaked in gradually increasing concentrations of Ammosamides up to a final concentration of 2 mM. For each step of incubation, the crystals were incubated for 10 minutes in the presence of Ammosamides.

2.2.6.5 Crystallization of Human Nonmuscle Myosin-2C Motor Domain Fused to Alpha Actinin Repeats (2R) from *Dictyostelium discoideum*

The nonmuscle myosin-2C motor domain fused with two spectrin like alpha actin repeats (2R) was crystallized in the pre-power stroke state ($\text{Mg}^{2+}\cdot\text{ADP}\cdot\text{VO}_4$). Crystallization conditions were: 50mM Tris pH 8.2, 10 % PEG 5K MME, 1 % MPD and 200 mM NaCl. Protein and mother solution were mixed in a 1:1 ratio. Rectangular plate shaped crystals of the motor domain construct of nonmuscle myosin-2C grew in hanging drops using vapour diffusion at 8 $^{\circ}\text{C}$ by mixing 2 μl of protein solution (~ 12 mg/ml) with 2 μl of 50mM Tris pH 8.2, 10 % PEG-5K MME, 1 % (v/v) MPD and 0.2 M sodium chloride. Crystals with a size of 400 x 250 x 400 μm grew in 4 weeks.

2.2.6.6 Crystal Freezing and Data Collection

For myosin 2:effector soaked/co-crystallized crystals the cryo-solution, i.e. a solution that protects from the formation of ice upon freezing, was the same as the crystallization conditions with an additional 150mM NaCl and 20-25 % (w/v) ethylene glycol (Garman, 2003; Garman & Doublet, 2003). For non-muscle myosin-2C crystals, the cryo-solution was the same as the crystallization condition with an additional 20 % (w/v) ethylene glycol. Protein crystals were transferred in serial steps of increasing concentrations of the cryo-solution. Once the final concentration of the cryo-solution step reached, the crystals were then transferred into liquid nitrogen using a nylon loop or MiTeGen loops and stored at 100 K until data collection. At 100 K crystals were re exposed to X-rays, because at this temperature radiation damage is lower than at room temperature. Also, conformational disorder and thermal vibrations are reduced at this temperature

(Nave & Garman, 2005). In general, for diffraction of macromolecule crystals, either home sources or synchrotron sources were used. *Dd* myosin-2•ammosamide complexes were collected at home source (Bruker proteum X8 rotating anode, CuK α : 1.5418Å). Nonmuscle myosin-2C crystals and *Dd* myosin 2•PCIP complex data were collected at synchrotron source BESSY, BL14.1, Berlin.

2.2.6.7 X-ray Diffraction

X-ray diffraction from crystalline solids occurs as a result of the interaction of X-rays with the electron charge distribution in the crystal lattice. The ordered nature of the electron charge distribution, whereby most of the electrons are distributed around atomic nuclei which are regularly arranged with translational periodicity, means that superposition of the scattered X-ray amplitudes will give rise to regions of constructive and destructive interference producing a diffraction pattern (Hiltner & Krieger, 1969; Marchesini et al, 2003).

The diffraction maxima are some times individually considered to be the result of diffraction of the incident X-ray beam of Wavelength (λ) from crystal lattice planes, having miller indices $h k l$ and spacing d_{hkl} . Diffraction occurs at an angle of incidence equal to the Bragg angle θ_B , i.e. Bragg's law is obeyed:

$$\lambda = 2d_{hkl} \sin \theta_B$$

The way in which the separate scattered or diffracted rays combine to form an image depends on three factors associated with each ray: (a) the direction, (b) the amplitude and (c) the phase. In X-ray crystallography, the diffracted beams are separately observed and their intensities measured as the blackness of spots on an X-ray film or by direct quantum counting in a diffractometer. By identifying the Miller indices (hkl) of the crystal plane-giving rise to each diffracted beam, the direction of the beam is specified. From the measured intensity of the beam its amplitude can be deduced. The amplitude of the wave $|F_{hkl}|$ is proportional to the square root of the intensity measured on the detector. So two of the three necessary pieces of information about each beam are known, but unfortunately

there is no direct method available yet for observing the phase of each diffracted beam, which is the third piece of information needed before mathematical recombination is possible to produce an image of the structure. This constitutes what is known as the phase problem in crystallography (Taylor, 2003).

The solution of a crystal structure therefore consists of applying some technique for obtaining the approximate phases of at least some of the X-ray reflections, and the process of structure refinement is one in which the knowledge of phases is extended to all reflections and is made as accurate as possible for all reflections. Apart from the direct methods of obtaining some initial phases, both the solution and refinement processes depend on the ability to calculate structure factors for a proposed approximate arrangement of some or all of the atoms in the crystal structure.

It is possible to calculate simultaneously both the amplitude $|F_{hkl}|$ and phase α_{hkl} of each beam that would be diffracted by the proposed structure. Since the phases cannot be compared with any observable quantities, the validity of the proposed structure must be tested by comparison of the calculated values of the amplitudes of the structure factor F_c with the observed amplitudes $|F_o|$. This is represented by a *reliability index* or *R factor*:

$$R_{factor} = \frac{\sum ||F_o| - |F_c||}{\sum |F_o|}$$

Electron density at a position (xyz) in the unit cell of a crystal is the summation of all the hkl planes, which in words one can express as: electron density at (xyz) = the sum of contributions to the point (xyz) of waves scattered from plane (hkl) whose amplitude depends on the number of electrons in the plane, added with the correct relative phase relationship or, mathematically,

$$\rho(x, y, z) = \frac{1}{V} \sum_{hkl} |F_{hkl}| \exp(i\alpha_{hkl}) \exp(-2\pi i(hx + ky + lz))$$

Where, V is the volume of the unit cell and α_{hkl} is the phase associated with the structure-factor amplitude $|F_{hkl}|$.

In this thesis, *Dd* myosin 2•ammosamide complexes diffracted from 2.4 Å to 2.9 Å on Bruker proteum X8 rotating anode. Nonmuscle myosin-2C data diffracted to 2.0 Å and *Dd* myosin 2•PCIP complex diffracted to 2.5 Å at the synchrotron source BESSY, BL14.1 in Berlin.

2.2.6.8 Data Processing

Dd myosin 2•PCIP complex data was indexed, integrated and scaled with XDS (Kabsch, 2010). Nonmuscle myosin-2C data processing was performed using XDS and SADABS (Blessing, 1995). *Dd* myosin-2•ammosamide complexes data were collected at home source rotating anode generator and processed with proteum suite (Proteum X8, Bruker Inc).

2.2.6.9 Structure Solution

Phase problem can be partially solved by having an atomic model, from which estimates of the phases can be computed. Such a model can be obtained when the structure of a related protein is already known, or even the same protein from a different crystal form. But to build up an atomic model of the new crystal form, it is necessary to work out how the model should be oriented and position in the new cell. Rossmann *et al.* introduced the powerful molecular replacement technique to solve that problem (Rossmann & Blow, 1962).

2.2.6.9.1 Molecular Replacement

In this thesis, molecular replacement (Rossmann & Blow, 1962) was used as a method for solving the initial structure solution. Molecular replacement can be used to solve a structure with a good starting model covering reasonably large fraction of the structure in the crystal. As a rule of thumb, molecular replacement with modern programs will probably be fairly straightforward if the model is fairly complete and shares at least 30% sequence identity with the unknown structure. It becomes progressively more difficult as the model becomes less complete or shares less sequence identity (Taylor, 2003).

The molecular replacement (MR) solution of human nonmuscle myosin-2C motor domain construct in pre-power stroke state was obtained by using the template smooth muscle myosin motor domain (1BR4). Phaser (McCoy, 2007) module in Phenix (Adams et al, 2010) suite was used for this purpose. The MR solution for *Dd* myosin-2 motor domains was achieved by using the template *Dd* myosin-2 motor domain crystal structures (1YV3 in case of PCIP bound structure and 2XEL in case of ammosamide bound structures). For *Dd* myosin-2 motor domain molecular replacement solution MolRep module (Vagin & Teplyakov, 1997) of CCP4 suite was used.

2.2.6.9.2 Structure Refinement

Refinement of human nonmuscle myosin-2C motor domain in pre-power stroke state was carried out with Phenix.refine module (Afonine et al, 2010). Refinement of *Dd* myosin-2 motor domain complexed to the PCIP was carried out using CNS (Brunger et al, 1998). Refinement of *Dd* myosin-2 motor domain complexed to the Ammosamide effectors was carried out using Phenix.refine. Further manual building and refinement of model were carried out using COOT in all cases of structural solution (Emsley et al, 2010).

2.2.6.9.3 Structure Validation

Validation of the refined models is very important in order to remove model geometric errors, clashes and artifacts. After refinement of the crystal structures, all models were initially validated in COOT and then further validated using Molprobit (Davis et al, 2007a) and Procheck (Laskowski et al, 1993).

2.2.7 Homology Modeling

Homology modeling of protein refers to constructing an atomic-resolution model of the "*target*" protein from its amino acid sequence and an experimental three-dimensional structure of a related homologous protein known as the "*template*". Homology modeling is also known as "comparative modeling".

Homology models of class-1 myosins (*Dd* myosin-1B, *Rn* myosin-1b, *Rn* myosin-1c), class-2 (*Oc* myosin-2) and class-5 myosins (*Dd* myosin-5B) were built using MODELLER 9v6 (Sali & Blundell, 1993). The motor domain structure of *Dd* myosin-1E (1LKX) was used as template to built *Dd* myosin-1B, *Rn* myosin-1b, and *Rn* myosin-1c myosin motor domains. The motor domain structures of *Dd* myosin-2 (2JJ9) and *Gg* myosin-5a (1OE9) were used as templates to built *Oc* myosin-2 and *Dd* myosin-5B motor domains respectively. All motor domain models of myosins were built using closely related pre-power stroke state motor domain template structures with sequence similarity greater than 60%. Missing loop regions in the homology models were built by Modeller, followed by energy minimization using GROMACS 4.0 (Van Der Spoel et al, 2005).

All homology models were validated by Procheck (Laskowski et al, 1993). For building homology models, the following strategy has been implemented (Figure 2.5). *Pf*MyoA–MTIP and *Pk*MyoA–MTIP complex structures (2QAC and 2AUC) were used as templates to model the structures of *Tg*MyoA, *Tg*MLC1, *Tg*MyoD and *Tg*MLC2 (Polonais et al, 2011). Only the 14 most C-terminal residues were used for modeling of *Tg*MyoA (residues 806 to 819) and *Tg*MyoD (residues 803 to 816). Residues 69 to 213 of *Tg*MLC1 and residues 228 to 364 of *Tg*MLC2 were used for homology models. All models were built using MODELLER (Sali & Blundell, 1993).

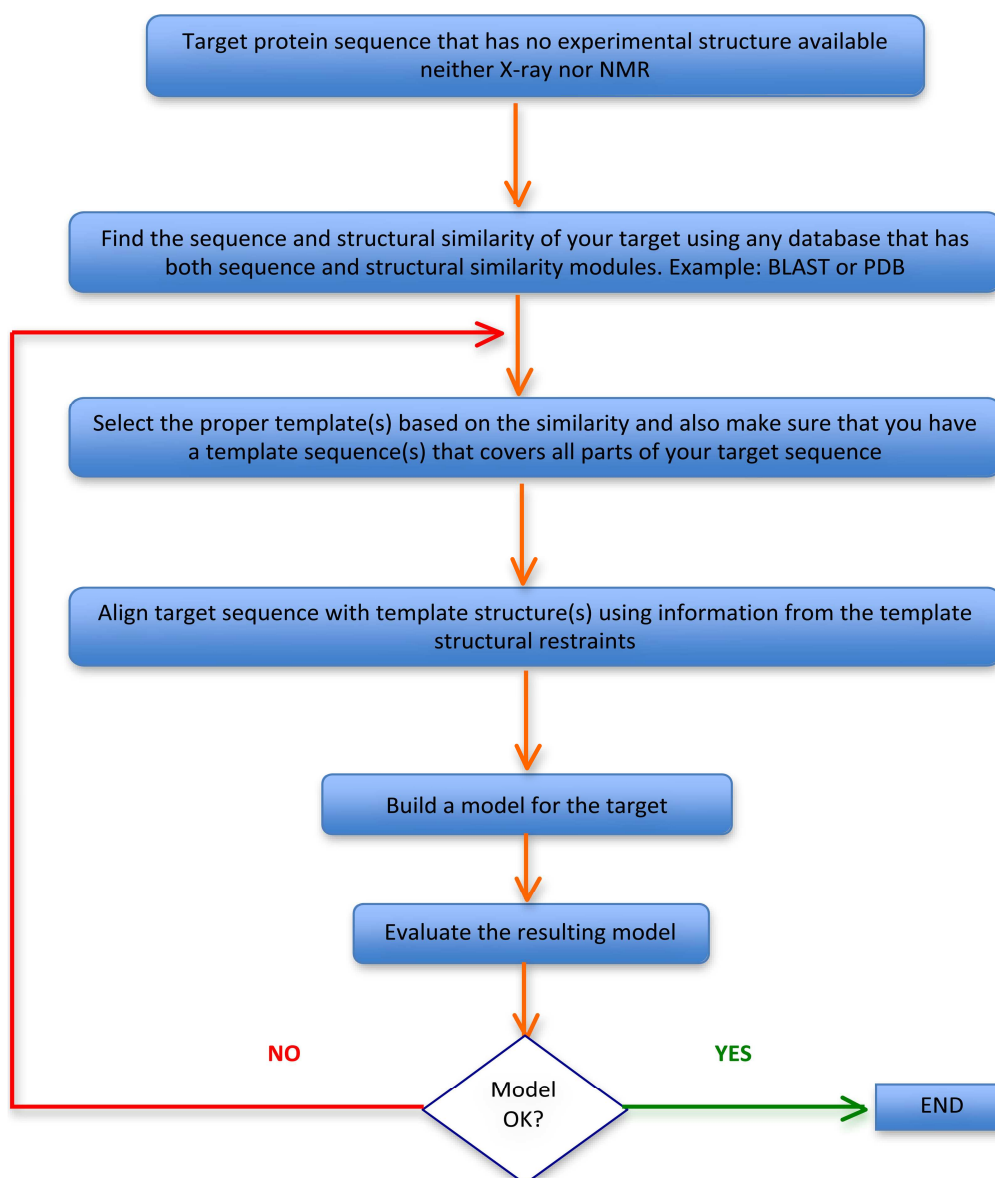


Figure 2.5. Flowchart of homology modeling

2.2.8 Docking

The number of proteins with a known three-dimensional structure is increasing rapidly, and structures produced by structural genomics initiatives are beginning to become publicly available. The increase in the number of structural targets is in part due to improvements in techniques for structure determination, such as high-throughput X-ray crystallography. With large-scale structure-determination, many current target proteins have been selected for their therapeutic potential. Computational methodologies have become a crucial component of many drug

discovery programs, from hit identification to lead optimization and beyond, and approaches such as ligand- or structure-based virtual screening techniques are widely used in many discovery efforts. One key methodology — docking of small molecules to protein binding sites — was pioneered during the early 1980s and remains a highly active area of research (Jackson & Sternberg, 1995; Jones et al, 1997). When only the structure of a target and its active or binding site is available, high-throughput docking is primarily used as a hit-identification tool. However, similar calculations are often also used later on during lead optimization, when modifications to known active structures can quickly be tested in computer models before compound synthesis.

2.2.8.1 Protein-Ligand or Myosin Effector Docking

The ligand (PCIP) was generated and energy minimized with ChemDraw (CambridgeSoft). Protein input files for docking were prepared by GOLD (Verdonk et al, 2003). Initially, blind docking of PCIP for all the myosins was performed. It was observed that PCIP has shown preference to the PBP binding pocket (with highest Goldscore of 30 to 40 depending on myosin isoform). PCIP binding site was focused based on blind docking results and also from the experimental binding mode of PCIP. Local docking was performed using partial flexible docking feature of GOLD, 8-10 residues in each case, for protein side chains in the binding pocket and limited the search to a radius of 10 Å from the active site.

The binding pocket was defined as all residues within 10 Å of atom 2746 (-Nz atom of Lys186 in *Dd* myosin-1B), atom 1523 (-Nz atom of Lys189 in *Rn* myosin-1c), atom 1515 (-Nz atom of Lys192 in *Rn* myosin-1b), atom 2789 (-Nz atom of Lys186 in *Dd* myosin-1E) and atom 4234 (-Nz atom of Lys289 in *Dd* myosin-5B). Docking was performed using the 'Genetic algorithm' implemented in GOLD. "Goldscore-Chemscore" has been used as a customized protocol for consensus docking. In this protocol, the dockings produced with the Goldscore function are used for initial scoring and then the Chemscore function is used for final ranking. Twenty solutions were generated for each myosin. In all instances, at least one

of the top five solutions (Goldscore 35 to 40) converged to a similar pose for the myosins tested. The best poses deviated by ~ 1 Å, when compared to the experimental ligand bound structure (2XEL).

2.2.8.2 Protein-Protein or Peptide Docking

Initially, the modelled *Tg*MyoA tail and *Tg*MyoD tail was manually docked and guided by the pose of the *Pf*MyoA tail in the Plasmodium MTIP-MyoA crystal structure (Bosch et al, 2006; Bosch et al, 2007). Finally, the side chains of the MLC1: MyoA complex and MLC2: MyoD complex of *T. gondii* were energy minimized until convergence was achieved using the default parameterization in GROMOS force field (Van Der Spoel et al, 2005). Also, Particle swarm optimization (PSO) technique was employed in combination with genetic algorithm of autodock (Goodsell et al, 1996; Namasivayam & Gunther, 2007) and GOLD (Verdonk et al, 2003) to find the optimal protein-peptide complex. Similar results were obtained independently using ROSETTADOCK (Lyskov & Gray, 2008).

3. RESULTS

3.1 Small Molecule Effectors

3.1.1 Pentachloropseudilin

Recently, the total synthesis of halogenated pseudilins, natural products containing a 2-arylpyrrole moiety and their synthetic analogues have been described (Martin et al, 2009a). Pentabromopseudilin (PBP) was subsequently identified as a potent inhibitor of vertebrate myosin-5 motor activity. An IC_{50} of 400 nM was determined for the inhibition of vertebrate myosin-5 ATPase activity by PBP (Fedorov et al, 2009). Based on this finding, related compounds to identify myosin effectors with altered selectivity for the members of different myosin classes were screened. Pentachloropseudilin (PCIP), a chemical and structural analogue of PBP, was identified in this screening as a potent inhibitor of class-1 myosins.

In the current project, the effects of PCIP on myosin kinetics, actomyosin kinetics and myosin motor functions were described. Co-crystallization trials with class-1 myosins in the presence of PCIP were unsuccessful. Since most of the class-1 myosin motor domains have 50% to 60% sequence similarity with class 2 myosin motor domains, *Dictyostelium discoideum* myosin-2 (*Dd* myosin-2) was used as a model system to interpret the binding site of PCIP in other myosin isoforms. The resulting structure shows that the inhibitor binds in the same allosteric pocket as PBP, but the conformation of the inhibitor and details of its interaction with myosin are different. Molecular modeling and docking studies predicted preferential binding of PCIP to class-1 myosins, a result that was confirmed by direct binding studies, cell-based assays, and *in vitro* enzyme assays.

3.1.1.1 Mechanism of PCIP-Mediated Inhibition of Myosin Motor Activity

In the present work, PCIP was shown as potent inhibitor of myosin motor activity. PCIP, a structural analogue of pentabromopseudilin (PBP) (Fedorov et al, 2009) (Figure 3.1.1.1).

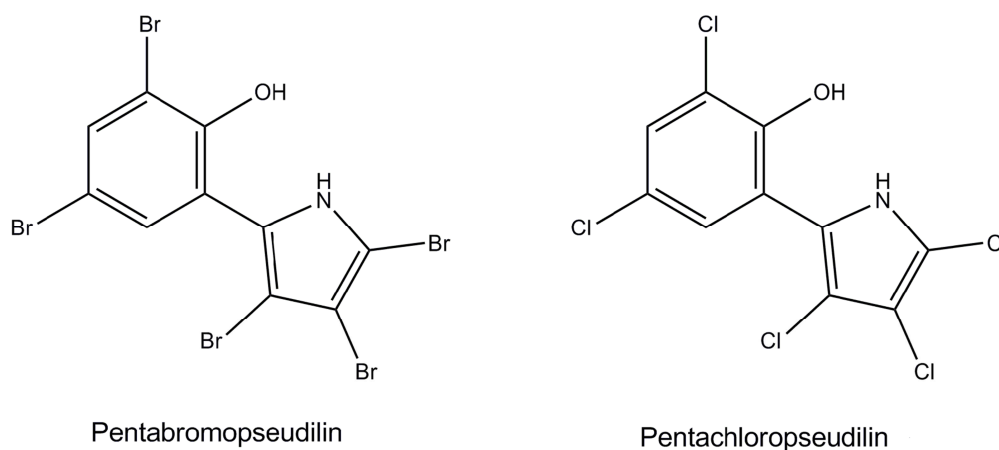


Figure 3.1.1.1: Schematic representation of PBP and PCIP.

To elucidate the inhibitory potency and selectivity of PCIP, the action of PCIP on the actomyosin ATPase activity of myosins from different classes was tested. For the steady-state ATPase assay, different myosin isoforms were preincubated with varying concentrations of PCIP at 25 °C. For the purpose of reproducibility and accuracy, all independent measurements were performed in triplicates. The results of the PCIP mediated inhibition of the actomyosin steady-state ATPase activity of a wide range of different myosins from various classes are summarized in Figure 3.1.1.2.

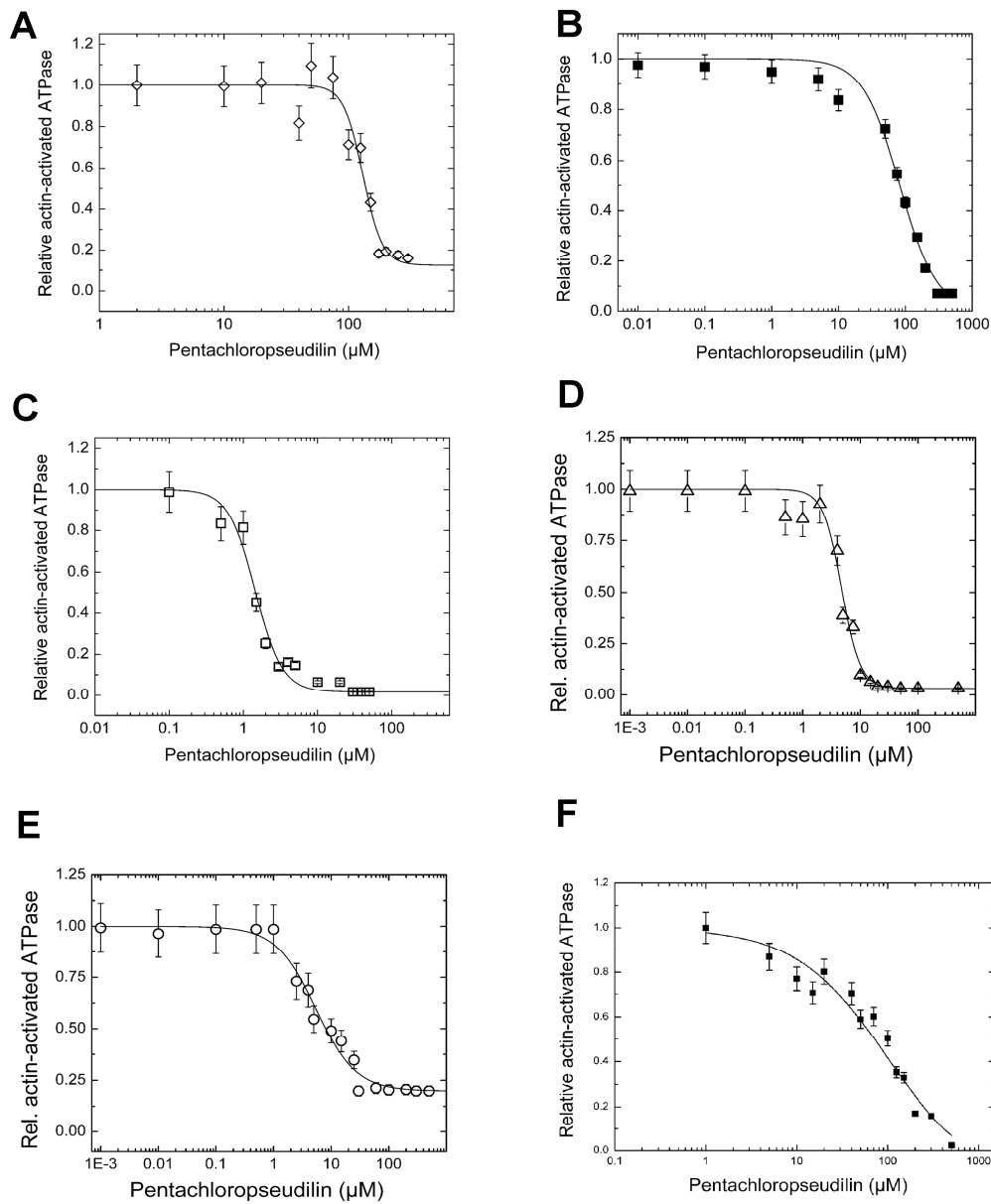


Figure 3.1.1.2: F-actin activated ATPase of different myosins in the presence of PCIP. The semi-logarithmic normalized plot shows the concentration dependence of PCIP inhibition for (A) *Dd* myosin-2, (B) *Dd* myosin-1B, (C) *Rn* myosin-1b, (D) *Rn* myosin-1c, (E) *Oc* myosin-2 (HMM) and (F) *Dd* myosin-5b. The concentrations of PCIP required for half-maximal inhibition (IC_{50}) of the different myosin motors were determined from sigmoidal fits of the data.

Addition of PCIP greatly decreased the rate of actin-activated ATP turnover for members of myosin classes-1, -2, and -5, whereas human myosin-6 and myosin-7a motor domain constructs showed no sign of inhibition in the presence of 100 μM PCIP. The most potent inhibition was observed for class-1 myosins. Plots of the observed rates against the logarithm of inhibitor concentration were fitted with sigmoidal functions. The IC_{50} values for *Dd* myosin-1B, *Rn* myosin-1b and *Rn* myosin-1c correspond to 1.0 μM , 5.0 μM and 5.6 μM , respectively (Figure 3.1.1.2). The potency of PCIP for the inhibition of class-2 and class-5 myosins was considerably lower. IC_{50} values corresponding to 126 μM , 91 μM , and 99 μM were observed with *Dd* myosin-2, *Oc* myosin-2, and *Dd* myosin-5B, respectively (Figure 3.1.1.2).

To investigate the interaction of PCIP with class-1 myosins in detail, we took advantage of the 30% increase in fluorescence intensity that is observed upon binding to myosin. Stopped-flow transients were observed after the rapid mixing of PCIP with myosin motor domain constructs. The fluorescence transients were well described by single exponential functions. A typical transient obtained for PCIP binding upon *Dd* myosin-1B is shown in the inset of figure 3.1.1.3. The observed rate constants were linearly dependent on the PCIP concentration in the range from 1-10 μM (Figure 3.1.1.3A).

An apparent second-order rate constant for PCIP binding to *Dd* myosin-1B ($k_{+1} = 0.48 \pm 0.04 \times 10^{-9} \mu\text{M}^{-1}\text{s}^{-1}$) was given by the gradient of the plot, while the y-intercept defines an apparent dissociation rate constant of $k_{-1} = 0.0024 \pm 0.0002 \text{ s}^{-1}$. The ratio k_{-1}/k_{+1} defines an apparent dissociation equilibrium constant (K_{d}) of $5.0 \pm 0.9 \mu\text{M}$. Alternatively, K_{d} was determined by plotting the observed changes in fluorescence amplitude against the PCIP concentration (Figure 3.1.1.3B). The resulting data were well described by a hyperbola and gave a value of $4.2 \pm 0.8 \mu\text{M}$ for K_{d} .

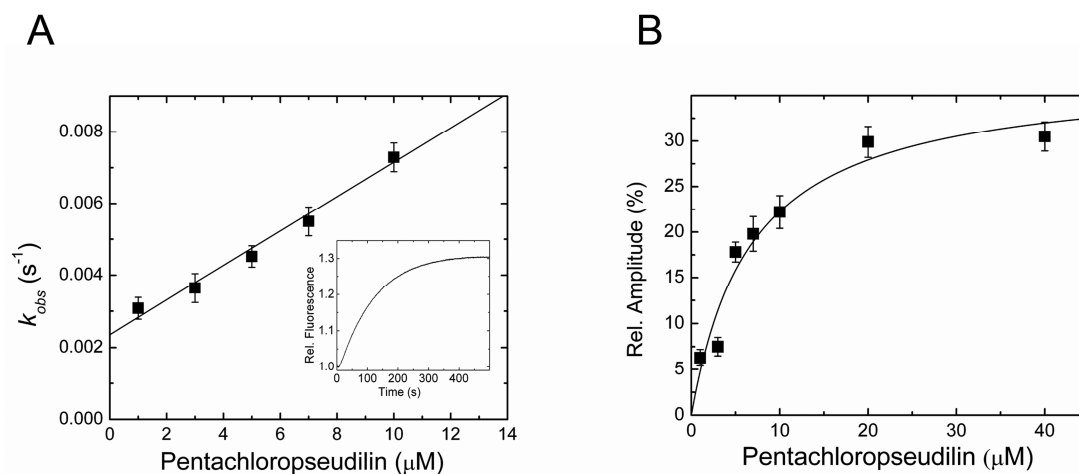


Figure 3.1.1.3: (A) Binding and dissociation kinetics for the interaction of PCIP with *Dd* myosin-1B. Rates were determined by the concomitant change in fluorescence intensity. (B) A hyperbolic fit to the data gives a K_d of $4.2 \pm 0.8 \mu\text{M}$ for PCIP binding to *Dd* myosin-1B. (The assays and the figure were produced in collaboration with Dr. Manuel H. Taft, Institute for Biophysical Chemistry, Hannover Medical School.)

3.1.1.2 PCIP is a Reversible Inhibitor of Myosin Motor Activity

PCIP binding reduced the affinity of myosin for filamentous actin (F-actin) in the presence of ATP. Further, the coupling between actin and nucleotide binding sites was affected thereby interfering with the activation of the ATPase activity of myosin by F-actin. To estimate the extent to which PCIP binding affects coupling, the ATPase activity for *Dd* myosin-1B over the range from 1 to 70 μM F-actin were determined (Figure 3.1.1.4). Values for k_{cat} and $K_M(\text{actin})$ were estimated from fits of hyperbolic functions to the data. The apparent second order rate constant for actin binding in the presence of ATP ($k_{cat}/K_M(\text{actin})$) is a direct measure of the coupling efficiency. Addition of 5 μM PCIP lead to a more than 30-fold reduction in coupling efficiency from $0.028 \mu\text{M}^{-1}\text{s}^{-1}$ to $0.00088 \mu\text{M}^{-1}\text{s}^{-1}$.

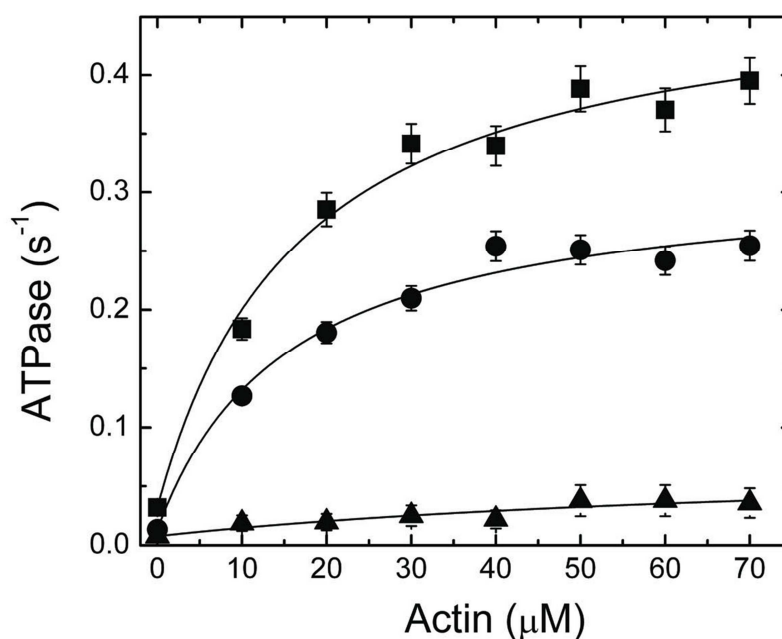


Figure 3.1.1.4: PCIP-mediated inhibition of the actin-activated ATPase activity of *Dd* myosin-1B. Hyperbolic fits to the data at 0 μM (■), 1 μM (●), and 5 μM PCIP (▲) are shown. Increasing the PCIP concentration leads to a gradual inhibition of the actin-activated ATPase activity and leads to a more than 30-fold reduction in coupling efficiency.

3.1.1.3 *In vitro* Motility Assay of *Dd* myosin-1B in the Presence of PCIP

A direct weakening of the actin-myosin interaction was observed following the addition of PCIP to actomyosin decorated glass surfaces in the *in vitro* motility assay. A *Dd* myosin-1B motor domain construct, fused to an artificial lever arm of 12 nm in length, moved F-actin with an average velocity of $1.01 \pm 0.13 \mu\text{m}\cdot\text{s}^{-1}$ in the *in vitro* motility assay (Durrwang et al, 2006). The addition of 2 μM PCIP resulted in a more than 2-fold reduction of the average sliding velocity to $0.51 \pm 0.08 \mu\text{m}\cdot\text{s}^{-1}$ (Figure 3.1.1.5A). Furthermore, this direct functional assay revealed that the inhibition of myosin motor activity by PCIP is reversible. Washout of the inhibitor resulted in complete recovery of motile activity (Figure 3.1.1.5B).

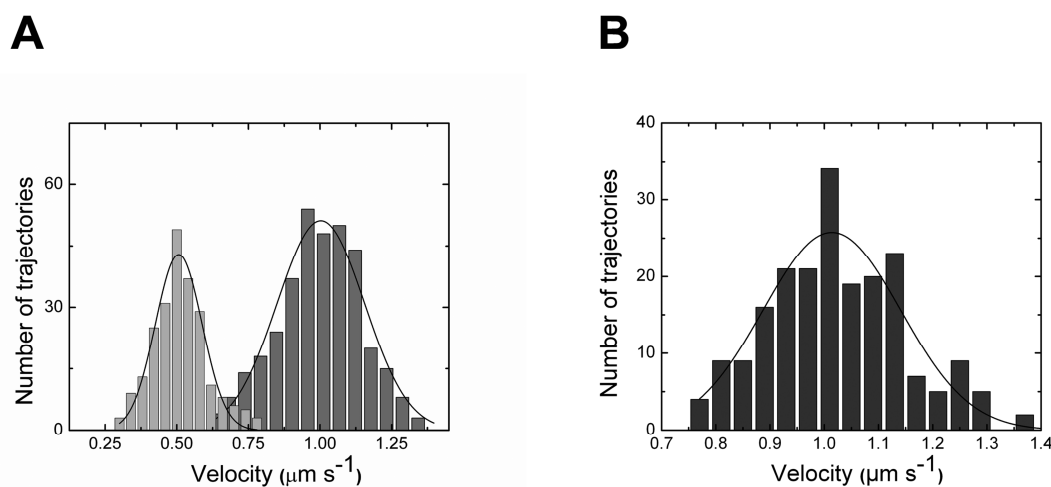


Figure 3.1.1.5: (A) *Dd* myosin-1B moves actin filaments in the *in vitro* motility assay with an average velocity of $1.01 \pm 0.13 \mu\text{m}\cdot\text{s}^{-1}$ (dark grey bars). In the presence of 2 μM PCIP (light grey bars), filament velocity is reduced to $0.51 \pm 0.1 \mu\text{m}\cdot\text{s}^{-1}$. (B) Washout of the inhibitor increased the average velocity to $1.01 \pm 0.3 \mu\text{m}\cdot\text{s}^{-1}$, which was similar to the motile activity of uninhibited *Dd* myosin-1B. (This assay and the figure were produced in collaboration with Dr. Falk K. Hartmann, Institute for Biophysical Chemistry, Hannover Medical School).

3.1.1.4 PCIP Inhibits Cellular Functions of Human Myosin-1c

In mammals, myosin-1c is involved in a number of highly specialized and tissue specific functions, such as the adaptation of mechano-electrical transduction in the hair cells of the inner ear and the translocation of GLUT4 transporters to the plasma membrane in adipocytes (Bose et al, 2002; Gillespie & Cyr, 2004). In addition, myosin-1c was described to play a role in the late endocytic pathway delivering endocytosed macromolecules to the lysosome for degradation (Poupon et al, 2003). This observation was well supported by the finding that the inhibition of myosin-1c function by either PCIP or RNA interference causes identical defects in lysosome morphology and intracellular localization of this organelle (Figure 3.1.1.6). HeLa cells were treated for 16 hours with PCIP concentrations in the range from 1-5 μM display large, ring-like Lamp1 positive lysosomes clustered in the perinuclear region. These morphological changes were clearly visible at the lowest PCIP concentration used (Figure 3.1.1.6). Loss of myosin-1c production after transfection of siRNA specific for myosin-1c induces identical morphological changes in the endo-lysosomal system of HeLa cells (Figure 3.1.1.6). Other changes and more general cytotoxic effects were

only observed at PCIP concentrations higher than 25 μM . These results indicate that in mammalian cells, PCIP can be used at concentrations smaller than 5 μM for selective inhibition of myosin-1c function and that the drug does not interfere with other enzymes in this concentration range.

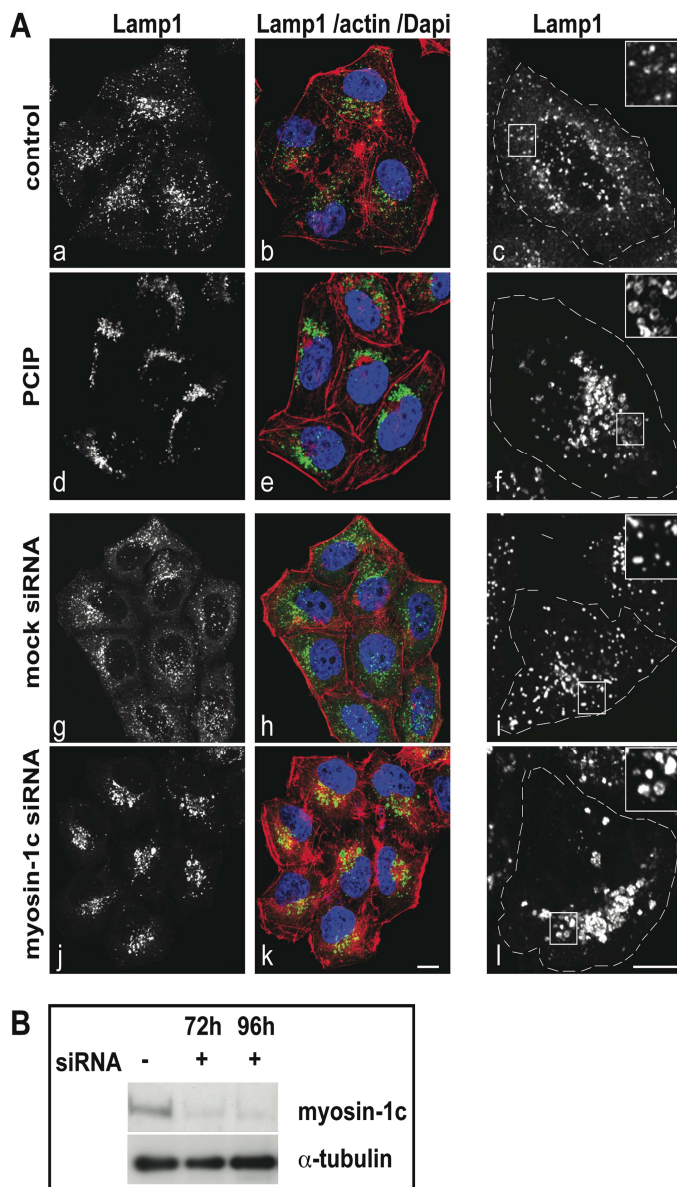


Figure 3.1.1.6: Inhibition of *Hs* myosin-1c by PCIP causes clustering and swelling of mammalian lysosomes. **(A)** In control HeLa cells without PCIP treatment (a, b and c) or siRNA transfection (g, h and i) the lysosomes are small vesicular organelles that are distributed throughout the cells with a slight enrichment in the perinuclear region and the vicinity of the Golgi complex. In PCIP-treated (d, e and f) and myosin-1c siRNA transfected cells (j, k and l) the lysosomes are densely clustered in the perinuclear region. They are frequently tethered to form larger aggregates and are swollen to a larger size. The left panels (a, d, g and j) show confocal images of a group of cells stained for lysosomes with an antibody to Lamp1, the middle panels (b, e, h and k) show merged color images labeled for lysosomes in green, actin filaments in red and the nucleus in blue. The right hand panels (c, f, i, and l) show enlarged confocal images of single cells further highlighting the aggregated swollen lysosomes in PCIP-treated and myosin-1c siRNA-depleted cells. The small inserts in the right hand panels are higher magnifications of the boxed regions. Bar: 10 μm . **(B)** Mock and myosin-1c siRNA treated HeLa cells were blotted and probed with antibodies to myosin-1c and α -tubulin as a loading control to confirm the successful myosin-1c knockdown. The assay was performed & the figure is contributed by Hemma Brandstadt and Folma Buss, Cambridge University, UK.

3.1.1.5 The Structural Basis of PCIP-Mediated Inhibition

Co-crystallization studies were performed with motor domain constructs derived from three class-1 isoforms. However, these constructs were proved refractory to crystallization. Therefore, PCIP was co-crystallized with the *Dd* myosin-2 motor domain, which was complexed to Mg^{2+} -ADP-meta-vanadate (Figure 3.1.1.7). These crystals were diffracted to 2.5 Å resolution and further data analysis indicated a space group C222₁. The nucleotide binding pocket of *Dd* myosin-2 is highly conserved among different myosin isoforms (Hiratsuka, 1994). Few of the conserved residues surrounding ADP.VO₃ are depicted in the following Figure 3.1.1.7.

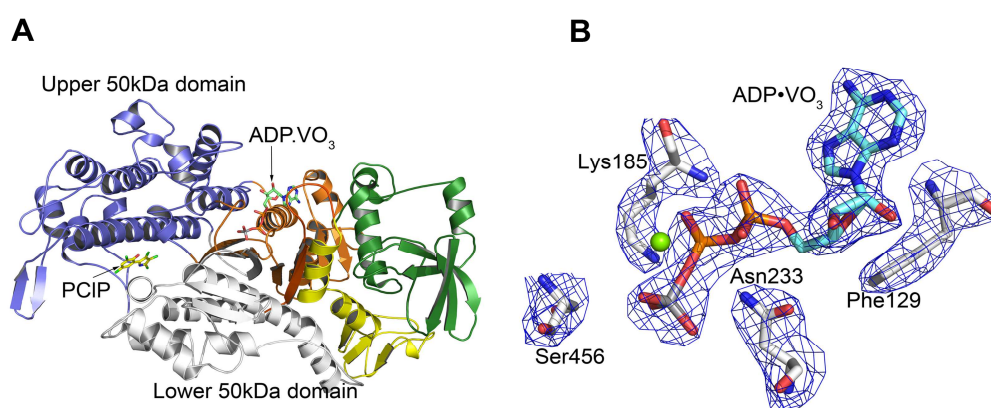


Figure 3.1.1.7: Section (A) was shown as the overview of ADP.VO₃ and PCIP binding sites in *Dd* myosin-2 motor domain. Section (B) ADP.VO₃ was shown in the nucleotide-binding pocket of *Dd* myosin-2: PCIP complex. Electron density, 2f_oc, shown here was contoured at 1.5 σ .

The crystallographic results were in good agreement with the allosteric mechanisms inferred from the kinetic data. The tip of the 50-kDa domain and near actin binding residues are involved in PCIP binding. PCIP binds at a distance of approximately 16 Å from the nucleotide-binding site (Figure 3.1.1.7A). This is the same allosteric binding pocket previously described for PBP (Fedorov et al, 2009). However, both the conformation of PCIP and details of the interaction with myosin residues in the binding pocket differ from those observed with PBP. The average r.m.s. deviation for PCIP and PBP was 2.3 Å. The planar *anti*-conformer of PCIP binds to myosin. This differs from the binding mode of PBP, where the *syn*-conformer is observed to bind with the phenyl and pyrrole ring systems bent 12° out of plane and twisted 20° against each other (Fedorov et al, 2009). Towards the actin-binding interface, PCIP is enclosed by the strut

loop (Asn588–Gln593) and loop 2 (Asp614–Thr629). Towards the core of the motor domain the binding pocket is lined by helix 10 (Lys265–Val268) and helix 18 (Val411–Leu441) from the upper 50-kDa domain. Additionally, helix 26 (Val630–Glu646) and the loop connecting β 7 (Ile253–Leu261) with helix 10 contribute to the binding pocket (Figure 3.1.1.8B and 3.1.1.8C). The total protein surface area in contact with PCIP comprises 240 Å².

A network of interactions stabilizes PCIP binding. Important binding site rearrangements include a change in the orientation of the side chain of Lys265, which moves 3.1 Å from its position in the uninhibited form to facilitate formation of a hydrogen bond between the ϵ -amino group and the hydroxyl group of PCIP. The amino group of the pyrrole ring interacts with the main chain carbonyl groups of Ile617 and Ser619. Two water molecules form part of a network of interactions that involves the main chain carbonyl groups of Ala420 and Pro591, the side chains of Lys265 and Asp590, and the hydroxyl and 2-chloro groups of the phenyl ring. Additional interactions are formed between the side chains of Arg428 and Leu431 and chloro groups of the inhibitor (Figure 3.1.1.8D).

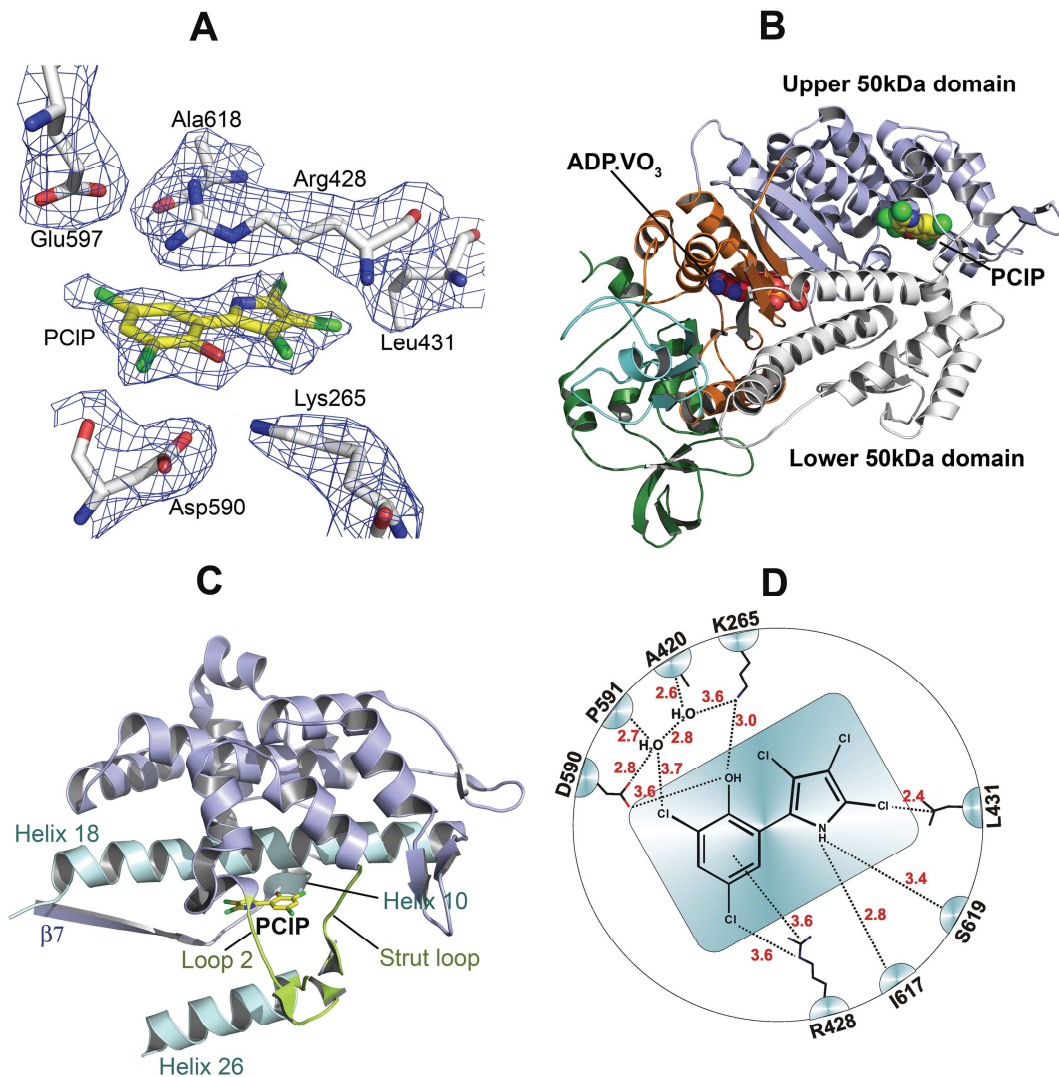


Figure 3.1.1.8: Structure of *Dd* myosin-2 motor domain in complex with PCIP and Mg²⁺-ADP-meta-vanadate. **(A)** Section of the 2Fo-Fc electron density omit map, contoured at 1.0 σ , depicting the PCIP binding site. **(B)** Overall view of the myosin motor domain in ribbon representation. PCIP and ADP•VO₃ are shown in spheres mode; N-terminal residues are shown in green and the C-terminal converter region in cyan. **(C)** Close-up view of allosteric binding pocket with protein residues in cartoon representation and PCIP in stick representation. Important structural features around the binding pocket are colored and labeled accordingly. **(D)** Schematic view of the anti-conformer of PCIP and its contact residues. Contacts with residues closer than 4 Å are shown.

Table 22: Summary of data collection and refinement statistics

<i>Dd</i> Myosin-2 – ADP•VO₃ – pentachloropseudilin	
Data collection	
Space group	C222 ₁
Wavelength (Å)	0.9871
Cell dimensions	
a, b, c (Å)	89.53, 147.49, 153.78
α , β , γ (°)	90, 90, 90
R _{sym} (%)	6.2 (48.3)*
I / σ I	15.97 (5.01)
Completeness (%)	99.8 (100)
Redundancy	8.2 (8.4)
Refinement	
Resolution (Å)	24.6-2.5
R _{work} / R _{free} (%)	22.9 / 25.3
No. reflections	
working / test set	33755/ 1777
No. atoms	
Protein	6240
Ligands/ions	48/ 1
Water	458
R.m.s. deviations	
Bond lengths (Å)	0.008
Bond angles (°)	1.6
Ramachandran plot	92.3/7.7/0
(% Favored/allowed/outliers) [§]	

*Values in the parenthesis are for highest resolution (2.60-2.50).

[§]Residues in favored, allowed, and outlier regions of the Ramachandran plot as reported by MolProbity (Davis et al, 2007a).

3.1.1.6 Myosin Isoform-Dependent Interactions with PCIP

To rationalize the structural basis for the experimentally observed preferred inhibition of class-1 myosins, we performed docking studies using the crystal-

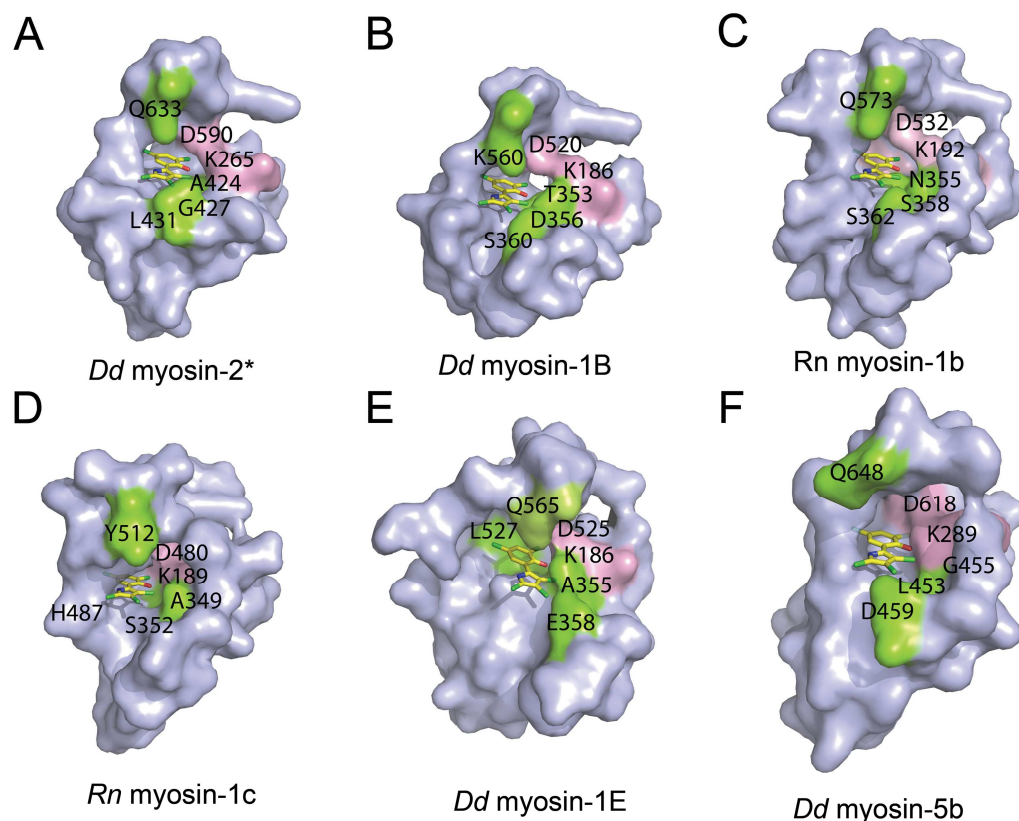


Figure 3.1.1.9: Surface representation of the PCIP binding site in different myosin isoforms. Highly conserved residues interacting with PCIP are shown in pink. Non-conserved residues interacting with PCIP are colored green. Amino acid residues are indicated using the single letter code. PCIP binding pocket of (A) *Dd* myosin-2 crystal structure [*reference structure], (B) *Dd* myosin-1B, (C) *Rn* myosin-1b, (D) *Rn* myosin-1c, (E) *Dd* myosin-1E, and (F) *Dd* myosin-5b.

structure of the motor domain of *Dd* myosin-1E (1LKX) and homology models of *Dd* myosin-1B, *Dd* myosin-5B, *Rn* myosin-1b and *Rn* myosin-1c in the pre-power stroke state. For all myosin isoforms tested, initial blind docking studies predict that PCIP binds to the same site described above for the complex with the *Dd* myosin-2 motor domain. To achieve better sampling of the translational, rotational, and torsional degrees of freedom of the ligand, local docking using a 10 Å grid around this site was performed (Gherzi & Sanchez, 2009). The highest ranked binding poses are shown in Figure 3.1.1.9 and the predicted contact

residues for PCIP in complex with the individual myosin isoforms are shown in Table 28.

The results of the docking studies indicated that the contact between the hydroxyl group of PCIP and Lys265 is a common and important feature of the interaction between myosin and effector molecule. Additionally, the polarity of the allosteric binding pocket appears to make an important contribution to the preferred binding of PCIP to class-1 myosins (Figure 3.1.1.9).

3.1.1.7 Energetic Coupling between Active and Allosteric Binding Sites

Since X-ray crystallography favors particular stable intermediates, observable changes resulting from the binding of an allosteric effector tend to be subtle in terms of impact on an experimentally determined 3D structure (Goodey & Benkovic, 2008). Experimental manifestations of an allosteric effect are thus frequently limited to the rates of interchange between different conformer populations at any given point along the enzymatic reaction coordinate (Swain & Gierasch, 2006). Typical for this type of energetic coupling between the active and allosteric sites, the available X-ray structures in the presence (2XEL) and absence (2JJ9) of bound PCIP do not indicate a major conformational change. The myosin backbone C_α atoms in both structures superimpose with an RMSD of 0.41Å.

Analysis of pre-power stroke state myosin structures in the absence (2JJ9) and presence of PCIP (2XEL) indicate the existence of two communication pathways that transmit information between the allosteric and nucleotide binding sites: a direct communication pathway (Figure 3.1.1.10) and a pathway that operates via global changes (Figure 3.1.1.12).

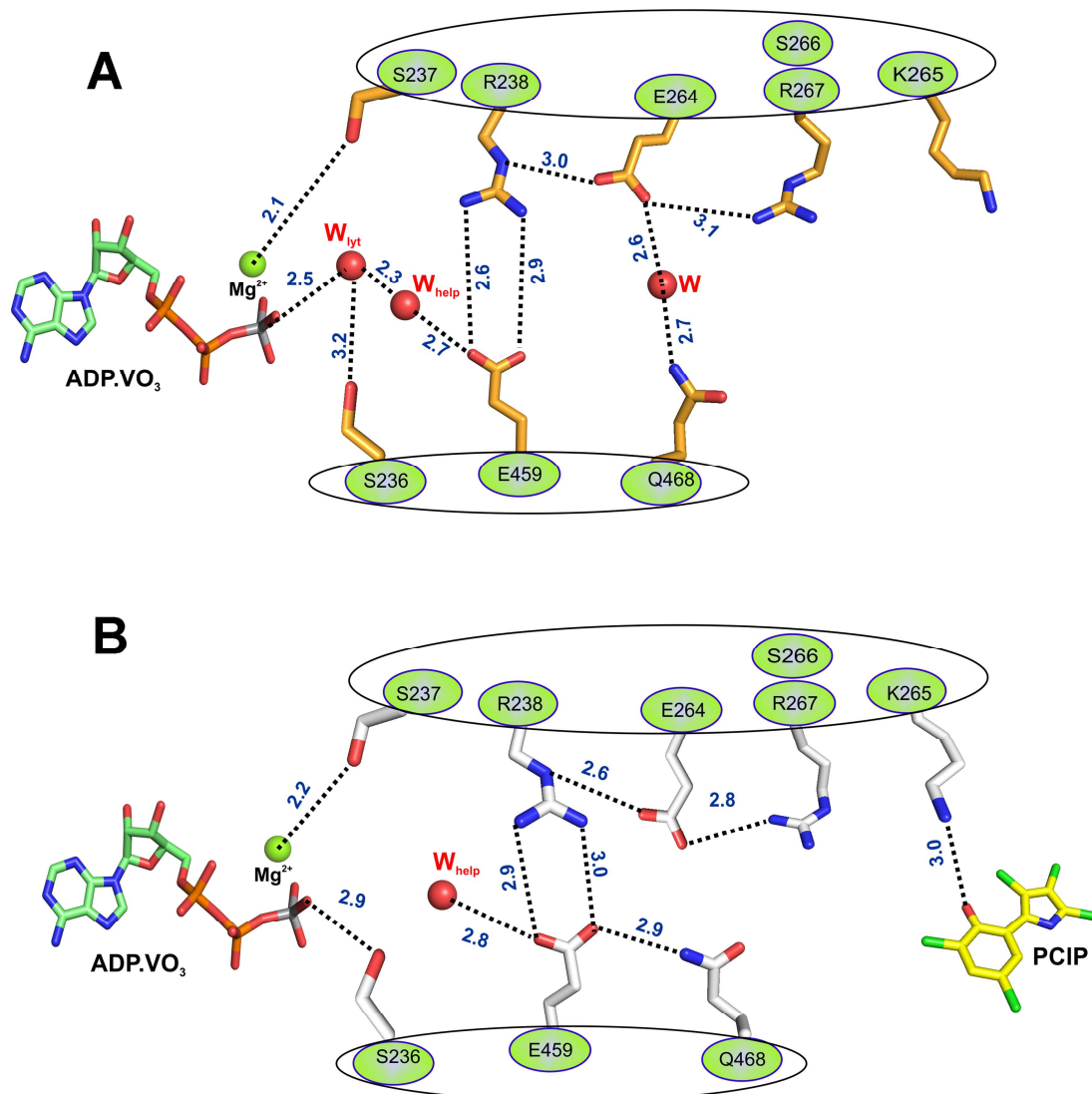


Figure 3.1.1.10: Schematic illustration of the relay pathway connecting the allosteric pocket and the nucleotide-binding site in the absence and presence of PCIP. (A) Residues involved in the relay pathway and selected side chains are shown for the myosin motor domain in the absence of PCIP (2JJ9). (B) PCIP induced changes in the orientation of selected side chains along the relay pathway. Distances between residues are shown as dashed lines indicated in Å. Main chain interactions are not explicitly shown. Magnesium ion (green) and waters (red) are shown as spheres; W_{lyt} denotes the lytic water molecule and W_{help} denotes the helper water.

A network of hydrogen bonds is extended over a distance of 19 Å forming a direct link between PCIP and the γ -phosphate position of ATP. Side chains as well as main chain interactions are part of this network. Lys265 is the starting point for this allosteric relay mechanism. The ϵ -amino group of Lys265 moves 3.1 Å from its position in the uninhibited form to facilitate an interaction with the hydroxyl group of PCIP. The salt-bridge connecting Arg238 in Switch I with Glu459 in Switch II forms part of the relay path. The distance between Arg238 and Glu459 increases by 0.3 Å upon PCIP binding. Other key residues involved in the relay mechanism are S236 and S237 in Switch I, Gln468 in the relay helix, and residues K265, S266 and R267 in helix 10 (Figure 3.1.1.10A). The major consequence of the rearrangements induced by PCIP-binding is the displacement of the “catalytic water” molecule at the active site (Figure 3.1.1.10B). In contrast, the catalytic water positioned appropriately for in-line attack to the γ -phosphate analogue of nucleotide, is present in the active site of the pre-power stroke state structures with bound ADP-VO₃ (2JJ9), ATP- γ -S, (1MMG), ADP-AlF₄ (1W9L), and mantADP-BeF_x (1D1C) (Gulick et al, 2000; Gulick et al, 1997).

In the absence of PCIP the $2F_o-F_c$ electron density for Mg.ADP.VO₃ in structure 2JJ9 allows the unambiguous placement of an extra water molecule (Figure 3.1.1.11A). This water molecule is ideally positioned for inline attack relative to V _{γ} and can thus act as catalytic water. PCIP-binding induces the displacement of the catalytic water (Figure 3.1.1.11B).

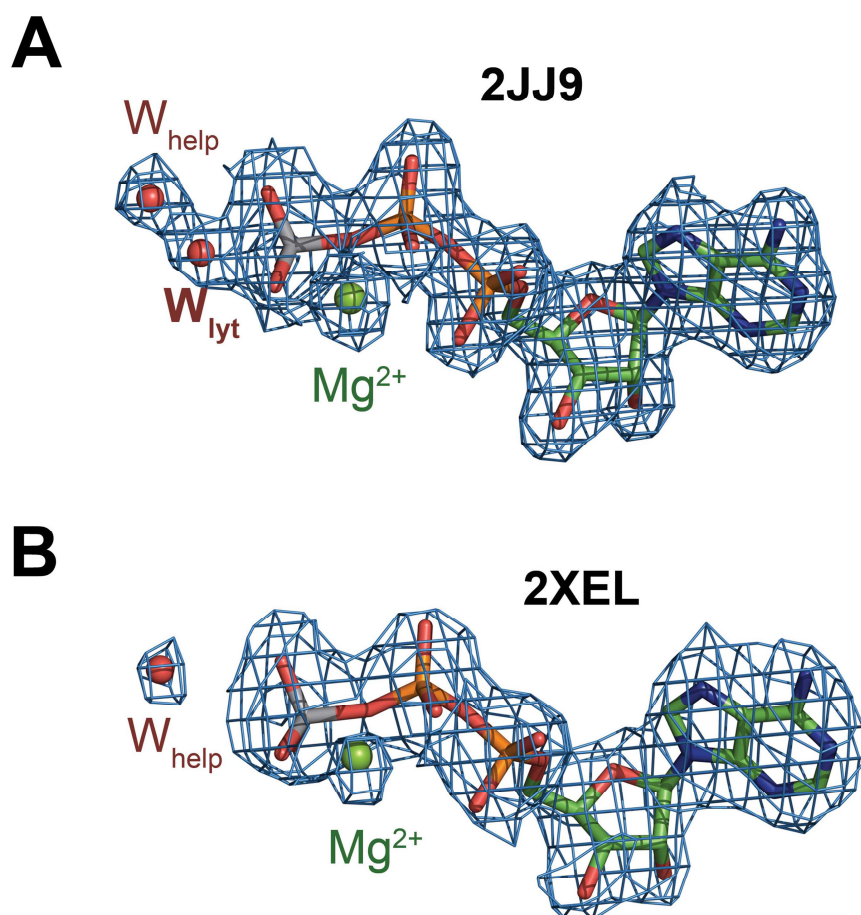


Figure 3.1.1.11: (A) Mg.ADP.VO₃ fit into the 2F_o-F_c electron density map from structure 2JJ9 obtained in the absence of PCIP. (B) Mg.ADP.VO₃ fit into the 2F_o-F_c electron density map from structure 2XEL obtained in the absence of PCIP. The 2F_o-F_c electron density maps are contoured at 1.5 σ . Side chains and ADP-meta-vanadate are shown in stick mode. Magnesium ion (green) and waters (red) are shown as spheres; W_{lyt} denotes the lytic water molecule and W_{help} denotes the helper water.

Global changes induced by effector binding, which contribute to the allosteric communication, are indicated by B-factor analysis. Plots showing the difference in B-factor (ΔB) between the free and inhibitor-bound structures per residue indicate changes in protein dynamics throughout the motor domain (Figure 3.1.1.12).

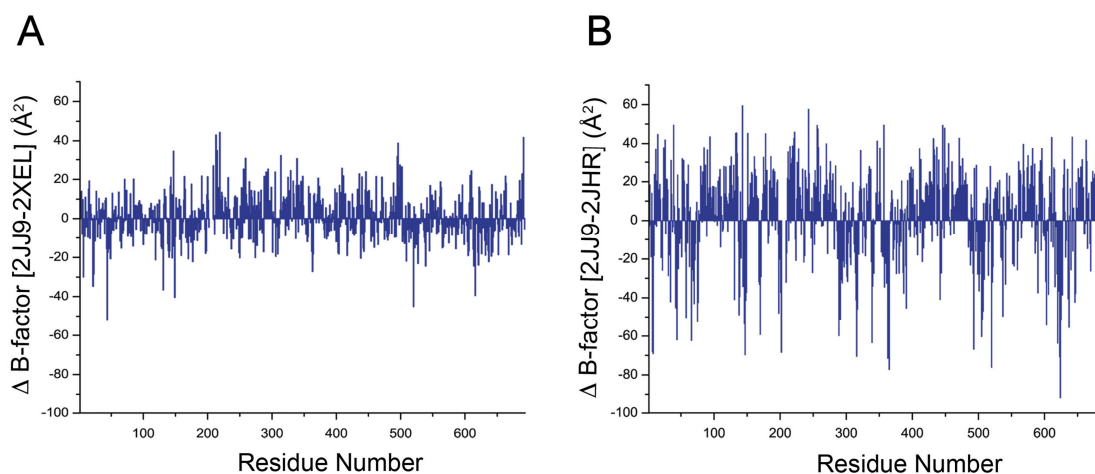


Figure 3.1.1.12: Flexibility of the myosin-2 motor domain in the presence and absence of bound PCIP. B-factors describe the size of displacements available to the individual atoms in an X-ray structure. They provide thus information about the relative flexibility of different parts of a structure. We used normalized B-factors to compare the relative flexibility of the myosin-2 motor domain in the presence and absence of bound PCIP and PBP. Normalized B-factors were calculated as $B = (B_{\text{atom}}/B_{\text{average}}) \times 100$, where B_{atom} is the B-factor of an individual protein atom and B_{average} is the average B-factor of the whole protein molecule. Histogram showing ΔB , the difference in the normalized B-factors ($B_{2JJ9} - B_{2XEL}$) plotted against residues 1 to 693 of the *Dd* myosin-2 motor domain. Positive ΔB values indicate higher B-factors of ligand free structure over ligand bound structure, whereas negative ΔB values represent higher B-factors of ligand bound structure.

Differences in the flexibility of surface loops and secondary structure elements in the nucleotide-binding region can be related to PCIP binding (Figure 3.1.1.12A). Changes in B-factor induced by the binding of PBP to myosin-2, shown in Figure 3.1.1.12B, are even more pronounced. This observation is in good agreement with the more potent effect of PBP on myosin-2 activity (Fedorov et al, 2009).

3.1.2 Ammosamides

Deep-sea microbes are rich in valuable metabolites that can target the structural components of the cytoskeleton (Fenical & Jensen, 2006). Natural compounds like ammosamides were isolated from the *Streptomyces* strain CNR-698 (Macmillan et al, 2008), which was isolated from bottom sediments of the deep-sea in the Bahamas Islands (Hughes et al, 2009b). The same group of researchers performed the total synthesis of ammosamides (Hughes & Fenical, 2010).

3.1.2.1 Ammosamides Target Myosin-2

This work was carried out with the basic idea that ammosamides target myosins as described by Hughes *et al.* (Hughes et al, 2009a). Hence, a meaningful collaboration with the group of Prof. William Fenical, Scripps Institution of Oceanography, UCSD, USA has been established in order to investigate the kinetic and structural basis of the ammosamide mediated effects on myosins. As small molecule effectors, ammosamide A, ammosamide B and other ammosamide derivatives (Figure 3.1.2.1) were selected and tested in the actin-activated steady-state ATPase assay, in single-turnover stopped-flow experiments and in crystallographic approaches to obtain a better understanding of the molecular mechanisms underlying their efficacy on myosin motor domains.

Prior to the experimental procedures, all compounds were solubilized in 80 % (w/v) DMSO. To minimize the side effects, the working concentration of DMSO in the kinetic and crystallographic studies was maintained below 2 % (w/v). Initially, in a rapid screen, the actin-activated steady-state ATPase activity of *Dd* myosin-2 in the presence of 10 μ M and 100 μ M ammosamides was determined.

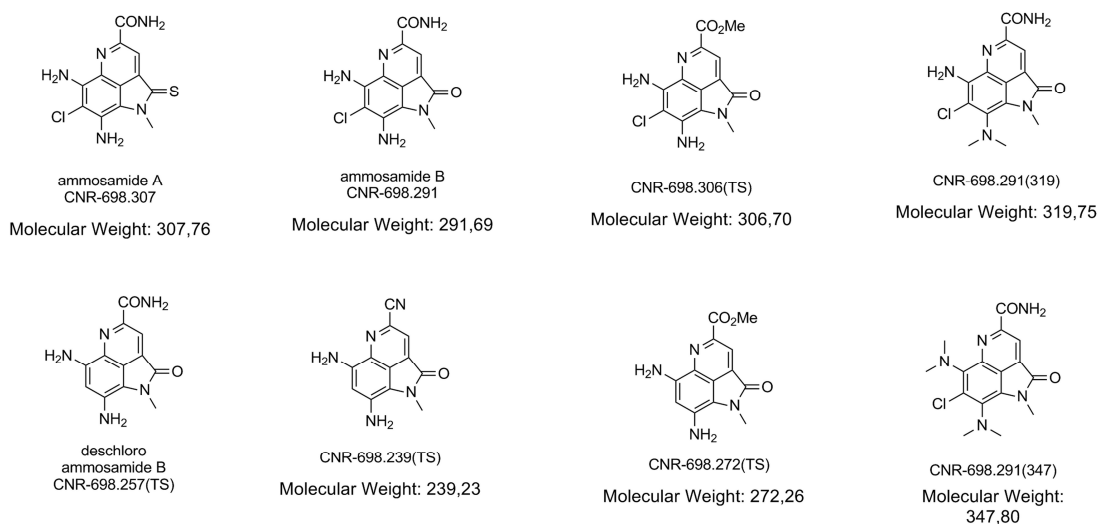


Figure 3.1.2.1: Schematic representation of the ammosamides studied in the present work.

Out of eight compounds tested, ammosamide A (CNR-698.307), ammosamide B (CNR-698.291), deschloroammosamide B (CNR-698.257) and ammosamide 272 (CNR-698.272) display a clear inhibition pattern of the *Dd* myosin-2 ATPase activity. Although, it was known that ammosamide A and B inhibits skeletal myosin-2 (Hughes et al, 2009a), this study showed that two other ammosamide derivatives, deschloroammosamide B (Des B) and ammosamide 272, exhibit inhibitory effects on *Dd* myosin-2. The remaining ammosamides did not show any effect at concentrations as high as 500 μ M. Hence, the remainder of the present work focuses on the detailed kinetic and structural analysis of the compounds displaying inhibitory activity.

3.1.2.2 Ammosamides Inhibit Myosin-2 ATPase Activity

To explain the inhibitory potency of ammosamides, the action of these natural compounds on the actomyosin ATPase activity of *Dd* myosin-2, *Hs* nonmuscle myosin-2C and *Hs* myosin-7a was tested under steady-state conditions. In the experimental set up, myosin motor domain constructs were preincubated with varying concentrations of ammosamides at 25°C for 30 minutes prior to the measurements. The results of the ammosamide mediated inhibition of the actomyosin steady-state ATPase activity of *Dd* myosin-2 is shown in Figure 3.1.2.2.

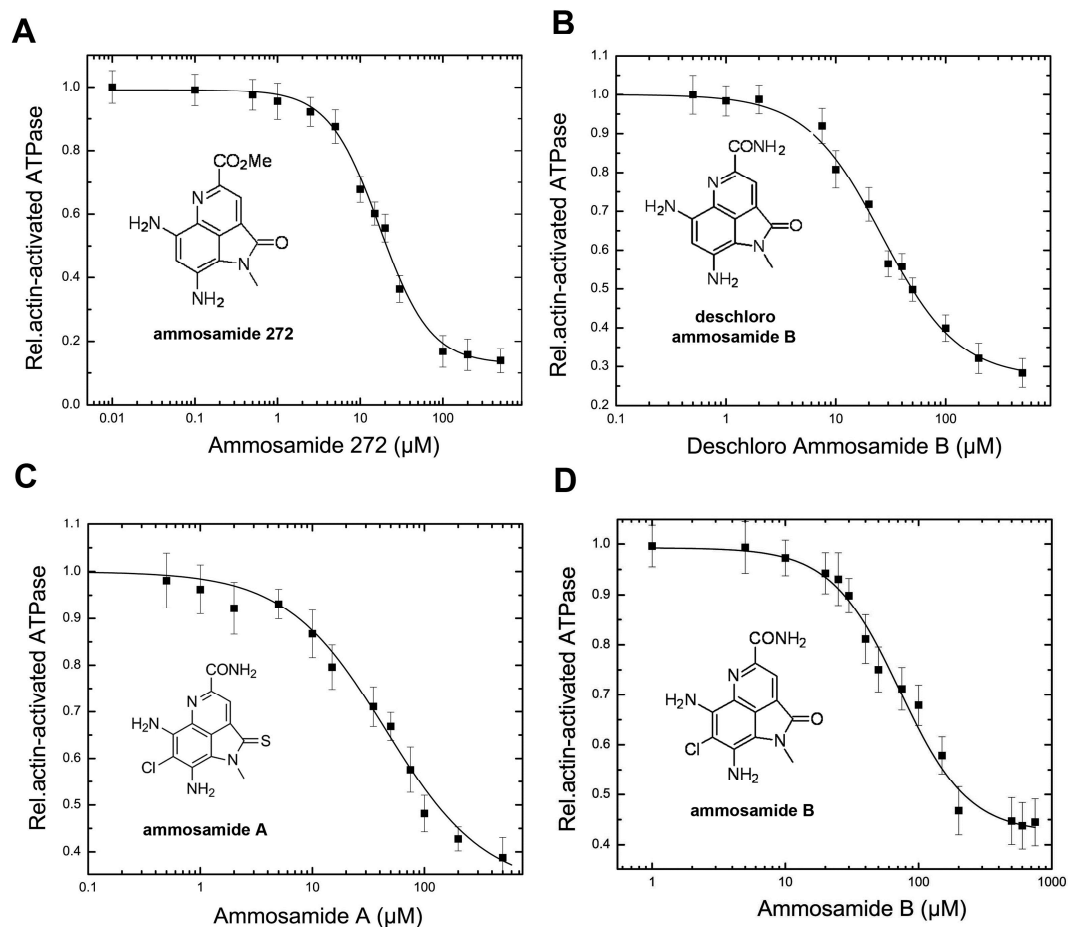


Figure 3.1.2.2: Inhibition of the actin-activated ATPase activity of *Dd* myosin-2 in the presence of ammosamides. The semi-logarithmic normalized plots show the concentration dependence of the ammosamide mediated inhibition of *Dd* myosin-2 ATPase activity as a function of (A) ammosamide 272, (B) Des B, (C) ammosamide A and (D) ammosamide B concentration. Fitting results give IC_{50} values of $17.16 \pm 0.74 \mu\text{M}$, $25.21 \pm 2.39 \mu\text{M}$, $45.71 \pm 5.12 \mu\text{M}$ and $72.38 \pm 5.96 \mu\text{M}$ for ammosamide 272, deschloro ammosamide B, ammosamide A and ammosamide B, respectively.

As depicted in Figure 3.1.2.2, addition of ammosamides greatly decreased the rate of actin-activated ATP turnover for *Dd* myosin-2. The plots of the observed rates against the logarithm of inhibitor concentrations were fitted with sigmoidal functions. The IC_{50} values for ammosamide 272, Des B, ammosamide A and ammosamide B correspond to $17.16 \pm 0.74 \mu\text{M}$, $25.21 \pm 2.39 \mu\text{M}$, $45.71 \pm 5.12 \mu\text{M}$, and $72.38 \pm 5.96 \mu\text{M}$, respectively. In contrast, human nonmuscle myosin-2C and myosin-7a motor domain constructs showed no sign of inhibition in the presence of $100 \mu\text{M}$ ammosamides (data not shown). Interestingly, the most potent inhibition of the *Dd* myosin-2 actin-activated ATPase activity was observed for ammosamide 272 and the less potent inhibition was observed in the

case of ammosamide B.

3.1.2.3 Single-Turnover Experiments with Ammosamides

To gain details about the kinetic steps affected by ammosamide binding, single-turnover stopped-flow experiments were performed with *Dd* myosin-2 using mantATP as a substrate (Figure 3.1.2.3).

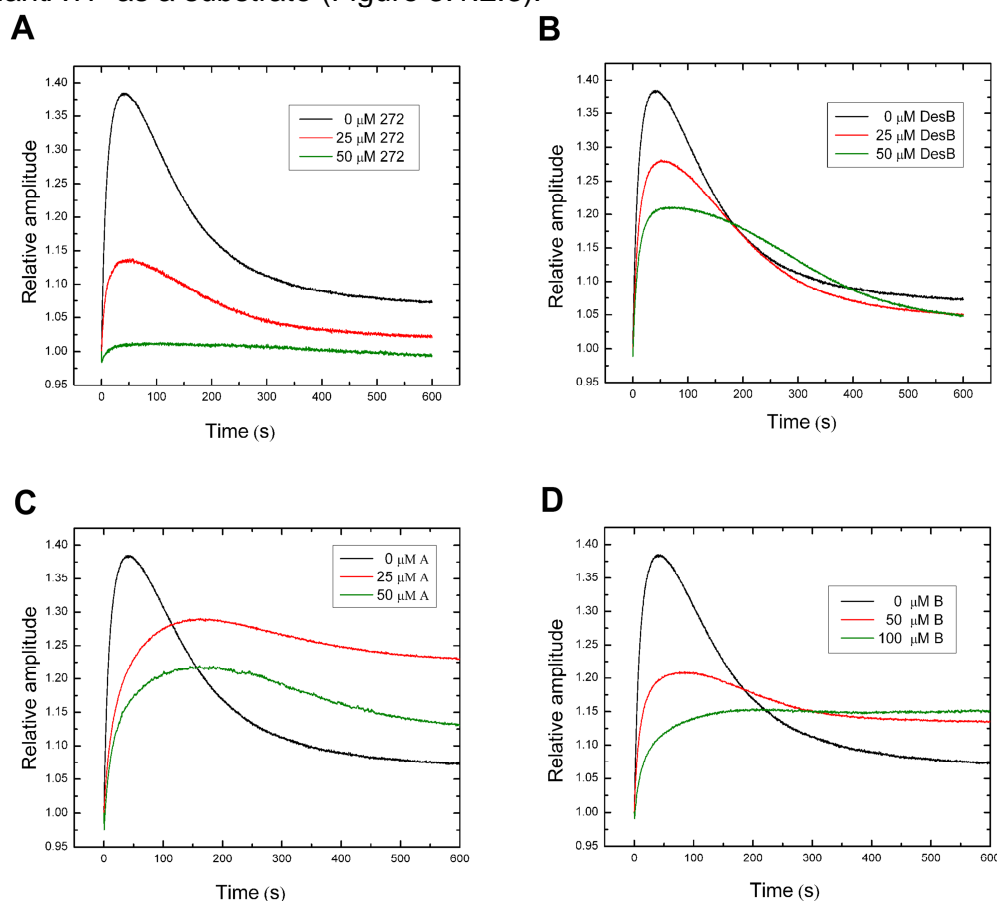


Figure 3.1.2.3: Single turnover experiments showing the changes in fluorescence signal upon mixing $0.5 \mu\text{M}$ *Dd* myosin-2 with $0.4 \mu\text{M}$ mantATP in the presence of increasing concentrations of (A) ammosamide 272, (B) Des B, (C) ammosamide A and (D) ammosamide B over a time range of 600 seconds.

In the absence of ammosamides, the time evolution of the reaction can be separated in three phases: an initial rise in mant-fluorescence corresponding to mantATP binding to myosin, a short plateau phase determined by the rate of the conformational change that follows mantATP binding, and a drop in mant-fluorescence corresponding to release and rebinding of mantADP (Fedorov et al, 2009). All three phases are extended in the presence of ammosamides in a concentration dependent manner. However, the extension of different phases in

single-turnover experiments was larger in the case of ammosamide 272 and was smaller for ammosamide B at same concentrations.

3.1.2.4 Structural Basis of Ammosamides Inhibition

Ammosamides inhibit rabbit skeletal muscle myosin-2, but the structural basis for the mode of inhibition is not yet evident (Hughes et al, 2009a). In order to explain the structural basis of inhibition, the crystal structures of ammosamide 272 and ammosamide B in complex with the *Dd* myosin-2 motor domain were solved at a resolution of 2.5 Å and 2.3 Å, respectively. The structures of ammosamides were determined in a C-centered orthorhombic form. Both ammosamide bound structures revealed the presence of two molecules and similar binding sites (Figure 3.1.2.4). One of the molecules binds in the allosteric pseudilin-binding pocket (Fedorov et al, 2009) (Figure 3.1.2.4). The second molecule binds in a novel-binding site adjacent to the helix-loop-helix and the helix connecting to the relay loop. The structures of ammosamide A and Des B bound to myosin motor domain remain to be solved.

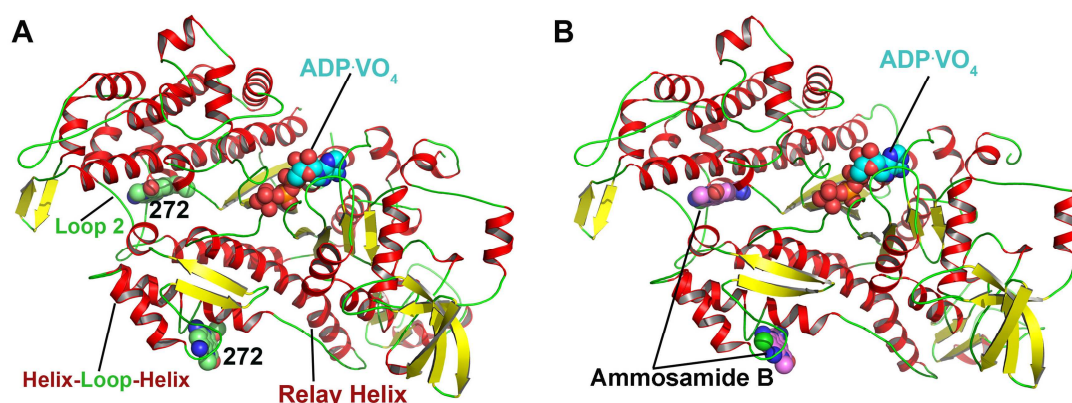


Figure 3.1.2.4: Overview of the crystal structures of the *Dd* myosin-2 motor domain complexed with ADP•VO₄ and (A) ammosamide 272 and (B) ammosamide B. For clarity, ammosamide 272 was labeled as 272 and myosin motor domain was colored according to the secondary structure pattern. The ammosamide 272 is colored in green and ammosamide B colored in violet and ADP•VO₄ was colored in cyan. Functional groups (-OH, -NH₂) of ammosamides were colored according to the element color. All the heterogens were shown in sphere representation.

Ammosamide 272 and ammosamide B molecules bound in the characterized pseudilin-binding pocket (Chinthalapudi et al, 2011; Fedorov et al, 2009) comprise 100% occupancy and 68% occupancy, respectively (Figure 3.1.2.5). Both ammosamides show better fitting to the pseudilin-binding pocket because of their bulky rings and substituents, which geometrically fits to the much available space of the allosteric binding site.

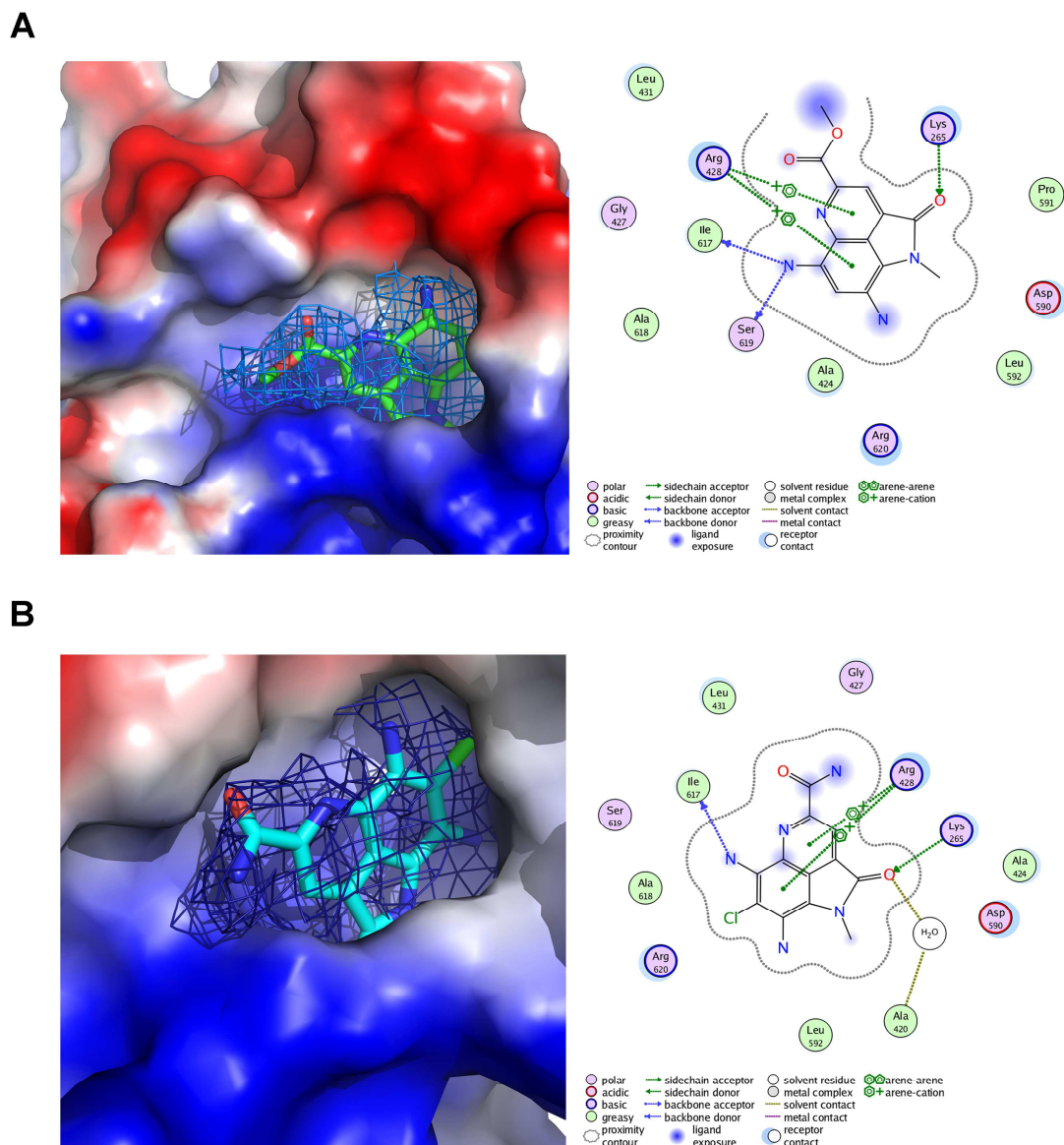
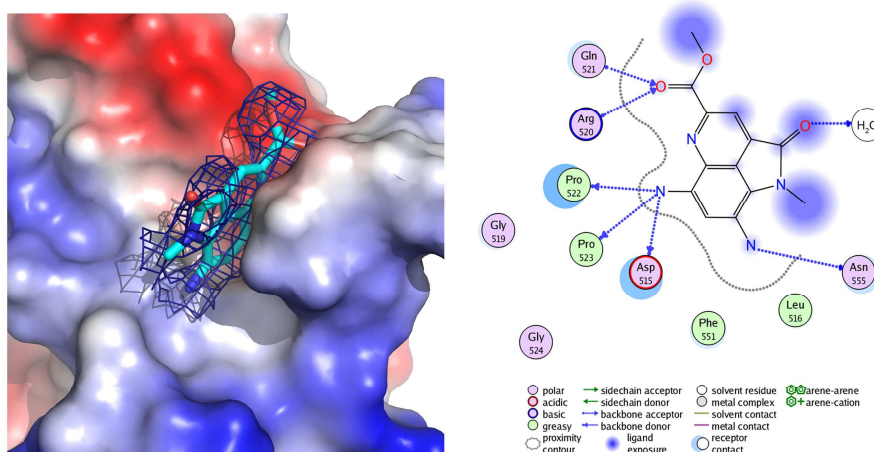


Figure 3.1.2.5: Section (A, left panel) shows the electrostatic potential surface with 2Fo-Fc electron density map of ammosamide 272, which was contoured at 1σ . Section (A, right panel) shows the schematic interaction of ammosamide 272 with *Dd* myosin 2 at the PCIP site. Section (B, left panel) shows the electrostatic potential surface of ammosamide B and the 2Fo-Fc electron density of the molecule, which was contoured at 0.7σ . Section (B, right panel) shows the schematic interaction of ammosamide B with *Dd* myosin 2 at the PCIP site.

As a common feature, both ammosamides align their carbonyl groups, which are substituted on the pyrrolidine ring, to Lys265 of *Dd* myosin-2 to form an ideal hydrogen bond, both in the direction and also in the distance (2.5 Å). Thus, the presence of interactions with Lys265 indicates the importance of this residue in

mediating the allosteric inhibition. Residues Asp590, Ser619 and Ile617 form hydrogen bonds with the compound. In the case of ammosamide B, Ser619 only forms van der Waals interaction with the compound. Arg428 was identified as the cation- π interaction contributor in both cases.

A



B

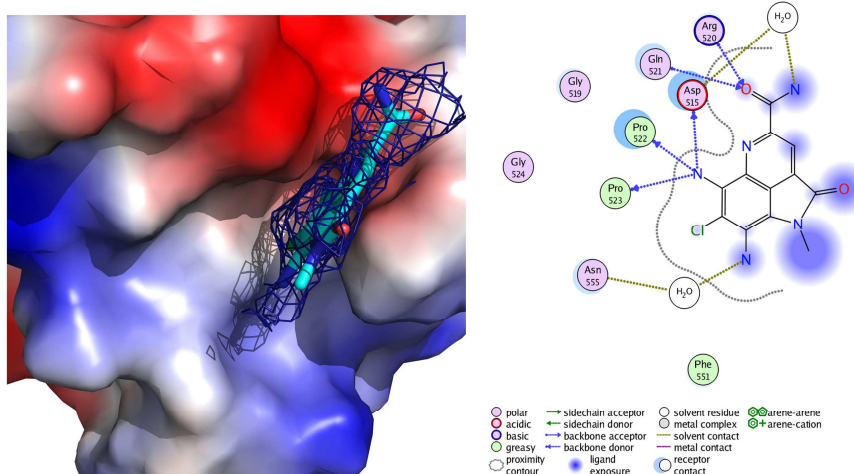


Figure 3.1.2.6: Section (A, left panel) shows the electrostatic potential surface of the myosin-2 motor domain at the novel-binding site of the ammosamide 272. The 2Fo-Fc electron density map of ammosamide 272 was contoured at 0.8σ . Section (A, right panel) shows the schematic interaction of ammosamide 272 with *Dd* myosin 2 at the Proline bulge (Pro522 and Pro523). Section (B, left panel) shows the electrostatic potential surface of the myosin-2 motor domain at the 2nd binding site of the ammosamide B. The 2Fo-Fc electron density map of ammosamide B was contoured at 0.8σ . Section (B, right panel) shows the schematic interaction of ammosamide B with *Dd* myosin-2.

Furthermore, residues Ile617, Leu592, Ala424, Ala618, and Leu431 are involved in hydrophobic contributions. Figure 3.1.2.5, schematically summarizes the

interactions between ammosamides and residues of the pseudilin binding site.

The second binding site of ammosamides within the *Dd* myosin-2 motor domain was identified as a novel-binding site for myosin inhibitors. As depicted in Figure 3.1.2.4, the novel allosteric binding pocket is located adjacent to the 2nd helix (residues 524-534) of the helix-loop-helix motif and near the relay loop. This allosteric site is one of the easily accessible solvent channels of the myosin motor domain. Molecules of ammosamide 272 and ammosamide B comprise 80% and 71% occupancy in this binding pocket, respectively. Close-up views of the inhibitors bound in the identified binding pocket and the interaction profile with neighboring amino acids are depicted in Figure 3.1.2.6.

Detailed structural analysis of the second allosteric binding site revealed that the aromatic/hydrophobic rings of the ammosamides face towards the hydrophobic core, which consists of amino acids Leu516, Pro522, Pro523 and Phe551. One of the amino groups at the C6 atom of the '4,6-diamine benzene' of the ammosamide forms a hydrogen bond network with the backbone carbonyl oxygen atoms of Asp515, Pro522 and Pro523. Furthermore, the amino group on the C4 atom of the '4,6-diamine benzene' of ammosamide 272 present towards the helix-loop-helix forms a direct interaction with Asn555 (Figure 3.1.2.6). In the case of ammosamide B, a water molecule mediates this interaction.

The carbonyl moiety in the 'methoxy carbonyl' of ammosamide 272 or 'amide' of ammosamide B forms hydrogen bonds with the backbone carbonyl moiety of Gln521 and Arg520. Furthermore, the Carbonyl bond in the 'N-Methyl-2-pyrrolidone' or the 'N-methyl γ -lactam' group forms a solvent interaction in the case of ammosamide 272. This interaction is absent in the ammosamide B bound structure. However, most of the interactions, in ammosamide 272 and ammosamide B, are conserved. Even the orientation of the inhibitors is preserved. Although structures of ammosamide A and Des B are not yet solved, above results indicate that most of the ammosamides follow similar structural basis of allosteric inhibition.

3.2 Human Nonmuscle Myosin-2C (NMH-2C)

Myosins have been implicated in various motile processes, including organelle translocation, ion-channel gating, and cytoskeleton reorganization. Class-2 myosins involve the largest group with several subfamilies including skeletal, cardiac, smooth muscle and nonmuscle myosins (Berg et al, 2001). Cytoplasmic, nonmuscle myosins are among the most prevalent myosins and are expressed in a spatial and developmentally dependent manner (Golomb et al, 2004; Maupin et al, 1994; Simerly et al, 1998). Nonmuscle myosins are major cytoskeletal proteins that interact with actin and are involved in wide range of cellular functions like cell adhesion (Betapudi et al, 2006), cell migration (Even-Ram et al, 2007) and cytokinesis (Pollard, 2010). Three separate genes (*MYH9*, *MYH10*, *MYH14*) encode the nonmuscle myosin heavy chain (NMHC-2) proteins (NMHC-2A, -2B, and -2C, respectively), which together with the light chains are referred to as NM2A, NM2B, and NM2C (Vicente-Manzanares et al, 2009a). At the protein level, all nonmuscle myosin heavy chains have a basic domain architecture consisting of three structural units: a catalytic motor domain, a neck domain comprising 2 IQ motives that bind the regulatory as well as the essential light chain, and a rod-like tail domain that forms an alpha-helical coiled-coil (Kengyel et al; Sellers, 2000a). The presence of the extended coiled-coil region promotes self-association into short bipolar filaments (Niederman & Pollard, 1975; Verkhovsky et al, 1995). These filaments power interactions with actin filaments producing force, driving directed movement and maintain tension forces.

3.2.1 Crystal Structure of Human Nonmuscle Myosin-2C (NMH-2C) Motor Domain in the Pre-Power Stroke State

The splice variants of nonmuscle myosin-2C have been kinetically well described (Heissler & Manstein, 2011). The putative amino acid sequences between the nonmuscle myosin-2C motor domains of the transcript variants are well conserved with an identity of 96-99% (Heissler & Manstein, 2011). In this study, *Hs* NM2C0, one of the three splice variants of nonmuscle myosin 2C comprising the shortest loop-1 and loop-2, was used for the structural analysis (Heissler & Manstein, 2011). For clarity, *Hs* NM2C0 will be addressed as NM2C for the rest of the document. It was observed that the native NM2C motor domain with a non-conserved, unique N-terminal extension (residues 1 to 45) of NM2C were refractory for crystallization (Figure 3.2.1). This unique N-terminal extension of NM2C was identified as highly disordered and hence, it was truncated in order to improve the chances of obtaining crystals. It was also observed that the truncated motor domain has similar ATPase activity compared to native motor domain of NM2C0. Further, the NM2C motor domain was fused to two *Dictyostelium discoideum* α -actinin repeats that can functionally replace the lever arm (Kliche et al, 2001).

The recombinant protein was produced in the baculovirus/*sf9* system and purified to homogeneity by Ni-NTA affinity chromatography and gel filtration. The crystallization trials were performed with ~12 mg/ml of protein and multiple rectangular-plate like stacked crystals were grown in 3 weeks (Figure 3.2.2).

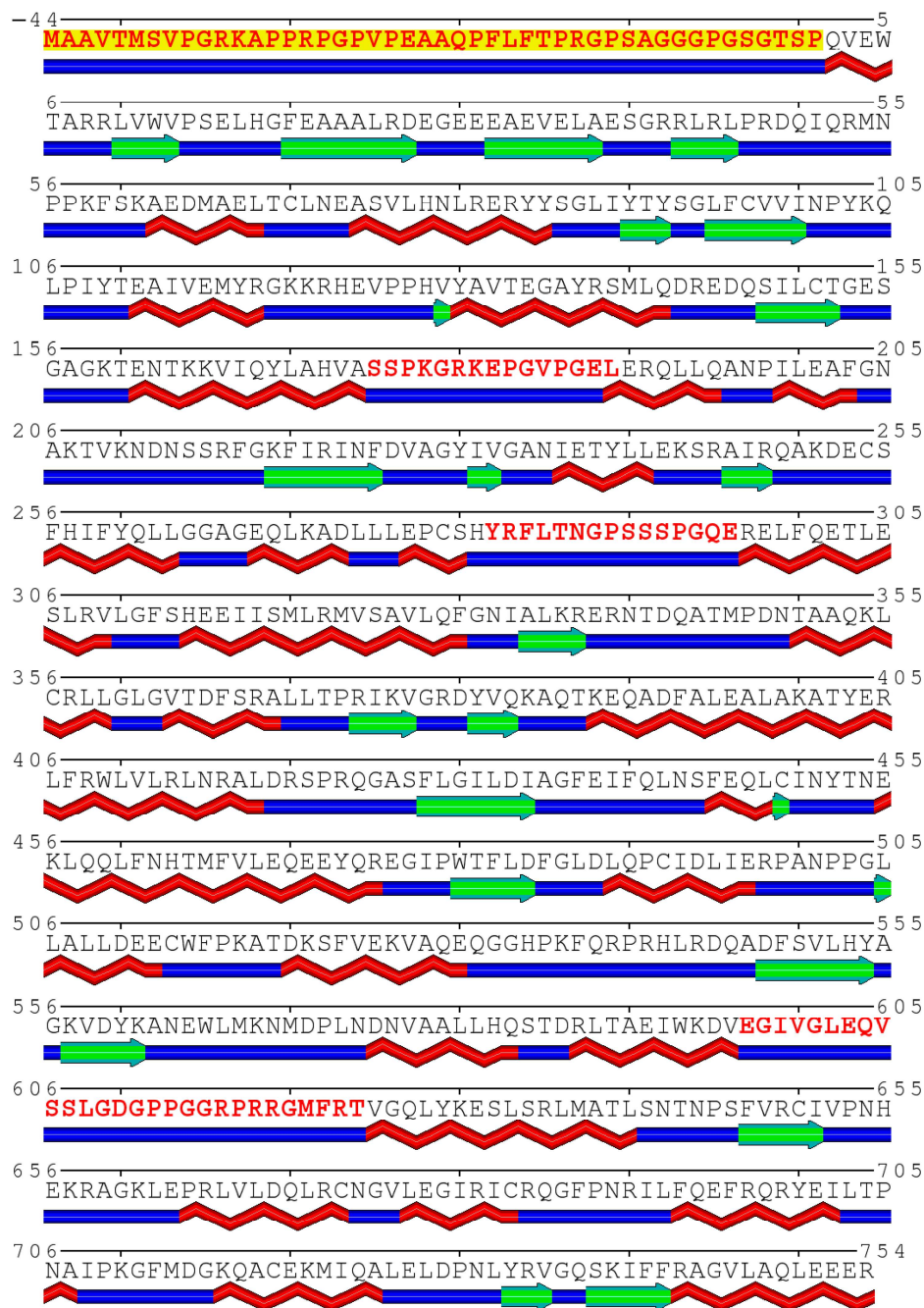


Figure 3.2.1: Sequence of NM2C0 with predicted secondary structure representation. Residues labeled in red are (a) Unique N-terminal extension (1st 45 residues in yellow), (b) loop-1 (175-189), (c) Upper 50 kDa loop (282-296) and (d) extended loop-2 (597-624). The predicted secondary structures (DSSP prediction) like α -helices are shown in zigzag representation, β -sheets as arrows and loops & turns are represented in cylinders. The N-terminal 45 residues highlighted in yellow are truncated in the crystallized motor domain. Therefore, the construct numbering starts from a starting methionine (residue 1), followed by the second residue Glutamine.

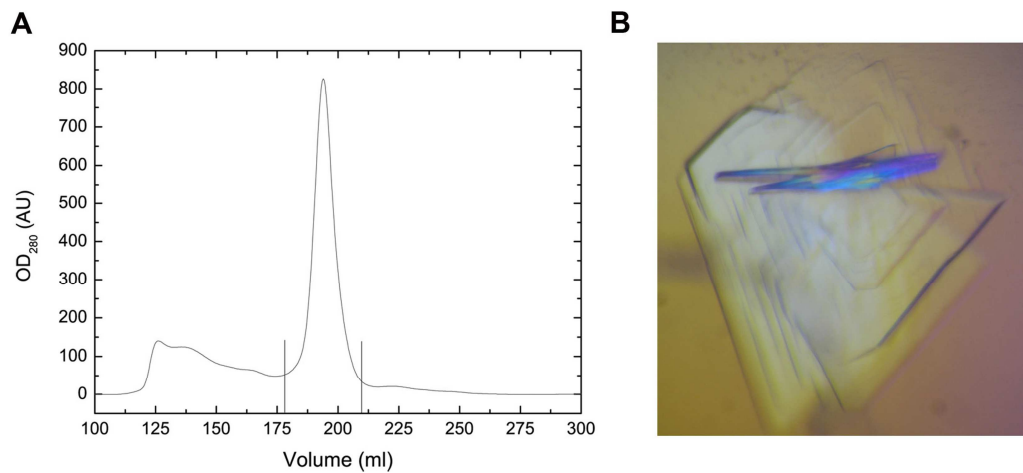


Figure 3.2.2: (A) Gel filtration elution profile of the N-terminal truncated NM2C motor domain construct. For crystallization purpose, only the central peak fractions were collected. (B) Stacked rectangular plates of NM2C crystals.

The crystal structure of NM2C complexed with the transition state analogue $\text{Mg}^{2+}\text{-ADP}\cdot\text{VO}_4$ was solved at 2.25 Å resolution in the pre-power stroke state conformation (Figure 3.2.3).

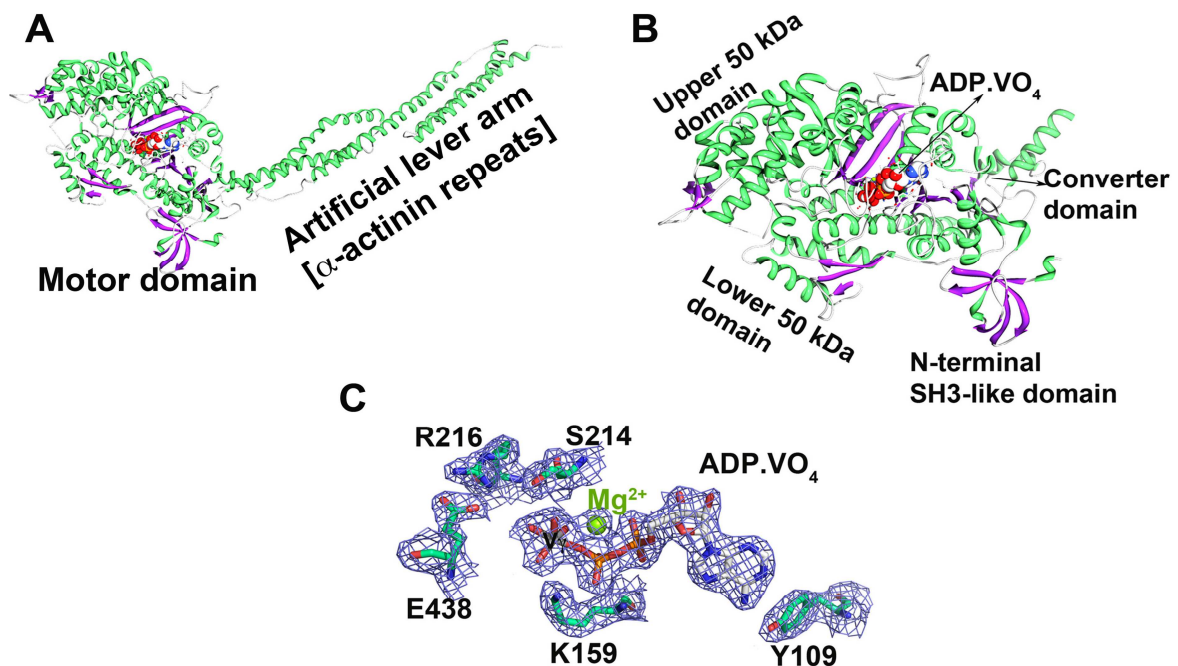


Figure 3.2.3: (A) Overview of the structure of NM2C motor domain fused to two α -actinin repeats, which mimic the natural lever arm. (B) Close up view of the motor domain. Coloring was done according to the secondary structure. Helices are shown in green, sheets are shown in violet and the loops/turns are shown in white. (C) The $2F_o - F_c$ electron density map of $\text{Mg}^{2+}\cdot\text{ADP}\cdot\text{VO}_4$ and key residues shown in the active site are contoured at 1.5σ .

Crystallographic refinement statistics are given in Table 23. The detailed structural analysis of the human NM2C MD provides the identification of novel structural features as well as similarities and variations of its structure in comparison to other class-2 myosins.

Table 23: Data Collection and Crystallographic Refinement Statistics

Data collection & Refinement Statistics	Hs NM2C – ADP•VO₄
Data collection	
Space group	P22121
Wavelength (Å)	0.91841 (BL 14.1, BESSY)
Cell dimensions	
a, b, c (Å)	81.12, 125.61, 153.96
α, β, γ (°)	90, 90, 90
R _{sym} (%)	12 (23)*
I / σ[I]	13.60 (2.70)
Completeness (%)	99.9 (100)
Redundancy	14.95 (14.9)
Refinement	
Resolution (Å)	34.77-2.25
R _{work} / R _{free} (%)	20.5 / 25.7
No.reflections working / test set	75206/ 3785
No. atoms	
Protein	7727
Ligands/ions	45/ 1
Water	522
R.m.s. deviations	
Bond lengths (Å)	0.015
Bond angles (°)	1.83
Ramachandran plot (% Favored/allowed/outliers) [§]	92.3/7.7/0

* Values in parentheses are for highest-resolution shell (2.35–2.25).

[§] Residues in favored, allowed, and outlier regions of the Ramachandran plot as reported by MolProbity module in Phenix crystallographic software (Davis et al, 2007b).

3.2.2 Comparison of Pre-power Stroke State Structures of Class-2 Myosins

The motor domain (MD) of NM2C displays an overall topology that is very similar to that of other class-2 myosin isoforms in the pre-power stroke state (Figure 3.2.4), such as the MD of the scallop striated muscle myosin complexed with ADP•VO₄ [1QVI], (Gourinath et al, 2003) and the MD of the chicken smooth muscle myosin complexed with ADP•BeF_x [1BR4] (Dominguez et al, 1998).

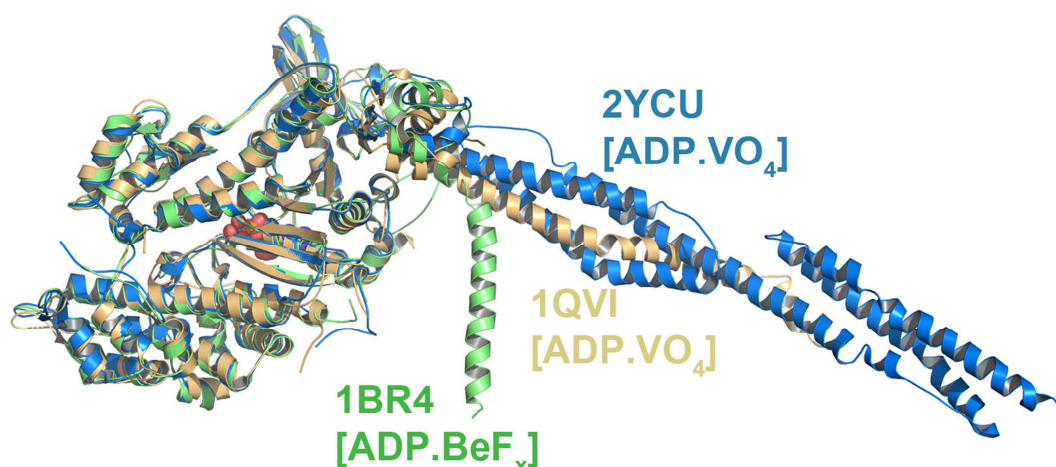


Figure 3.2.4: Pre-power stroke state structures of *Hs* NM2C motor domain fused to an artificial lever arm [2YCU] colored in blue, scallop striated Myosin S1 [1QVI] in light orange and chicken smooth Myosin S1 [1BR4] in green. For clarity, myosin light chains from 1QVI and 1BR4 are not shown in the figure.

NM2C motor domain shows that the nucleotide-binding pocket comprises the purine-binding loop or adenine binding loop [A-loop] (NPxxxxxY) on one side and the switch-1 (NxxSSR), P-loop (GESGAGKT) and switch-2 (DlxGFE) elements that sandwich the polyphosphate moiety of the nucleotide on the other side (Figure 3.2.5). As in other structural studies of class-2 myosins, the present work shows that the ATP analogue ADP•VO₄ forms strong interactions with switch-1 residues in the active site, inducing switch-1 to close. Closing of switch-1 results in a movement of the loop towards the β - and γ -phosphates of the bound nucleotide. Additionally, switch-2 closes by moving the lower part of β -strand 5 back into the plane of the seven-stranded β -sheet (Gourinath et al, 2003; Kliche et al, 2001). Switch-2 closing induces formation of the kink in the relay helix, causing a 60° rotation of the converter domain and the neck helix into the up position (Kliche et al, 2001).

The structural analysis revealed a root mean square deviation (rmsd) between the C $_{\alpha}$ atoms of human NM2C MD and chicken smooth Myosin MD of 0.74 Å as well as C $_{\alpha}$ atoms of human NM2C MD and scallop striated Myosin MD of 0.76 Å. As depicted in Figure 3.2.5, the catalytically active core region of the myosin motor domain is highly conserved indicating the preservation of the basic motor

function and ATPase activity.

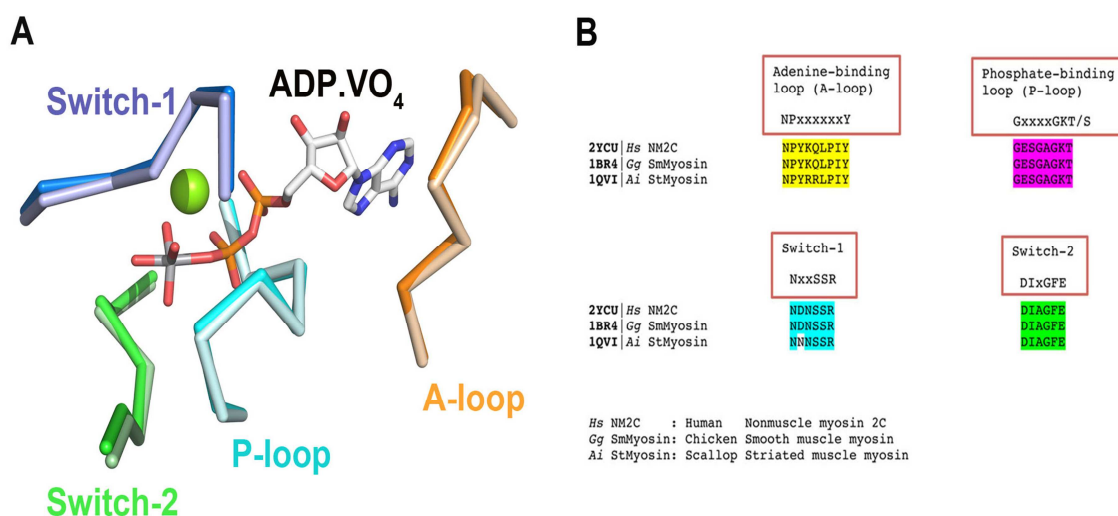


Figure 3.2.5: (A) Highly conserved active site elements are shown in ribbon representation. (B) Corresponding sequence alignments of these sites are shown for *Hs* NM2C (2YCU), *Ai* stMyosin [1QVI], and *Gg* smMyosin [1BR4].

It is of note that the surface loops-1 and -2 were excluded from the rmsd calculations, since the loop regions were truncated or missing in the reference X-ray structures. Despite its high sequence homology with the motor domain structures of smooth muscle myosin [1BR4] (88%) and striated muscle myosin [1QVI] (68%), NM2C motor domain has shown significant differences in the important surface loops like loop-3, and a new loop introduced here as the “Upper 50 kDa loop (327-341)” (Figure 3.2.6).

Atomic models of the actomyosin complex implicate loop-3 as major contributor of myosins secondary actin binding region (Geeves et al, 2005; Lorenz & Holmes, 2010; Van Dijk et al, 1999). The length of the NM2C loop-3 is similar to smooth muscle myosins (15 residues) but substantially shorter when compared to other class-2 myosins (≥ 19 residues). Furthermore, the orientation of loop-3 in the NM2C structure is different from other related myosin isoforms (Figure 3.2.6). These structural features cause an increase in the accessible surface area between actin and loop-3, which is in striking contrast to other class-2 myosins.

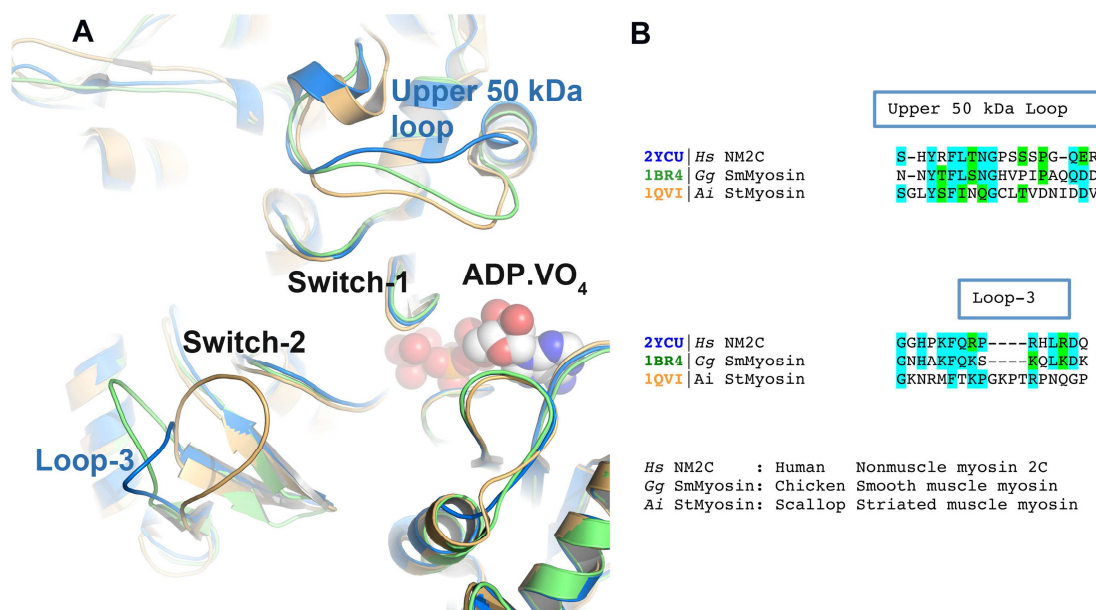


Figure 3.2.6: (A) Variations in the surface loops like Upper 50 kDa loop and loop-3 of nonmuscle myosin-2C (blue), smooth muscle myosin (green) and the muscle myosin were shown (light orange). (B) Sequence alignment of the Upper 50 kDa loop and loop-3. Identical residues are marked in cyan; similar residues in green, non-conserved residues are not highlighted.

The Upper 50 kDa loop forms an integral part of a small helix-loop-helix motif, and is one of the connecting links between the active site and the Upper 50 kDa subdomain (Risal et al, 2004). The present NM2C structure reveals prominent changes within the Upper 50 kDa subdomain. The major contribution in conformational changes is from the Upper 50 kDa loop followed by the rearrangements of the helices in the Upper 50 kDa subdomain (Figure 3.2.7). In addition, other surface loops like loop-4 and cardiomyopathy loop (CM-loop), which are playing an important role in the actin-binding interface, show significant conformational changes. In the pre-power stroke state structure of scallop striated muscle myosin (1QVI), key residues D320 and N321 from this Upper 50 kDa loop interact with switch-1 residues N239 and K233.

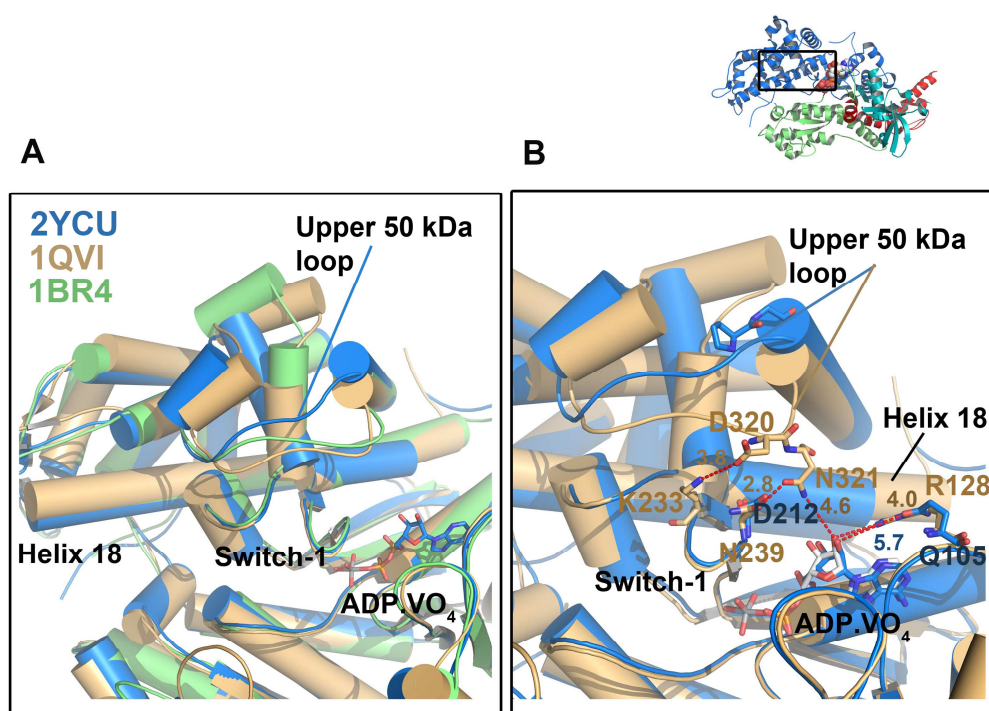


Figure 3.2.7: (A) Close-up view of the superimposition of the Upper 50 kDa loop of nonmuscle myosin-2C (blue), smooth muscle myosin (green) and the muscle myosin (light orange). (B) Interactions between Upper 50 kDa loop and the switch-1 region are compared between the nonmuscle myosin-2C (blue), and the muscle myosin (light orange). To avoid complexity, interactions of these regions in chicken smooth muscle myosin [1BR4] were not shown. Q105 of NM2C is 4.4 Å away from N3 atom of adenine ring and 5.8 Å away from the O2' of ribose in the active site. Residue N321 is only ~4.6 Å away from the hydroxyl group of C2' of the ribose ring in the ADP. This hydroxyl group of ribose (~4.0 Å) and one of the nitrogen [N3] of adenine (3.2 Å) also forms an interaction with the residue R128 in the case of muscle myosin.

Interestingly, N231 of muscle myosin is replaced by G294 in the NM2C sequence. Further, the Upper 50 kDa loop is substantially shortened in length in comparison to both, smooth muscle (1BR4) and striated myosin (1QVI). In addition to the shortened length, this region coupled to further conformational changes in the Upper 50 kDa domain. These rearrangements resulted in a large gap (9.5 Å) in between Upper 50 kDa loop and switch-1. Consequently, the gap between C2' of ADP and the Upper 50 kDa loop increases to ~12 Å.

Sequential studies show that R128 of striated muscle myosin is replaced by Q105 in the purine-binding loop of NM2C. Significance of this modification involves the lack of interactions between ADP and Q105 in the NM2C active site (Figure 3.2.7). These intra domain rearrangements suggest a mechanism of

coupling between the Upper 50 kDa loop and active site region. The position of the loop might play a very important role in actin binding dynamics as this loop might act like a lid on the distal part of the actin-binding cleft.

3.2.4 Unique Features of Lever Arm

The structural analysis of the NM2C motor domain further revealed striking differences between the pre-power stroke state structures of the chicken smooth muscle myosin, scallop striated muscle myosin and nonmuscle myosins in the orientation of the lever arm (Figure 3.2.8).

The reactive thiol helices preceding the converter domain are varied in their conformation when compared to chicken smooth muscle myosin (1BR4) and resemble those described for scallop-striated myosin (1QVI). This finding was unexpected because of the high sequence similarity between smooth- and nonmuscle myosins. The reactive thiols in NM2C and scallop striated muscle myosin are slightly bent when compared to the kink in the chicken smooth muscle myosin. Gourinath *et al* have shown that the difference between pre-power stroke state structures of *Ai* stMyosin (1QVI) and *Gg* smMyosin (1BR4) is associated with a “pliant region”, which is part of the heavy chain at the MD/lever arm junction (Gourinath et al, 2003).

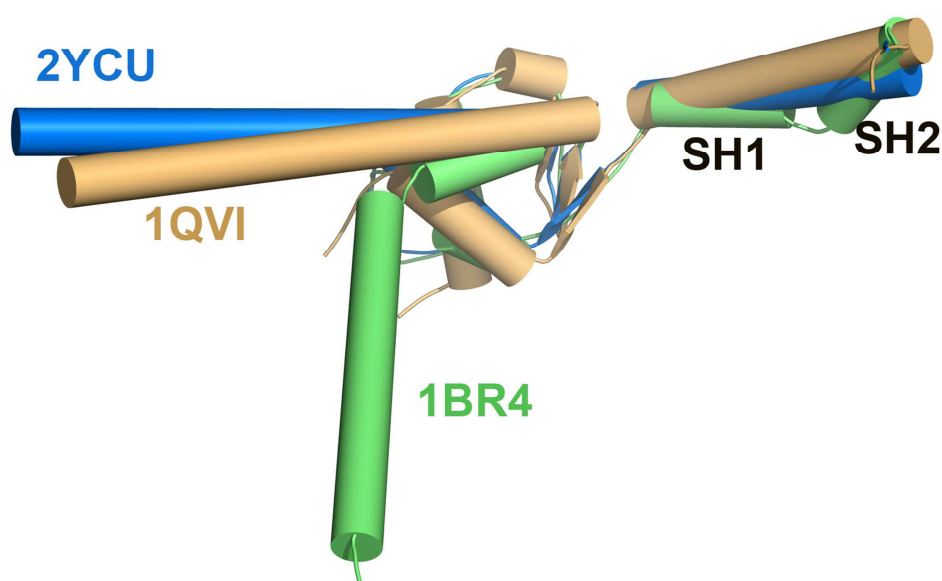


Figure 3.2.8: Orientation of lever arm and reactive thiol helices (SH1 and SH2) in three pre-power stroke state structures. The reactive thiol regions shown in smooth muscle myosin (1BR4), scallop-striated myosin (1QVI) and nonmuscle myosin-2C (2YCU) are two small helices. A small kink is present in the SH1 and SH2 helices of scallop-striated myosin (1QVI) and *Hs* NM2C (2YCU). The extent of kink in the reactive thiol helices in smooth muscle myosin (1BR4) is larger than the above-mentioned myosins.

In contrast, in NM2C, an artificial lever arm [α -actinin repeats] (Kliche et al, 2001) is attached at the end of the converter domain (R754), which is exactly at the position of the plaint region. Even though the NM2C structure lacks light chains, the α -actinin repeats align in the same orientation as the lever arm of scallop striated muscle myosin with a slight change in the orientation of about $\sim 10^\circ$ to 15° . The difference between the lever arms of chicken smooth muscle myosin (1BR4) and NM2C can be explained in the same terms as the lever arms of striated muscle myosin (1QVI) and smooth muscle myosin (1BR4). This finding supports the results from Anson *et al.* highlighting that the artificial lever arm is not only a useful tool for the recombinant protein production and functional studies of the myosin motor domain but indeed mimics the structure of the natural lever arm without bound light chains (Anson et al, 1996b).

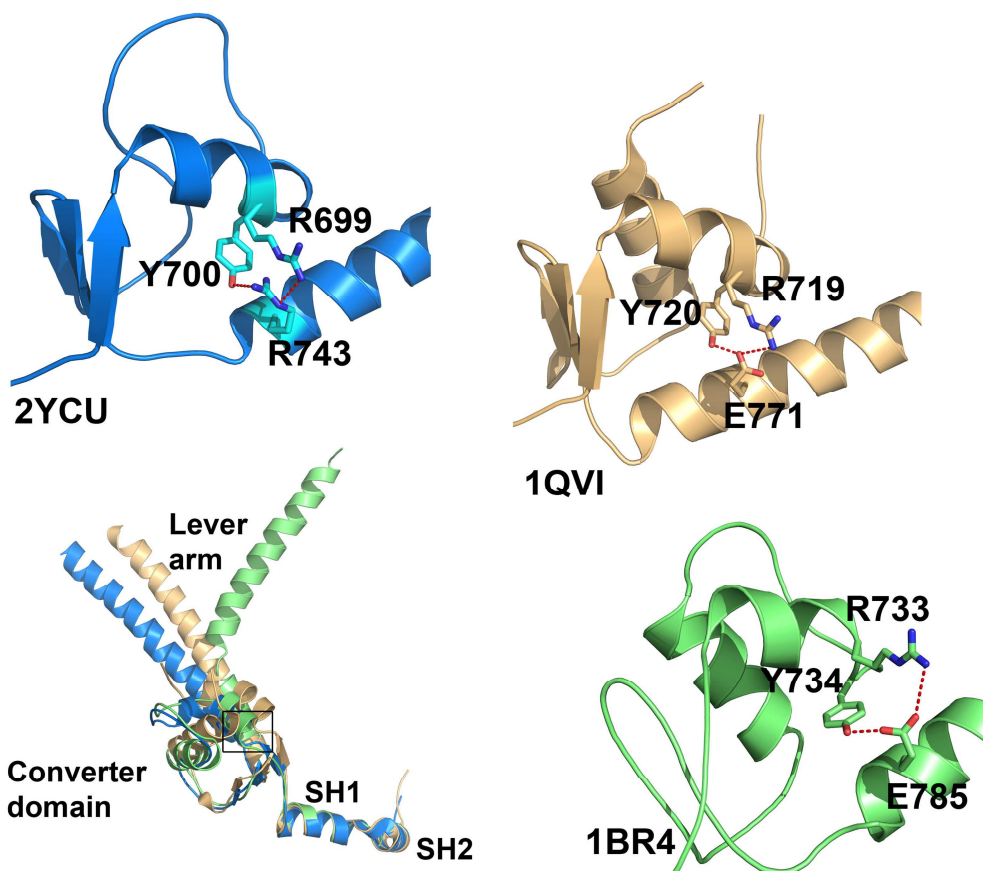


Figure 3.2.9: Crucial interactions in the junction of converter and the beginning of the lever arm. It is also observed that a crucial interaction between the converter domain and the start of the lever arm is mediated by strong hydrogen bonding interactions in the above-mentioned myosins. Further, it is important to note that a positive Arginine (R743) in the NM2C motor domain replaces the conserved Glutamate at the beginning of the lever arm.

In the interface between converter and the start of the lever arm, residues Arginine and Tyrosine from converter domain are involved in a strong hydrogen bonding with a Glutamate in the lever arm of chicken smooth muscle myosin (1BR4) and scallop striated muscle myosin (1QVI) pre-power stroke state structures. However, in the case of *Hs* NM2C, an Arginine is replaced the conserved Glutamate at the start of the lever arm (Figure 3.2.9). Furthermore, the guanidine group of R743 from the lever arm is not forming an ideal hydrogen bond with the converter domain residue R699.

3.3 Structural Models of *Toxoplasma gondii* Myosin Heavy Chain (MHC) and Myosin Light Chain (MLC) Complexes

TgMyoA is the best-understood Apicomplexan myosin motor. *TgMyoA* is a very short myosin heavy chain with a short neck and no true tail domain (Foth et al, 2006). It is a fast, single-headed and plus-end directed molecular motor with kinetic and mechanical characteristics that are similar to fast skeletal muscle myosin-2 (Herm-Gotz et al, 2002). *MyoA* co-localizes with a myosin light chain that is referred as “myosin light chain 1 (*TgMLC1*) in *T.gondii* (Herm-Gotz et al, 2002) and myosin-tail-interacting protein (MTIP) in *Plasmodium spp* (Baum et al, 2006). The interaction of the MTIP/MLC1 is dependent on a dibasic motif in the C-terminal part of *MyoA*, i.e., the “degenerate” IQ motif (Hettmann et al, 2000; Opitz & Soldati, 2002).

3.3.1 Structural model of *TgMLC1* in Complex with *TgMyoA*-tail

To gain further insight into the interaction of *TgMyoA*-MLC1 complex, homology models of the C-terminal *TgMyoA* tail (residues 806 to 819) and *TgMLC1* (residues 69 to 213) were built using the *PfMTIP:MyoA* crystal structure as template (Bosch et al, 2006). Protein-peptide docking was performed later using these models. *TgMyoD* and *TgMyoA* are highly conserved (51% of identity, 69.6% of similarity). Also, the C-terminal part of *PfMyoA*, *TgMyoA* and *TgMyoD* are highly conserved (Figure 3.3.1). *TgMLC2* sequence is less conserved (15% of identity, 25% of similarity) because of the presence of a long N-terminal extension in *TgMLC2* when compared to *PfMTIP* (Polonais et al, 2011).

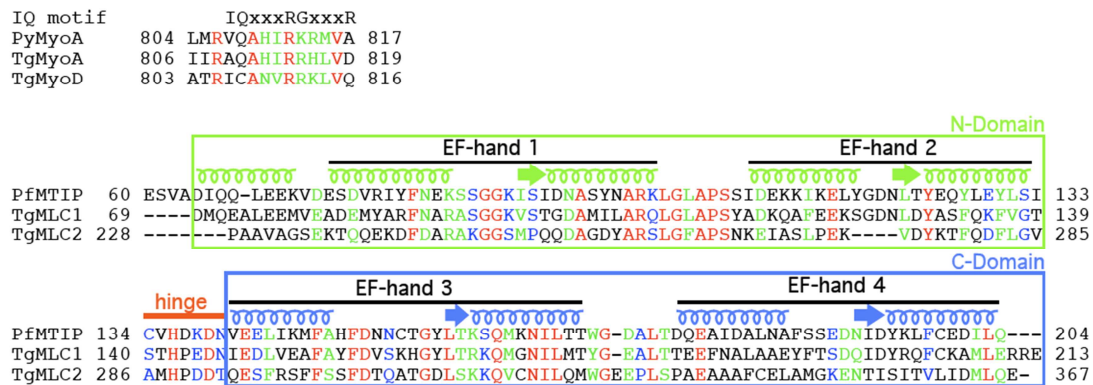


Figure 3.3.1: Sequence alignment of the C-terminal part of PyMyoA, TgMyoA and TgMyoD and of the CaM-like domain of PfMTIP, TgMLC1 and TgMLC2. The positions of the secondary structure elements (helices represented as springs and strands represented as arrows) are based on the PyMyoA–PfMTIP crystal structure (2QAC) (Bosch et al, 2006).

The resulting homology model of the TgMLC1-MyoA complex shows that the two MLC1 subdomains surround the MyoA-tail helix in a clamp-like manner (Figure 3.3.2). For clarity, the two proteins will be referred as MLC1 and MyoA for the rest of the document. The MLC1 model is predicted to consist of two CaM-like subdomains. The N-Domain formed by residues 69 to 139 contains two EF-hand motifs; the C-Domain formed by residues 147 to 213 contains two more EF-hand motifs. The subdomains are predicted to be connected by a short unstructured “hinge” loop formed by residues 140 to 146. MyoA tail residues 806 to 819 form an IQ-like motif with the sequence ‘AQAHIRRHLLVD’.

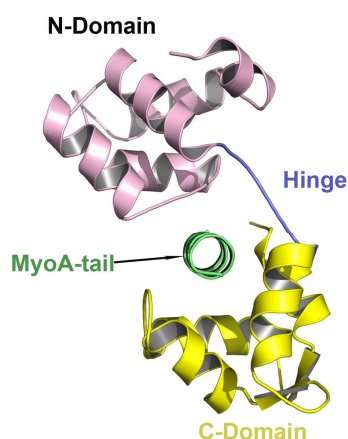


Figure 3.3.2: TgMyoA-MLC1 complex showing the compact binding with distinct N- and C-Domain. The N-Domain is colored in light pink, the C-Domain is colored in yellow and the middle hinge region is colored in blue. The MyoA-tail is presented in green.

The interface accessible surface area of MLC1-MyoA complex is 1108 Å², whereas the corresponding surface area in *Pf*MTIP-MyoA is 958 Å². Thus, *Tg*MLC1 forms the better compact contact area with the MyoA-tail than *Pf*MTIP. The interface of MLC1:MyoA consists reasonable percentage of non-polar residues (46 %) than the charged (23 %) and polar amino acids (31 %). The MyoA-tail is buried by numerous interactions ranging from strong salt-bridges, hydrogen bonding to moderate hydrophobic interactions. Apolar residues F154, L174, L181 and F204 from the C-Domain of MLC1 form hydrophobic interactions with the N-terminal residues (I811, L815) of MyoA-tail (Figure 3.3.3A).

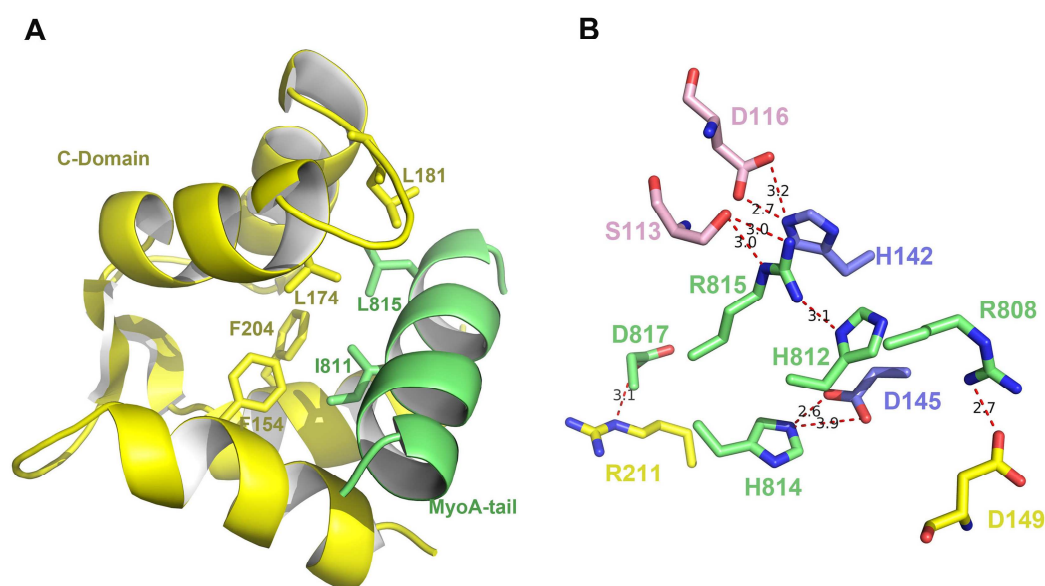


Figure 3.3.3: Homology models depicting the hydrophobic interactions between C-Domain of MLC1 and MyoA-tail (A) and the hydrophilic network of MyoA-MLC1 complex (B). Residues are colored according to the location.

In the *Tg*MyoA model, R815 occupies the 7th position of the IQ motif forming a tight network of hydrogen bonds with residues in the C-Domain (Figure 3.3.3B). In addition, H816 replaces a conserved positive residue (Arginine or Lysine) in this position in *Pf*MyoA and *Tg*MyoD. The tighter interactions with the C-Domain may contribute to the compactness of the interface. Conserved basic residues R808 and R815 in the MyoD-tail helix are involved in a tight network of polar

interactions with MLC1 residues D149, D116 and S113. H814 of MyoA-tail forms a hydrogen bond with D145 in the MLC1 hinge region (Figure 3.3.3B). Also, the interaction is further stabilized by the H142 residue of the hinge region, which forms a tight network with the N-Domain residue D116. All these interactions thus contribute to the stability of the MLC1-MyoA complex.

3.3.2 The Compact Structure of *Tg*MLC2 in Complex with *Tg*MyoD-tail

In order to build the structural models of *Tg*MyoD and *Tg*MLC2 lacking N-terminal, the *Pf*MTIP–MyoA crystal structure (Bosch et al, 2007) was used as a template for homology modeling. For simplicity, the two proteins will be referred as MLC2 and MyoD for the remainder of the text. The MLC2 model is predicted to consist of two subdomains. The N-Domain formed by residues 228 to 292 contains EF-hand motifs 1 and 2, whereas the C-Domain formed by residues 299 to 367 contains EF-hand motifs 3 and 4. In analogy to the *Pf*MTIP structure (Bosch et al, 2006), the subdomains are predicted to be connected by a short unstructured ‘hinge’ loop formed by residues 293 to 298 (Figure 3.3.1). MyoD-tail residues 803 to 816 containing a degenerate IQ motif (ICANVRRKLVQ) are modeled as an α -helix.

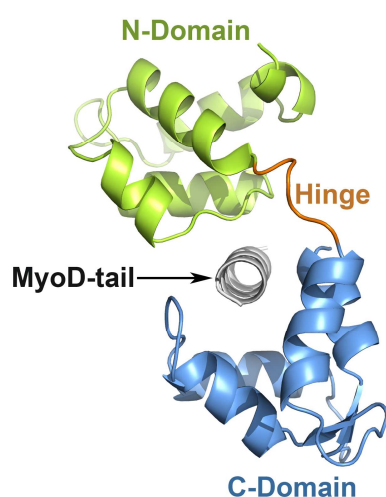


Figure 3.3.4: Cartoon representation of the *Tg*MyoD-tail bound to *Tg*MLC2, view along the MyoD-tail helix, in white. The N-Domain is colored in green and the C-Domain is colored in blue.

The resulting model of the MLC2–MyoD complex shows that the two MLC2 subdomains surround the MyoD-tail helix in a clamp-like manner (Figure 3.3.4).

The MLC2–MyoD interface contains predominantly non-polar residues (55%). Charged and polar neutral amino acids contribute for 28 and 17%, respectively. Similar to the experimentally solved structures, the N-Domain is predicted to form crucial interactions with the tail region (Bosch et al, 2006; Bosch et al, 2007). In contrast, the interactions involving the C-Domain appear more dominant than in *PfMTIP–MyoA* crystal structure (Bosch et al, 2007). Previous studies have shown that a glycine or other small residue is not required at the seventh position of the IQ motif to accommodate MLC binding (Bosch et al, 2007).

In fact, the same group (Bosch et al, 2007) showed through mutagenesis and structural studies that mutation of G812K in *PfMyoA* promotes a compact conformation of the complex. In the *TgMyoD* model, R812 occupies the seventh position of the IQ motif forming a tight network of hydrogen bonds with residues in the C-Domain (Figure 3.3.5A). The tighter interactions with the C-Domain may contribute to the compactness of the interface. The predicted accessible surface area in the interface of the MyoD–MLC2 complex corresponds to 884 Å², compared to 1108 Å² for the homology-modeled *TgMLC1–MyoA* complex and 958 Å² for the *PfMTIP–MyoA* complex (Bosch et al, 2007).

Residues F305, F306, F309 and F342 from the C-Domain of MLC2 form a hydrophobic cluster that interacts with residues A803, I806, C807, A808 and V810 in the MyoD-tail helix (Figure 3.3.5B). The presence of C807, which replaces the conserved glutamine in the MyoD IQ motif, favors the interaction with the hydrophobic cluster in the C-Domain of MLC2.

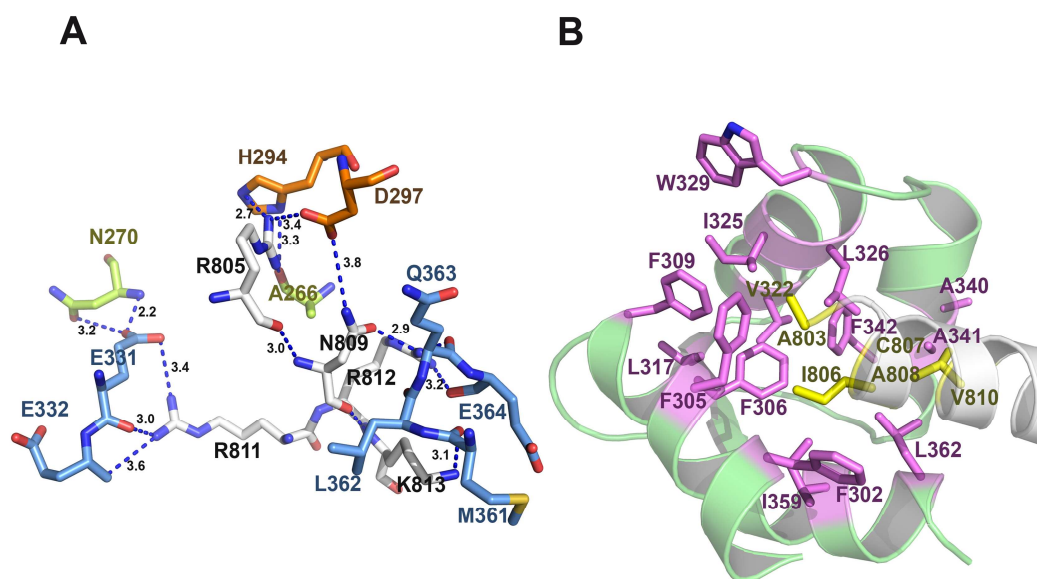
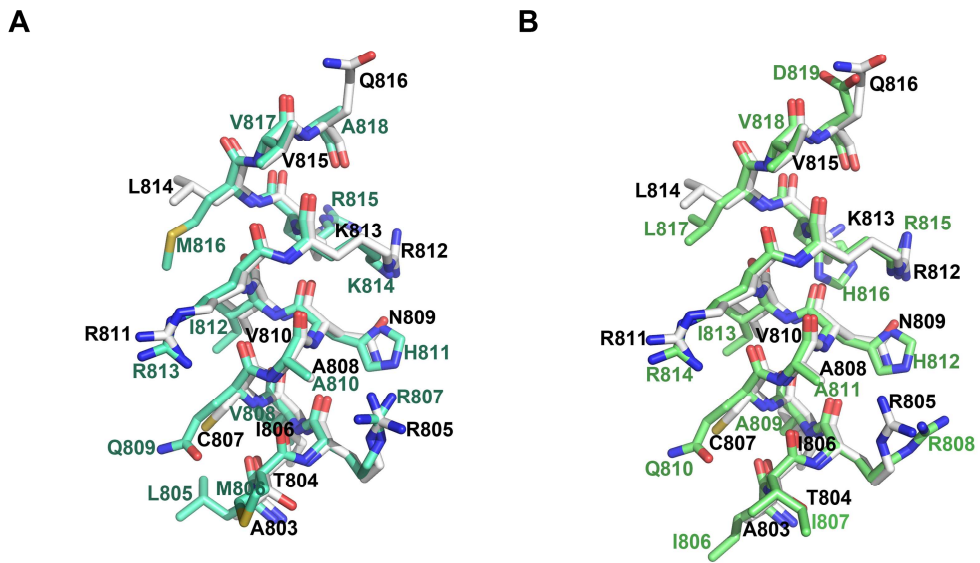


Figure 3.3.5: Interaction network of *Tg*MLC2-MyoD. (A) Hydrophilic network around the MyoD-tail shown as stick representation in white. The contacting residues of *Tg*MLC2 are colored according to their location: C-Domain residues are colored in blue, hinge region residues in orange and N-Domain residues in green. Distances are shown in Å. (B) Illustration of hydrophobic interactions between the N-terminal extremity of MyoD-tail and C-Domain of *Tg*MLC2. Non-polar residues of the C-Domain of *Tg*MLC2 are shown as stick representation in violet, and MyoD-tail buried non-polar residues are shown as sticks in yellow.

Glutamine, being a polar residue, cannot be accommodated in this position. N809 of MyoD-tail is one of the key residues in the interface with MLC2. Mostly, histidine residues are preferred in this position and H811 as well as H812 are the corresponding residues in *Tg*MyoA and *Pf*MyoA. The *Pf*MyoA and *Tg*MyoA tail regions differ in MyoD positions 804 and 807 that are involved in the interactions with MLC2 (Figure 3.3.6A). Conserved basic residues R811 and R812 in the MyoD-tail helix are involved in a tight network of polar interactions with MLC2 residues E331, E332, M361 and L362, E364. R805 forms hydrogen bonds with H294 and D297 in the MLC2 hinge region (Figure 3.3.6). Thus, most residues in the MLC2 C-Domain are predicted to be involved in direct interaction with the MyoD-tail.



3.4 Structural and Kinetic Characterization of Human Nonmuscle Myosin-2A and its Switch-2 Mutant

The most important structural elements that enable the allosteric coupling between the myosin motor domain and F-actin include the P-loop, switch-1 and switch-2 (Nagy et al, 2010). These switch motifs form part of the nucleotide binding site (Geeves et al, 2005). Structurally, switch-1 and switch-2 contact the nucleotide at the rear of the nucleotide binding-site and act as γ -phosphate sensors (Geeves et al, 2005; Reubold et al, 2003). In the ATP-bound state, the switch elements move towards each other. In the ADP-bound state, they move apart from each other (Geeves et al, 2005; Reubold et al, 2003). This mechanism is the base for the enzymatic mechanism of ATP hydrolysis and the production of mechanical work (Nagy et al, 2010).

3.4.1 Switch-2 Motif in Different Myosin Isoforms

Class-2 myosins have either Serine or Alanine in the 3rd position of the switch-2 loop whereas most unconventional myosins (class-1, class-5 and class-7 myosins) either have Phenylalanine or Tyrosine in this position (Figure 3.4.1).



Figure 3.4.1: Sequence alignment of the switch-2 loop (DIXGFE) region of different myosin classes from different species.

In the present work, the question why class-2 myosins do have different residue at the 3rd position of the switch-2 loop was addressed. To answer this question,

nonmuscle myosin 2A (NM2A) was chosen as a model system to analyze the effect of the mutation A454S in the consensus sequence DIXFGE of the switch-2 loop. The aim was to study the influence of the point mutation on the chemomechanical coupling and the actomyosin ATPase cycle. To accomplish this, the complete kinetic characterization of human nonmuscle myosin-2A and nonmuscle myosin-2A-A454S was performed. Further, *in silico* modeling techniques were used to build a structural model of the myosin motor domains. Throughout the work, the native myosin will be referred to as wild type (Wt) and nonmuscle myosin-2A-A454S will be referred to as A454S. NM2A constructs comprising amino acids 1-775 of human NM2A motor domain and in the case of A454S additionally the switch-2 mutation A454S, each fused to an artificial lever arm were produced in the baculovirus/Sf9 system and purified to homogeneity as described in section 2.2.3.6. The artificial lever arm comprises two spectrin-like repeats from *Dictyostelium discoideum* and functionally replaces the native light chain binding region (Anson et al, 1996a; Kliche et al, 2001). The advantage of the fusion-constructs is the production of single headed, constitutively active myosin motor domain constructs. It was previously shown that the fusion of the artificial lever arm to the myosin motor domain does not alter the native kinetic and functional properties of myosin motor domains of different classes of various species (Durrwang et al, 2006; Heissler & Manstein, 2011; Liao et al, 2009; Taft et al, 2008).

The steady-state and transient kinetic parameters of the ATPase cycle of both constructs were studied using stopped-flow and spectroscopic methods. The transient kinetic analysis of the individual rate and equilibrium constants of relevant steps of the ATPase cycle enables a detailed description of the enzymology and mechanic function of the myosin motor domain. The observation that the ADP interaction of NM2A is regulated by the concentration of free magnesium ions and that the mutation A454S in the switch-2 region is modulator of the ADP kinetics shows a new aspect of the chemomechanical coupling of the myosin motor domain.

3.4.2 *In silico* modeling of *Hs* NM2A and its switch mutant A454S

To gain the structural details of the nucleotide-binding pocket, a homology model of NM2A motor domain the pre-power stroke state was built (Figure 3.4.2). As the nucleotide-binding pocket is highly conserved in myosins, the x-ray structure of *Hs* nonmuscle muscle myosin-2C (PDB-code 2YCU) was used as a template. ADP.VO₄ was superimposed exactly onto the nucleotide analogue structure in the model for clarity and analysis purpose. To generate a model of A454S, *in silico* mutagenesis of Alanine 454 to Serine (A454S) was performed and the resulting structure was energy-minimized by using Gromacs (Van Der Spoel et al, 2005).

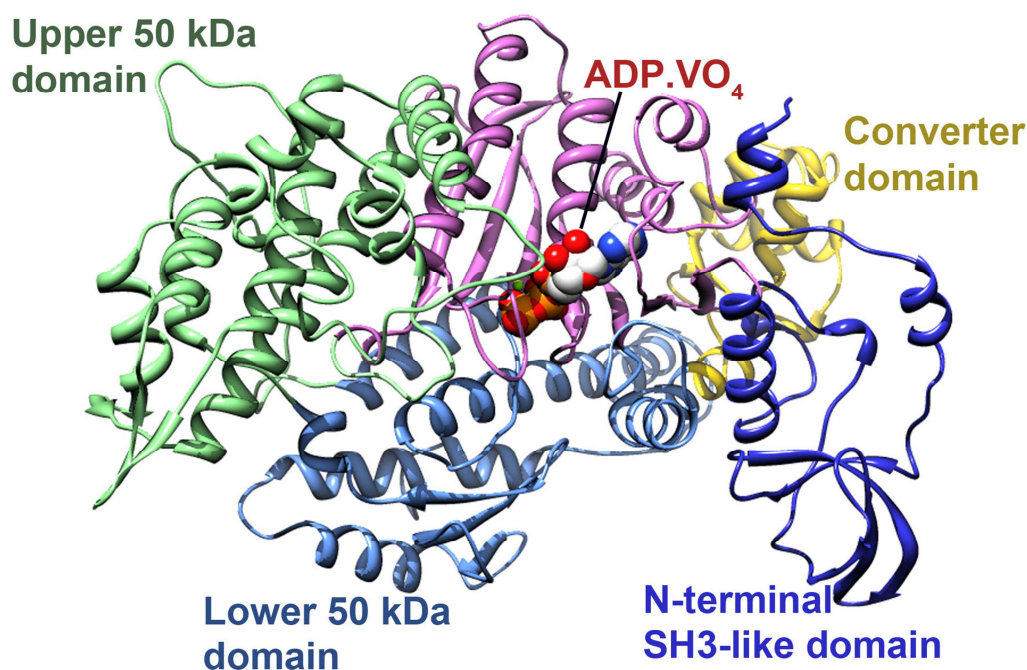


Figure 3.4.2: Overall view of the *Hs* NM2A motor domain structure. This model was built by using the crystal structure of *Hs* NM2C motor domain (PDB-code: 2YCU) as a template.

The structural model of *NM2A* motor domain revealed that the bound nucleotide is surrounded by three loops whose sequences are highly conserved among the myosin family: the P-loop (residues 173-179), switch-1 loop (229-234) and switch-2 loop (452-458). The consensus sequence (DIXGFE) of the switch-2 loop exhibits an Alanine at the 3rd (central) position. Examination of the *in silico*

mutation *A454S* revealed that Ser454 in the switch-2 loop forms an ideal hydrogen bond with the back bone atoms of the residues S233 and F235 in the switch-1 loop. Further, S233 coordinates to the magnesium ion. The Wt structure revealed that A454 is not interacting with any switch-1 residue. Since alanine lacks a polar side chain capable to form a hydrogen bond, no direct interaction via A454 is possible (Figure 3.4.3).

This observation can be hypothesized in the following way.

- (1) No hydrogen bonding interaction with switch-1 is possible when Ala454 is present in the central position of switch-2. This can lead to faster release of magnesium during the hydrolysis reaction in the wild type, as the S233 is only coordinated to the magnesium ion but not to A454.

- (2) In the case of *A454S*, Ser454 interaction to switch-1 may lead to a slower release of the magnesium ion because of the additional bond energies on the Ser233.

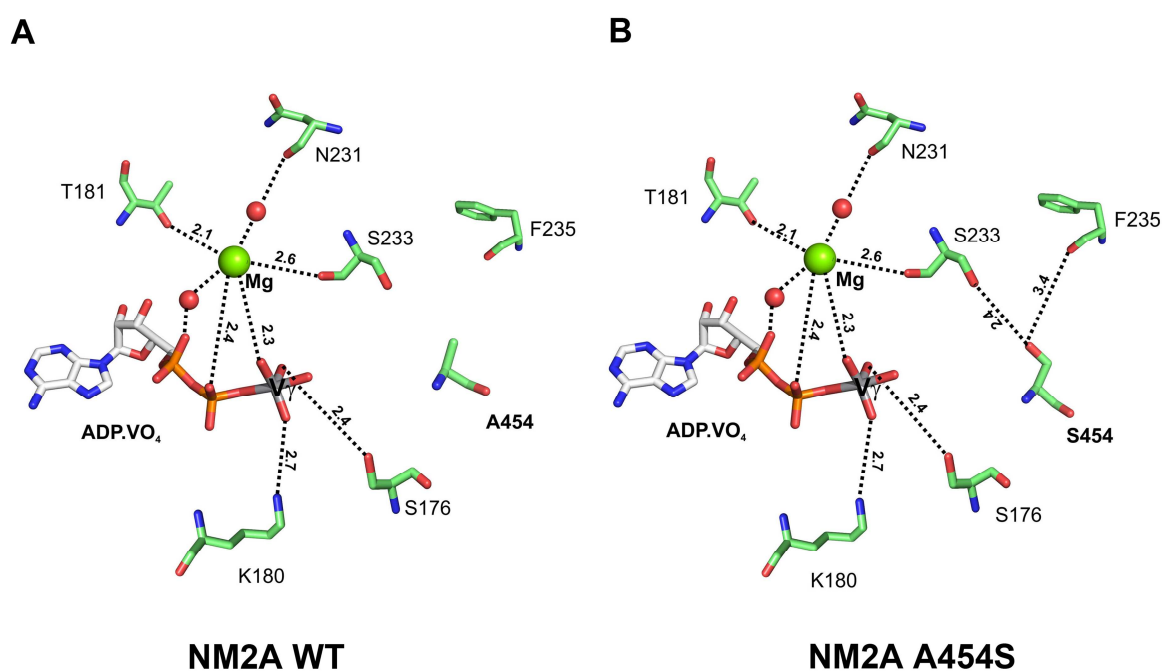


Figure 3.4.3: Close-up view of the nucleotide binding pocket of *Hs* NM2A Wt and A454S. Red spheres shown are the predicted waters from *Hs* NM2C structure (PDB: 2YCU). The predicted distances in the network between N231, water and Magnesium (Mg) as well as the predicted distance between oxygen from P_α, water and Mg are not shown. These water positions are at the equivalent positions of waters in *Hs* NM2C motor domain and also other myosin 2 isoform motor domain pre-power stroke state structures. The predicted distances are shown in Å.

3.4.3 Expression and Purification

The expression and purification of Wt and A454S were performed as described in section 2.2.3.6. Typically, recombinant protein was prepared to homogeneity from 5-10 L *Sf9* insect cells by Ni²⁺-chelate affinity chromatography and subsequent gel filtration. A representative SDS-PAGE analysis and gel filtration elution profile are shown in Figure 3.4.4.

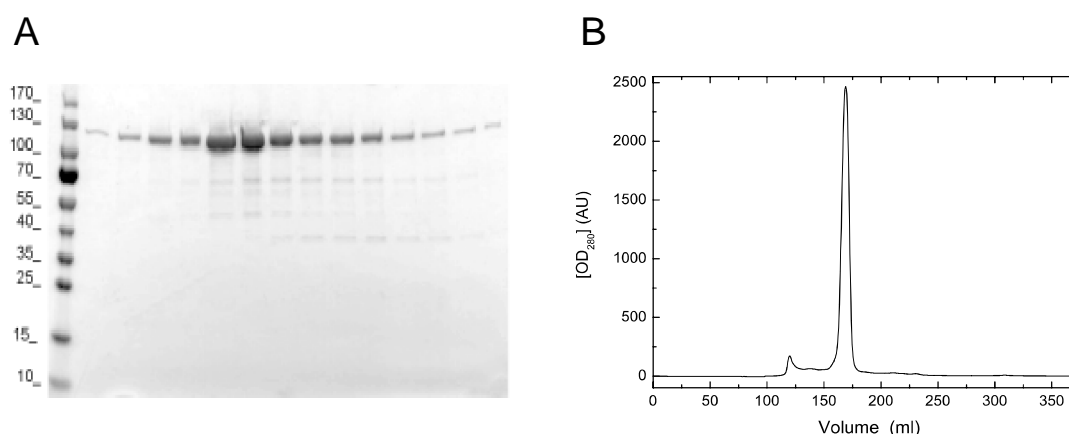


Figure 3.4.4: Purification of NM2A Wt and A454S. (A) SDS-PAGE analysis of fractions obtained through gel filtration step of NM2A Wt. The first lane shows the standard protein size marker. (B) Gel filtration elution profile of A454S. The protein elutes as a single peak with an elution volume between 155 and 180 ml. Fractions of the main peak were pooled and used for the kinetic characterization.

3.4.4 Kinetic Measurements

The kinetic measurements were interpreted in terms of the basic kinetic scheme depicted in Figure 3.4.5. The upper line of the scheme represents the pathway with the steps ATP binding, ATP hydrolysis and product release in the absence of F-actin. The lower line represents the same steps in the presence of F-actin. The asterisk (*) symbol represents changes in fluorescence intensity.

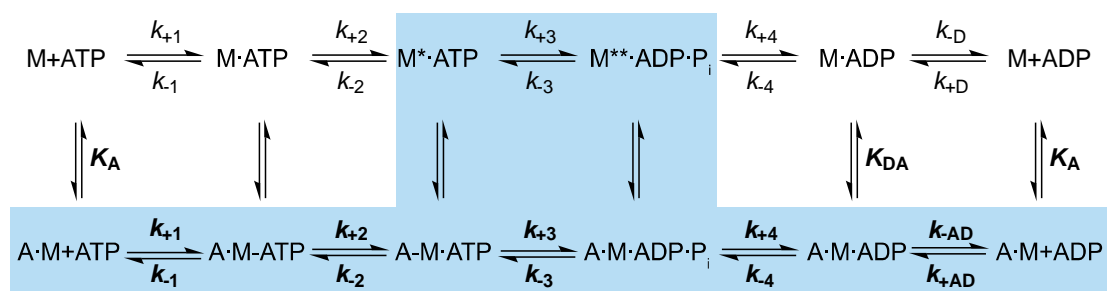


Figure 3.4.5: Basic kinetic mechanism of the actomyosin ATPase. The abbreviations used are as follows: A=F-actin, M=myosin, P_i=inorganic phosphate. The predominant flux of the reaction pathway is highlighted in blue. Rate constants are referred to as k_{+n} and k_{-n} , respectively. Dissociation equilibrium constants are denoted as K_n . Bold notation (\mathbf{K}_n , \mathbf{k}_{+n}) represents the kinetic constants in the presence of F-actin. Subscript A and D refer to actin and ADP, respectively. \mathbf{K}_A represents the affinity of myosin for F-actin, \mathbf{K}_D the affinity of ADP for myosin, \mathbf{K}_{AD} the affinity of ADP for the actomyosin complex, and \mathbf{K}_{DA} the affinity of actin for myosin in the presence of saturating concentrations of ADP according to Heissler and Manstein (Heissler & Manstein, 2011).

3.4.4.1 Active-site Titration

The exact number of active sites of the produced myosin motor domain constructs was analyzed prior to the kinetic characterization. To assay the number of active myosin motor domains, 0.5 μM myosin was mixed with increasing amounts of mantATP (0.005-0.35 μM) in a stopped-flow spectrophotometer. The obtained transients follow a double-exponential behavior. As depicted in Figure 3.4.6, the dependence of relative amplitude increased with increasing nucleotide concentration and reached a plateau. Linear fit of both, the initial slope and the plateau phase results in a point of intersection that corresponds to the amount of active sites in the preparations. Under the experimental conditions, points of intersection at 0.091 μM mantATP and 0.113 μM mantATP were determined for Wt and A454S, corresponding to 36.5% and 45% active myosin motor domains, respectively.

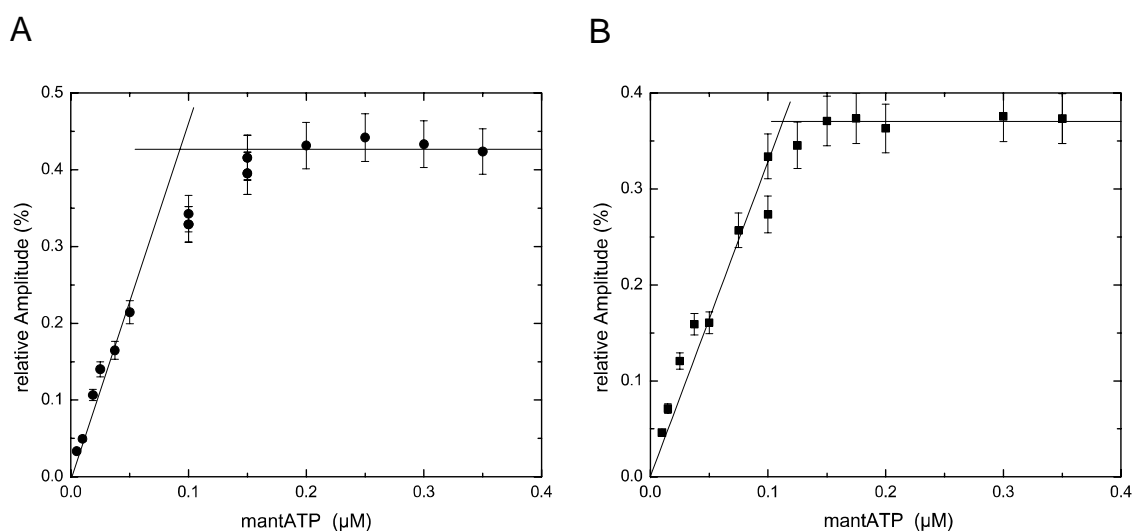


Figure 3.4.6: Active-site titration of Wt (A) and A454S (B). The dependence of the observed relative amplitude was plotted as function of [mantATP]. Linear fit to the initial slope and plateau-phase defines a point of intersection that corresponds to the active myosin concentration of the protein preparation. Active concentrations of 36.5% and 45% were determined for Wt and A454S, respectively.

3.4.4.2 Steady-State ATPase Activity

The steady-state ATPase activity of Wt and A454S was assayed with the NADH-coupled assay in the presence of an ATP regeneration system. The active myosin concentration for both, mutant and Wt was kept at 0.73 μM and 0.9 μM .

In the absence of F-actin, a basal ATPase activity of $k_{\text{basal}}=0.013\pm 0.001 \text{ s}^{-1}$ and $k_{\text{basal}}=0.004\pm 0.002 \text{ s}^{-1}$ was determined for Wt and A454S, respectively. As depicted in Figure 3.4.7, the ATPase activity of Wt and A454S was activated 10-fold by F-actin. Especially for the mutant, it was very difficult to quantify the ATPase activity in precision, but estimated from fitting the data sets to a hyperbolic equation suggest a v_{max} of $0.11\pm 0.01 \text{ s}^{-1}$ and $0.04\pm 0.004 \text{ s}^{-1}$ for Wt and A454S at a F-actin concentration of 140 μM with K_{app} values $>140 \mu\text{M}$ for both proteins. Wt and A454S show comparable basal ATPase activities ($k_{\text{basal}}=0.013 \text{ s}^{-1}$ and 0.007 s^{-1}) and maximal ATPase activities ($v_{\text{max}}=0.17\pm 0.005 \text{ s}^{-1}$ and $0.13\pm 0.01 \text{ s}^{-1}$) as human nonmuscle myosins-2A and -2B S1-like constructs characterized in previous studies (Kovacs et al, 2003; Wang et al, 2003). It is of note that K_{app} parameters determined in the present study are 2 fold higher than those obtained by Kovacs and coworkers (Kovacs et al, 2003) for human NM2A S1-construct. This difference might be attributed to different buffer conditions and a different assay temperature. Low v_{max} and high K_{app} parameters indicate a very weak coupling between the nucleotide binding site and the actin binding region of both, Wt and A454S, and was already described for human nonmuscle myosin-2C isoforms (Heissler & Manstein, 2011). The parameters of the steady-state ATPase measurements are listed together with published data from a previous study in Table 24.

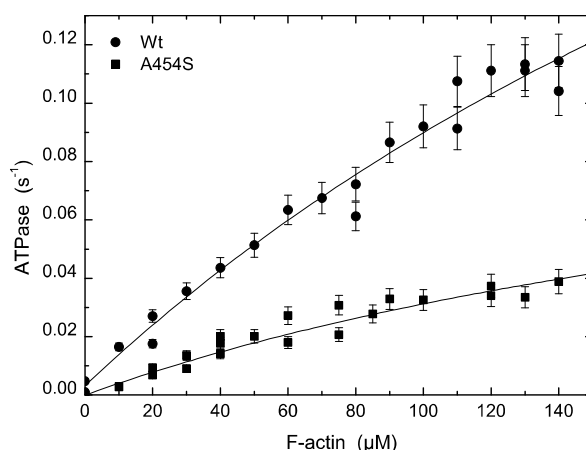


Figure 3.4.7: Actin-activated steady-state ATPase activity of Wt and A454S. The plot shows the F-actin-dependence of the steady-state ATPase activity. Hyperbolic fit of the data sets gives the parameter v_{\max} of $0.11 \pm 0.01 \text{ s}^{-1}$ and $0.04 \pm 0.004 \text{ s}^{-1}$ for Wt and A454S at a concentration of $140 \text{ } \mu\text{M}$ F-actin. It is of note that the parameter K_{app} is $>140 \text{ } \mu\text{M}$. Therefore, the given values need to be treated with some caution. The basal ATPase activity was subtracted from the data in the presence of F-actin.

Table 24: Kinetic parameters of the basal and actin-activated steady-state ATPase activity.

Parameter	Signal or calculation	NM2A-Wt	NM2A-A454S	NM2A (Kovacs et al, 2003)
$k_{\text{basal}} [\text{s}^{-1}]$	NADH Assay	0.013 ± 0.001	0.004 ± 0.002	0.013 ± 0.004^2
$v_{\max} [\text{s}^{-1}]$	NADH Assay ¹	0.11 ± 0.01	0.04 ± 0.004	0.17 ± 0.005^2
$K_{\text{app}} [\mu\text{M}]$	NADH Assay	>140	>140	72.4 ± 4^2
$v_{\max}/K_{\text{app}} [\mu\text{M}^{-1}\text{s}^{-1}]$	$v_{\max}/K_{\text{app}}^3$	~ 0.0008	~ 0.0003	~ 0.002

¹ at $140 \text{ } \mu\text{M}$ F-actin, the highest F-actin concentration experimentally accessible

² Experimental conditions: 25°C , 2 mM MgCl_2 , 1 mM ATP (Kovacs et al, 2003)

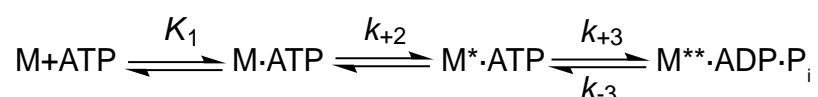
³ At $140 \text{ } \mu\text{M}$ F-actin

In comparison with the steady-state ATPase activity of other class-2 nonmuscle myosins determined in previous studies, a common feature of all myosin motors is a very slow ATPase activity ($0.13\text{-}0.23 \text{ s}^{-1}$) (Heissler & Manstein, 2011; Kovacs et al, 2003; Wang et al, 2003). The behavior is in striking contrast to other class-2

myosins such as skeletal, smooth muscle, and cardiac myosin ($0.7\text{-}29\text{ s}^{-1}$) (Marston & Taylor, 1980; Wagner, 1981). The point mutation A454S in human nonmuscle myosin-2A results in a 3-fold reduced steady-state turnover when compared to the kinetic parameter obtained for Wt at a F-actin concentration of $140\text{ }\mu\text{M}$. This behavior indicates that the mutant comprises the intact capability to bind and hydrolyze ATP, even though either the rates of nucleotide binding, hydrolysis or product release are reduced (Nagy et al, 2010). Interestingly, a point mutation Y439A present at the equivalent position in switch-2 of murine myosin-5a had shown a ~ 8 -fold reduction in v_{max} (Nagy et al, 2010).

3.4.4.3 Interaction between Myosin and ATP

ATP binding to Wt and A454S was monitored the fluorescence enhancement upon ATP binding to myosin according to the following scheme.



The intrinsic tryptophan fluorescence was excited at a wavelength of 297 nm and the emission was detected through a WG320 cut-off filter. The fluorescence signals were biphasic with the observed rate constant depending hyperbolically on the nucleotide concentration (Figure 3.4.8B). A hyperbolic fit of the data sets defines the parameter $1/K_1$ to $78.09 \pm 10.08\text{ }\mu\text{M}$ for Wt and $167.04 \pm 17.72\text{ }\mu\text{M}$ for A454S. The plateau phase describes the rate of ATP hydrolysis ($k_{+3} + k_{-3}$) to $44.85 \pm 1.36\text{ s}^{-1}$ and $174.88 \pm 5.27\text{ s}^{-1}$ for Wt and A454S. Up to a concentration of $50\text{ }\mu\text{M}$ ATP, the observed rate constants depend linearly on $[\text{ATP}]$ (data not shown) defining the second order rate constant for ATP binding, $K_1 k_{+2}$ to $0.39 \pm 0.01\text{ }\mu\text{M}^{-1}\text{s}^{-1}$ and $0.77 \pm 0.03\text{ }\mu\text{M}^{-1}\text{s}^{-1}$ for Wt and mutant, respectively.

By using the fluorescent mant analogue mantATP as a substrate, a $K_1 k_{+2}$ of $0.86 \pm 0.02\text{ }\mu\text{M}^{-1}\text{s}^{-1}$ and $1.00 \pm 0.02\text{ }\mu\text{M}^{-1}\text{s}^{-1}$ for Wt and mutant was obtained when fitting the dependence of the observed rate constants against the mantATP concentration with a linear function (Figure 3.4.8A).

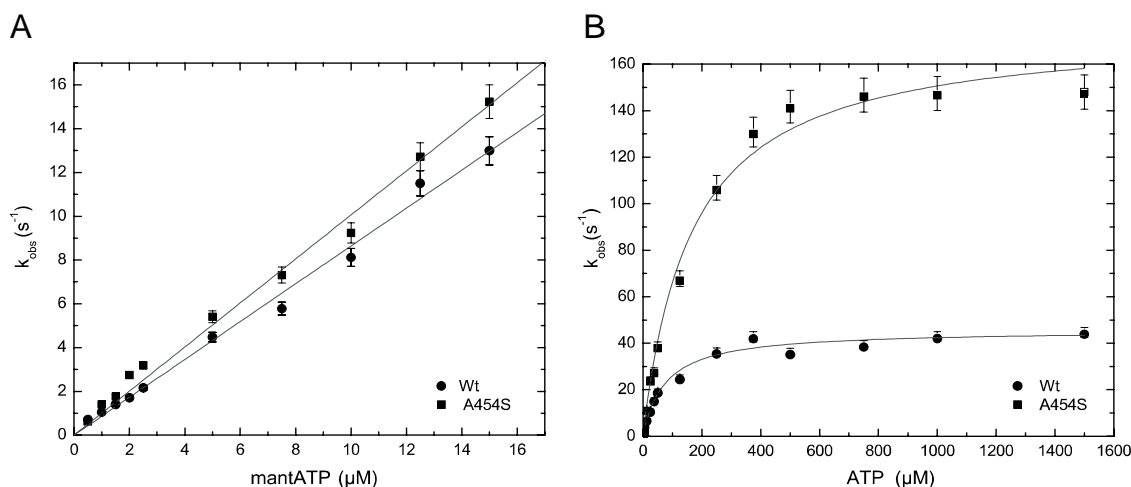


Figure 3.4.8: ATP binding to Wt and A454S. (A) Dependence of the observed rate constants upon mixing myosin with increasing concentrations of mantATP. Linear fit to the data set defines the apparent second-order rate constant K_1k_{+2} of $0.86\pm 0.02 \mu\text{M}^{-1}\text{s}^{-1}$ and $1.00\pm 0.02 \mu\text{M}^{-1}\text{s}^{-1}$ for Wt and A454S, respectively. (B) ATP-dependence of the observed rate constants (k_{obs}) of the transient fluorescence increase upon mixing myosin with ATP. Hyperbolic fits to the individual data sets define the rate of ATP hydrolysis ($k_{+3}+k_{-3}$) to $44.85\pm 1.36 \text{ s}^{-1}$ and $174.88\pm 5.27 \text{ s}^{-1}$ for Wt and A454S. The second-order binding rate constant K_1k_{+2} was determined to $0.39\pm 0.01 \mu\text{M}^{-1}\text{s}^{-1}$ and $0.77\pm 0.03 \mu\text{M}^{-1}\text{s}^{-1}$ for Wt and mutant from the initial slope. Half saturation ($1/K_1$) was reached at $78.09\pm 10.08 \mu\text{M}$ ATP for Wt and $167.04\pm 17.72 \mu\text{M}$ ATP for A454S.

The kinetic parameters describing the interaction between myosin and ATP are summarized in Table 25.

3.4.4.4 Interaction between Actomyosin and ATP

The interaction between the rigor complex and ATP was modeled as a two-step binding reaction according to the following scheme.



Rapid mixing of pyrene-actomyosin with increasing ATP concentrations in a stopped-flow apparatus resulted in a time-dependent fluorescence increase. The obtained transients were fitted with an exponential function. As depicted in Figure 3.4.9A, the secondary plot of the observed rate constants (k_{obs}) versus the ATP concentration follows a hyperbolic behavior. Fitting of the data sets gives the maximum isomerization rate constants k_{+2} of $204.63\pm 16.02 \text{ s}^{-1}$ and $160.41\pm 15.30 \text{ s}^{-1}$ for Wt and A454S at saturating ATP. Half saturation, corresponding to $1/K_1$,

was reached at ATP concentrations of $643.68 \pm 126.95 \mu\text{M}$ and $502.76 \pm 112.09 \mu\text{M}$ for Wt and A454S, respectively. Linear fits of the initial slopes define the second order rate binding constants K_1k_{+2} of $0.26 \pm 0.04 \mu\text{M}^{-1}\text{s}^{-1}$ and $0.24 \pm 0.04 \mu\text{M}^{-1}\text{s}^{-1}$ for Wt and A454S (Figure 3.4.9A).

Additionally, the increase in fluorescence upon mixing $0.3 \mu\text{M}$ actomyosin with increasing concentrations of mantATP results in an exponential fluorescence increase. As depicted in Figure 3.4.9B, the dependence of the observed rate constants (k_{obs}) on the mantATP concentration is linear in the assayed concentration range up to $15 \mu\text{M}$ mantATP. Linear fits to the data sets give the second order rate constants for ATP binding to the actomyosin complex K_1k_{+2} of $0.11 \pm 0.01 \mu\text{M}^{-1}\text{s}^{-1}$ and $0.27 \pm 0.02 \mu\text{M}^{-1}\text{s}^{-1}$ for Wt and A454S, respectively.

The kinetic parameters describing the interaction between the actomyosin and ATP are summarized in Table 25.

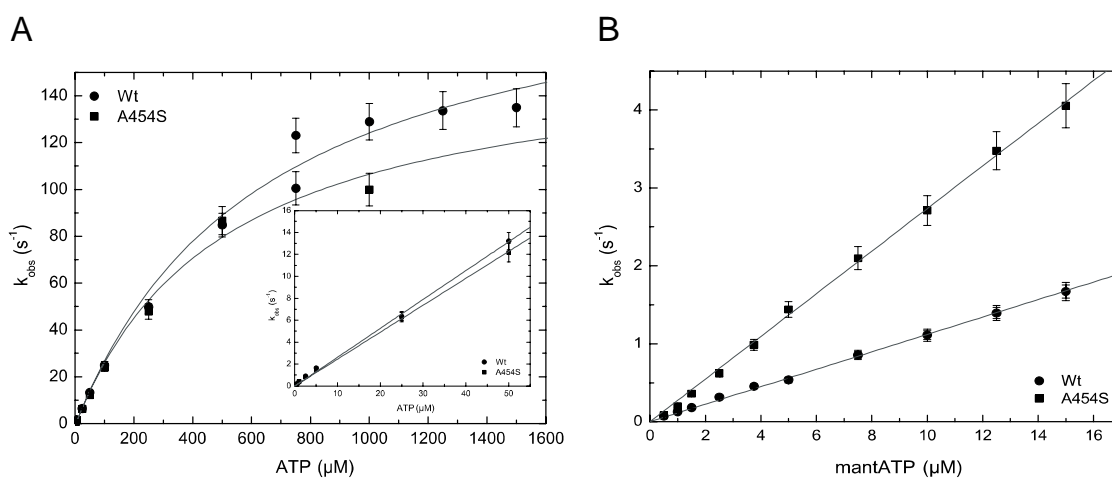


Figure 3.4.9: Interaction of actomyosin with ATP. ATP-concentration dependence of the observed rate constants upon mixing pyrene-labeled actomyosin with increasing concentrations of ATP. Hyperbolic fits to the data sets define the parameters k_{+2} at the plateau phase as well as K_1k_{+2} from the initial slope (*inset*). The values $1/K_1$ indicate half-saturating ATP concentrations, are listed in Table 25. (B) Dependence of the observed rate constants upon mantATP binding to actomyosin on the nucleotide concentration. Linear fit of the data sets define the second-order binding rate constant K_1k_{+2} to $0.11 \pm 0.01 \mu\text{M}^{-1}\text{s}^{-1}$ and $0.27 \pm 0.02 \mu\text{M}^{-1}\text{s}^{-1}$ for Wt and A454S, respectively.

Table 25: Kinetic parameters of the interaction of myosin and actomyosin with ATP.

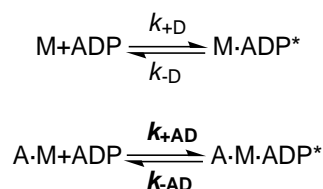
Parameter	Signal	NM2A-Wt	NM2A-A454S	NM2A (Kovacs et al, 2003)
K_1k_{+2} [$\mu\text{M}^{-1}\text{s}^{-1}$]	Tryptophan	0.39±0.01	0.77±0.03	0.56±0.01
K_1k_{+2} [$\mu\text{M}^{-1}\text{s}^{-1}$]	mantATP	0.86±0.02	1.00±0.02	1.03±0.14
$1/K_1$ [μM]	Tryptophan	78.09±10.08	167.04±17.72	n.d.
$k_{+3}+k_{-3}$ [s^{-1}]	Tryptophan	44.85±1.36	174.88±5.27	14.1±0.5
K_1k_{+2} [$\mu\text{M}^{-1}\text{s}^{-1}$]	Pyrene-actin	0.26±0.04	0.24±0.04	0.21±0.04
K_1k_{+2} [$\mu\text{M}^{-1}\text{s}^{-1}$]	mantATP	0.11±0.01	0.27±0.02	0.14±0.003
$1/K_1$ [μM]	Pyrene-actin	643.68±126.9	502.76±112.09	≈900
		5		
k_{+2} [s^{-1}]	Pyrene-actin	204.63±16.02	160.41±15.30	≈190

The interactions between myosin and actomyosin with ATP do not reveal major impact of the A454S mutation on NM2A ATP-binding kinetics. The A454S mutant exhibits slightly accelerated ATP binding properties as the Wt. In the absence of F-actin, the rate constant of the ATP hydrolysis step ($k_{+3}+k_{-3}$) is 4-fold faster in A454S when compared to the Wt. Additionally, the association rate constant $1/K_1$ is 2 fold reduced in A454S in comparison to Wt.

The comparison of the determined rate and dissociation equilibrium constants of the interaction between actomyosin and ATP indicate, that the point mutation A454S does not markedly change the actomyosin-substrate interaction.

3.4.4.5 Interaction of Myosin and ADP

The fluorescence enhancement of mantATP upon binding to myosin and actomyosin is analyzed in terms of the following scheme, in which the asterisk (*) represents the high fluorescent state of mantADP.



The fluorescent ADP analogue mantADP was used to characterize the interaction of ADP and myosin. MantADP binding to myosin was performed under pseudo-first order conditions. The time courses of the fluorescence

enhancement upon mantADP binding to Wt and A454S were fitted double-exponentially. As depicted in the k_{obs} versus mantADP plot (Figure 3.4.10A), the rate of the fast phase of Wt depends linearly on the nucleotide concentration up to 7.5 μM (Figure 3.4.10A). Linear approximation of the data set defines the second-order rate constant k_{+D} to $4.39 \pm 0.28 \mu\text{M}^{-1}\text{s}^{-1}$ and the rate constant of ADP release k_{-D} to $0.68 \pm 1.06 \text{ s}^{-1}$ from the slope and intercept of the linear fit. As shown in Figure 3.4.10A for A454S, the observed rate constants show a hyperbolic dependence on [mantADP]. Extrapolating the fit to zero [mantADP] suggests a rate constant for ADP release k_{-D} of $0.77 \pm 0.05 \text{ s}^{-1}$. Linear fit of the initial slope (with a fixed k_{-D} of $0.77 \pm 0.05 \text{ s}^{-1}$) of the data set indicates a second order binding rate constant k_{+D} of $2.71 \pm 0.04 \mu\text{M}^{-1}\text{s}^{-1}$.

The ADP dissociation from myosin was assayed by chasing the myosin•mantADP complex with excess ATP. The fluorescence of the mant-moiety was excited at a wavelength of 365 nm and the time courses of the fluorescence decay were monitored after passage through a KV389 cut-off filter. As shown in Figure 3.4.10B, the transients follow a single-exponential function plus lag-phase for Wt and A454S. Dissociation rate constants k_{-D} of $0.38 \pm 0.01 \text{ s}^{-1}$ and $0.54 \pm 0.02 \text{ s}^{-1}$ were determined for Wt and A454S, respectively.

Furthermore, the ADP release kinetic from Wt and A454S was determined in an independent experiment, in which the myosin•ADP complex was chased with excess ATP. The change in intrinsic protein fluorescence was excited at 297 nm and the time dependent fluorescence increase was monitored through a WG320 filter. Exponential fits to the fluorescence transients define the rate constant of ADP release k_{-D} to $0.34 \pm 0.01 \text{ s}^{-1}$ and $0.47 \pm 0.03 \text{ s}^{-1}$ for Wt and A454S, respectively.

The results of the independent measurements of the ADP release kinetics from myosin are in good agreement with the parameters obtained from the binding titrations and listed in Table 26.

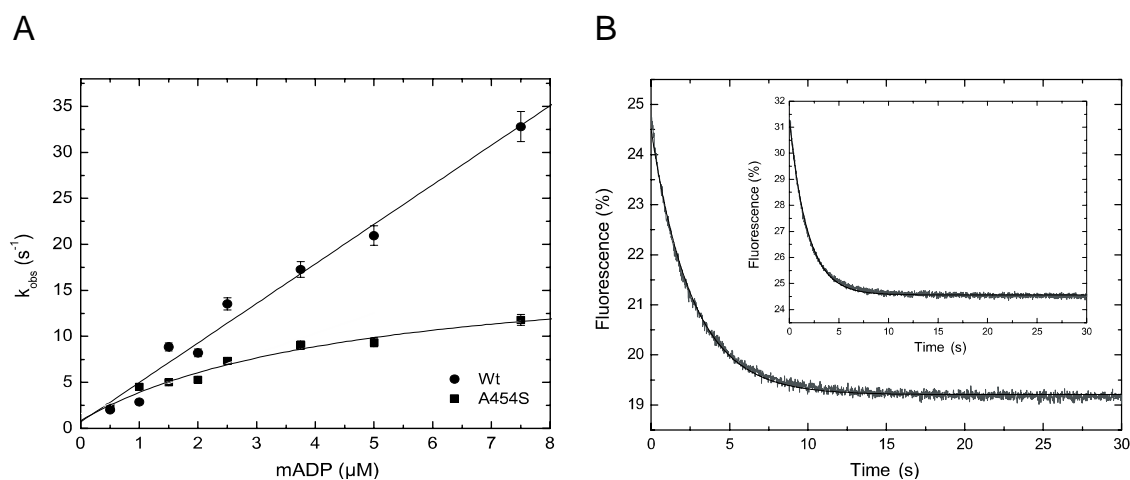


Figure 3.4.10: ADP binding and dissociation from myosin. (A) MantADP dependence of the observed rate constants upon myosin binding to Wt and A454S. In the concentration range examined, Wt shows a linear behavior, defining the second-order rate constant k_{+D} to $4.39 \pm 0.28 \mu\text{M}^{-1}\text{s}^{-1}$. For A454S, the observed rate constants depend hyperbolically on the mantADP concentration. Linear fit of the initial slope defines k_{+D} to $2.71 \pm 0.04 \mu\text{M}^{-1}\text{s}^{-1}$. From the ordinates of the fits, k_{-D} values of $0.68 \pm 1.06 \text{ s}^{-1}$ and k_{-D} of $0.77 \pm 0.05 \text{ s}^{-1}$ were determined for Wt and A454S, respectively. (B) ADP dissociation from myosin Wt and A454S (*inset*). The shown transients were obtained by caging $0.15 \mu\text{M}$ myosin and $1.5 \mu\text{M}$ mantADP with $500 \mu\text{M}$ ATP. The shown transient for Wt has an amplitude of -5.275 and a k_{obs} of 0.38 s^{-1} . The shown transient for the A454S mutant has an amplitude of -6.71% and a k_{obs} of 0.54 s^{-1} .

Calculation of the dissociation equilibrium constants of ADP binding to myosin K_D from the ratio k_{-D}/k_{+D} gives constants of $0.16 \pm 0.03 \mu\text{M}$ for Wt and $0.28 \pm 0.02 \mu\text{M}$ for A454S.

3.4.4.6 Interaction between Actomyosin and ADP

In the presence of F-actin, mantADP binding to the rigor complex was assayed by mixing actomyosin under pseudo-first order conditions with increasing amounts of mantADP in a stopped-flow spectrophotometer. The transients were fitted to double-exponentials. As depicted in Figure 3.4.11A, the observed rate constants depend linearly on the mantADP concentration in the concentration range examined. Fitting a straight line to the data set of Wt defines the second order rate constant for mantADP binding to the rigor complex k_{+AD} of $4.92 \pm 0.09 \mu\text{M}^{-1}\text{s}^{-1}$ and k_{-AD} of $1.69 \pm 0.25 \text{ s}^{-1}$ from the slope and the intercept, respectively. For A454S, the fit parameters $k_{+AD} = 5.52 \pm 0.11 \mu\text{M}^{-1}\text{s}^{-1}$ and k_{-AD} of $0.41 \pm 0.31 \text{ s}^{-1}$ were obtained.

The actin-activated ADP release from actomyosin was assayed by chasing the ternary actomyosin.mantADP complex with excess ATP. The obtained fluorescence transients were fitted to single exponentials defining the constants $k_{-AD} = 2.39 \pm 0.21 \text{ s}^{-1}$ and $k_{-AD} = 0.52 \pm 0.05 \text{ s}^{-1}$ for Wt and A454S, respectively. For instance, a transient of the reaction between A454S is shown in Figure 3.4.11B.

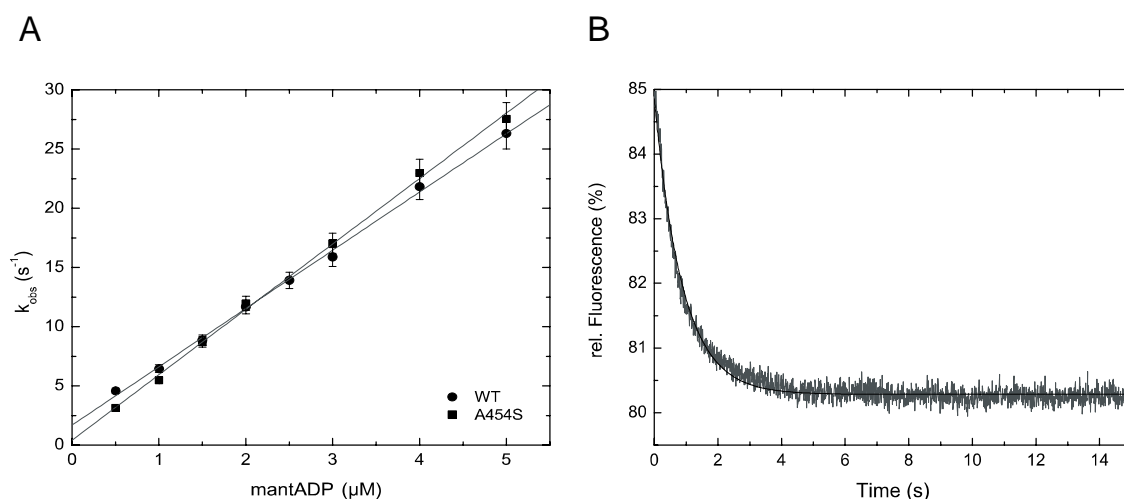


Figure 3.4.11: Interaction between actomyosin and ADP. (A) MantADP-dependence of the observed rate constants upon binding mantADP to Wt and A454S, respectively. Linear fit to the individual data sets define the second-order rate constants k_{+AD} of $4.92 \pm 0.09 \mu\text{M}^{-1}\text{s}^{-1}$ and $k_{+AD} = 5.52 \pm 0.11 \mu\text{M}^{-1}\text{s}^{-1}$ for Wt and A454S. The corresponding intercepts correspond to $k_{-AD} = 1.69 \pm 0.25 \text{ s}^{-1}$ and $k_{-AD} = 0.41 \pm 0.31 \text{ s}^{-1}$ for WT and A454S. (B): Transient of the reaction between $0.3 \mu\text{M}$ actomyosinA454S.mantADP with excess ATP at a total magnesium concentration of 0.175 mM . The FRET signal was excited at 297 nm and the fluorescence decrease was detected after passage through a KV389 filter. The shown transient was fitted to a single-exponential function and comprises amplitude of -4.56% and an observed rate constant of 1.13 s^{-1} .

Calculation of the dissociation equilibrium constant of ADP binding to the actomyosin complex K_{AD} from the ratio k_{-AD}/k_{+AD} gives constants of $0.34 \pm 0.06 \mu\text{M}$ for Wt and $0.07 \pm 0.06 \mu\text{M}$ for A454S. All kinetic parameters of the interaction between myosin and actomyosin with ADP are listed in Table 26.

3.4.4.7 Magnesium-sensitivity

To further investigate the interaction between actomyosin and ADP, the effect of the concentration of free Mg^{2+} ions on the ADP-release kinetics from actomyosin was characterized for Wt and A454S. As depicted in Figure 3.4.12, the ADP release from actomyosin declines with increasing concentrations of free Mg^{2+} . In case of Wt, increasing concentrations free Mg^{2+} in the concentration range

between 0.02 and 9.5 mM inhibits the actin-activated ADP release from $5.77 \pm 0.37 \text{ s}^{-1}$ to $2.07 \pm 0.19 \text{ s}^{-1}$. For A454S, increasing concentrations of free Mg^{2+} between 0.02 mM and 19.5 mM reduces the ADP release kinetics from actomyosin ~ 3.3 -fold from $1.30 \pm 0.12 \text{ s}^{-1}$ to $0.42 \pm 0.03 \text{ s}^{-1}$. The inhibitory constant lies at $0.45 \pm 0.09 \text{ mM}$ and $1.17 \pm 0.39 \text{ mM}$ free Mg^{2+} for Wt and A454S mutant, respectively. The point mutation A454S therefore drastically reduces the rate constant of ADP release without abolishing the magnesium-sensitive regulatory mechanism of NM2A.

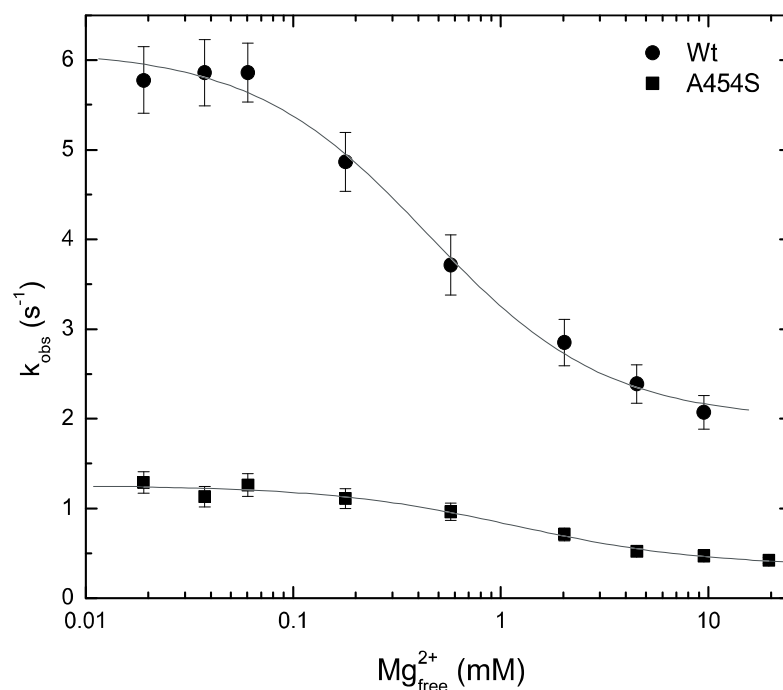


Figure 3.4.12: Magnesium-sensitivity. Increasing the free Mg^{2+} ion concentration reduces the actin-activated ADP release for Wt and A454S 2.8-3.3-fold. The inhibitory constant K_i lies with $0.45 \pm 0.09 \text{ mM}$ and $1.17 \pm 0.39 \text{ mM}$ free Mg^{2+} for Wt and A454S mutant in the concentration range of physiological free Mg^{2+} . This experiment was performed in collaboration with Dr. Sarah M. Heissler, BPC, MHH.

Table 26: Summarizes all kinetic constants of the interaction between actomyosin and myosin with ADP and free Mg²⁺.

Parameter	Signal or calculation	NM2A-Wt	NM2A-A454S	NM2A(Kovacs et al, 2003)
k_{+D} [$\mu\text{M}^{-1}\text{s}^{-1}$]	mantADP	4.29±0.28	2.71±0.04	0.55±0.06
k_{-D} [s^{-1}]	mantADP ¹	0.68±0.09	0.77±0.05	0.54±0.23
	mantADP ²	0.38±0.01	0.54±0.02	1.12±0.13
	Tryptophan ²	0.34±0.01	0.47±0.03	n.d.
K_D [μM]	k_{-D}/k_{+D}	0.16±0.03	0.28±0.02	1.5±0.4
k_{+AD} [$\mu\text{M}^{-1}\text{s}^{-1}$]	mantADP	4.92±0.09	5.52±0.11	2.72±0.16
k_{-AD} [s^{-1}]	mantADP ¹	1.69±0.25	0.41±0.31	1.72±0.38
	mantADP ²	2.39±0.21	0.52±0.05	2.68±0.30
K_i [Mg ²⁺] (mM)	mantADP ²	0.45±0.09	1.17±0.39	n.d.
K_{AD} [μM]	k_{-AD}/k_{+AD}	0.34±0.06	0.07±0.06	0.8±0.2

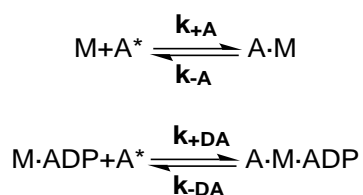
¹From the intercept of the k_{obs} versus [mantADP] plot

²From ATP chasing experiment

The comparison of Wt nonmuscle myosin-2A and A454S indicate that the ADP kinetics in the absence of F-actin are not markedly changed. However, in the presence of F-actin, ADP release from A454S is ~5-fold reduced when compared with Wt, whereas the binding rate constants are comparable. This behavior leads to a ~5-fold increased ADP-affinity of A454S when compared to Wt NM2A. A ~5-fold reduction in the actin-activated ADP release rates was also observed for murine Y439S myosin-5a, the corresponding switch-2 mutation in myosin-5a (Nagy et al, 2010).

3.4.4.8 Interaction of Myosin and Myosin.ADP with F-actin

The interaction between myosin and F-actin in the presence and absence of ADP was monitored from the fluorescence enhancement upon pyrene-actin binding to myosin according to the following scheme:



In the scheme, A* represents the high fluorescent state of pyrene-actin, and A the quenched state.

Experimentally, the pyrene fluorescence was excited at 365 nm and the time dependent change in fluorescence signal was monitored through a KV389 cut-off filter. The myosin:pyrene-actin concentrations were kept constant at a ratio of 1:5. Both, in the presence and absence of ADP (250 μM), the time courses follow double exponential functions. The slow phase presumably originates from photo-bleaching and was neglected in the further analysis. The dependence of the fast phase as a function of the pyrene-actin concentration is depicted in Figure 3.4.13. In the absence of ADP, linear fit of the data sets gives the second order rate constants for F-actin binding k_{+A} of $0.96 \pm 0.02 \mu\text{M}^{-1}\text{s}^{-1}$ and k_{+A} of $1.03 \pm 0.23 \mu\text{M}^{-1}\text{s}^{-1}$ for WT and A454S, respectively (Figure 3.4.13A). In the presence of saturating ADP, rates of $k_{+DA} = 0.19 \pm 0.004 \mu\text{M}^{-1}\text{s}^{-1}$ and $0.80 \pm 0.04 \mu\text{M}^{-1}\text{s}^{-1}$ were obtained for Wt and A454S (Figure 3.4.13B).

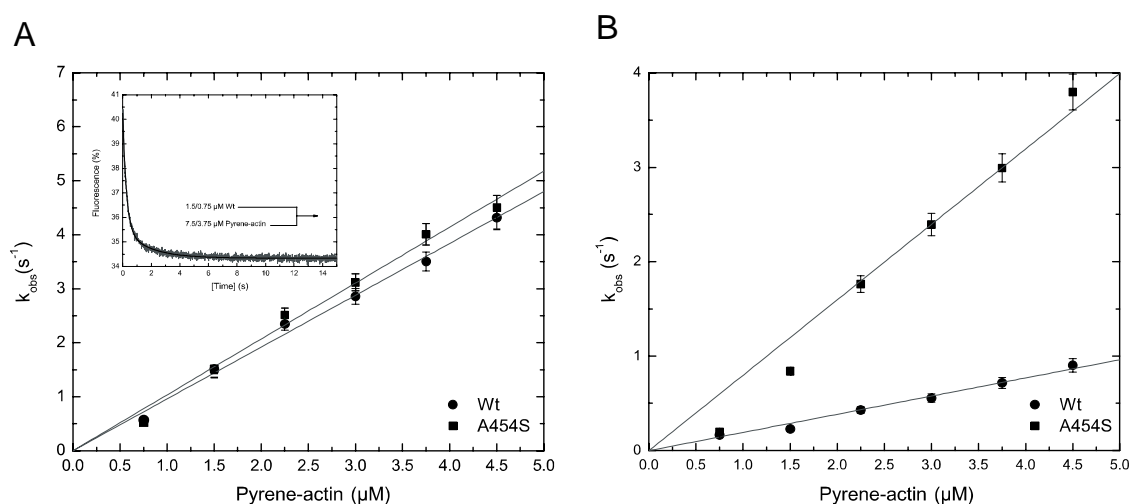


Figure 3.4.13: Interaction between myosin and myosin.ADP with F-actin. (A) F-actin dependence of the observed rate constants upon myosin binding to F-actin. Linear fit of the data sets for Wt and A454S define the second-order rate constants $k_{+A} = 0.96 \pm 0.02 \mu\text{M}^{-1}\text{s}^{-1}$ and $k_{+A} = 1.03 \pm 0.23 \mu\text{M}^{-1}\text{s}^{-1}$ for Wt and A454S, respectively. *Inset*, representative transient upon mixing 0.75 μM Wt and 3.75 μM F-actin in a stopped-flow spectrophotometer. (B) F-actin dependence of the observed rate constants upon myosin.ADP binding to F-actin. Linear fit of the data sets for Wt and A454S define the second-order rate constants $k_{+DA} = 0.19 \pm 0.004 \mu\text{M}^{-1}\text{s}^{-1}$ and $k_{+DA} = 0.80 \pm 0.04 \mu\text{M}^{-1}\text{s}^{-1}$ for Wt and A454S, respectively.

F-actin release from the rigor complex was studied by mixing 0.75 μM pyrene-labeled actomyosin with 20 μM F-actin in a stopped-flow apparatus. The time-dependent fluorescence increase was fitted to double-exponentials (Figure 3.4.14A). The rate constants of the fast phase reflects the rate constant of F-actin

release k_A to $\sim 0.00019 \text{ s}^{-1}$ and $\sim 0.00024 \text{ s}^{-1}$ for Wt and A454S. The slow phase was neglected in the following data analysis. The origin of the slow phase is presumable photobleaching and was further investigated in the present work. When performed the same assay in the presence of saturating ADP ($100 \mu\text{M}$), dissociation rate constants k_{DA} of $0.04 \pm 0.002 \text{ s}^{-1}$ and $0.07 \pm 0.004 \text{ s}^{-1}$ were determined from the single exponential fits to the fluorescence increase for Wt and A454S, as depicted in Figure 3.4.14B.

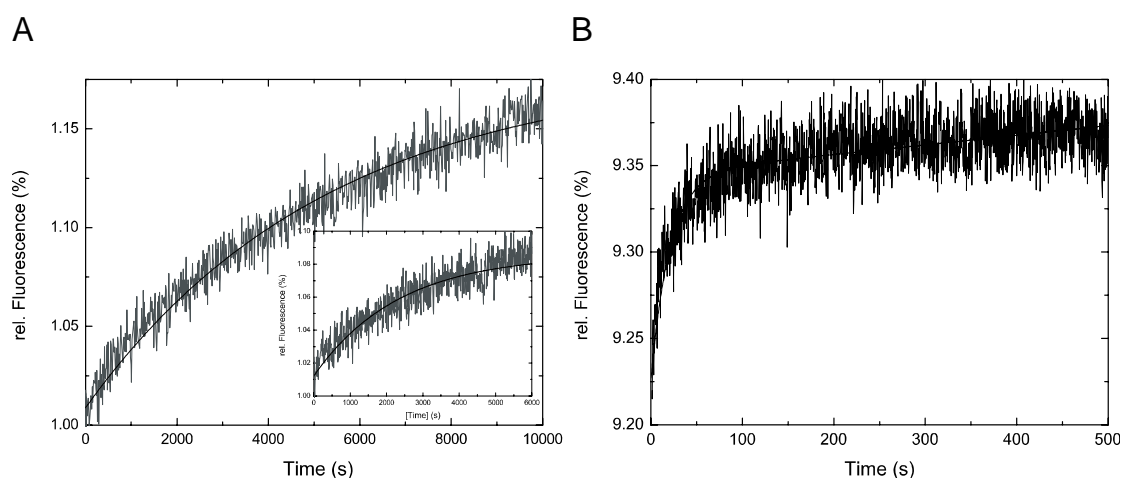


Figure 3.4.14: Determination of the F-actin release rate from Wt and A454S in the presence and absence of saturating ADP. (A) Single-exponential fit to the fluorescence transients gives k_A of $\sim 0.00019 \text{ s}^{-1}$ and k_A of $\sim 0.00024 \text{ s}^{-1}$ for Wt and A454S (*inset*), respectively. (B) F-actin release from NM2A. Single-exponential fit to the data set defines k_{DA} to $0.04 \pm 0.002 \text{ s}^{-1}$.

The calculation of the dissociation equilibrium constants for F-actin binding to myosin, K_A , from the ratio of the dissociation and binding rate constants indicates values of $\sim 0.0002 \mu\text{M}$ for Wt and A454S, respectively. In the presence of saturating ADP, values of $\sim 0.21 \mu\text{M}$ and $\sim 0.08 \mu\text{M}$ were calculated for the dissociation equilibrium constant of F-actin binding to Wt and A454S. All kinetic parameters of the interaction between myosin and F-actin in the presence and absence of nucleotide are summarized in Table 27.

Table 27: Kinetic parameters for the interaction between myosin and myosin.ADP with F-actin.

Parameter	Signal or calculation	NM2A	A454S	NM2A(Kovacs et al, 2003)
k_{+A} [$\mu\text{M}^{-1}\text{s}^{-1}$]	Pyrene-actin	0.96 ± 0.02	1.03 ± 0.23	0.73 ± 0.03
k_{-A} [s^{-1}]	Pyrene-actin	~ 0.00019	~ 0.00024	< 0.007 ($K_A \cdot k_{+A}$)
K_A [μM]	k_{-A}/k_{+A}			< 0.01
k_{+DA} [$\mu\text{M}^{-1}\text{s}^{-1}$]	Pyrene-actin	0.19 ± 0.004	0.80 ± 0.004	0.19 ± 0.02
k_{-DA} [s^{-1}]	Pyrene-actin	$\sim 0.04 \pm 0.002$	$\sim 0.07 \pm 0.004$	≈ 0.004 ($K_{DA} \cdot k_{+DA}$)
K_{DA} [μM]	k_{-DA}/k_{+DA}	~ 0.21	~ 0.08	≈ 0.02

4. Discussion

4.1 Pentachloropseudilin as a Potent Class-1 Myosin Inhibitor

Natural compounds, such as pseudilins have been identified as potent effectors of myosin motor activity (Martin et al, 2009a). Recently, Pentabromopseudilin (PBP) was reported as a potent inhibitor of myosin motor activity (Fedorov et al, 2009). PBP has five bromine substitutions on its pseudilin backbone. The size of the bromine atoms is bigger than the chlorine atoms but the electronegativity of chlorines is much higher than the bromines. The size of the halogens is one of the key factors for the steric accommodation of the pseudilins in the allosteric binding pocket.

Myosin	Conserved residues in the PCIP-binding pocket			Variable residues in the PCIP-binding pocket				IC ₅₀ (μM)
<i>Dd</i> myosin-1B	Lys186	Leu522	Asp520	Thr353	Asp356	Ser360	Lys560	1.0 ±0.5
<i>Rn</i> myosin-1b	Lys192	Leu534	Asp532	Asn355	Ser358	Ser362	Gln573	5.02±1.7
<i>Rn</i> myosin-1c	Lys189	Ile482	Asp480	Ala349	Ser352	Thr356	Tyr512	5.6±5.1
<i>Oc</i> myosin-2	Lys273	Leu604	Asp602	Ala433	Glu436	Leu440	Leu653	91.2±26
<i>Dd</i> myosin-5b	Lys289	Ile620	Asp618	Phe452	Gly455	Asp459	Gln648	99.1±47.5
<i>Dd</i> myosin-2	Lys265	Leu592	Asp590	Ala424	Gly427	Leu431	Gln633	126.6±21

Table 28: PCIP-binding site and the contact residues for different myosin isoforms. Selected conserved and variable residues found in *Dd* myosin-1B, *Rn* myosin-1b, *Rn* myosin-1c, *Oc* myosin-2 and *Dd* myosin-5b structural models corresponding to selected residues in the crystal structure of *Dd* myosin-2 that interact with pentachloropseudilin are shown. The level of inhibition (IC₅₀) is shown for each myosin isoform. Residues in the binding pocket are color-coded according to their polarity. Uncharged polar residues are shown in yellow, acidic residues in green, basic residues in red and non-polar residues in gray.

Pentabromopseudilin (PBP), which was shown previously to be very potent against different myosin isoforms, especially against class-5 myosins (Fedorov et al, 2009), accommodates its bulkier substitutions better than PCIP in the

allosteric binding pocket of *Dd* myosin-2. Pentachloropseudilin (PCIP) on the other hand possess five chlorines and this confers greater electronegativity to this pseudilin derivative. Compared to other myosin isoforms, class-1 myosins comprise a highly polar allosteric binding pocket (Table 28 and Figure 3.1.1.9). Thus, PCIP being a more polar compound compared to PBP shows potent inhibition against class-1 myosins motor activity.

4.1.1 Conformational Changes in the Allosteric Binding Pocket

Myosin does not undergo any major conformational changes in the backbone atoms upon binding PCIP. Indeed, the C α atoms of the inhibitor-bound and unbound Mg•ADP•metavanadate complexes superimpose with an r.m.s. deviation of 0.41 Å. Comparison of allosteric binding sites of PCIP and PBP has shown significant local conformational changes. The average r.m.s. deviation for superimposed PCIP and PBP molecules was 2.3 Å. Also, both the conformation of PCIP and details of the interaction with myosin residues in the binding pocket differ from those observed with PBP. The planar *anti*-conformer of PCIP binds to myosin (Figure 4.1). This differs from the binding mode of PBP, where the *syn*-conformer is observed to bind with the phenyl and pyrrole ring systems bent 12° out of plane and twisted 20° against each other (Fedorov et al, 2009). Further analysis showed that the translation in the magnesium position is small (~0.2 - 0.3 Å), when compared to unbound and bound PCIP structures.

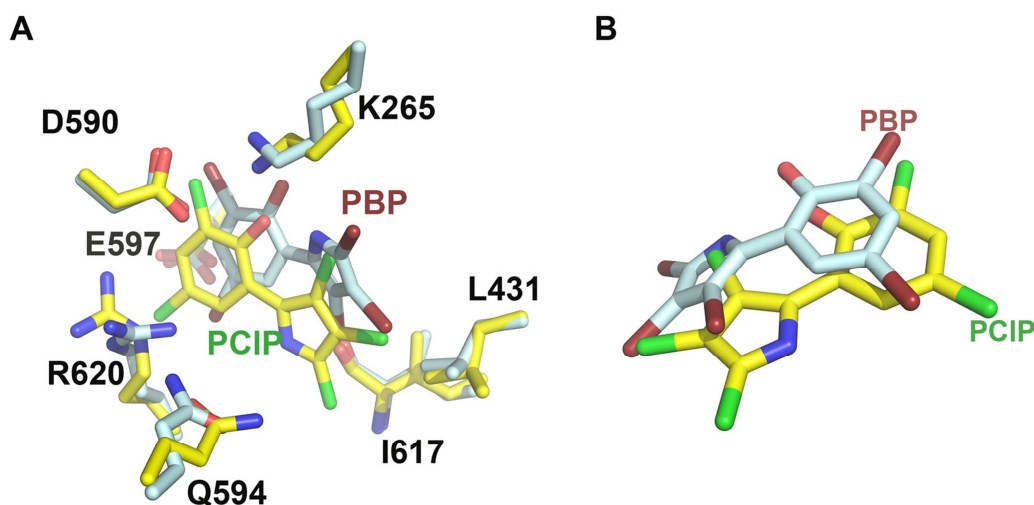


Figure 4.1: Dissimilarities in the allosteric binding site of PBP and PCIP bound myosin motor domain structures. (A) Close-up view of the superimposed binding site residues in the PCIP structure (2XEL) and PBP structure (2JHR) in the pseudilin-binding pocket. (B) Close-up view of the superimposed PCIP and PBP molecules in the allosteric binding pocket.

4.1.2 PCIP Induced Novel Allosteric Relay Mechanism

Originally, allostericity was defined as mere structural change between two states, which involves typical macromolecular conformational changes (Formanek et al, 2006; Gibriel & Doelle, 1975; Hope et al, 1975). Recently another mechanism of allostericity surfaced that the plausible mechanism of allostericity in some cases may operate by causing a shift of the protein to a different ensemble of conformations and this change may not be observable in an experimentally determined 3D structure (Cui & Karplus, 2008; Pan et al, 2000). A general model is presented in this work, whereby ligand-induced small changes in protein dynamics could produce allosteric communication between distinct binding sites, even in the absence of a macromolecular conformational change. In this study, *Dd* myosin-2 does not undergo any major global conformational changes upon binding pentachloropseudilin. However, that does not rule the possibility of the presence of the allosteric mechanism (Tsai et al, 2008). Allostericity can be attributed to the scaffold shape, differences in electrostatic distribution and the presence & absence of catalytic water in the case of myosins (Figure 3.1.1.10 and 3.1.1.11).

Structural dissection of the pre-power stroke myosin structures in the presence and absence of PCIP revealed the existence of a novel allosteric communication pathway between allosteric and nucleotide binding sites. A tight interaction network extended over a distance of 19 Å forming a direct link between PCIP and the γ -phosphate position of ATP. Slight conformational changes observed in the rotamers of the allosteric relay path residues from the allosteric binding pocket, switch-1 and switch -2. However, the major difference between the PCIP bound and unbound structures was the lack of catalytic water in the nucleotide-binding site. This catalytic water is present in the active site of the pre-power stroke state structures with bound ADP-VO₃ (2JJ9), ATP- γ -S, (1MMG), ADP-AIF₄ (1W9L), and mantADP-BeF_x (1D1C) (Gulick et al, 2000; Gulick et al, 1997). Different theories have been proposed for the importance of this catalytic water as a nucleophile and γ -phosphate as the general base for the ATP hydrolysis (Li & Cui, 2004; Rayment et al, 1996). Hence, lack of catalytic water is coupled to the allosteric mechanism in the PCIP bound structure.

Further analysis of pseudilin bound structures revealed similar allosteric pathway in PBP bound (2JHR) and dichlorotribormospseudilin bound (2XO8) pre-power stroke state myosin motor domain structures. The major differences with the various pseudilin bound structures are the orientation of the allosteric effector in the binding pocket and also K265 conformational changes to interact with the pseudilin in the allosteric-binding pocket. The similarities comprise the same residues in the allosteric path as PCIP and as a hallmark; catalytic water is absent in all these structures.

In conclusion, allosteric effectors that target myosin motors with high affinity and specificity are key tools in cytoskeletal research. As described in the present work, the natural product PCIP can be used as a potent and selective inhibitor of class-1 myosins in cell biological studies. The optical properties of the compound allow the direct observation of its binding interactions with myosins. Our detailed kinetic and structural analysis indicates that PCIP is a non-competitive, reversible inhibitor of myosin motor activity that acts in part by reducing the coupling between the actin- and nucleotide-binding sites. Isoform-specific differences in

the potency of PCIP-mediated inhibition can be rationalized by differences in the size and polarity of the allosteric binding pockets of myosin isoforms (Figure 4.1). In contrast to these differences in size and polarity, the residues involved in the relay pathway connecting the allosteric and active sites over a distance of 19 Å show a higher degree of conservation between myosin isoforms (Figure 4.2).

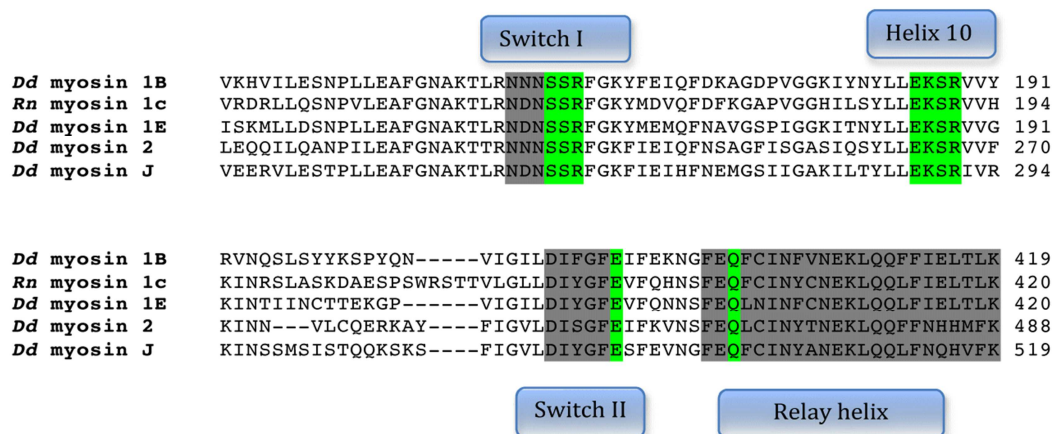


Figure 4.2: Alignment of residues in the allosteric relay path in different myosin isoforms. This figure shows the residues in the allosteric path from PCIP binding residues in helix 10 to the nucleotide-binding site. Residues colored in green are involved in the allosteric relay. Further, adjacent residues belonging to the same motif or secondary structure element are shown in grey color.

This suggests that the same communication pathway plays an important role in coupling information between the actin-binding region and the nucleotide-binding site during normal, uninhibited catalytic ATP-turnover.

4.2 Ammosamides as Allosteric Myosin Effectors

Deep-sea sediments are rich sources of natural compounds. Ammosamides are one such compound isolated from the sediments of the deep sea. Hughes *et al.* used a fluorescent-labeled probe, which is a conjugate of coupled ammosamide B with an acid, to verify the role of the ammosamides on cell cycle, cytokinesis and cell migration. Subsequent histological, confocal and mass-spectrometric studies indicated that marine compounds, such as ammosamides have profound role in inhibiting some of the class-2 myosins (Hughes *et al.*, 2009a). However, these studies haven't provided the details of the nature of inhibition and the mode

of binding to myosin.

To carry forward, in this thesis, kinetic and structural studies on ammosamides were performed and the possible effect of ammosamides on *Dd* myosin-2 motor domain has been explained. Out of eight derivatives of ammosamides, only four of them have shown significant effect on myosin-2 motor domain. Steady-state ATPase assays with myosin motor domain in the presence of ammosamides have shown that the ammosamide 272 was more than 4 fold ($IC_{50} = 17.2 \mu\text{M}$) potent inhibitor compared to ammosamide B ($IC_{50} = 72.4 \mu\text{M}$). Similar results have been observed in the single-turnover experiments (Figure 3.1.2.3).

In the absence of ammosamides, the time evolution of the reaction could be separated in three phases: an initial rise in mant fluorescence corresponding to binding of mantATP, a short, plateau phase determined by the rate of the conformational change that follows mantATP binding, and a drop in mant fluorescence corresponding to release and rebinding of mantADP ($k_{-4} + k_{+4}$). All three phases were extended in the presence of ammosamides. The extension of the plateau phase in the presence of ammosamides can be interpreted as the consequence of both slower mantATP hydrolysis and increased mantADP affinity. Crystallographic studies have shown that ammosamides preferentially bound to two allosteric sites in *Dd* myosin-2 motor domain. One of the binding sites of ammosamides is the pseudilin-binding site and the other one is adjacent to helix-loop-helix. From crystallographic refinements, it was predicted that pseudilin-binding site is the high affinity-binding site (occupancy 100 %) compared to the second binding site (occupancy 60-70 %). This different occupancy phenomenon was observed both in ammosamide 272 and ammosamide B crystal structures. However, the inhibition of myosin motor activity possibly because of synergistic effect of the ammosamide in both binding sites.

It was clear from the pseudilin bound myosin structures that an allosteric mechanism operates between the pseudilin binding site and the nucleotide-binding site. As ammosamides bound in the same site, the possibility of allosteric relay mechanism can't be ruled out (Chinthalapudi et al, 2011). The presence or

absence of the lytic water is crucial for the allosteric inhibitory relay path. However, the presence of ADP.VO₄ in the crystallization trials not allowed any firm conclusions on the allosteric relay path as one of the oxygen from orthovanadate occupies the same position as the lytic water.

Additionally, the presence of second binding pocket next to the helix-loop-helix and in close proximity to the relay helix may have an indirect effect on nucleotide binding and release kinetics (Figure 3.1.2.6). Single turnover experiments have shown that ammosamides may inhibit three phases of ATP binding, hydrolysis and ADP release kinetics of *Dd* myosin-2. Even though, the exact nature of the inhibition is not yet deciphered, it can be hypothesized that the synergistic action of ammosamides from two different allosteric binding sites in myosin motor domain is responsible for cumulative inhibitory effect on myosin motor activity.

4.3 Pre-power Stroke State of Nonmuscle Myosin-2C

This study has shown for the first time the crystal structure of “human” myosin motor domain. Comparison of the nonmuscle myosin isoforms: NM2A, NM2B and NM2C have shown >85 % sequence similarity in their motor domains. This indicates that nonmuscle myosin isoforms evolved from a common origin with alternative splicing as the major source of functional diversity (Kondrashov & Koonin, 2003).

The pre-power stroke state of NM2C MD and its key features have been described in comparison with structures of chicken smooth muscle myosin (1BR4) and striated muscle myosin (1QVI) in the same conformational state. The main differences included the variation in the length of the surface loop-1, loop-2, loop-3 and Upper 50 kDa loops. In addition, the structural analysis showed striking conformational differences in the Upper-50 kDa loop and the structural elements of the Upper 50 kDa subdomain. Significant differences were described for loop-3 when compared to the conformations of other class-2 myosins, which can be attributed to both length and sequence composition. The loops mentioned above as well as the connecting secondary structures interact with each other and undergo coupled distortions. Highlighting a vast sequence variability and

composition among myosin isoforms and sequence variations in loop regions may likely allow kinetic tuning by altering the rates of transitions between kinetic states of the actomyosin ATPase cycle (Heissler *et al*, 2011; Kelley *et al*, 1993).

To understand the kinetic and structural features of nonmuscle myosins is very important, not only in the viewpoint of molecular motors but also in the perspective of diseases, as NM2C was implicated in causing autosomal dominant hearing loss and other defects in auditive functions (Donaudy *et al*, 2004). Also, other nonmuscle myosin-2 isoforms like NM2A and NM2B have been associated with giant-platelet disorders like May-Heggling anomaly and Fetchner syndrome (Althaus & Greinacher, 2009; Hu *et al*, 2002). Understanding the structural features of nonmuscle myosins and mapping their mutations specific to a particular disease will be of very significance in the future studies.

4.4 Toxoplasma MHCs: MLCs Interaction

TgMyoD is the smallest *T.gondii* MHC and is the closest relative to *TgMyoA*. It exhibits the same kinetic characteristics as *TgMyoA* (Herm-Gotz *et al*, 2006). These studies indicate that the orthologous proteins of apicomplexan MHCs or MLCs have similar kinetic features or structural features (Bosch *et al*, 2006). Hence, modeling and guiding the docking in the previously available experimental structural poses is very informative and reliable. Molecular docking studies predict that the MLC2 forms a tight clamp around the MyoD-tail helix and adopts a more closed and compact conformation than observed in the structures of other MLC–MHC complexes. Special features in both the light and heavy chains are contributing to this compactness and the uniqueness of the MLC2–MyoD interface. The unique composition and the tight MLC2–MyoD interface make it an attractive target for the development of anti-coccidian drugs.

Given the absence of the actin—myosin machinery in the human host and its remote homology to host myosin heavy chains, the myosin tail interacting protein (MTIP) in complex with the myosin heavy chain tail (Myosin-A/D-tail) is an attractive drug target. This is because human heavy myosins have distant homology, only 37 % identity, to apicomplexan myosin heavy chains. Also, this

holds true for MTIPs or MLCs of apicomplexans (27 % identity and 52 % similarity). Since, the MHCs (*TgMyoD*, *TgMyoA* and *PfMyoA*) are well conserved among apicomplexans (80 % to 85 % identity), it could also be hypothesized to be a unique drug target in *T.gondii* or *P.falciparum*. In fact, recent studies indicated that apicomplexan MTIP-MHCs are suitable targets for drug discovery (Kortagere et al, 2011; Kortagere et al, 2010). Hence, small molecule compounds, which are designed to inhibit a specific protein–protein interaction, are expected to diminish the likelihood of acquired drug resistance by the parasite through permissible complementary mutations of interacting residues.

4.5 Kinetic and Structural Characterization of Nonmuscle Myosin-2A Switch-2 Mutant A454S

In the present work, the question how evolutionary conserved mutations within the conserved switch-2 region of class-2 myosins alter their kinetic properties was addressed. Therefore, human NM2A was chosen as a model system to study the effect of the A454S mutation on the kinetic properties of the enzyme. *In vitro* steady-state and transient-state kinetic techniques in combination with *in silico* modeling approaches were combined to interpret the obtained data.

The kinetic parameters of the extensive kinetic analysis of both proteins are listed in Table 29. The comparison of the steady-state and transient kinetic features of NM2A Wt and A454S indicate, that A454S inhibits normal motor functions, as expected from the fact that the residue is not conserved among myosins and that serine occupies the analogue position in the switch-2 region of other myosins like *Dd* myosin-2 (Sasaki et al, 1998). Main kinetic difference between the two myosin motors is a reduced ATP turnover under steady-state conditions, both, in the absence and presence of F-actin. Interestingly, the extent to which F-actin can increase the basal ATPase activity under steady-state conditions, k_{basal} , is equal. These findings indicate, that the A454S comprises the intact capability to bind F-actin and hydrolyze ATP, even though neither the rates of nucleotide binding, hydrolysis nor product release are reduced (Nagy et al, 2010).

To further investigate which kinetic step in the ATPase cycle is influenced by the switch-2 mutation A454S, transient kinetic stopped-flow assays were performed.

The kinetic parameters for ATP-binding to myosin and actomyosin indicate slightly elevated binding rate constants for A454S when compared to Wt. Mutation-induced changes were observed for the equilibrium constant for ATP-binding ($1/K_1$) and the ATP hydrolysis ($k_{+3}+k_{-3}$). Since the both kinetic steps, ATP binding and hydrolysis are much faster than the steady-state turnover, they do not rate-limit the steady-state cycling rate.

ADP kinetics in the presence of F-actin implicate, that A454S binds the nucleotide with the same speed as the Wt, whereas the release rate is 4-5 times slower than in the Wt motor. The calculation of the dissociation equilibrium constants for ADP binding indicates that A454S exhibits a 5-fold increased ADP affinity than the native motor. Both, Wt and switch-2 mutant show a weak or no enhancement of the ADP release by F-actin (k_{-AD}/k_{-D}). Correspondingly, the thermodynamic coupling constant K_{DA}/K_D is low and 10 decreased for A454S in comparison to Wt. The Mg^{2+} -dependence of the actin-activated ADP release rates indicate, that both NM2A and A454S show a magnesium-sensitive product release as already described for NM2C (Heissler & Manstein, 2011).

Previous studies of Rosenfeld *et al.* conclude that a fast release of Mg^{2+} implies an accelerated ADP release and that Mg^{2+} would leave the nucleotide-binding pocket prior to ADP (Rosenfeld2005). These findings are supported by structural studies on myosin-5, revealing a structure with ADP weakly bound and without magnesium bound in the nucleotide-binding pocket (Coureux et al, 2004; Rosenfeld et al, 2005).

These findings support the structural analysis of the nucleotide-binding pocket of homology models of NM2A Wt and A454S in order to explain the decreased actin-activated ADP release rates of A454S and the magnesium-sensitivity of both myosin motors. Although the homology models represent the nucleotide-binding pocket in the actin-detached state, it is assumed that the main features

resemble those of the actomyosin•ADP state from which ADP is released (Nagy 2010).

The structural analysis attributes the reduced ADP release rates in A454S to the formation of an ideal hydrogen bond between S454 with the backbone atoms of the residues S233 and F235 in the switch-1 loop. In addition, S233 coordinates to the Mg^{2+} ion. The additional hydrogen bonds might interfere with the coupling of switch-1 and switch-2 movements accompanying the Mg^{2+} release (Nagy 2010). This hypothesis is supported by an accompanying paper from Fujita-Becker *et al* (Fujita-Becker *et al*, 2005) suggesting that the interactions of the Y439, equivalent to S454 in NM2A, hydroxyl-moiety may be important for controlling Mg^{2+} -dependent ADP release in myosin-1.

This interference with the movement of switch-1 and -2 by the additional hydrogen bond in A454S results in reduced Mg^{2+} release rates which can be directly linked to a decreased nucleotide release rate and an increased ADP affinity. Since the Mg^{2+} coordination by the residues N231, T181 and S233 is equal in both nucleotide-binding pockets, the magnesium-sensitivity remains conserved in both motors. Hence, the decrease of the ADP release rate constants with increasing concentrations of Mg^{2+} can be directly explained by simple mass action (Heissler & Manstein, 2011).

Table 29: Summary of *Hs* NM2A and its switch-2 mutant kinetic analysis

Parameter	Signal or calculation	NM2A-Wt	NM2A-A454S
Steady-state ATPase activity			
k_{basal} [s^{-1}]	NADH Assay	0.013±0.001	0.004±0.002
v_{max} [s^{-1}]	NADH Assay ¹	0.11±0.01	0.04±0.004
K_{app} [μM]	NADH Assay	>140	>140
$v_{\text{max}}/K_{\text{app}}$ [$\mu\text{M}^{-1}\text{s}^{-1}$]	$v_{\text{max}}/K_{\text{app}}$ ¹	~0.0008	~0.0003
ATP interaction			
K_1k_{+2} [$\mu\text{M}^{-1}\text{s}^{-1}$]	Tryptophan	0.39±0.01	0.77±0.03
K_1k_{+2} [$\mu\text{M}^{-1}\text{s}^{-1}$]	mantATP	0.86±0.02	1.00±0.02
$1/K_1$ [μM]	Tryptophan	78.09±10.08	167.04±17.72
$k_{+3}+k_{-3}$ [s^{-1}]	Tryptophan	44.85±1.36	174.88±5.27
K_1k_{+2} [$\mu\text{M}^{-1}\text{s}^{-1}$]	Pyrene-actin	0.26±0.04	0.24±0.04
K_1k_{+2} [$\mu\text{M}^{-1}\text{s}^{-1}$]	mantATP	0.11±0.01	0.27±0.02
$1/K_1$ [μM]	Pyrene-actin	643.68±126.95	502.76±112.09
ADP interaction			
k_{+D} [$\mu\text{M}^{-1}\text{s}^{-1}$]	mantADP	4.29±0.28	2.71±0.04
k_{-D} [s^{-1}]	mantADP ²	0.68±0.09	0.77±0.05
	mantADP ³	0.38±0.01	0.54±0.02
	Tryptophan ³	0.34±0.01	0.47±0.03
K_D [μM]	k_{-D}/k_{+D}	0.16±0.03	0.28±0.02
k_{+AD} [$\mu\text{M}^{-1}\text{s}^{-1}$]	mantADP	4.92±0.09	5.52±0.11
k_{-AD} [s^{-1}]	mantADP ²	1.69±0.25	0.41±0.31
	mantADP ³	2.39±0.21	0.52±0.05
K_i [Mg^{2+}] (mM)	mantADP ³	0.45±0.09	1.17±0.39
K_{AD} [μM]	k_{-AD}/k_{+AD}	0.34±0.06	0.07±0.06
Coupling	K_{DA}/K_D	~2.1	~0.25
ADP release rate enhancement by F-actin	k_{-AD}/k_{-D}	~2.5-7	~0.53-1.1
F-Actin interaction			
k_{+A} [$\mu\text{M}^{-1}\text{s}^{-1}$]	Pyrene-actin	0.96±0.02	1.03±0.23
k_{-A} [s^{-1}]	Pyrene-actin	~0.00019	~0.00024
K_A [μM]	Pyrene-actin	~0.0002	~0.0002
k_{+DA} [$\mu\text{M}^{-1}\text{s}^{-1}$]	Pyrene-actin	0.19±0.004	0.80±0.04
k_{-DA} [s^{-1}]	Pyrene-actin	0.04±0.002	~0.07±0.004
K_{DA} [μM]	Pyrene-actin	~0.21	~0.08

¹ at 140 μM F-actin, the highest F-actin concentration that was experimentally accessible

² From the intercept of the k_{obs} versus mantADP plot

³ From ATP chasing experiment

5. References

- Adams PD, Afonine PV, Bunkoczi G, Chen VB, Davis IW, Echols N, Headd JJ, Hung LW, Kapral GJ, Grosse-Kunstleve RW, McCoy AJ, Moriarty NW, Oeffner R, Read RJ, Richardson DC, Richardson JS, Terwilliger TC, Zwart PH (2010) PHENIX: a comprehensive Python-based system for macromolecular structure solution. *Acta Crystallogr D Biol Crystallogr* **66**: 213-221
- Afflitto JJ, Inchiosa MA, Jr. (1979) Decrease in rat cardiac myosin ATPase with aortic constriction: prevention by thyroxine treatment. *Life Sci* **25**: 353-364
- Afonine PV, Mustyakimov M, Grosse-Kunstleve RW, Moriarty NW, Langan P, Adams PD (2010) Joint X-ray and neutron refinement with phenix.refine. *Acta Crystallogr D Biol Crystallogr* **66**: 1153-1163
- Allingham JS, Smith R, Rayment I (2005) The structural basis of blebbistatin inhibition and specificity for myosin II. *Nat Struct Mol Biol* **12**: 378-379
- Althaus K, Greinacher A (2009) MYH9-related platelet disorders. *Semin Thromb Hemost* **35**: 189-203
- Anan R, Greve G, Thierfelder L, Watkins H, McKenna WJ, Solomon S, Vecchio C, Shono H, Nakao S, Tanaka H, et al. (1994) Prognostic implications of novel beta cardiac myosin heavy chain gene mutations that cause familial hypertrophic cardiomyopathy. *J Clin Invest* **93**: 280-285
- Anderson DW, Probst FJ, Belyantseva IA, Fridell RA, Beyer L, Martin DM, Wu D, Kachar B, Friedman TB, Raphael Y, Camper SA (2000) The motor and tail regions of myosin XV are critical for normal structure and function of auditory and vestibular hair cells. *Hum Mol Genet* **9**: 1729-1738
- Anson M, Geeves MA, Kurzawa SE, Manstein DJ (1996a) Myosin motors with artificial lever arms. *Embo J* **15**: 6069-6074
- Anson M, Geeves MA, Kurzawa SE, Manstein DJ (1996b) Myosin motors with artificial lever arms. *Embo J* **15**: 6069-6074
- Antunes EM, Copp BR, Davies-Coleman MT, Samaai T (2005) Pyrroloiminoquinone and related metabolites from marine sponges. *Nat Prod Rep* **22**: 62-72
- Aotani Y, Nagata H, Yoshida M (1997) Lymphostin (LK6-A), a novel immunosuppressant from *Streptomyces* sp. KY11783: structural elucidation. *J Antibiot (Tokyo)* **50**: 543-545
- Asherie N (2004) Protein crystallization and phase diagrams. *Methods* **34**: 266-272
- Bai Y, Mao QQ, Qin J, Zheng XY, Wang YB, Yang K, Shen HF, Xie LP (2010) Resveratrol induces apoptosis and cell cycle arrest of human T24 bladder cancer cells in vitro and inhibits tumor growth in vivo. *Cancer Sci* **101**: 488-493
- Batra R, Geeves MA, Manstein DJ (1999) Kinetic analysis of Dictyostelium discoideum myosin motor domains with glycine-to-alanine mutations in the reactive thiol region. *Biochemistry* **38**: 6126-6134
- Batra R, Manstein DJ (1999) Functional characterisation of Dictyostelium myosin II with conserved tryptophanyl residue 501 mutated to tyrosine. *Biol Chem* **380**: 1017-1023

- Baum J, Richard D, Healer J, Rug M, Krnjanski Z, Gilberger TW, Green JL, Holder AA, Cowman AF (2006) A conserved molecular motor drives cell invasion and gliding motility across malaria life cycle stages and other apicomplexan parasites. *J Biol Chem* **281**: 5197-5208
- Bereiter-Hahn J, Kajstura J (1988) Scanning microfluorometric measurement of TRITC-phalloidin labelled F-actin. Dependence of F-actin content on density of normal and transformed cells. *Histochemistry* **90**: 271-276
- Berg JS, Powell BC, Cheney RE (2001) A millennial myosin census. *Mol Biol Cell* **12**: 780-794
- Bergman LW, Kaiser K, Fujioka H, Coppens I, Daly TM, Fox S, Matuschewski K, Nussenzweig V, Kappe SH (2003) Myosin A tail domain interacting protein (MTIP) localizes to the inner membrane complex of Plasmodium sporozoites. *J Cell Sci* **116**: 39-49
- Betapudi V, Licate LS, Egelhoff TT (2006) Distinct roles of nonmuscle myosin II isoforms in the regulation of MDA-MB-231 breast cancer cell spreading and migration. *Cancer Res* **66**: 4725-4733
- Blessing RH (1995) An empirical correction for absorption anisotropy. *Acta Crystallogr A* **51 (Pt 1)**: 33-38
- Bosch J, Turley S, Daly TM, Bogh SM, Villasmil ML, Roach C, Zhou N, Morrissey JM, Vaidya AB, Bergman LW, Hol WG (2006) Structure of the MTIP-MyoA complex, a key component of the malaria parasite invasion motor. *Proc Natl Acad Sci U S A* **103**: 4852-4857
- Bosch J, Turley S, Roach CM, Daly TM, Bergman LW, Hol WG (2007) The closed MTIP-myosin A-tail complex from the malaria parasite invasion machinery. *J Mol Biol* **372**: 77-88
- Bose A, Guilherme A, Robida SI, Nicoloso SM, Zhou QL, Jiang ZY, Pomerleau DP, Czech MP (2002) Glucose transporter recycling in response to insulin is facilitated by myosin Myo1c. *Nature* **420**: 821-824
- Bourne HR, Sanders DA, McCormick F (1991) The GTPase superfamily: conserved structure and molecular mechanism. *Nature* **349**: 117-127
- Brunger AT, Adams PD, Clore GM, DeLano WL, Gros P, Grosse-Kunstleve RW, Jiang JS, Kuszewski J, Nilges M, Pannu NS, Read RJ, Rice LM, Simonson T, Warren GL (1998) Crystallography & NMR system: A new software suite for macromolecular structure determination. *Acta Crystallogr D Biol Crystallogr* **54**: 905-921
- Buxton DB, Golomb E, Adelstein RS (2003) Induction of nonmuscle myosin heavy chain II-C by butyrate in RAW 264.7 mouse macrophages. *J Biol Chem* **278**: 15449-15455
- Cecchini M, Houdusse A, Karplus M (2008) Allosteric communication in myosin V: from small conformational changes to large directed movements. *PLoS Comput Biol* **4**: e1000129
- Cheung A, Dantzig JA, Hollingworth S, Baylor SM, Goldman YE, Mitchison TJ, Straight AF (2002) A small-molecule inhibitor of skeletal muscle myosin II. *Nat Cell Biol* **4**: 83-88
- Chinthalapudi K, Taft MH, Martin R, Heissler SM, Preller M, Hartmann FK, Brandstaetter H, Kendrick-Jones J, Tsiavaliaris G, Gutzeit HO, Fedorov R, Buss F, Knölker HJ,

- Coluccio LM, Manstein DJ (2011) Mechanism and specificity of Pentachloropseudilin-Mediated Inhibition of Myosin Motor Activity. *Journal of biological chemistry* **accepted**
- Conibear PB, Bagshaw CR, Fajer PG, Kovacs M, Malnasi-Csizmadia A (2003) Myosin cleft movement and its coupling to actomyosin dissociation. *Nat Struct Biol* **10**: 831-835
- Coureux PD, Sweeney HL, Houdusse A (2004) Three myosin V structures delineate essential features of chemo-mechanical transduction. *Embo J* **23**: 4527-4537
- Coureux PD, Wells AL, Menetrey J, Yengo CM, Morris CA, Sweeney HL, Houdusse A (2003) A structural state of the myosin V motor without bound nucleotide. *Nature* **425**: 419-423
- Criddle AH, Geeves MA, Jeffries T (1985) The use of actin labelled with N-(1-pyrenyl)iodoacetamide to study the interaction of actin with myosin subfragments and troponin/tropomyosin. *Biochem J* **232**: 343-349
- Cui Q, Karplus M (2008) Allostery and cooperativity revisited. *Protein Sci* **17**: 1295-1307
- Daily MD, Gray JJ (2007) Local motions in a benchmark of allosteric proteins. *Proteins* **67**: 385-399
- Davis IW, Leaver-Fay A, Chen VB, Block JN, Kapral GJ, Wang X, Murray LW, Arendall WB, 3rd, Snoeyink J, Richardson JS, Richardson DC (2007a) MolProbity: all-atom contacts and structure validation for proteins and nucleic acids. *Nucleic Acids Res* **35**: W375-383
- Davis IW, Leaver-Fay A, Chen VB, Block JN, Kapral GJ, Wang X, Murray LW, Arendall WB, Snoeyink J, Richardson JS, Richardson DC (2007b) MolProbity: all-atom contacts and structure validation for proteins and nucleic acids. *Nucleic Acids Res* **35**: W375-383
- Dominguez R, Freyzon Y, Trybus KM, Cohen C (1998) Crystal structure of a vertebrate smooth muscle myosin motor domain and its complex with the essential light chain: visualization of the pre-power stroke state. *Cell* **94**: 559-571
- Donaudy F, Snoeckx R, Pfister M, Zenner HP, Blin N, Di Stazio M, Ferrara A, Lanzara C, Ficarella R, Declau F, Pusch CM, Nurnberg P, Melchionda S, Zelante L, Ballana E, Estivill X, Van Camp G, Gasparini P, Savoia A (2004) Nonmuscle myosin heavy-chain gene MYH14 is expressed in cochlea and mutated in patients affected by autosomal dominant hearing impairment (DFNA4). *Am J Hum Genet* **74**: 770-776
- Durrwang U, Fujita-Becker S, Erent M, Kull FJ, Tsiavaliaris G, Geeves MA, Manstein DJ (2006) Dictyostelium myosin-IE is a fast molecular motor involved in phagocytosis. *J Cell Sci* **119**: 550-558
- Emsley P, Lohkamp B, Scott WG, Cowtan K (2010) Features and development of Coot. *Acta Crystallogr D Biol Crystallogr* **66**: 486-501
- Even-Ram S, Doyle AD, Conti MA, Matsumoto K, Adelstein RS, Yamada KM (2007) Myosin IIA regulates cell motility and actomyosin-microtubule crosstalk. *Nat Cell Biol* **9**: 299-309
- Fedorov R, Bohl M, Tsiavaliaris G, Hartmann FK, Taft MH, Baruch P, Brenner B, Martin R, Knolker HJ, Gutzeit HO, Manstein DJ (2009) The mechanism of pentabromopseudilin inhibition of myosin motor activity. *Nat Struct Mol Biol* **16**: 80-88
- Fenical W, Jensen PR (2006) Developing a new resource for drug discovery: marine actinomycete bacteria. *Nat Chem Biol* **2**: 666-673

- Fisher AJ, Smith CA, Thoden JB, Smith R, Sutoh K, Holden HM, Rayment I (1995) X-ray structures of the myosin motor domain of *Dictyostelium discoideum* complexed with MgADP.BeFx and MgADP.AIF₄. *Biochemistry* **34**: 8960-8972
- Formanek MS, Ma L, Cui Q (2006) Reconciling the "old" and "new" views of protein allostery: a molecular simulation study of chemotaxis Y protein (CheY). *Proteins* **63**: 846-867
- Foth BJ, Goedecke MC, Soldati D (2006) New insights into myosin evolution and classification. *Proc Natl Acad Sci U S A* **103**: 3681-3686
- Friedman AL, Geeves MA, Manstein DJ, Spudich JA (1998) Kinetic characterization of myosin head fragments with long-lived myosin.ATP states. *Biochemistry* **37**: 9679-9687
- Fujita-Becker S, Durrwang U, Erent M, Clark RJ, Geeves MA, Manstein DJ (2005) Changes in Mg²⁺ ion concentration and heavy chain phosphorylation regulate the motor activity of a class I myosin. *J Biol Chem* **280**: 6064-6071
- Fujita-Becker S, Reubold TF, Holmes KC (2006) The actin-binding cleft: functional characterisation of myosin II with a strut mutation. *J Muscle Res Cell Motil* **27**: 115-123
- Furch M, Fujita-Becker S, Geeves MA, Holmes KC, Manstein DJ (1999) Role of the salt-bridge between switch-1 and switch-2 of *Dictyostelium* myosin. *J Mol Biol* **290**: 797-809
- Furch M, Geeves MA, Manstein DJ (1998) Modulation of actin affinity and actomyosin adenosine triphosphatase by charge changes in the myosin motor domain. *Biochemistry* **37**: 6317-6326
- Garman E (2003) 'Cool' crystals: macromolecular cryocrystallography and radiation damage. *Curr Opin Struct Biol* **13**: 545-551
- Garman EF, Double S (2003) Cryocooling of macromolecular crystals: optimization methods. *Methods Enzymol* **368**: 188-216
- Gaskins E, Gilk S, DeVore N, Mann T, Ward G, Beckers C (2004) Identification of the membrane receptor of a class XIV myosin in *Toxoplasma gondii*. *J Cell Biol* **165**: 383-393
- Gasteiger E, Hoogland C, Gattiker A, Duvaud S, Wilkins MR, Appel RD, Bairoch A (2005) *Protein Identification and Analysis Tools on the ExPASy Server*. Human press.
- Geeves MA, Fedorov R, Manstein DJ (2005) Molecular mechanism of actomyosin-based motility. *Cell Mol Life Sci* **62**: 1462-1477
- Geeves MA, Holmes KC (1999) Structural mechanism of muscle contraction. *Annu Rev Biochem* **68**: 687-728
- Geisterfer-Lowrance AA, Kass S, Tanigawa G, Vosberg HP, McKenna W, Seidman CE, Seidman JG (1990) A molecular basis for familial hypertrophic cardiomyopathy: a beta cardiac myosin heavy chain gene missense mutation. *Cell* **62**: 999-1006
- Ghera D, Sanchez R (2009) Improving accuracy and efficiency of blind protein-ligand docking by focusing on predicted binding sites. *Proteins* **74**: 417-424
- Gibriel AY, Doelle HW (1975) Investigation into pyruvate kinases from *Escherichia coli* K-12 grown under aerobic and anaerobic conditions. *Microbios* **12**: 179-197
- Gillespie PG, Cyr JL (2004) Myosin-1c, the hair cell's adaptation motor. *Annu Rev Physiol* **66**: 521-545

- Golomb E, Ma X, Jana SS, Preston YA, Kawamoto S, Shoham NG, Goldin E, Conti MA, Sellers JR, Adelstein RS (2004) Identification and characterization of nonmuscle myosin II-C, a new member of the myosin II family. *J Biol Chem* **279**: 2800-2808
- Goodey NM, Benkovic SJ (2008) Allosteric regulation and catalysis emerge via a common route. *Nat Chem Biol* **4**: 474-482
- Goodsell DS, Morris GM, Olson AJ (1996) Automated docking of flexible ligands: applications of AutoDock. *J Mol Recognit* **9**: 1-5
- Gourinath S, Himmel DM, Brown JH, Reshetnikova L, Szent-Györgyi AG, Cohen C (2003) Crystal structure of scallop Myosin s1 in the pre-power stroke state to 2.6 Å resolution: flexibility and function in the head. *Structure* **11**: 1621-1627
- Gulick AM, Bauer CB, Thoden JB, Pate E, Yount RG, Rayment I (2000) X-ray structures of the Dictyostelium discoideum myosin motor domain with six non-nucleotide analogs. *J Biol Chem* **275**: 398-408
- Gulick AM, Bauer CB, Thoden JB, Rayment I (1997) X-ray structures of the MgADP, MgATP γ S, and MgAMPPNP complexes of the Dictyostelium discoideum myosin motor domain. *Biochemistry* **36**: 11619-11628
- Gunasekaran K, Ma B, Nussinov R (2004) Is allostery an intrinsic property of all dynamic proteins? *Proteins* **57**: 433-443
- Hakansson S, Morisaki H, Heuser J, Sibley LD (1999) Time-lapse video microscopy of gliding motility in *Toxoplasma gondii* reveals a novel, biphasic mechanism of cell locomotion. *Mol Biol Cell* **10**: 3539-3547
- Hammer JA, Jung G, Korn ED (1986) Genetic evidence that *Acanthamoeba* myosin I is a true myosin. *Proc Natl Acad Sci U S A* **83**: 4655-4659
- Heissler SM, Manstein DJ (2011) Comparative kinetic and functional characterization of the motor domains of human nonmuscle myosin-2C isoforms. *J Biol Chem*
- Herm-Gotz A, Delbac F, Weiss S, Nyitrai M, Stratmann R, Tomavo S, Sibley LD, Geeves MA, Soldati D (2006) Functional and biophysical analyses of the class XIV *Toxoplasma gondii* myosin D. *J Muscle Res Cell Motil* **27**: 139-151
- Herm-Gotz A, Weiss S, Stratmann R, Fujita-Becker S, Ruff C, Meyhofer E, Soldati T, Manstein DJ, Geeves MA, Soldati D (2002) *Toxoplasma gondii* myosin A and its light chain: a fast, single-headed, plus-end-directed motor. *Embo J* **21**: 2149-2158
- Herrmann C, Wray J, Travers F, Barman T (1992) Effect of 2,3-butanedione monoxime on myosin and myofibrillar ATPases. An example of an uncompetitive inhibitor. *Biochemistry* **31**: 12227-12232
- Hettmann C, Herm A, Geiter A, Frank B, Schwarz E, Soldati T, Soldati D (2000) A dibasic motif in the tail of a class XIV apicomplexan myosin is an essential determinant of plasma membrane localization. *Mol Biol Cell* **11**: 1385-1400
- Higuchi H, Takemori S (1989) Butanedione monoxime suppresses contraction and ATPase activity of rabbit skeletal muscle. *J Biochem* **105**: 638-643
- Hiltner PA, Krieger IM (1969) Diffraction of Light by Ordered Suspensions. *Journal of Physical Chemistry* **73**: 2306
- Hiratsuka T (1994) Nucleotide-induced closure of the ATP-binding pocket in myosin subfragment-1. *J Biol Chem* **269**: 27251-27257

- Hirokawa N, Nitta R, Okada Y (2009) The mechanisms of kinesin motor motility: lessons from the monomeric motor KIF1A. *Nat Rev Mol Cell Biol* **10**: 877-884
- Hodge T, Cope MJ (2000) A myosin family tree. *J Cell Sci* **113 Pt 19**: 3353-3354
- Holmes KC (1997) The swinging lever-arm hypothesis of muscle contraction. *Curr Biol* **7**: R112-118
- Holmes KC, Angert I, Kull FJ, Jahn W, Schroder RR (2003) Electron cryo-microscopy shows how strong binding of myosin to actin releases nucleotide. *Nature* **425**: 423-427
- Homer MJ, Aguilar-Delfin I, Telford SR, 3rd, Krause PJ, Persing DH (2000) Babesiosis. *Clin Microbiol Rev* **13**: 451-469
- Hope DB, Walti M, Winzor DJ (1975) Co-operative binding of oxytocin to bovine neurophysin II. *Biochem J* **147**: 377-379
- Hu A, Wang F, Sellers JR (2002) Mutations in human nonmuscle myosin IIA found in patients with May-Hegglin anomaly and Fechtner syndrome result in impaired enzymatic function. *J Biol Chem* **277**: 46512-46517
- Hughes CC, Fenical W (2010) Total synthesis of the ammosamides. *J Am Chem Soc* **132**: 2528-2529
- Hughes CC, MacMillan JB, Gaudencio SP, Fenical W, La Clair JJ (2009a) Ammosamides A and B target myosin. *Angew Chem Int Ed Engl* **48**: 728-732
- Hughes CC, MacMillan JB, Gaudencio SP, Jensen PR, Fenical W (2009b) The ammosamides: structures of cell cycle modulators from a marine-derived *Streptomyces* species. *Angew Chem Int Ed Engl* **48**: 725-727
- Jackson RM, Sternberg MJ (1995) A continuum model for protein-protein interactions: application to the docking problem. *J Mol Biol* **250**: 258-275
- Jana SS, Kim KY, Mao J, Kawamoto S, Sellers JR, Adelstein RS (2009) An alternatively spliced isoform of non-muscle myosin II-C is not regulated by myosin light chain phosphorylation. *J Biol Chem* **284**: 11563-11571
- Johnson KA (1998) Advances in transient-state kinetics. *Curr Opin Biotechnol* **9**: 87-89
- Johnson KA, Porter ME (1982) Transient state kinetic analysis of the dynein ATPase. *Prog Clin Biol Res* **80**: 101-106
- Jones G, Willett P, Glen RC, Leach AR, Taylor R (1997) Development and validation of a genetic algorithm for flexible docking. *J Mol Biol* **267**: 727-748
- Kabsch W (2010) Xds. *Acta Crystallogr D Biol Crystallogr* **66**: 125-132
- Keeley A, Soldati D (2004) The glideosome: a molecular machine powering motility and host-cell invasion by Apicomplexa. *Trends Cell Biol* **14**: 528-532
- Kelley CA, Takahashi M, Yu JH, Adelstein RS (1993) An insert of seven amino acids confers functional differences between smooth muscle myosins from the intestines and vasculature. *J Biol Chem* **268**: 12848-12854
- Kengyel A, Wolf WA, Chisholm RL, Sellers JR Nonmuscle myosin IIA with a GFP fused to the N-terminus of the regulatory light chain is regulated normally. *J Muscle Res Cell Motil* **31**: 163-170
- Kliche W, Fujita-Becker S, Kollmar M, Manstein DJ, Kull FJ (2001) Structure of a genetically engineered molecular motor. *Embo J* **20**: 40-46

- Kolomeisky AB, Fisher ME (2007) Molecular motors: a theorist's perspective. *Annu Rev Phys Chem* **58**: 675-695
- Kondrashov FA, Koonin EV (2003) Evolution of alternative splicing: deletions, insertions and origin of functional parts of proteins from intron sequences. *Trends Genet* **19**: 115-119
- Koppole S, Smith JC, Fischer S (2006) Simulations of the myosin II motor reveal a nucleotide-state sensing element that controls the recovery stroke. *J Mol Biol* **361**: 604-616
- Korn ED, Atkinson MA, Brzeska H, Hammer JA, 3rd, Jung G, Lynch TJ (1988) Structure-function studies on *Acanthamoeba* myosins IA, IB, and II. *J Cell Biochem* **36**: 37-50
- Kortagere S, Mui E, McLeod R, Welsh WJ (2011) Rapid discovery of inhibitors of *Toxoplasma gondii* using hybrid structure-based computational approach. *J Comput Aided Mol Des*
- Kortagere S, Welsh WJ, Morrisey JM, Daly T, Ejigiri I, Sinnis P, Vaidya AB, Bergman LW (2010) Structure-based design of novel small-molecule inhibitors of *Plasmodium falciparum*. *J Chem Inf Model* **50**: 840-849
- Koshland DE, Jr., Nemethy G, Filmer D (1966) Comparison of experimental binding data and theoretical models in proteins containing subunits. *Biochemistry* **5**: 365-385
- Kouyama T, Mihashi K (1981) Fluorimetry study of N-(1-pyrenyl)iodoacetamide-labelled F-actin. Local structural change of actin protomer both on polymerization and on binding of heavy meromyosin. *Eur J Biochem* **114**: 33-38
- Kovács M, Tóth J, Hetényi C, Málnási-Csizmadia A, Sellers JR (2004) Mechanism of blebbistatin inhibition of myosin II. *J Biol Chem* **279**: 35557-35563
- Kovacs M, Wang F, Hu A, Zhang Y, Sellers JR (2003) Functional divergence of human cytoplasmic myosin II: kinetic characterization of the non-muscle IIA isoform. *J Biol Chem* **278**: 38132-38140
- Laemmli UK (1970) Cleavage of structural proteins during the assembly of the head of bacteriophage T4. *Nature* **227**: 680-685
- Laskowski RA, MacArthur MW, Moss DS, Thornton JM (1993) PROCHECK: a program to check the stereochemical quality of protein structures. *J Appl Crystallogr* **26**: 283-291
- Leal A, Ende S, Stengel C, Huehne K, Loetterle J, Barrantes R, Winterpacht A, Rautenstrauss B (2003) A novel myosin heavy chain gene in human chromosome 19q13.3. *Gene* **312**: 165-171
- Lehar J, Stockwell BR, Giaever G, Nislow C (2008) Combination chemical genetics. *Nat Chem Biol* **4**: 674-681
- Levin RM, Weiss B (1976) Mechanism by which psychotropic drugs inhibit adenosine cyclic 3',5'-monophosphate phosphodiesterase of brain. *Mol Pharmacol* **12**: 581-589
- Li G, Cui Q (2004) Mechanochemical coupling in Myosin: A theoretical Analysis with Molecular Dynamics and Combined QM/MM Reaction Path Calculations. *J Phys Chem B* **108**: 3342-3357
- Liang Y, Wang A, Probst FJ, Arhya IN, Barber TD, Chen KS, Deshmukh D, Dolan DF, Hinnant JT, Carter LE, Jain PK, Lalwani AK, Li XC, Lupski JR, Moeljopawiro S, Morell R, Negrini C, Wilcox ER, Winata S, Camper SA, Friedman TB (1998) Genetic mapping

- refines DFNB3 to 17p11.2, suggests multiple alleles of DFNB3, and supports homology to the mouse model shaker-2. *Am J Hum Genet* **62**: 904-915
- Liao JC, Elting MW, Delp SL, Spudich JA, Bryant Z (2009) Engineered myosin VI motors reveal minimal structural determinants of directionality and processivity. *J Mol Biol* **392**: 862-867
- Limouze J, Straight AF, Mitchison T, Sellers JR (2004) Specificity of blebbistatin, an inhibitor of myosin II. *J Muscle Res Cell Motil* **25**: 337-341
- Lorenz M, Holmes KC (2010) The actin-myosin interface. *Proc Natl Acad Sci U S A* **107**: 12529-12534
- Lymn RW, Taylor EW (1971) Mechanism of adenosine triphosphate hydrolysis by actomyosin. *Biochemistry* **10**: 4617-4624
- Lyskov S, Gray JJ (2008) The RosettaDock server for local protein-protein docking. *Nucleic Acids Res* **36**: W233-238
- Macmillan J, Hughes C, LaClair JJ, Jensen PR, Fenical W (2008) Ammosamides A and B from a marine-derived *Streptomyces* CNR-698, GenBank-EU863183. *Unpublished*
- Manstein DJ, Hunt DM (1995) Overexpression of myosin motor domains in *Dictyostelium*: screening of transformants and purification of the affinity tagged protein. *J Muscle Res Cell Motil* **16**: 325-332
- Manstein DJ, Ruppel KM, Kubalek L, Spudich JA (1991) Manipulation and expression of molecular motors in *Dictyostelium discoideum*. *J Cell Sci Suppl* **14**: 63-65
- Manstein DJ, Ruppel KM, Spudich JA (1989) Expression and characterization of a functional myosin head fragment in *Dictyostelium discoideum*. *Science* **246**: 656-658
- Marchesini S, Chapman H, Hau-Riege S, London R, Szoke A, He H, Howells M, Padmore H, Rosen R, Spence J, Weierstall U (2003) Coherent X-ray diffractive imaging: applications and limitations. *Opt Express* **11**: 2344-2353
- Marston SB, Taylor EW (1980) Comparison of the myosin and actomyosin ATPase mechanisms of the four types of vertebrate muscles. *J Mol Biol* **139**: 573-600
- Martin R, Jager A, Bohl M, Richter S, Fedorov R, Manstein DJ, Gutzeit HO, Knolker HJ (2009a) Total synthesis of pentabromo- and pentachloropseudilin, and synthetic analogues--allosteric inhibitors of myosin ATPase. *Angew Chem Int Ed Engl* **48**: 8042-8046
- Martin RE, Marchetti RV, Cowan AI, Howitt SM, Broer S, Kirk K (2009b) Chloroquine transport via the malaria parasite's chloroquine resistance transporter. *Science* **325**: 1680-1682
- Maupin P, Phillips CL, Adelstein RS, Pollard TD (1994) Differential localization of myosin-II isozymes in human cultured cells and blood cells. *J Cell Sci* **107 (Pt 11)**: 3077-3090
- McCoy AJ (2007) Solving structures of protein complexes by molecular replacement with Phaser. *Acta Crystallogr D Biol Crystallogr* **63**: 32-41
- Meissner M, Schluter D, Soldati D (2002) Role of *Toxoplasma gondii* myosin A in powering parasite gliding and host cell invasion. *Science* **298**: 837-840
- Melchionda S, Ahituv N, Bisceglia L, Sobe T, Glaser F, Rabionet R, Arbones ML, Notarangelo A, Di Iorio E, Carella M, Zelante L, Estivill X, Avraham KB, Gasparini P

- (2001) MYO6, the human homologue of the gene responsible for deafness in Snell's waltzer mice, is mutated in autosomal dominant nonsyndromic hearing loss. *Am J Hum Genet* **69**: 635-640
- Mermall V, Post PL, Mooseker MS (1998) Unconventional myosins in cell movement, membrane traffic, and signal transduction. *Science* **279**: 527-533
- Monod J, Wyman J, Changeux JP (1965) On the Nature of Allosteric Transitions: A Plausible Model. *J Mol Biol* **12**: 88-118
- Mooseker MS, Foth BJ (2008) The Structural and Functional Diversity of the Myosin Family of Actin-Based Molecular Motors. In *Collection* Vol. 7, pp 1-34.
- Morris E (1843) Malaria, Its Causes, Effects, and Treatment. *Prov Med J Retrospect Med Sci* **6**: 447-449
- Morrisette NS, Sibley LD (2002) Cytoskeleton of apicomplexan parasites. *Microbiol Mol Biol Rev* **66**: 21-38; table of contents
- Murphy CT, Spudich JA (2000) Variable surface loops and myosin activity: accessories to a motor. *J Muscle Res Cell Motil* **21**: 139-151
- Nagy NT, Sakamoto T, Takacs B, Gyimesi M, Hazai E, Bikadi Z, Sellers JR, Kovacs M (2010) Functional adaptation of the switch-2 nucleotide sensor enables rapid processive translocation by myosin-5. *Faseb J* **24**: 4480-4490
- Namasivayam V, Gunther R (2007) pso@autodock: a fast flexible molecular docking program based on Swarm intelligence. *Chem Biol Drug Des* **70**: 475-484
- Nave C, Garman EF (2005) Towards an understanding of radiation damage in cryocooled macromolecular crystals. *J Synchrotron Radiat* **12**: 257-260
- Niederman R, Pollard TD (1975) Human platelet myosin. II. In vitro assembly and structure of myosin filaments. *J Cell Biol* **67**: 72-92
- Opitz C, Soldati D (2002) 'The glideosome': a dynamic complex powering gliding motion and host cell invasion by *Toxoplasma gondii*. *Mol Microbiol* **45**: 597-604
- Pan H, Lee JC, Hilser VJ (2000) Binding sites in *Escherichia coli* dihydrofolate reductase communicate by modulating the conformational ensemble. *Proc Natl Acad Sci U S A* **97**: 12020-12025
- Patel H, Margossian SS, Chantler PD (2000) Locking regulatory myosin in the off-state with trifluoperazine. *J Biol Chem* **275**: 4880-4888
- Perreault-Micale CL, Kalabokis VN, Nyitray L, Szent-Györgyi AG (1996) Sequence variations in the surface loop near the nucleotide binding site modulate the ATP turnover rates of molluscan myosins. *J Muscle Res Cell Motil* **17**: 543-553
- Pollard TD (2010) Mechanics of cytokinesis in eukaryotes. *Curr Opin Cell Biol* **22**: 50-56
- Pollard TD, Korn ED (1973) *Acanthamoeba* myosin. I. Isolation from *Acanthamoeba castellanii* of an enzyme similar to muscle myosin. *J Biol Chem* **248**: 4682-4690
- Polonais V, Javier Foth B, Chinthalapudi K, Marq JB, Manstein DJ, Soldati-Favre D, Frenal K (2011) Unusual anchor of a motor complex (MyoD-MLC2) to the plasma membrane of *Toxoplasma gondii*. *Traffic* **12**: 287-300

- Ponomarev MA, Furch M, Levitsky DI, Manstein DJ (2000) Charge changes in loop 2 affect the thermal unfolding of the myosin motor domain bound to F-actin. *Biochemistry* **39**: 4527-4532
- Popovych N, Sun S, Ebricht RH, Kalodimos CG (2006) Dynamically driven protein allostery. *Nat Struct Mol Biol* **13**: 831-838
- Poupon V, Stewart A, Gray SR, Piper RC, Luzio JP (2003) The role of mVps18p in clustering, fusion, and intracellular localization of late endocytic organelles. *Mol Biol Cell* **14**: 4015-4027
- Preller M, Manstein DJ (2011) Myosin Motors: Structural Aspects and Functionality. In *Comprehensive Biophysics* Vol. 4. Elsevier
- Probst FJ, Fridell RA, Raphael Y, Saunders TL, Wang A, Liang Y, Morell RJ, Touchman JW, Lyons RH, Noben-Trauth K, Friedman TB, Camper SA (1998) Correction of deafness in shaker-2 mice by an unconventional myosin in a BAC transgene. *Science* **280**: 1444-1447
- Rayment I, Rypniewski WR, Schmidt-Bäse K, Smith R, Tomchick DR, Benning MM, Winkelmann DA, Wesenberg G, Holden HM (1993) Three-dimensional structure of myosin subfragment-1: a molecular motor. *Science* **261**: 50-58
- Rayment I, Smith C, Yount RG (1996) The active site of myosin. *Annu Rev Physiol* **58**: 671-702
- Reayi A, Arya P (2005) Natural product-like chemical space: search for chemical dissectors of macromolecular interactions. *Curr Opin Chem Biol* **9**: 240-247
- Redowicz MJ (2007) Unconventional myosins in muscle. *Eur J Cell Biol* **86**: 549-558
- Reubold TF, Eschenburg S, Becker A, Kull FJ, Manstein DJ (2003) A structural model for actin-induced nucleotide release in myosin. *Nat Struct Biol* **10**: 826-830
- Richards TA, Cavalier-Smith T (2005) Myosin domain evolution and the primary divergence of eukaryotes. *Nature* **436**: 1113-1118
- Risal D, Gourinath S, Himmel DM, Szent-Györgyi AG, Cohen C (2004) Myosin subfragment 1 structures reveal a partially bound nucleotide and a complex salt bridge that helps couple nucleotide and actin binding. *Proc Natl Acad Sci USA* **101**: 8930-8935
- Ritchie MD, Geeves MA, Woodward SK, Manstein DJ (1993) Kinetic characterization of a cytoplasmic myosin motor domain expressed in Dictyostelium discoideum. *Proc Natl Acad Sci U S A* **90**: 8619-8623
- Rosenfeld SS, Houdusse A, Sweeney HL (2005) Magnesium regulates ADP dissociation from myosin V. *J Biol Chem* **280**: 6072-6079
- Rosenfeld SS, Xing J, Chen LQ, Sweeney HL (2003) Myosin IIb is unconventionally conventional. *J Biol Chem* **278**: 27449-27455
- Rossmann MG, Blow DM (1962) The detection of sub-units within the crystallographic asymmetric unit. *Acta crystallographica* **15**: 24-31
- Sali A, Blundell TL (1993) Comparative protein modelling by satisfaction of spatial restraints. *J Mol Biol* **234**: 779-815
- Sasaki N, Ohkura R, Sutoh K (2000) Insertion or deletion of a single residue in the strut sequence of Dictyostelium myosin II abolishes strong binding to actin. *J Biol Chem* **275**: 38705-38709

- Sasaki N, Shimada T, Sutoh K (1998) Mutational analysis of the switch II loop of Dictyostelium myosin II. *J Biol Chem* **273**: 20334-20340
- Schliwa M, Woehlke G (2003) Molecular motors. *Nature* **422**: 759-765
- Schröder RR, Manstein DJ, Jahn W, Holden H, Rayment I, Holmes KC, Spudich JA (1993) Three-dimensional atomic model of F-actin decorated with Dictyostelium myosin S1. *Nature* **364**: 171-174
- Sellers JR (2000a) Myosins: a diverse superfamily. *Biochim Biophys Acta* **1496**: 3-22
- Sellers JR (2000b) Myosins: a diverse superfamily. *Biochim Biophys Acta* **1496**: 3-22
- Sellers JR, Wang F, Chantler PD (2003) Trifluoperazine inhibits the MgATPase activity and in vitro motility of conventional and unconventional myosins. *J Muscle Res Cell Motil* **24**: 579-585
- Sellin LC, McArdle JJ (1994) Multiple effects of 2,3-butanedione monoxime. *Pharmacol Toxicol* **74**: 305-313
- Shang H, Pan L, Yang S, Chen H, Cheng MS (2010) [Progress in the study of tubulin inhibitors]. *Yao Xue Xue Bao* **45**: 1078-1088
- Shen CH, Shee JJ, Wu JY, Lin YW, Wu JD, Liu YW (2010) Combretastatin A-4 inhibits cell growth and metastasis in bladder cancer cells and retards tumour growth in a murine orthotopic bladder tumour model. *Br J Pharmacol* **160**: 2008-2027
- Shimada T, Sasaki N, Ohkura R, Sutoh K (1997) Alanine scanning mutagenesis of the switch I region in the ATPase site of Dictyostelium discoideum myosin II. *Biochemistry* **36**: 14037-14043
- Sibley LD, Hakansson S, Carruthers VB (1998) Gliding motility: an efficient mechanism for cell penetration. *Curr Biol* **8**: R12-14
- Simerly C, Nowak G, de Lanerolle P, Schatten G (1998) Differential expression and functions of cortical myosin IIA and IIB isotypes during meiotic maturation, fertilization, and mitosis in mouse oocytes and embryos. *Mol Biol Cell* **9**: 2509-2525
- Smith GE, Summers MD, Fraser MJ (1983) Production of human beta interferon in insect cells infected with a baculovirus expression vector. *Mol Cell Biol* **3**: 2156-2165
- Stewart MA, Franks-Skiba K, Chen S, Cooke R (2010) Myosin ATP turnover rate is a mechanism involved in thermogenesis in resting skeletal muscle fibers. *Proc Natl Acad Sci U S A* **107**: 430-435
- Swain JF, Gierasch LM (2006) The changing landscape of protein allostery. *Curr Opin Struct Biol* **16**: 102-108
- Taft MH, Hartmann FK, Rump A, Keller H, Chizhov I, Manstein DJ, Tsiavaliaris G (2008) Dictyostelium myosin-5b is a conditional processive motor. *J Biol Chem* **283**: 26902-26910
- Tang S, Liao JC, Dunn AR, Altman RB, Spudich JA, Schmidt JP (2007) Predicting allosteric communication in myosin via a pathway of conserved residues. *J Mol Biol* **373**: 1361-1373
- Taylor G (2003) The phase problem. *Acta Crystallogr D Biol Crystallogr* **59**: 1881-1890

- Trybus KM, Waller GS, Chatman TA (1994) Coupling of ATPase activity and motility in smooth muscle myosin is mediated by the regulatory light chain. *J Cell Biol* **124**: 963-969
- Tsai CJ, del Sol A, Nussinov R (2008) Allostery: absence of a change in shape does not imply that allostery is not at play. *J Mol Biol* **378**: 1-11
- Uyeda TQ, Ruppel KM, Spudich JA (1994) Enzymatic activities correlate with chimaeric substitutions at the actin-binding face of myosin. *Nature* **368**: 567-569
- Vagin A, Teplyakov A (1997) MOLREP: an Automated Program for Molecular Replacement. *J Appl Crystallogr* **30**: 1022-1025
- Vale RD (1996) Switches, latches, and amplifiers: common themes of G proteins and molecular motors. *J Cell Biol* **135**: 291-302
- Vale RD (2003) The molecular motor toolbox for intracellular transport. *Cell* **112**: 467-480
- Van Der Spoel D, Lindahl E, Hess B, Groenhof G, Mark AE, Berendsen HJ (2005) GROMACS: fast, flexible, and free. *J Comput Chem* **26**: 1701-1718
- Van Dijk J, Furch M, Lafont C, Manstein DJ, Chaussepied P (1999) Functional characterization of the secondary actin binding site of myosin II. *Biochemistry* **38**: 15078-15085
- Veigel C, Schmidt CF (2011) Moving into the cell: single-molecule studies of molecular motors in complex environments. *Nat Rev Mol Cell Biol* **12**: 163-176
- Verdonk ML, Cole JC, Hartshorn MJ, Murray CW, Taylor RD (2003) Improved protein-ligand docking using GOLD. *Proteins* **52**: 609-623
- Verkhovsky AB, Borisy GG (1993) Non-sarcomeric mode of myosin II organization in the fibroblast lamellum. *J Cell Biol* **123**: 637-652
- Verkhovsky AB, Svitkina TM, Borisy GG (1995) Myosin II filament assemblies in the active lamella of fibroblasts: their morphogenesis and role in the formation of actin filament bundles. *J Cell Biol* **131**: 989-1002
- Vicente-Manzanares M, Ma X, Adelstein RS, Horwitz AR (2009a) Non-muscle myosin II takes centre stage in cell adhesion and migration. *Nat Rev Mol Cell Biol* **10**: 778-790
- Vicente-Manzanares M, Ma X, Adelstein RS, Horwitz AR (2009b) Non-muscle myosin II takes centre stage in cell adhesion and migration. *Nat Rev Mol Cell Biol* **10**: 778-790
- von Delius M, Geertsema EM, Leigh DA (2010) A synthetic small molecule that can walk down a track. *Nature Chemistry* **2**: 96-101
- Wagner PD (1981) Formation and characterization of myosin hybrids containing essential light chains and heavy chains from different muscle myosins. *J Biol Chem* **256**: 2493-2498
- Walsh DP, Chang YT (2006) Chemical genetics. *Chem Rev* **106**: 2476-2530
- Wang F, Kovacs M, Hu A, Limouze J, Harvey EV, Sellers JR (2003) Kinetic mechanism of non-muscle myosin IIB: functional adaptations for tension generation and maintenance. *J Biol Chem* **278**: 27439-27448

Warshaw DM, Desrosiers JM, Work SS, Trybus KM (1990a) Mechanical interaction of smooth muscle crossbridges modulates actin filament velocity in vitro. *Prog Clin Biol Res* **327**: 815-826

Warshaw DM, Desrosiers JM, Work SS, Trybus KM (1990b) Smooth muscle myosin cross-bridge interactions modulate actin filament sliding velocity in vitro. *J Cell Biol* **111**: 453-463

Wolf A, Cowen D, Paige B (1939) Human Toxoplasmosis: Occurrence in Infants as an Encephalomyelitis Verification by Transmission to Animals. *Science* **89**: 226-227

6. Publications and Presentations

6.1 Publications:

Chinthalapudi K., Taft M. H., Martin R., Heissler S. M., Preller M., Hartmann F. K., Brandstaetter H., Kendrick-Jones J., Tsiavaliaris G., Gutzeit H. O., Fedorov R., Buss F., Knölker H-J., Coluccio L. M., and Manstein D. J. (2011) Mechanism and specificity of Pentachloropseudilin-Mediated Inhibition of Myosin Motor Activity. *J. Biol. Chem.* 286(34): 29700 -29708

Preller M., Chinthalapudi K., Martin R., Knölker H-J., and Manstein D. J. (2011) Inhibition of ATPase Activity by Halogenated Pseudilins: A Structure-Activity Study. *J. Med. Chem.* 54(11): 3675-3685

Polonais V., Javier Foth B., Chinthalapudi K., Marg J. B., Manstein D. J., Soldati-Favre D., and Frénel K (2011) Unusual Anchor of a Motor complex (MyoD-MLC2) to the Plasma Membrane of *Toxoplasma gondii*. *Traffic.* 12(3): 287-300

Chinthalapudi K., Heissler S. M and Manstein D. J. Crystal Structure of Human Nonmuscle Myosin-2C Motor Domain in Pre-power Stroke State (Manuscript in Preparation)

Chinthalapudi K., Hughes C. C., Fenical W., and Manstein D. J. Structural and Functional Dissection of Allosteric Inhibition of Myosin Motor Domains using Ammosamides (Manuscript in Preparation)

Chinthalapudi K., Heissler S. M. and Manstein D. J. Kinetic and Functional Characterization of Human Nonmuscle Myosin-2A and its Switch-2 Mutant (Manuscript in Preparation)

Publications from Previous work:

Chinthalapudi K., Kumar M., Kumar S., Jain R., Alam N., and Gourinath S. (2008) Crystal Structure of Native O-acetyl-serine-sulfhydrylase from *Entamoeba histolytica* and its Complex with Cysteine: Structural Evidence for Cysteine Binding and Lack of Interactions with Serine Acetyl Transferase. *Proteins.* 72(4): 1222-32

Chinthalapudi K., Jain R., Kashav T., Wadhwa D., Alam N., and Gourinath S. (2007) Crystallization and Preliminary Crystallographic Analysis of Cysteine Synthase from *Entamoeba histolytica*. *Acta Crystallogr. Sec. F.* 63: 512-515

6.2 Poster Presentations

Chinthalapudi K., Taft M. H., Martin R., Hartmann F. K., Tsiavaliaris G., Gutzeit H. O., Fedorov R., Knölker H-J., Coluccio L. M., and Manstein D. J. "Molecular Mechanism of Pentachloropseudilin-Mediated Inhibition of Myosin Motor Activity". Winter School - Soft X-rays in Macromolecular Crystallography" 18.02.2009-20.02.2009, BESSY, Berlin, Germany

Chinthalapudi K., Taft M. H., Martin R., Hartmann F. K., Tsiavaliaris G., Gutzeit H. O., Fedorov R., Knölker H-J., Coluccio L. M., and Manstein D. J. "Molecular Mechanism of Pentachloropseudilin-Mediated Inhibition of Myosin Motor Activity". EMBO practical course: Scientific programming and data visualization for structural biology. 5.5.2010-7.5.2010, Heidelberg, Germany

Chinthalapudi K., Taft M. H., Martin R., Heissler S. M., Preller M., Hartmann F. K., Tsiavaliaris G., Gutzeit H. O., Fedorov R., Knölker H-J., Coluccio L. M., and Manstein D. J. "Molecular Mechanism of Pentachloropseudilin-Mediated Inhibition of Myosin Motor Activity". Myosin, Muscle and Many other Motors Conference, 20/6/2010-26/10/2010, Alpbach, Austria

Curriculum Vitae

Name: Krishna Chinthalapudi
Date of Birth: 23.07.1982
Place of Birth: Srikakulam
Nationality: India

Education:

1999 - 2002 Bachelor of Science (B.Sc.) in Biotechnology
Andhra University, India

2003 - 2005 Master of Science (M.Sc.) in Life Sciences
Jawaharlal Nehru University (JNU), India

Since October, 2007 Doctor of Philosophy (Ph.D.) under the supervision of Prof. Dr. Dietmar J. Manstein, Institute for Biophysical Chemistry, Hannover, Germany

Research Experience:

08.2005-07.2007 Junior Research Fellow, Indian Council of Medical Research (ICMR) Fellowship, under the supervision of Dr. Samudrala Gourinath, JNU, New Delhi, India